

# Manipulation and Read-out of Spins in Quantum Dots



# Manipulation and Read-out of Spins in Quantum Dots

## Proefschrift

ter verkrijging van de graad van doctor  
aan de Technische Universiteit Delft,  
op gezag van de Rector Magnificus prof. dr. ir. J.T. Fokkema,  
voorzitter van het College voor Promoties,  
in het openbaar te verdedigen op woensdag 12 november 2008 om 10:00 uur

door

**Ivo Timon VINK**

natuurkundig ingenieur  
geboren te Alkmaar.

Dit proefschrift is goedgekeurd door de promotoren:

Prof. dr. ir. L. M. K. Vandersypen

Prof. dr. ir. L. P. Kouwenhoven

Samenstelling van de promotiecommissie:

Rector Magnificus,

voorzitter

Prof. dr. ir. L. M. K. Vandersypen Technische Universiteit Delft, promotor

Prof. dr. ir. L. P. Kouwenhoven Technische Universiteit Delft, promotor

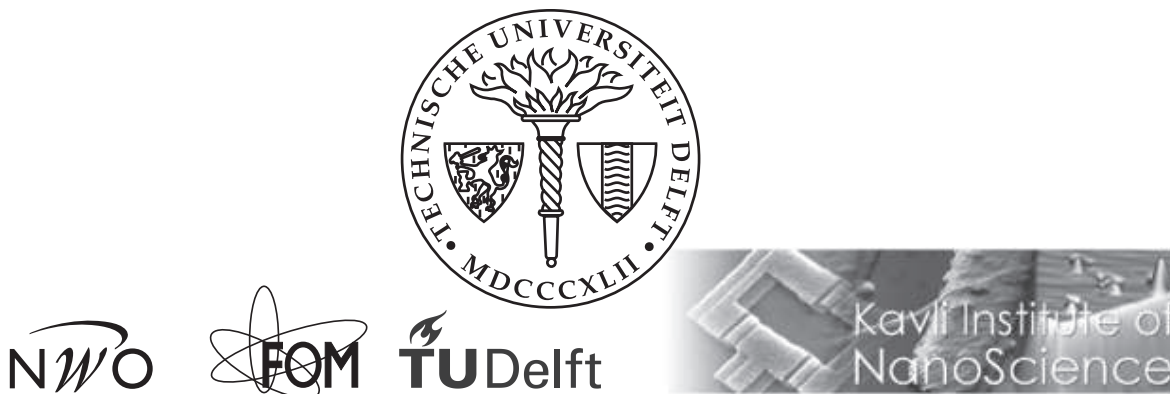
Prof. dr. K. Ensslin Eidgenössische Technische Hochschule Zürich,  
Zürich, Zwitserland

Prof. dr. D. M. Zumbühl University of Basel, Basel, Zwitserland

Prof. dr. S. G. Lemay Technische Universiteit Delft

Prof. dr. ir. H. S. J van der Zant Technische Universiteit Delft

Dr. ir. C. H. van de Wal Rijksuniversiteit Groningen



*Published by:* Ivo Vink

*Coverdesign:* Thomas Dieben, denieuwegeneratie architecten vormgevers, Amsterdam

*Coverimage:* Real-time single electron tunneling to and from a quantum dot  
measured by an adjacent QPC charge sensor.

*Printed by:* Printpartners Ipskamp, Enschede

ISBN: 978-90-8593-043-3

Casimir PhD Series, Delft-Leiden 2008-04

Copyright © 2008 by Ivo Vink

An electronic version of this thesis is available at [www.library.tudelft.nl/dissertations](http://www.library.tudelft.nl/dissertations)

# Preface

When I joined the Quantum Transport group (QT) in 2003 to do my MSc research I thought that it would be my last year in physics and that one year later I would be working in industry somewhere, like many of my friends. I did really like to study physics but I just didn't see myself continuing in physics. Mainly because I expected the people to be ... let's put it this way ... the stereotype physicist, and I didn't think I would fit in. This turned out to be far from the truth as I experienced during my MSc research. QT is an extremely energetic and enthusiastic group of people not only sharing a passion for physics but also interest in sports, cinema, music etc. From day one I felt at home and I started to enjoy doing physics even more than I already did.

At the end of that year I had to decide what to do next, and by then I knew that the thing I would enjoy most for the next 4 years would be doing a PhD. The next question was where to do it. On top of good facilities and infrastructure, a lot of knowledge and scientific output, QT is just a great bunch of people. For me this was the decisive factor to stay in the group for my PhD. Since I didn't want it to feel like a continuation of the MSc project I wanted to go abroad for some time so before starting the PhD. The good contacts of the group were used and I had the opportunity to work in Robert Schoelkopf's group at Yale and in Don Eiglers lab at the IBM Almaden Research Center in California.

In October 2004 I rejoined the spin-qubit team that consisted at that time of Jeroen Elzerman, Ronald Hanson, Laurens Willems van Beveren and Frank Koppens, supervised by Lieven Vandersypen and Leo Kouwenhoven. The research in this thesis has been done in this spin-qubit team and I would like to express my thanks to everybody who was a part of this team.

I'll start with my advisor Lieven Vandersypen. Lieven, I would like to thank you for all the freedom you give us in the lab. Even though you have expanded your empire to include graphene (searching for the 'perfect qubit'), you still manage to be on top of things and to structure the research that is going on in your lab. Thanks for teaching me how to present physics (even by dancing). Jeroen, you introduced me to the world of quantum dots and were able to explain everything in such a calm and clear way! Ronald, Ronnie, S-prof, I would like

to thank you for not only being a great supervisor and sparring partner, but a friend in general. It's good to have you back in Delft! Laurens, Lauie, Kunnykun, the guy who thought me the fine art of nanoscale fabrication and how to dance with a dilution refrigerator. Thanks for the (nightly) bike rides and for always being able to cheer people up. Frank (Houje) Koppens, it will be quiet in the corridors now nobody is around to produce strange sounds. You're always welcome to climb through my window again! Katja, you are a wonderful person. I enjoyed working with you as much as having fun outside of the lab. Enfin, I hope that your excellent Dutch will not deteriorate into Flemish. Tristan, I guess I have thank you for teaching me more about myself than about physics. Lars and Floris, good luck on the CPHASE, I really hope you will make it work! Furthermore I must not forget to thank the students who chose to do a MSc project in the Spin-Qubit Team. Jort, Benoit, Wouter, Christo, Klaas-Jan, Han and Victor, thanks for leaving your marks on B-057/B-059.

During this PhD I was fortunate to work closely together with three students, who were crucial for the results, understanding and fun in the lab. Tjitte, the guy who can see electrons tunnel real-time within 400 ns using his famous 4-threshold stepfinder routine, while at the same time watching music videos of Katja Schuurman on a €12.000,- oscilloscope. It was a lot of fun chasing sources of interference and gift wrapping the new helium liquefier with you! Shi-Chi, your new measurement program has set a new standard for QT. It was nice to have you in the lab when we got up close and personal with those damn nuclei. Ryan, it was great to see you work with such a motivation that you would lose track of time completely (or do you actually live in a different time zone?). Next time I have to break out of the physics building at 05:00 am I will call you for advice! Thanks for taking charge detection to a next level.

Besides MSc and BSc students, I also had the pleasure to introduce first-year students into the quantum world. "Thanks" for showing me that first-year students can do the same measurements as a PhD student.

Many of the experiments in this thesis (probably honest to say *all* of the experiments) were not possible without Raymond Schouten. When I joined QT electronics was more or less just a black (or galvanic) box to me. I am glad that I had the opportunity to work with you and learning how to get insight in electronic circuits and how to measure the tiniest of signals. I'm curious what kind of creations the 'vrijdagmiddag experimentjes' will lead to in the future.

When you can measure these tiny signals but don't understand them it is good to have friends in theory departments all over the world. Discussions with Daniel Loss, Hansres Engel and Daniel Klauser from Basel, and Leonid Levitov and Mark Rudner from MIT helped tremendously to better understand the electron

and nuclear spin dynamics. I would especially like to thank Jeroen Danon and Yuli Nazarov. I enjoyed bringing theory and experiment together with you!

Whenever I had problems with pumps, fridges, helium, or whatever, I just had to track down the source of the whistling in the corridors (outside 'het stiltecentrum'): Bram. Thanks a lot for all the practical help, your 'AIO-heropvoedingcentrum', your stories and humor during the coffee breaks and for showing me how easy it is to say 'no' to everybody. Remco, I really am trying to make it to the Spartaan one day. It's nice to have you and Peter (the new Jut & Jul) sneaking through the corridors. I'm grateful to Bram, Remco, Peter, Wim and Willem for quenching the thirst of our dot-fridges with about 30.000 liters of liquid helium. I would also like to complement Pfeiffer for making turbo pumps that run for weeks without the necessary cooling water.

Yuki, Angèle and Ria, thank you for the paperwork and all other support. Yuki, I'm glad we finally started the shabu-shabu / tempura exchange program.

Research on solid state quantum information processing has many shapes and forms. Electron spins in lateral GaAs quantum dots is only one approach that QT has to offer. Hans and Leo have created a scientific Walhalla where many people work on many system towards a common goal. Hans and Leo, thanks for making QT such a unique place and the scientific staff for keeping it this way. Hans, teaching first-year students with you was very educational (for me as well). Even though it was really time consuming I had a lot of fun doing it. I would like to thank Leo for showing that enthusiasm is nothing without a focus. I admire your amazing sense of direction for scientific research. If you need a real-size Spinoza in your living room again you know who to call! Kees, you keep amazing me with your physical intuition as well as your discrimination of 'hangmokken'. Val, your enthusiasm is really contagious. I'm looking forward to the next chapter of the Rubidium Saga. And Ad, I hope the quantum phase will slip soon! It is time for another qubit in our QT collection.

I would like to thank all former group members for making QT what it is today. Especially Alexander ter Haar, Silvano de Franceschi, Jorden van Dam and Hubert Heersche (the former Jut & Jul).

There are some people in QT who deserve a special thanks: Pieter, I want you to know how much I appreciated our discussions about physics, religion, etc. You (and your sound system) made F-031 home-base. I'm glad I have you in my Entourage<sup>TM</sup>, be it on the other side of the desk or upstairs! Floris, you are one of the gluons that hold a group like QT together. Thanks for being direct (or is it blunt?) and – never gonna give you up, never gonna let you down ... – the coffee break reminders. Let's do your chicken dance Down Under some time! Gary, thanks for all discussions, bike rides, parties in Dublin, whiskies and of

course the Garypedia. Reinier, good luck with sticking photons to a surface and installing x-terminals on everything you get your hands on. Maarten van Kouwen, I hope your PC, EL, LED, EILE, LEBEHR, and all other experiments one can abbreviate will succeed in the coming year. Juriaan, hardcore-shell nanowire man, no doubt that next year some beautiful dots will be formed in B-013. And Floor, I'm glad the gap could be tuned in the nick of time! Finally, I wish all other PhD students the best results and a lot of fun obtaining them!

Experiments in the lab do not work out without fun outside the lab. I must not forget to thank my VvTP-board, studievriendjes and former housemates of Brabantse Turfmarkt 70. Thomas Dieben, many thanks for designing the cover of this thesis - très, très chique! Erik Henstra, thanks for the 'borreltjes', dinners and for your collection of 'Hennies films'. Jur, I liked your surprise attacks to trick me into a bike ride or a dinner! And Jo-tje, borrelqueen of the foute vrijdag, thanks for all the 'kleine drankjes' that always turn out not to be that small.

Sander, Buul, I have always appreciated your interest in what I was doing and physics in general. I'm happy that you will sit in front of me during the defence. And Jelle, we miss you in the group. I'm glad you'll be sitting next to Sander! And of course that you'll be escalating one more party out of hand.

I would like to take this opportunity to apologize to everybody for the times I was too busy to pick up my phone, reply to your emails, had to cancel appointments or show up too late. Mea maxima culpa! Thanks for your patience and understanding!

I thank my parents and my brother for their unconditional and continuous love and support in everything I do. And last but not least, I would like to thank Hotmail for their long-term email storage and Sietske for making good use of that. Thanks for being who you are!  $\infty$

Ivo Vink

Delft, October 2008





# Contents

<b>1</b>	<b>Introduction</b>	<b>1</b>
1.1	Quantum mechanics . . . . .	1
1.2	Computing in a quantum world . . . . .	2
1.3	Quantum bits . . . . .	2
1.4	Single spins as quantum bits . . . . .	4
1.5	Outline of this thesis . . . . .	6
	References . . . . .	8
<b>2</b>	<b>Quantum dots and measurement techniques</b>	<b>9</b>
2.1	Quantum dots . . . . .	9
2.2	Confining electrons in a semiconductor . . . . .	10
2.3	Device fabrication . . . . .	10
2.4	Measurement setup . . . . .	12
2.4.1	Dilution refrigerator and device cooling . . . . .	12
2.4.2	Measurement electronics . . . . .	13
2.4.3	Measurement wires . . . . .	15
2.4.4	Filtering . . . . .	16
2.4.5	High-frequency signals . . . . .	16
	References . . . . .	19
<b>3</b>	<b>Spin states of confined electrons and interactions with their environment</b>	<b>21</b>
3.1	Electron spin states in a single quantum dot . . . . .	22
3.2	Double dot spin states . . . . .	24
3.2.1	Pauli spin blockade . . . . .	25
3.3	Singlet-triplet mixing by the nuclear spins . . . . .	26
3.4	Relaxation and decoherence . . . . .	29
3.5	Spin-orbit interaction . . . . .	31
3.6	Interaction with the nuclear spin bath . . . . .	32
3.6.1	Hyperfine interaction . . . . .	32

3.6.2	Spin dephasing due to the nuclear field . . . . .	34
3.6.3	Spin decoherence due to nuclear dynamics . . . . .	35
	References . . . . .	37
<b>4</b>	<b>Single-shot read-out of two-electron spin states using spin-dependent tunnel rates</b>	<b>41</b>
4.1	Read-out of electron spin states . . . . .	42
4.1.1	Spin read-out scheme using spin-dependent tunnel rates . .	42
4.1.2	Measurement visibility of the read-out . . . . .	44
4.1.3	Single-shot read-out of the two-electron spin states . . . .	45
4.1.4	Magnetic field dependence of the triplet-to-singlet relaxation	48
4.1.5	Read-out of nearly degenerate states . . . . .	49
4.2	Repeated measurements . . . . .	50
4.2.1	Short read-out pulses . . . . .	50
4.2.2	Single measurement . . . . .	52
4.2.3	Repeated measurements . . . . .	52
4.2.4	Varying the time between measurements and the measurement time . . . . .	53
4.3	High-fidelity measurements of two-electron spin states . . . . .	56
4.3.1	Energy-selective read-out of the two-electron spin states with spin-dependent tunnel rates . . . . .	57
4.3.2	Measurement fidelity of the read-out . . . . .	59
4.4	Summary . . . . .	60
	References . . . . .	61
<b>5</b>	<b>Experimental signature of phonon-mediated spin relaxation</b>	<b>63</b>
5.1	Introduction . . . . .	64
5.2	Device and characterization . . . . .	65
5.3	Determination of the singlet-triplet splitting . . . . .	65
5.4	Singlet-triplet relaxation time as a function of their energy splitting	67
5.5	A simple model for the phonon mediated relaxation . . . . .	68
5.6	Discussion . . . . .	70
	References . . . . .	72
<b>6</b>	<b>A cryogenic amplifier for fast real-time detection of single-electron tunneling</b>	<b>75</b>
6.1	Introduction . . . . .	76
6.2	Charge detection setup . . . . .	76
6.2.1	Probing current fluctuations with a HEMT . . . . .	77

6.2.2	DC-biasing of the HEMT . . . . .	77
6.2.3	Amplifying AC-signals . . . . .	79
6.2.4	Other parts of the setup . . . . .	79
6.3	Determination of the bandwidth . . . . .	81
6.4	Sources of noise . . . . .	81
6.4.1	HEMT current noise . . . . .	81
6.4.2	HEMT voltage noise . . . . .	84
6.4.3	QPC shot noise . . . . .	85
6.5	Measurement of real-time tunneling of single electrons . . . . .	85
6.6	Conclusion and recommendations . . . . .	87
	References . . . . .	88
<b>7</b>	<b>Improving the cryogenic charge detection setup</b>	<b>91</b>
7.1	Introduction . . . . .	92
7.2	HEMT amplifier test circuit . . . . .	92
7.3	Biasing the HEMT . . . . .	93
7.3.1	Different HEMT dissipations . . . . .	93
7.3.2	Optimal DC bias point . . . . .	96
7.4	Transconductance and output impedance . . . . .	98
7.5	HEMT voltage noise spectra . . . . .	99
7.5.1	Most suitable HEMT . . . . .	101
7.6	Improvements of the charge detection setup . . . . .	102
7.6.1	Signal amplitude . . . . .	102
7.6.2	Noise contributions . . . . .	104
7.6.3	Signal-to-noise ratio . . . . .	106
7.7	Conclusions . . . . .	106
	References . . . . .	107
<b>8</b>	<b>Driven coherent oscillations of a single electron spin in a quantum dot</b>	<b>109</b>
8.1	Introduction . . . . .	110
8.2	Device and ESR detection concept . . . . .	111
8.3	Role of the nuclear spin bath for ESR detection . . . . .	113
8.4	ESR spectroscopy . . . . .	114
8.5	Coherent Rabi oscillations . . . . .	116
8.6	Theoretical model . . . . .	118
8.7	Time evolution of the spin states during RF bursts . . . . .	119
8.8	Quantum gate fidelity . . . . .	119
8.9	Additional material . . . . .	121

8.9.1	Generation of the oscillating magnetic field . . . . .	121
8.9.2	Photon assisted tunneling due to electric fields . . . . .	121
8.9.3	Lifting spin blockade by nuclear spins or ESR: additional figures . . . . .	126
	References . . . . .	126
<b>9</b>	<b>Locking electron spins into resonance by electron-nuclear feed-back</b>	<b>129</b>
9.1	Introduction . . . . .	130
9.2	Reverse dynamic nuclear spin polarization . . . . .	131
9.3	Sweep rate and power dependence . . . . .	133
9.4	Dragging the nuclear spin polarization . . . . .	133
9.5	Spontaneous nuclear spin depolarization . . . . .	136
9.6	Mechanisms for nuclear spin pumping . . . . .	137
9.7	Conclusion and recommendations . . . . .	139
	References . . . . .	140
<b>10</b>	<b>Conclusions and future directions</b>	<b>141</b>
10.1	Current status . . . . .	142
10.2	Improvements and future directions . . . . .	143
10.2.1	Spin qubit read-out . . . . .	143
10.2.2	Longer coherence times . . . . .	144
10.2.3	Improving qubit gates . . . . .	147
10.2.4	Scalability . . . . .	148
10.3	Conclusions . . . . .	149
	References . . . . .	150
<b>A</b>	<b>Singlet-Triplet relaxation as a function of their energy splitting</b>	<b>153</b>
A.1	Spin-orbit interaction . . . . .	153
A.2	Electron-phonon interaction . . . . .	154
A.3	Transition rates . . . . .	156
	References . . . . .	158
	<b>Summary</b>	<b>159</b>
	<b>Samenvatting</b>	<b>163</b>
	<b>Curriculum Vitae</b>	<b>167</b>
	<b>List of publications</b>	<b>169</b>

# Chapter 1

## Introduction

### 1.1 Quantum mechanics

For a little over 300 years, physicists have been studying the forces of nature. In 1687 Isaac Newton published his famous *Philosophiæ Naturalis Principia Mathematica* which forms the (mathematical) foundation of classical mechanics. This framework, together with Maxwell's theory of electromagnetism, accurately describes most of the world as we experience it in our daily lives.

However, at the end of the 19th century it became apparent that these classical theories fail to describe matter at the atomic scale. For instance, they can neither explain phenomena such as the photoelectric effect (where electrons are emitted from matter after the absorption of radiation) nor why the negatively charged electron does not collapse onto the positive atomic nucleus. So physicists set out to develop a theory that could explain the weird behavior of small particles and light.

The result was the theory of quantum mechanics, which emerged in the 1920s. This theory has a number of properties that are very counter-intuitive, e.g. it ascribes to all particles a wave function, responsible for intriguing effects such as energy quantization, interference and tunneling through classically impenetrable barriers. Amongst other things, it describes how electrons propagate through materials, the processes which cause light emission, and the microscopic origin of magnetism.

The great success of quantum mechanics leads many scientists to believe that quantum mechanics is a true fundamental theory of nature, of which the classical theories just represent a limiting case. How this 'macroscopic' classical world emerges from the 'microscopic' quantum world is still subject of debate [1].

Quantum mechanics has also resulted in well-known applications such as lasers and Magnetic Resonance Imaging (MRI). The transistor, the fundamental build-

ing block of computers and other modern electronic devices, was invented by scientists who were studying electronic behavior at the interface of a metal and a semiconductor.

## 1.2 Computing in a quantum world

The processing power of a classical computer depends on the number of transistors on the microprocessor. Due to advancing fabrication technologies this number has increased dramatically in the last decades to a stunning 800 million transistors per chip. These transistors have dimensions of only 45 nm. This is so small that more than 10 million transistors fit onto a space no bigger than the tip of a pen. Being this small, these transistors do no longer behave completely classical. Effects such as quantum mechanical tunneling, which results in gate leakage currents, pose one of the most difficult obstacles for further decreasing the transistor size.

Rather than viewing the quantum mechanical behavior as a problem for future computers, we might ask ourselves whether it is possible to actually *use* quantum phenomena for computing. One approach is to integrate a quantum property in a computing scheme based on classical logic. For example, the field of *spintronics* aims to use the spin degree of freedom of electrons as a carrier of classical information [2]. Alternatively, we can try to build a computer that exploits the unique features of quantum mechanics to perform computations that are not possible classically: a *quantum computer*.

## 1.3 Quantum bits

To build such a quantum computer we need quantum bits, the building blocks for quantum information processing. A quantum bit (qubit) is the quantum mechanical analog of a classical bit (binary digit), which is a two-level system taking a value of either 0 or 1. A qubit is a quantum mechanical system and therefore obeys the laws of quantum mechanics rather than classical mechanics. Two important consequences of quantum mechanics, essential to quantum computing, are that states of a qubit can be in a *superposition*, and that qubits can be *entangled*.

Unlike a classical two-level system, which is always either in state 0 or in state 1, a quantum two-level system can be state 0 *and* state 1 at the same time. In that case the qubit is in a so-called *superposition* of states  $|0\rangle$  and  $|1\rangle$ :  $\alpha|0\rangle + \beta|1\rangle$ , where the coefficients  $\alpha$  and  $\beta$  are the probability amplitudes of the

states  $|0\rangle$  and  $|1\rangle$ , which have to satisfy  $|\alpha|^2 + |\beta|^2 = 1$ . The evolution of this system is deterministic, as it is governed by a first-order differential equation – the Schrödinger equation. However, coupling this quantum system to a measurement apparatus forces it into one of the possible measurement eigenstates in an apparently non-deterministic way: the particular measurement outcome is random, only the probability for each outcome can be determined [3] ( $|\alpha|^2$  for  $|0\rangle$ , and  $|\beta|^2$  for  $|1\rangle$ ). What exactly constitutes a measurement, which seems to be closely related to the transition from quantum to classical behavior, is not fully understood [4].

The second property of quantum mechanics we need is one which has been the subject of debate for many years: *entanglement*. By interacting with each other, two quantum two-level systems can become entangled, which means that we cannot describe one system independently of the other. For example, the state  $(|01\rangle - |10\rangle)/\sqrt{2}$  gives a complete description of the whole system, but the two subsystems do not have a definite state. Due to this strong connection between the two systems, a measurement made on one, which forces it into one of the two states  $|0\rangle$  or  $|1\rangle$ , immediately influences the state of the other, even though it may be arbitrarily far away. People have questioned whether it is not just a lack of our knowledge of some ‘hidden variable’ that hinders the prediction of a measurement outcome. However, measurements on so-called EPR pairs of photons (named after a famous thought experiment by Einstein, Podolsky and Rosen [5]) have clearly shown that the non-local correlations between the photons are significantly larger than permitted by any local hidden-variable theory [6, 7]. Thus, entanglement is real, and constitutes one of the essential resources for quantum computing.

Both the superposition principle and entanglement allow  $N$  qubits to represent  $2^N$  values at the same time. Since a quantum computer can process all these values at the same time, it can be exponentially faster than its classical counterpart. on first sight it may seem that this exponential computation power is not accessible. After the computation, the system will be in a superposition of measurement outcomes but, according to quantum mechanics, a measurement of the system will only yield one possible outcome. However, carefully designed algorithms (for solving certain problems) ensure that the measurement outcome yields the answer to that problem. Using such quantum algorithms, a quantum computer can indeed be far more efficient than a classical one, performing tasks that would take a classical computer as long as the lifetime of the universe. As thinking about quantum algorithms has only barely begun, it is not unreasonable to assume that more applications of quantum computing will be discovered in the future.

Another fundamental issue is the interaction of the quantum system with the (uncontrolled) environment, which inevitably disturbs the desired quantum evolution. This process, known as ‘decoherence’, results in errors in the computation. Additional errors are introduced by imperfections in the quantum operations that are applied. Fortunately, if the errors induced by decoherence are small enough, it is possible to detect and correct them faster than they propagate [8, 9]. Such methods only help if the error rate is small enough, which sets a so-called ‘accuracy threshold’ [10, 11]. This threshold is currently believed to be around  $10^{-4}$ , and implies that at least  $10^4$  qubit operations should be performed within the qubit coherence time.

Due to the development of quantum algorithms and error correction, quantum computation is feasible from a theoretical point of view. The challenge is building an actual quantum computer with a sufficiently large number of coupled qubits. Probably, more than a hundred qubits will be required for useful computations, but a system of about thirty qubits might already be able to perform valuable simulations of quantum systems.

Any quantum two-level system can in principle function as a qubit, but for a scalable quantum computer a number of additional features are required [12]. Essentially, we have to reconcile the conflicting demands of good access to the quantum system (in order to perform fast and reliable operations or measurements) with sufficient isolation from the environment (for long coherence times). Current state-of-the-art is a seven-bit quantum computer, built up from the nuclear spins of molecules in a liquid solution. In this system, Shor’s factoring algorithm has been demonstrated on the number 15 using nuclear magnetic resonance (NMR) techniques [13]. Practical limitations do not allow the NMR approach to be scaled up to more than about ten qubits. Therefore, many other implementations are currently being studied.

## 1.4 Single spins as quantum bits

Typically, microscopic systems such as atoms or ions have good coherence properties, but are not easily accessible or scalable; on the other hand, larger systems such as solid-state devices can be accessed and scaled more easily, but often lack a long coherence time. A solid-state device with a long coherence time would represent the best of both worlds.

Precisely such a system was proposed by Loss and DiVincenzo [14] in 1997: the spin orientation of a single electron trapped in a semiconductor quantum dot. An electron spin can point ‘up’ or ‘down’ with respect to an external magnetic



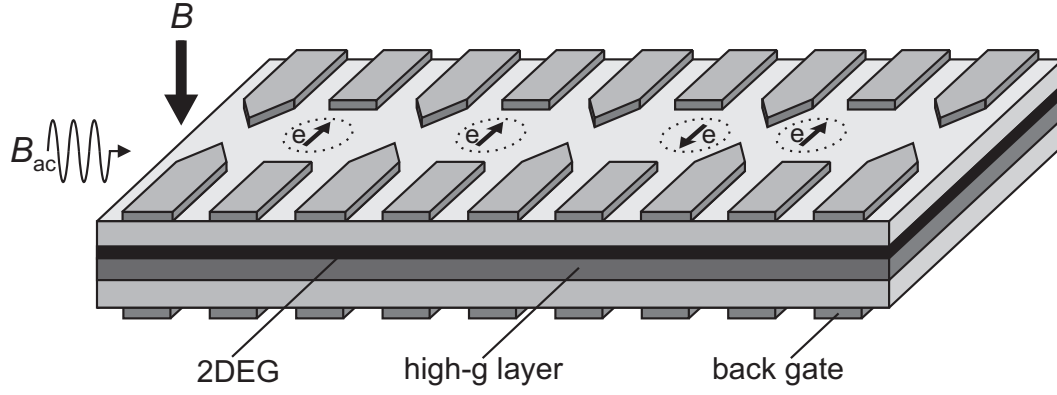


**Figure 1.1:** Schematic picture of the electron spin quantum computer as proposed by Loss and DiVincenzo [14]. The array of metal electrodes on top of a semiconductor heterostructure, containing a two-dimensional electron gas (2DEG) below the surface, defines a number of quantum dots (dotted circles), each holding a single electron spin (arrow). A magnetic field,  $B$ , induces a Zeeman splitting between the spin-up and spin-down states of each electron spin. The spin state is controlled either via an oscillating magnetic field,  $B_{ac}$  (on resonance with the Zeeman splitting), or via an oscillating electric field created with the back gates, which can pull the electron wavefunction into a layer with a large  $g$ -factor. Coupling between two spins is controlled by changing the voltage on the electrodes between the two dots. (Adapted from Ref. [14].)

field. These eigenstates,  $|\uparrow\rangle$  and  $|\downarrow\rangle$ , correspond to the two basis states of the qubit.

The electron is trapped on a quantum dot, which is basically a small electrically defined box with a discrete energy spectrum. The quantum dots that we use are defined by metal gate electrodes on top of a semiconductor (GaAs/AlGaAs) heterostructure (see Fig. 1.1). At the interface between GaAs and AlGaAs, conduction band electrons accumulate which can only move in the lateral direction, forming a two-dimensional electron gas (2DEG). Applying negative voltages to the surface gate electrodes locally depletes this 2DEG underneath these gates. The resulting quantum dots are very controllable and versatile systems, which can be manipulated and probed electrically. With the external magnetic field we can tune the energy splitting (Zeeman splitting) between  $|\uparrow\rangle$  and  $|\downarrow\rangle$ . In this way, two states of the qubit are energetically distinguishable.

To perform single-qubit operations, we can apply a microwave magnetic field on resonance with the Zeeman splitting. The oscillating magnetic component perpendicular to the static magnetic field results in a spin nutation. By applying the oscillating field for a fixed duration, a superposition of  $|\uparrow\rangle$  and  $|\downarrow\rangle$  can be created. This magnetic technique is known as electron spin resonance (ESR) [15].

Two-qubit operations can be carried out purely electrically, by varying the gate voltages that control the potential barrier between two dots. It has been shown [14] that the system of two electron spins on neighboring dots, coupled via a tunnel barrier, interacts via the Heisenberg exchange interaction. The strength of this interaction depends on the overlap of the electron wave functions, and can be controlled electrically. By turning on the two-spin interaction for a certain well-defined time, the two electron spins can be swapped or even entangled [16]. With combinations of arbitrary single-spin rotations and the two-spin interaction, any quantum gate can be implemented [14].

A last crucial ingredient is a method to read out the state of the spin qubit. This implies measuring the spin orientation of a single electron – a daunting task, since the electron spin magnetic moment is exceedingly small (equal to the Bohr magneton). Therefore, an indirect spin measurement is proposed [14]. First the spin orientation of the electron is correlated with its position, via ‘spin-to-charge conversion’. Then an electrometer is used to measure the position of the charge, thereby revealing its spin. In this way, the problem of measuring the spin orientation has been replaced by the much easier measurement of charge [17].

Finally, it should be stressed that our efforts to create a spin qubit are not purely application-driven but also to study fundamental physics. Having the ability to control and read out a single electron spin, we are in a unique position to study the interaction of the spin with its environment. This may lead to a better understanding of the physical processes that lead to decoherence, and allows us to study the semiconductor environment using the electron spin as a probe.

## 1.5 Outline of this thesis

This thesis describes a series of experiments aimed at understanding and controlling single electron spins confined in a semiconductor quantum dot, with the long-term goal of creating a small-scale quantum computer. The first chapters cover experiments aimed at one key ingredient for solid state quantum information processing: reading out the spin state. The following chapters describe another necessary ingredient: the coherent manipulation of a single electron spin.

*Chapter 2* starts by explaining the devices we use to isolate the single electron spins for our experiments: gate defined (double) quantum dots. In *chapter 3*, we continue to discuss the theory of electron spin states in (double) quantum dots and the most important interactions of the electron spin with its environment. These are the electron-phonon interaction together with the spin-orbit coupling,

and the hyperfine interaction with the nuclear spins in the host lattice.

In *chapter 4* we demonstrate one of the key ingredients for a quantum computer: single-shot read-out of the spin states. To convert the spin information to charge information, we have exploited spin-dependent tunnel rates, achieving a measurement visibility of more than 80%. We find that the relaxation can be very slow, with relaxation times up to milliseconds. We find a strong magnetic field dependence that hints at spin-orbit interaction as the dominant relaxation mechanism. Reducing the length of the read-out pulse together with fast reinitialization of the spin state allows us to perform repeated measurements, used to probe the evolution between two consecutive measurements. At the end of this chapter, we demonstrate that, if we not only exploit spin-dependent tunnel rates but spin-dependent energies as well, the read-out fidelity increases to 97.5%.

One key advantage of the tunnel rate selective read-out, the ability to read out (nearly) degenerate spin states, will be used in *chapter 5*. We vary the singlet-triplet energy splitting over a wide range by changing the electric and magnetic confinement, and measure the singlet-triplet relaxation time. The observed dependence on the energy splitting confirms that the spin-flip energy is dissipated in the phonon bath.

The following two chapters cover a novel approach to fast charge detection. This should increase the spin read-out fidelity and enable us to study faster real-time electron and nuclear dynamics. *Chapter 6* demonstrates that a cryogenic High Electron Mobility Transistor (HEMT) amplifier can be used to increase the bandwidth of a charge detection setup with a quantum point contact (QPC) charge sensor to 1 MHz. This setup is able to detect fluctuations in the occupation of an adjacent quantum dot as short as 400 nanoseconds. The equivalent input noise of the HEMT turns out to limit the signal-to-noise ratio. We investigate whether we can decrease the noise by using different (biasing of the) HEMTs and propose a setup with an improved signal to noise ratio in *chapter 7*. This chapter end the part of the thesis which is focused on reading out the spin states. The following chapters cover experiments on (coherent) manipulation of the electron spin.

In *chapter 8* we present the coherent manipulation of a single electron spin. By generating bursts of an oscillating magnetic field at the location of the quantum dot, we induce Rabi oscillations of the electron spin. The coherence properties of the electron spin are determined by its interaction with the nuclear spins of the host lattice. In *chapter 9* we study this interaction and try to use it in order to extend the electron spin coherence time. Concluding remarks and future directions will be presented in *chapter 10*.

## References

- [1] A. J. Leggett, A. Garg, Phys. Rev. Lett. **54**, 857 (1985), and A.J. Leggett, J. Phys. Condens. Matter **14**, R415 (2002).
- [2] S.A. Wolf *et al.*, Science **294**, 1488 (2001).
- [3] R.P. Feynman, *The Feynman Lectures on Physics*, Vol. 3 (Addison Wesley, 1970).
- [4] V.B. Braginsky and F.Y. Khalili, *Quantum Measurement* (Cambridge University Press, 1992).
- [5] A. Einstein, B. Podolsky, and N. Rosen, Phys. Rev. **47**, 777 (1935).
- [6] A. Aspect, P. Grangier, and G. Roger, Phys. Rev. Lett. **49**, 91 (1982).
- [7] J.S. Bell, *Physics* **1**, 195 (1964); S.J. Freedman and John Clauser, Phys. Rev. Lett. **28**, 14 (1972).
- [8] P.W. Shor, *Proceedings of 37th Annual Symposium on Foundations of Computer Science*, 56 (IEEE Press, 1996).
- [9] A.M. Steane, Phys. Rev. Lett. **77**, 793 (1996).
- [10] A.Y. Kitaev, *Quantum Communication, Computing, and Measurement*, edited by A.S. Holevo, O. Hirota and C.M. Caves, 181 (Plenum Press, 1997).
- [11] D. Aharonov and M. Ben-Or, quant-ph/9906129 (1999).
- [12] D.P. DiVincenzo, Fortschr. Phys. **48**, 771 (2000).
- [13] L.M.K. Vandersypen *et al.*, Nature **414**, 883 (2001).
- [14] D. Loss and D.P. DiVincenzo, Phys. Rev. A **57**, 120 (1998).
- [15] F.H.L. Koppens *et al.*, Nature **442**, 766-771 (2006).
- [16] J.R. Petta *et al.*, Science **309**, 2180 (2005).
- [17] J.M. Elzerman *et al.*, Nature **430**, 431 (2004).

## Chapter 2

# Quantum dots and measurement techniques

### 2.1 Quantum dots

A quantum dot is simply a small box that can be filled with electrons. The box is coupled via tunnel barriers to a source and drain reservoir, with which particles can be exchanged (see Fig. 2.1). By attaching current and voltage probes to these reservoirs, we can measure the electronic properties of the dot. The dot is also coupled capacitively to one or more ‘gate’ electrodes, which can be used to tune the electrostatic potential of the dot with respect to the reservoirs. When the size of the dot is comparable to the wavelength of the electrons that occupy it, the system exhibits a discrete energy spectrum, resembling that of an atom [1].

Because a quantum dot is such a general kind of system, there exist quantum dots of many different sizes and materials: for instance single molecules trapped between electrodes, metallic or superconducting nanoparticles, self-assembled quantum dots, semiconductor lateral or vertical dots, and also semiconductor nanowires or carbon nanotubes between closely spaced electrodes. In this thesis, we focus on lateral (gated) semiconductor quantum dots [2]. A big advantage of these lateral devices is that all relevant parameters can be controlled *in situ* which allows us to perform experiments which cover a wide range of parameter space with the same sample (design).

In this thesis, two different ways are used to probe the behavior of electrons on a quantum dot. In chapter 8 and 9, we measure the current due to transport of electrons through the dot, and in chapters 4, 5 and 6 we use an adjacent charge sensor to detect changes in the number of electrons on the dot.

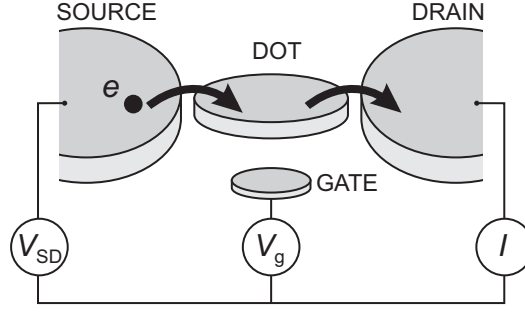


**Figure 2.1:** Schematic picture of a quantum dot in a lateral geometry. The quantum dot (represented by a disk) is connected to source and drain contacts via tunnel barriers, allowing the current through the device,  $I_{DOT}$ , to be measured in response to a bias voltage,  $V_{SD}$  and a gate voltage,  $V_g$ .

## 2.2 Confining electrons in a semiconductor

Confining electrons in a semiconductor starts by using a semiconductor heterostructure, a sandwich of different layers of semiconducting material, as illustrated in Fig. 2.2a. These layers, in our case GaAs and AlGaAs, are grown on top of each other using molecular beam epitaxy (MBE), resulting in very clean crystals. By doping the n-AlGaAs layer with Si, free electrons are introduced. These accumulate at the interface between GaAs and AlGaAs, typically 100 nm below the surface, forming a two-dimensional electron gas (2DEG) – a thin ( $\sim 10$  nm) sheet of electrons confined to two dimensions that can only move along the interface. The 2DEG can have a high mobility and relatively low electron density (typically  $10^5 - 10^6$  cm<sup>2</sup>/Vs and  $\sim 3 \times 10^{15}$  m<sup>-2</sup>, respectively). The low electron density results in a large Fermi wavelength ( $\sim 40$  nm) and a large screening length, which allows us to locally deplete the 2DEG with an electric field. This electric field is created by applying (negative) voltages to metal gate electrodes on top of the heterostructure (Fig. 2.2b). By choosing the geometry of the gate electrodes in a proper way, the electric fields can confine electrons into a small channel (1D confinement) or even into one or more small islands (0D confinement). These islands are the quantum dots.

## 2.3 Device fabrication

The gate electrodes are fabricated using electron-beam lithography. First, we spin a layer of organic resists (poly-methyl-methacrylate, PMMA) on the heterostructure surface (Fig. 2.3a). Then the gate pattern is defined by writing with a focused electron beam in the electron-sensitive resist. This locally breaks up the

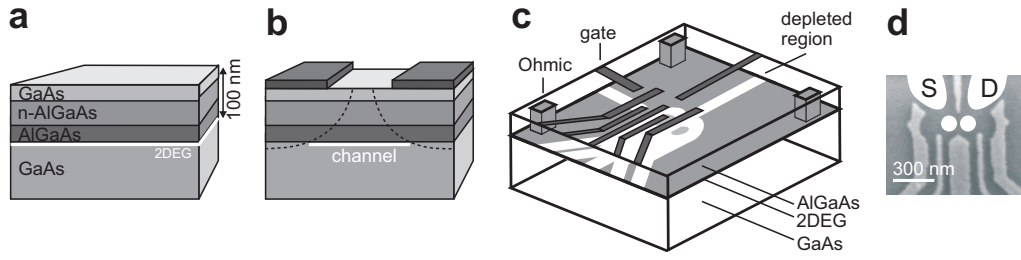


**Figure 2.2:** Confining electrons in a semiconductor. (a) Semiconductor heterostructure containing a 2DEG (indicated in white) approximately 100 nm below the surface, at the interface between GaAs and AlGaAs. The electrons in the 2DEG result from Si donors in the n-AlGaAs layer. (The thickness of the different layers is not to scale.) (b) By applying negative voltages to the metal electrodes on the surface of the heterostructure, the underlying 2DEG can be locally depleted. In this way, electrons can be confined to one or even zero dimensions. (c) Schematic view of a lateral quantum dot device. Negative voltages applied to metal gate electrodes (dark gray) lead to depleted regions (white) in the 2DEG (light gray). Ohmic contacts (light gray columns) enable bonding wires (not shown) to make electrical contact to the 2DEG reservoirs. (d) Scanning electron microscope image of an actual device, showing the gate electrodes (light gray) on top of the surface (dark gray). The two white dots indicate two quantum dots, connected via tunable tunnel barriers to a source (S) and drain (D) reservoir, indicated in white.

polymer chains, so that the exposed parts can be removed by a developer (solution of methyl isobutyl ketone, MIBK, and iso-propyl alcohol, IPA), see Fig. 2.3b. Note that there is some undercut of the PMMA layer. This undercut is caused by the significant electron scattering at the interface between GaAs and PMMA during the electron beam exposure.

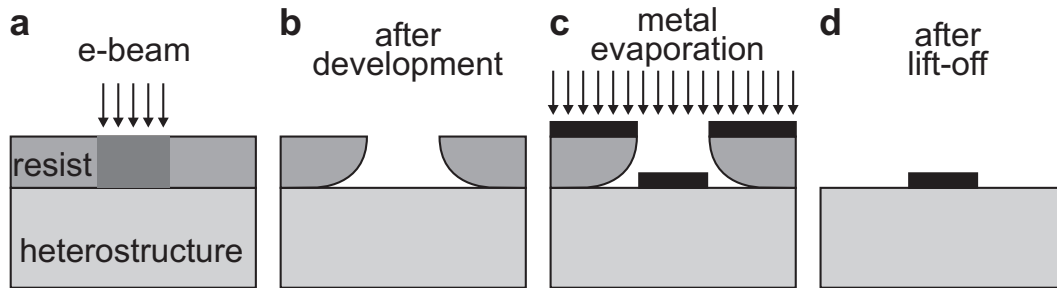


**Figure 2.3:** Fabrication of metal electrodes on the surface of the heterostructure. (a) Writing a pattern in the resist layer with an electron beam. (b) After developing, the resist has been locally removed. (c) Evaporating metal. (d) After lift-off, a metal electrode remains.

In the next step (Fig. 2.3c), metal is evaporated, which only makes contact to the heterostructure at the places where the resist has been exposed and removed. In our devices, the metal gates consist of a thin (5 nm) ‘sticking’ layer of titanium, with a 30 nm layer of gold on top. The last step is the removal of the remaining resist by acetone (Fig. 2.3d). This process, in which the metal on top of the resist is removed as well, is called ‘lift-off’. The lift-off process is facilitated by the undercut in the resist layer. Now metal electrodes are left at the places that were exposed to the electron beam. The electron beam can accurately write with a resolution of about 5 nm, but in practice the minimal width of a gate electrode is about 40 nm, limited by the development and the lift-off step.

In order to probe our system of confined electrons, we need to make electrical contact to the 2DEG. For this, we evaporate Ni/AuGe/Ni (5/150/25 nm) on the contact pads and rapidly anneal them at  $\sim 440$  degrees Celsius ( $\sim 60$  seconds). This forms Ohmic contacts with a resistance of about  $1\text{ k}\Omega$  that connect the 2DEG electrically to metal bonding pads on the surface. Metal wires bonded to these pads run toward the current or voltage probes, enabling us to perform transport measurements.

For the experiments described in chapter 8 and 9, we need a strong AC magnetic field at the location of the quantum dot. This will be generated by an on-chip coplanar stripline (CPS). To maximize this AC field, the CPS has to be positioned on top of the gate structure. In order to electrically isolate the CPS from the gates we use a 100 nm thick layer of calixarene, a very good dielectric [12].

An extensive description of all the steps of the lateral GaAs quantum dot fabrication process can be found in [13, 14].

## 2.4 Measurement setup

### 2.4.1 Dilution refrigerator and device cooling

To isolate an electron spin in a quantum dot well enough from the electrons in the (2DEG) reservoirs and being able to resolve small energies such as the Zeeman splitting, the device has to be cooled down to temperatures well below a Kelvin. In this thesis we have used two dilution refrigerators: an Oxford Kelvinox 300 and an Oxford Kelvinox 400HA. These dilution refrigerators both have a base temperature of about 10 mK. The Kelvinox 300 (400HA) has a cooling power in excess of 300 (400)  $\mu\text{W}$  (at 100 mK) and has a superconducting magnet that can apply high magnetic fields up to 16T (12T).

Although phonons in the semiconductor lattice will have a similar temperature



as the base temperature of the refrigerator, the electron temperature of the 2DEG is higher, generally around 100 mK. This has two reasons. First, due to weak electron-phonon coupling, electrons are cooled mostly via DC (bond)wires which are connected to the 2DEG via the Ohmic contacts. Furthermore, the electrons are susceptible to radiation or noise in the DC wires which are connected to the Ohmic contacts. In order to suppress radiation, the device is put inside a copper can which is cooled down to base temperature as well. This can protect the device from 4K radiation of the inner vacuum chamber (IVC). In order to suppress the noise in the DC wires, we use different filtering stages at different temperatures and covering different frequency ranges. This will be discussed in section 2.4.4.

## 2.4.2 Measurement electronics

A typical measurement involves applying a source-drain voltage over (a part of) the device, and measuring the resulting current as a function of the voltages applied to the gates. The electrical circuit for the voltage-biased current measurement and for applying the gate voltages in the Kelvinox 300 is shown in Fig. 2.4. The electrical scheme for the Kelvinox 400HA is conceptually the same. The most important parts of the measurement electronics – i.e. the current-to-voltage (IV-)converter, isolation amplifier, voltage source and digital-to-analog converters (DACs) – were all designed and built by Raymond Schouten at Delft University. The underlying principle of the setup is to isolate the sample electrically from interfering control and data-acquisition equipment. This is achieved via optical isolation at both sides of the measurement chain, i.e. in the voltage source, the isolation amplifier, as well as the DACs. In all these units, the electrical signal passes through analog optocouplers, which first convert it to an optical signal using an LED, and then convert the optical signal back using a photodiode. In this way, there is no galvanic connection between the two sides. In addition, all circuitry at the sample side is analog (even the DACs have no clock circuits or microprocessors), battery-powered, and uses a single clean ground (connected to the metal parts of the fridge) which is separated from the ground used by the ‘dirty’ electronics. All these features help to eliminate ground loops and reduce interference on the measurement signal.

Measurements are controlled by a computer running LabView. It sends commands via a fiber link to two DAC-boxes, each containing 8 digital-to-analog converters, and powered by a specially shielded transformer. Most of the DACs are used to generate the voltages applied to the gate electrodes (typically between 0 and -5 V). One of the DACs controls the source-drain voltage for the

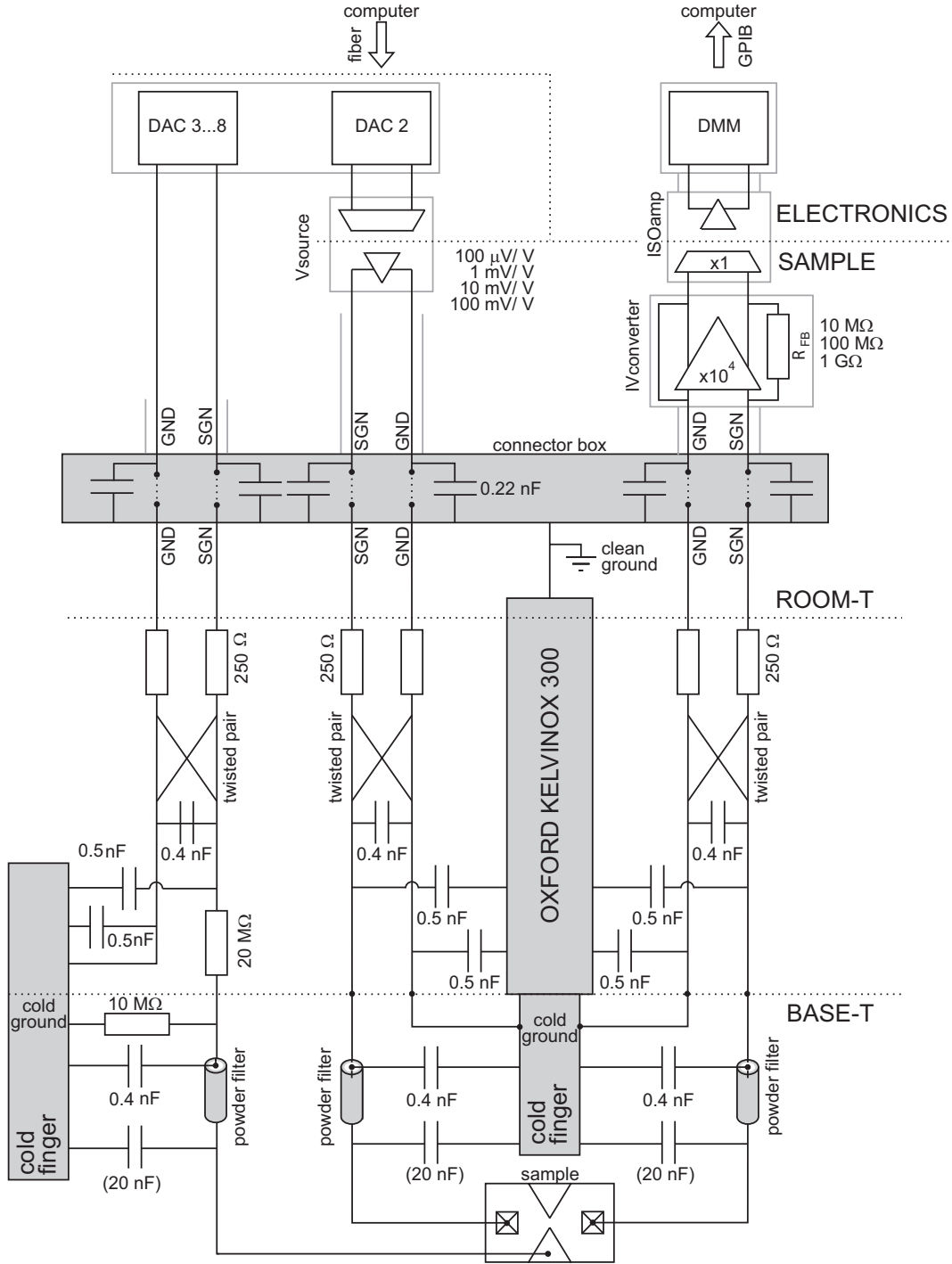


**Figure 2.4:** Electrical circuit for performing a voltage-biased current measurement and applying voltages to the gate electrodes in the Oxford Kelvinox 300 dilution refrigerator. Elements shown in gray are connected to ground. Gray lines indicate the shielding of the measurement electronics and wires. The circuit of the Oxford Kelvinox 400HA is conceptually the same.

device. The output voltage of this DAC (typically between +5 and -5V) is sent to a voltage source, which attenuates the signal by a factor 10,  $10^2$ ,  $10^3$  or  $10^4$  and provides optical isolation. The attenuated voltage is then applied to one of the Ohmic contacts connected to the source reservoir of the device.

The resulting current coming from the drain reservoir is fed to a room temperature (RT) low-noise IV-converter. In this thesis we use two types, depending on the desired bandwidth. The first one (used in chapters 8 and 9), is designed for low-frequency measurements. It has a noise floor of  $\sim 5$  fA/Hz<sup>1/2</sup>. The feedback resistance can be set to 10 M $\Omega$ , 100 M $\Omega$  or 1G $\Omega$ , with an input resistance that is a factor  $10^3$  or  $10^4$  smaller (for the ‘low noise’ or ‘low input resistance’ setting, respectively). The bandwidth will depend in the input impedance of the IV-converter and can be varied from approximately 50 Hz (1 G $\Omega$ , ‘low noise’ setting) to 1 kHz (10 M $\Omega$ , ‘low input resistance’ setting). The faster IV-converter, used in chapter 4 has a bandwidth of about 150 kHz, and a current noise of  $\sim 1$  pA/Hz<sup>1/2</sup> at 100 kHz. The feedback resistance is 10 M $\Omega$ , corresponding to an input resistance of 1.3 k $\Omega$ . When even higher bandwidths are required, cryogenic electronics can be installed inside the cryostat. To incorporate cryogenic electronics, parts of the electrical circuit as depicted in Fig. 2.4 has to be modified (see chapter 6).

The signal from the RT IV-converter is sent to an isolation amplifier, to provide optical isolation and possibly gain. Again we can choose a low-frequency version (up to  $\sim 1$  kHz) or a high-frequency one (up to  $\sim 300$  kHz). The voltage from the isolation amplifier is finally measured by a digital multimeter (Keithley 2700) and sent to the computer via a GPIB interface. Alternatively, we can use a lock-in amplifier (Stanford EG&G 5210) if the signal to be measured is periodic.

### 2.4.3 Measurement wires

To make contact to the sample,  $2 \times 12$  twisted pairs of wires run from two connector boxes at RT all the way down to the ‘cold finger’ at base temperature. The diameter and material of these wires is chosen to minimize the heat load on the mixing chamber. From RT to 1 Kelvin,  $2 \times 9$  pairs consist of manganine wires (100  $\mu\text{m}$  diameter), and  $2 \times 3$  pairs of copper wires (90  $\mu\text{m}$  diameter). From 1 Kelvin to the mixing chamber, superconducting ‘Niomax’ wires (50  $\mu\text{m}$  diameter) are used. From the mixing chamber to the bottom of the cold finger, where thermal conductivity is no longer a constraint, we have standard copper wires. At base temperature, one wire of each twisted pair is connected to ‘cold ground’ (i.e. the cold finger), which is electrically connected to clean ground via the metal parts of the fridge.

All wires are thermally anchored to the fridge, by carefully wrapping them around copper posts, at several temperature stages (4 K, 1 K,  $\sim 100$  mK and  $\sim 10$  mK). At RT, the resistance of the wires is about  $250\ \Omega$  ( $150\ \Omega$ ) for the manganine (copper) wires. At low temperature it is about  $50\ \Omega$ . The wires have various parasitic capacitances to their twisted partner and to ground, as indicated in Fig. 2.4.

#### 2.4.4 Filtering

The wires connect the device to the measurement electronics at room temperature, so they have to be carefully filtered to avoid that the electrons in the sample heat up due to spurious noise and interference. Several filtering stages are required for different frequency ranges (see Fig. 2.4). In the connector box at room temperature, all wires are connected to ground via  $0.22\ \text{nF}$  ‘feedthrough capacitors’. At base temperature, all signal wires run through ‘copper powder filters’ [9]. These are copper tubes filled with copper powder, in which 4 signal wires, with a length of about 2 meters each, are wound. The powder absorbs the high-frequency noise very effectively, leading to an attenuation of more than  $-60\ \text{dB}$  from a few  $100\ \text{MHz}$  up to more than  $50\ \text{GHz}$  [10].

To remove the remaining low-frequency noise, we solder a  $20\ \text{nF}$  capacitor between each signal wire and the cold finger ground. In combination with the  $\sim 100\ \Omega$  resistance of the wires, this forms a low-pass RC filter with a cut-off frequency of about  $100\ \text{kHz}$  (even  $10\ \text{kHz}$  for the wire connected to the RT IV-converter, due to its input resistance of about  $1.3\ \text{k}\Omega$ ). These filters are used for the wires connecting to Ohmic contacts (although they were not connected to all Ohmics to perform some of the high-bandwidth measurements described in this thesis). For the wires connecting to gate electrodes, a 1:3 voltage divider is present (consisting of a  $20\ \text{M}\Omega$  resistance in the signal line and a  $10\ \text{M}\Omega$  resistance to ground). In this way, the gate voltages are filtered by a low-pass RC filter with a cut-off frequency of about  $1\ \text{Hz}$ . Another advantage of the voltage divider is that the DAC resolution is effectively increased by a factor 3. By combining all these filters, the electrons in the sample can be cooled to an effective temperature below  $100\ \text{mK}$  (if no extra heat loads such as coaxial cables are present).

#### 2.4.5 High-frequency signals

##### Fast voltage pulses

High-frequency signals can be applied to gate electrodes via two coaxial cables. They consist of three parts, connected via standard  $2.4\ \text{mm}$  Hewlett Packard

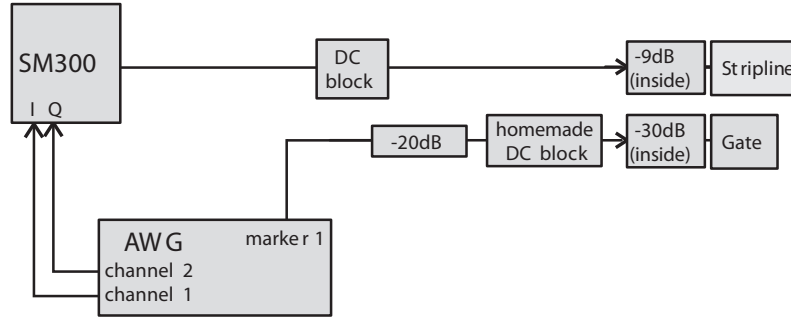
connectors (specified up to 50 GHz). From room temperature to 1 Kelvin, a 0.085 inch semi-rigid Be-Cu (inner and outer conductor) coaxial cable is used. From 1 Kelvin to the mixing chamber, we use 0.085 inch semi-rigid superconducting Nb-Nb. From the mixing chamber to the sample holder, flexible tin plated Cu coaxial cables are present. The outer conductors of the coaxes are thermally anchored at 4 K, 1 K,  $\sim 800$  mK,  $\sim 100$  mK and base temperature, by clamping each cable firmly between two copper parts. To thermalize also the inner conductor of the coax, we use Hewlett Packard 8490D attenuators (typically -20 dB) at 1 K. These attenuators cannot be used at the mixing chamber, as they tend to become superconducting below about 100 mK. The same problem occurs when using Inmet 50EH attenuators. Therefore we use attenuators from Weinschel which have proved not to become superconducting at base temperature.

To generate the high-frequency pulses, we use an arbitrary waveform generator (Sony Tektronix AWG520), which can generate complicated pulse shapes with a rise time of about 1 ns. With the cables described above, the fastest pulse flank we can transmit to the sample is about 200 ps. Microwave signals are transmitted with about 10 dB loss at 30 GHz.

Special care needs to be given to the connection from the coaxial cable to the chip, in order to minimize reflections. Although techniques such as Time-Domain Reflectometry (TDR) allow us to determine if and where reflections take place, it turns out to be practically impossible to eliminate reflections from the coaxial assembly. The sample holder we use, has an SMA connector that can be connected to the 2.4 mm coaxial cable. At the other end, the pin of the SMA connector sticks through a small hole in the chip carrier. This allows it to be soldered to a metal pad on the chip carrier, from which we can then bond to the chip. This sample holder is used to apply pulses to a gate electrode.

## Microwaves

In order to apply microwave signals to the coplanar stripline, used in chapter 8 and 9, we have mounted a coaxial line which also consist of three parts. Inside the cryostat (Kelvinox 400HA) they are connected via 2.4 mm (Hewlett Packard) connectors, which are specified up to 50 GHz, and a SMA feedthrough at room temperature, which is specified up to 18 GHz. From room temperature to 1 Kelvin, we use a silver-plated brass coaxial cable (Keycom ULT-05). This type of coax is optimized for performance at low temperature, high frequency transmission (up to 40 GHz) together with relatively low heat conductivity. From 1 Kelvin to the mixing chamber, we also use a semi-rigid Nb-Nb coax line (Keycom 085A). The coax is superconducting at these temperatures, which fully suppresses heat conduction. From the mixing chamber to the sample holder, we use a tin



SM300: Rohde&Schwarz vector source (9 kHz-3 GHz)

AWG: Arbitrary waveform generator, Tektronix AWG 520

DC block: picosecond (3 nF outer conductor, 2 nF inner conductor)

Home-made DC block (1.6  $\mu$ F outer conductor, 4.7 F inner conductor)

**Figure 2.5:** Block diagrams depicting generation of gate voltage pulse ( $\sim 1\mu s$ ) and phase-controlled RF burst sequences for magnetic ESR.

plated Cu coaxial cable which is flexible and therefore convenient to use. The outer conductor of the coax is thermally anchored to the dilution unit at 4K, 1K,  $\sim 800$  mK and  $\sim 40$  mK. The inner conductor is thermalized by an attenuator (Agilent, -6 dB) at 1 K as well as an attenuator at the mixing chamber (Weinschel model 84-3, -3 dB). The attenuation of the coax line (coax itself plus attenuator) used for excitation of the stripline is only 9 dB (compared to 30 dB for the coax line to the gate) because the mixing chamber cooling power is limited. Finally, we use a commercially available DC block (Picosecond model:5505) which intersects both inner and outer conductor of the coaxial lines with capacitors. This prevents that low-frequency noise / interference couples from the high frequency generators into the electrical circuit of the device. The phase-controlled RF burst sequences used for magnetic ESR (chapter 8 and 9) are generated with a vector source (Rohde&Schwarz SM300, 9 kHz to 3 GHz) with RF modulator, controlled by two channels of a Tektronix arbitrary waveform generator (see Fig. 2.5 for a block diagram). Voltage pulses are applied to the right side gate through a bias-tee, so that the gate can remain biased with a DC voltage as well. The bias-tee was home-made, with a rise time of 150 ps and a RC charging time of 10ms at 77K ( $R=10$  M $\Omega$ ,  $C=3.3$  nF). The CPS is contacted via a modified microwave probe (GGB Industries, Picoprobe model 50A, loss <1 dB, DC-50 GHz).

## References

- [1] L.P. Kouwenhoven, D.G. Austing, and S. Tarucha, Rep. Prog. Phys. **64** (6), 701 (2001).
- [2] L.P. Kouwenhoven, C.M. Marcus, P.L. McEuen, S. Tarucha, R.M. Westervelt, and N.S. Wingreen, in *Mesoscopic Electron Transport*, edited by L.L. Sohn, L.P. Kouwenhoven and G. Schön, (Kluwer, Series E **345**, 1997), p.105-214.
- [3] See e.g. R. Hanson, I. T. Vink, D. P. DiVincenzo, L. M. K. Vandersypen, J. M. Elzerman, L. H. Willems van Beveren, and L.P. Kouwenhoven, to be published in the Proceedings of the XXXIXth Rencontres de Moriond (La Thuile, 2004) “Quantum information and decoherence in nanosystems”; cond-mat/0407793.
- [4] N.W. Ashcroft and N.D. Mermin, *Solid state physics* (Brooks/Cole 1976).
- [5] S. Tarucha, D.G. Austing, Y. Tokura, W.G. van der Wiel and L.P. Kouwenhoven, Phys. Rev. Lett. **84**, 2485 (2000).
- [6] S. Tarucha, D.G. Austing, T. Honda, R.J. van der Hage and L.P. Kouwenhoven, Phys. Rev. Lett. **77**, 3613 (1996) .
- [7] V.N. Golovach and D. Loss, Europhys. Lett. **62**, 83 (2003).
- [8] G. Burkard, D. Loss, and D. P. DiVincenzo, Phys. Rev. B **59**, 2070 (1999).
- [9] J.M. Martinis, M.H. Devoret and J. Clarke, Phys. Rev. B **35**, 4682 (1987).
- [10] K. Bladh *et al.*, Rev. Sci. Instr. **74**,1323 (2003).
- [11] J.H. Davies, *The physics of low-dimensional semiconductors* (Cambridge University Press, 1998).
- [12] A. Holleitner, Appl. Phys. Lett. **82**, 1887 (2003).
- [13] L.H. Willems van Beveren, *Electron spins in few-electron lateral quantum dots*, PhD thesis, Delft University of Technology (2005).
- [14] F.H.L. Koppens, *Coherence and control of a single electron spin in a quantum dot*, PhD thesis, Delft University of Technology (2005).





## Chapter 3

# Spin states of confined electrons and interactions with their environment

To perform quantum information processing using electron spin states we require these spins to be localized. To this end, we confine electrons in single or double quantum dots. In this chapter we discuss the states that the spins occupy and how this leads to the spin-dependent transitions that allow us to measure the electron spin state. Interactions with the environment makes that quantum information, stored in an electron spin, is easily lost. Therefore, understanding the mechanisms that lead to the loss of quantum information and controlling these processes is crucial when developing a qubit. We discuss the most important interactions of a confined electron spin with its environment. These are the electron-phonon interaction together with the spin-orbit coupling, and the hyperfine interaction with the nuclear spins in the host semiconductor lattice.

### 3.1 Electron spin states in a single quantum dot

The fact that electrons carry spin determines the electronic states of the quantum dot, in quite the same way as it does in real atoms. In the simplest case – a dot containing just a single electron – spin leads to a splitting of all orbitals into Zeeman doublets, with the ground state corresponding to the electron spin pointing up  $|\uparrow\rangle$ , i.e. parallel to the magnetic field, and the excited state to the spin pointing down  $|\downarrow\rangle$ , i.e. antiparallel to the magnetic field. The difference between the corresponding energy levels  $E_\uparrow$  and  $E_\downarrow$  is given by the Zeeman energy,  $\Delta E_Z = g\mu_B B$ , which is approximately 25  $\mu\text{eV}/\text{T}$  in GaAs.

For two electrons in a quantum dot, the situation is a little more complicated. For an unperturbed Hamiltonian (i.e. without spin-orbit coupling terms, which is to first order a good approximation for our system), the two-electron state is the product of an orbital and spin part. Since electrons are fermions, the total two-electron state has to be anti-symmetric under exchange of the two particles. Therefore, if the orbital part is symmetric, the spin state must be anti-symmetric, and vice versa. The anti-symmetric spin part of the two-electron state is the spin singlet  $|S\rangle$ :

$$|S\rangle = \frac{|\uparrow\downarrow\rangle - |\downarrow\uparrow\rangle}{\sqrt{2}} \quad (3.1)$$

which has total spin  $S = 0$ . The symmetric part consist of the so-called spin triplets ( $|T_+\rangle$ ,  $|T_0\rangle$  and  $|T_-\rangle$ ):

$$|T_+\rangle = |\uparrow\uparrow\rangle \quad |T_0\rangle = \frac{|\uparrow\downarrow\rangle + |\downarrow\uparrow\rangle}{\sqrt{2}} \quad |T_-\rangle = |\downarrow\downarrow\rangle \quad (3.2)$$

which have total spin  $S = 1$  and a quantum number  $m_s$  (corresponding to the spin z-component) of 1, 0, and -1, respectively. In a finite magnetic field, the three triplet states are split by the Zeeman splitting,  $\Delta E_Z$ .

Even at zero magnetic field, the energy of the two-electron system depends on its spin configuration, through the requirement of anti-symmetry of the total state. If we consider just the two lowest orbitals,  $\varepsilon_0$  and  $\varepsilon_1$ , then there are six possibilities to fill these with two electrons (Fig. 3.1). At zero magnetic field [4], the two-electron ground state is always the spin singlet with both electrons on the lowest orbital (Fig. 3.1a), and the lowest excited states are then the three (degenerate) spin triplets (Fig. 3.1b–d). The energy gain of  $T_0$  with respect to the excited spin singlet  $S_1$  (Fig. 3.1e) is known as the exchange energy. It essentially results from the fact that electrons in the triplet states tend to avoid each other, reducing their mutual Coulomb energy. As the Coulomb interaction

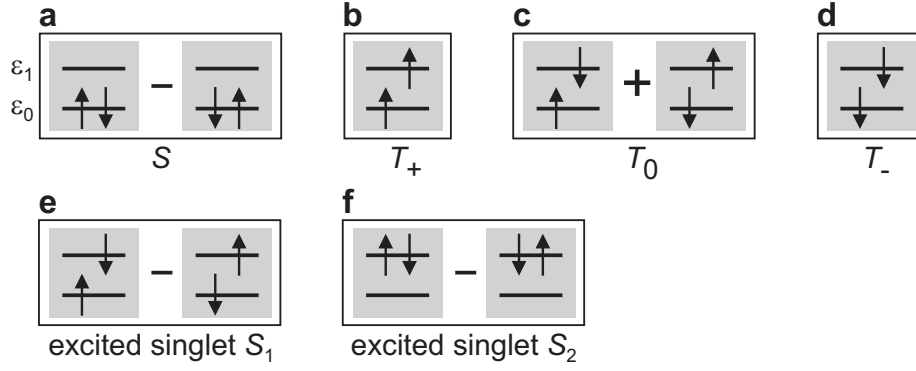


**Figure 3.1:** Schematic energy diagrams depicting the spin states of two electrons occupying two spin degenerate single-particle levels ( $\epsilon_0$  and  $\epsilon_1$ ). (a) Spin singlet, which is the ground state at zero magnetic field. (b)–(d) Lowest three spin triplet states,  $|T_+\rangle$ ,  $|T_0\rangle$  and  $|T_-\rangle$ , which have total spin  $S = 1$  and quantum number  $m_s = +1, 0$  and  $-1$ , respectively. In finite magnetic field, the triplet states are split by the Zeeman energy. (e) Excited spin singlet state,  $S_1$ . The energy difference between  $S_1$  and the triplet state  $T_0$  is the exchange energy. (f) Highest excited spin singlet state,  $S_2$ .

is very strong, the exchange energy can be quite large (a few  $100 \mu\text{eV}$ ) [5]. When a magnetic field is applied which has a component perpendicular to the 2DEG, this component not only couples to the electron spin but to the orbital as well. Increasing this field leads to a transition from a singlet to a triplet ground state [12]. This control over the singlet-triplet splitting will be used in chapter 5.

For more than two electrons, the spin states can be much more complicated [13]. However, in some cases and for certain magnetic field regimes they might be well approximated by a one-electron Zeeman doublet (when  $N$  is odd) or by two-electron singlet or triplet states (when  $N$  is even). But there are still differences – for instance, if  $N > 2$  the ground state at zero field can be a spin triplet, due to Hund’s rule [6].

As experiments on vertical dots have shown, the orbital part of the wave functions are in excellent agreement with single-particle Fock-Darwin states [1] since the confinement potential of semiconductor quantum dots is to a good approximation a parabolic well. The Fock-Darwin states can therefore be very helpful in explaining effects that arise from the spatial form of the electron wave function in the dot (e.g. the fact that different orbitals can have a very different tunnel coupling to the reservoir, see chapter 4).

## 3.2 Double dot spin states

The eigenstates of a two-electron double dot are also spin singlets and triplets. We can again use the diagrams in Fig. 3.1, but now the single-particle eigenstates  $\varepsilon_0$  and  $\varepsilon_1$  represent the symmetric and anti-symmetric combination of the lowest orbital on each of the two dots, respectively. Due to tunneling between the dots, with tunneling matrix element  $t$ ,  $\varepsilon_0$  (the ‘bonding state’) and  $\varepsilon_1$  (the ‘anti-bonding state’) are split by an energy  $2t$ . By filling the two states with two electrons, we again get a spin singlet ground state and a triplet first excited state (at zero field). However, the singlet ground state is not purely  $S$  (Fig. 3.1a), but also contains a small admixture of the excited singlet  $S_2$  (Fig. 3.1f). The admixture of  $S_2$  depends on the competition between inter-dot tunneling and the Coulomb repulsion, and serves to lower the Coulomb energy by reducing the double occupancy of the dots [7].

If we focus only on the singlet ground state and the triplet first excited states, then we can describe the two spins  $\vec{S}_1$  and  $\vec{S}_2$  by the Heisenberg Hamiltonian,  $H = J\vec{S}_1 \cdot \vec{S}_2$ . Due to this mapping procedure,  $J$  is now defined as the energy difference between the triplet state  $T_0$  and the singlet ground state, which depends on the details of the double dot orbital states. From a Hund-Mulliken calculation [8],  $J$  is approximately given by  $4t^2/U + V$ , where  $U$  is the on-site charging energy and  $V$  includes the effect of the long-range Coulomb interaction. By changing the overlap of the wave functions of the two electrons, we can change  $t$  and therefore  $J$ . Thus, control of the inter-dot tunnel barrier would allow us to perform operations such as swapping or entangling two spins.

The regime of interest for chapters 8 and 9 is where the occupancy of the double quantum dot can be (0,1), (1,1), or (0,2), with (m,n) the occupations of the left and right dots. In the (1,1) and (0,2) charge state, the four possible spin states are the singlet state ( $|S\rangle = |\uparrow\downarrow\rangle - |\downarrow\uparrow\rangle$ , normalization omitted for brevity) and the three triplets states  $|T^0\rangle = |\uparrow\downarrow\rangle + |\downarrow\uparrow\rangle$ ,  $|T^+\rangle = |\uparrow\uparrow\rangle$ ,  $|T^-\rangle = |\downarrow\downarrow\rangle$ . Due to a finite tunnel coupling  $t$  between the two dots, the (1,1) and (0,2) singlet states can hybridize close to the degeneracy of these two states. Around this degeneracy, the energy difference between the (0,2) and (1,1) triplet states is much larger than  $t$ , and therefore, we can neglect hybridization between these states and charge transitions to the (0,2) triplet state. We calculate the energy of the eigenstates via the system Hamiltonian, which is written in the basis states  $|S_{11}\rangle$ ,  $|T_{11}^+\rangle$ ,  $|T_{11}^-\rangle$ ,  $|T_{11}^0\rangle$  and  $|S_{02}\rangle$ . In the description, we neglect the thermal energy  $kT$ , which is justified when the (absolute) energy difference between the eigenstates and the Fermi energy of the left and right reservoir is larger than  $kT$ .

The Hamiltonian is given by

$$H_0 = - \Delta_{LR} |S_{02}\rangle \langle S_{02}| + \sqrt{2}t \left( |S_{11}\rangle \langle S_{02}| + |S_{02}\rangle \langle S_{11}| \right) - g\mu_B B_{\text{ext}} \left( |T_{11}^+\rangle \langle T_{11}^+| - |T_{11}^-\rangle \langle T_{11}^-| \right), \quad (3.3)$$

where  $\Delta_{LR}$  is the energy difference between the  $S_{11}$  and  $S_{02}$  state (level detuning, see Fig. 3.2a),  $t$  is the tunnel coupling between the  $S_{11}$  and  $S_{02}$  states, and  $B_{\text{ext}}$  is the external magnetic field in the z-direction. The eigenstates of the Hamiltonian in Eq.(3.3) for finite external field are shown in Fig. 3.2c. For  $|\Delta_{LR}| < t$ , the tunnel coupling  $t$  causes an anti-crossing of the  $S_{11}$  and  $S_{02}$  states.

### 3.2.1 Pauli spin blockade

Since interdot charge transitions conserve spin and obey spin selection rules, some transitions are forbidden even though the involved states are energetically available. This phenomenon is referred to as Pauli spin blockade. This can be explained using the energy diagrams in Fig. 3.2 to analyze the current-carrying cycle via the charge transitions:  $(1, 1) \rightarrow (0, 2) \rightarrow (0, 1) \rightarrow (1, 1)$ . For  $\Delta_{LR} < 0$ , transport is blocked by Coulomb blockade, because the  $(0, 2)$  state  $S_{02}$  is at a higher energy than the  $(1, 1)$  state  $S_{11}$ . For  $\Delta_{LR} \geq 0$ , two possible situations can occur. First, an electron that enters the left dot can form a double-dot singlet

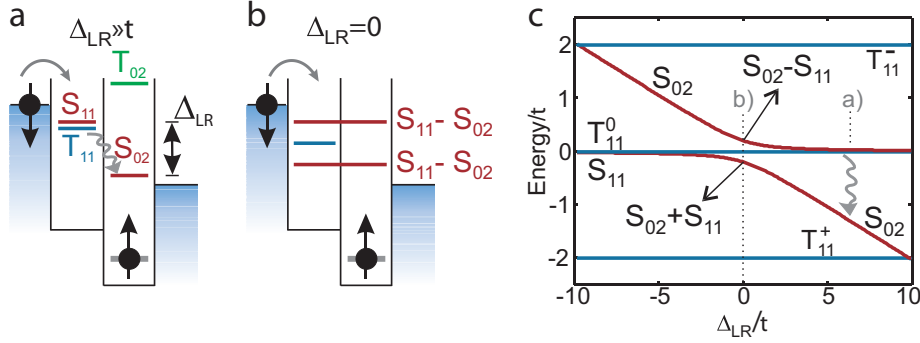


**Figure 3.2:** (a) A schematic of the double dot and the electro-chemical potentials (energy relative to the  $(0,1)$  state) of the relevant two-electron spin states. For detunings  $\Delta_{LR} > t$ , transitions from the  $S_{11}$  state to the  $S_{02}$  state are possible via inelastic relaxation with rate  $\Gamma_{\text{in}}$ . Spin blockade occurs when one of the  $T_{11}^i$  states is occupied. (b) Similar schematic for  $\Delta_{LR} = 0$ , where the singlet states are hybridized. Also in this case, spin blockade occurs when one of  $T_{11}^i$  states is occupied. (c) Energy levels as a function of detuning. At  $\Delta_{LR} = 0$ , the singlet states hybridize into bonding and anti-bonding states. The splitting between the triplet states corresponds to the Zeeman energy  $g\mu_B B_{\text{ext}}$ .

state  $S_{11}$  with the electron in the right dot. It is then possible for the left electron to move to the right dot because the right dot singlet state  $S_{02}$  is energetically accessible. Transitions from  $S_{02}$  to  $S_{11}$  are governed by coherent coupling between the states (Fig. 3.2b) or inelastic relaxation (Fig. 3.2a). From  $S_{02}$ , one electron tunnels from the right dot to the right lead and another electron can again tunnel into the left dot. The second possibility is that an electron entering the left dot forms a triplet state  $T_{11}^+$  with the electron in the right dot. In that case, the left electron cannot move to the right dot, as the right dot triplet state  $T_{02}$  is much higher in energy (due to the relatively large singlet-triplet splitting in a single dot). The electron can also not move back to the lead due to fast charge relaxation in the reservoir, and therefore, further current flow is blocked as soon as any of the (1,1) triplet states is formed (see schematics in Fig. 3.3a). The key experimental signature of Pauli spin blockade is the strong dependence of current flow on bias direction. For forward bias smaller than the singlet-triplet energy splitting  $\Delta_{ST}$ , current flow is strongly suppressed because as soon as one of the triplet states is occupied, the current-carrying cycle is interrupted (Fig. 3.3a). For a small reverse bias, only singlet states can be loaded and a current can always flow (Fig. 3.3b).

A second experimental signature of Pauli spin blockade is visible when the voltage bias is larger than the energy splitting  $\Delta_{ST}$  between the states  $T_{02}$  and  $S_{02}$ . Spin blockade is lifted when the relative dot alignment is such that the transition from the  $T_{11}$  state to  $T_{02}$  state is energetically allowed (Fig. 3.3).

### 3.3 Singlet-triplet mixing by the nuclear spins

Spin blockade only occurs if at least one of the eigenstates of the system Hamiltonian is a pure triplet state. If processes are present that induce transitions from all the three triplet states  $T_{11}^i$  to the singlet state  $S_{11}$ , spin blockade is lifted and a current will flow. As we will see below, the presence of the nuclear spins in the host semiconductor can give rise to such transitions.

The effect of the hyperfine interaction with the nuclear spins can be studied [14] by adding a static (frozen) effective nuclear field  $\mathbf{B}_N^L$  ( $\mathbf{B}_N^R$ ) at the left (right) dot to the system Hamiltonian:

$$\begin{aligned} H_{\text{nucl}} &= -\frac{g\mu_B}{\hbar}(\mathbf{B}_N^L \cdot \mathbf{S}_L + \mathbf{B}_N^R \cdot \mathbf{S}_R) \\ &= -\frac{g\mu_B}{2\hbar}[(\mathbf{B}_N^L - \mathbf{B}_N^R) \cdot (\mathbf{S}_L - \mathbf{S}_R) + (\mathbf{B}_N^L + \mathbf{B}_N^R) \cdot (\mathbf{S}_L + \mathbf{S}_R)], \end{aligned} \quad (3.4)$$

with  $\mathbf{S}_{L(R)}$  the spin operator for the left (right) electron. For the sake of convenience, we separate the inhomogeneous and homogeneous contribution, for rea-

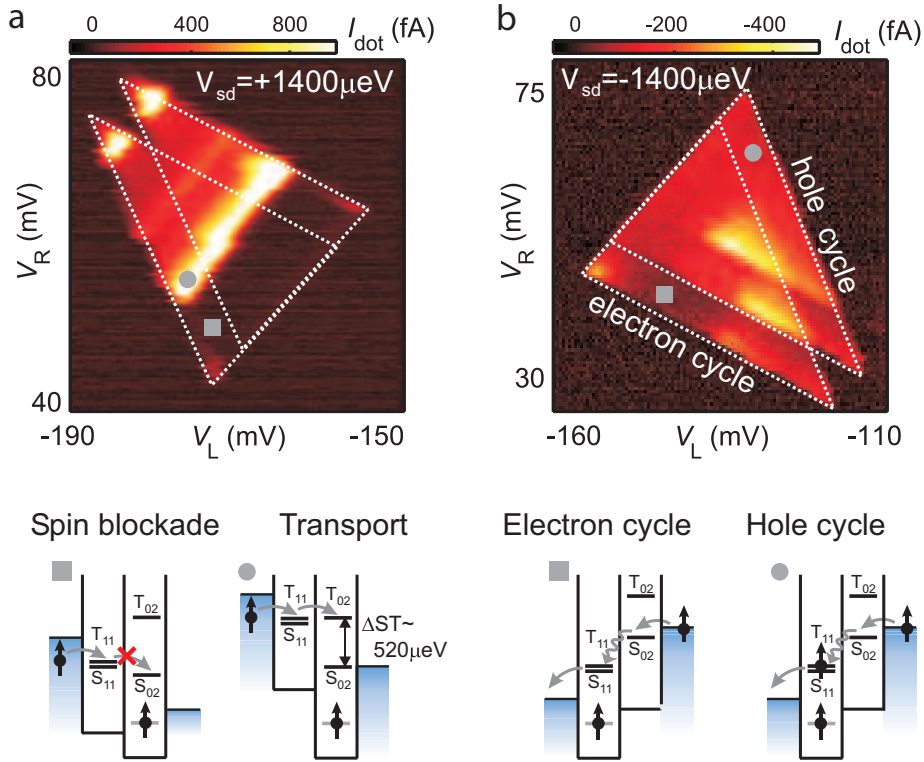


**Figure 3.3:** High bias transport measurements in the spin blockade regime. (a) Grayscale plot of the current through the double quantum dot under forward bias ( $1400 \mu\text{eV}$ ) as a function of the gate voltages controlling the left and right dot potential ( $V_L$  and  $V_R$ ) at  $B_{\text{ext}} = 100 \text{ mT}$ . The white dotted triangles define the region in gate space where transport is energetically allowed. Transport is suppressed due to spin blockade in part of the triangles (gray rectangle). Spin blockade is lifted (and transport is allowed) when the  $T_{02}$  state becomes energetically accessible from the  $T_{11}$  state (depicted by the gray circle). (b) Similar measurement as in (a), but for reverse bias ( $-1400 \mu\text{eV}$ ). Current flows in the entire region in gate space where it is energetically allowed (within the white dotted triangles).

sons which we will discuss later. Considering the nuclear field as static is justified since the tunneling rates and electron spin dynamics are expected to be much faster than the dynamics of the nuclear system [15, 16, 17]. Therefore, we will treat  $H_{\text{nuc}}$  as time-independent. The effect of nuclear reorientation will be included later by ensemble averaging.

We will show now that triplet states mix with the  $S_{11}$  state if the nuclear field is different in the two dots (in all three directions). This mixing will lift spin blockade, visible as a finite current running through the dots for  $\Delta_{\text{LR}} \geq 0$ . The effective nuclear field can be decomposed in a homogeneous and an inhomogeneous part (see right-hand side of Eq. (3.4)). The homogeneous part simply adds vectorially to the external field  $B_{\text{ext}}$ , changing slightly the Zeeman splitting and preferred spin orientation of the triplet states. The inhomogeneous part

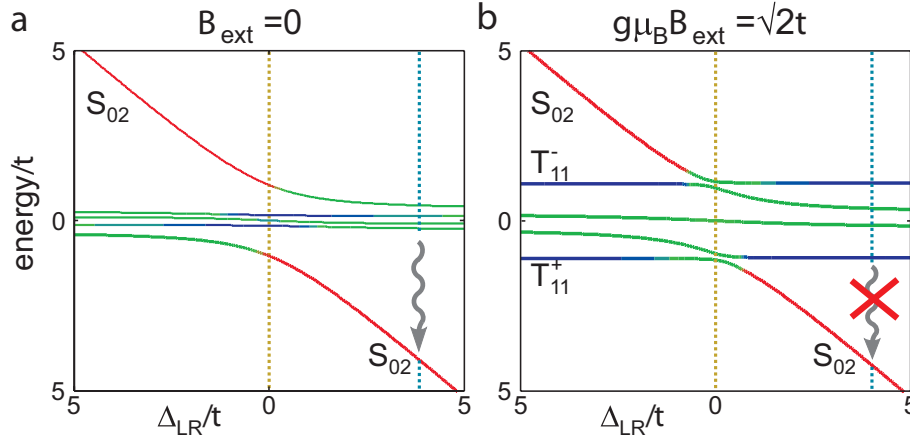


**Figure 3.4:** (a) Energies corresponding to the eigenstates of  $H_0 + H_{\text{nucl}}$  as a function of  $\Delta_{\text{LR}}$  ( $t \sim 2\Delta B_{\text{N},z}$ ). Singlet and triplet eigenstates are denoted by dark gray lines respectively. Hybridized states (of singlet and triplet) are denoted by light gray lines. For  $\Delta_{\text{LR}} \gg t$  and  $g\mu_B B_{\text{ext}} \gg g\mu_B \Delta B_{\text{N}}$ , the split-off triplets ( $T_{11}^+$  and  $T_{11}^-$ ) are hardly perturbed and current flow is blocked when they become occupied. Parameters:  $t = 0.2 \mu\text{eV}$ ,  $g\mu_B B_{\text{N},L} = (0.03, 0, -0.03) \mu\text{eV}$ ,  $g\mu_B B_{\text{N},R} = (-0.03, -0.06, -0.06) \mu\text{eV}$  and  $g\mu_B B_{\text{ext}} = 0.2 \mu\text{eV}$ .

$\Delta \mathbf{B}_{\text{N}} \equiv \mathbf{B}_{\text{N}}^L - \mathbf{B}_{\text{N}}^R$  on the other hand couples the triplet states to the singlet state, as can be seen readily by combining the spin operators in the following way

$$\begin{aligned}
 S_{\text{L}}^x - S_{\text{R}}^x &= \frac{\hbar}{\sqrt{2}} \left( |S_{11}\rangle \langle T_{11}^-| - |S_{11}\rangle \langle T_{11}^+| + h.c. \right) \\
 S_{\text{L}}^y - S_{\text{R}}^y &= \frac{\hbar}{\sqrt{2}} \left( i |S_{11}\rangle \langle T_{11}^-| - i |S_{11}\rangle \langle T_{11}^+| + h.c. \right) \\
 S_{\text{L}}^z - S_{\text{R}}^z &= \hbar \left( |S_{11}\rangle \langle T_{11}^0| + |T_{11}^0\rangle \langle S_{11}| \right).
 \end{aligned} \tag{3.5}$$

The first two expressions reveal that the inhomogeneous field in the transverse plane  $\Delta B_{\text{N}}^x$ ,  $\Delta B_{\text{N}}^y$  mixes the  $T_{11}^+$  and  $T_{11}^-$  states with  $S_{11}$ . The longitudinal component  $\Delta B_{\text{N}}^z$  mixes  $T_{11}^0$  with  $S_{11}$  (third expression). The degree of mixing between two states will depend strongly on the energy difference between them [18].

This is illustrated in Fig. 3.4a where the energies corresponding to the eigenstates of the Hamiltonian  $H_0 + H_{\text{nucl}}$  are plotted as a function of  $\Delta_{\text{LR}}$ . We first discuss the case where  $\Delta_{\text{LR}} \gg t$ . For  $g\mu_B B_{\text{ext}} < g\mu_B \sqrt{\langle \Delta B_{\text{N}}^2 \rangle}$ , the three triplet states are close in energy to the  $S_{11}$  state. Their intermixing will be strong, lifting spin blockade. For  $g\mu_B B_{\text{ext}} \gg g\mu_B \sqrt{\langle \Delta B_{\text{N}}^2 \rangle}$  the  $T_{11}^+$ , the  $T_{11}^-$  states are split off in energy by an amount of  $g\mu_B B_{\text{ext}}$ . Consequently the perturbation of these states caused by the nuclei will be small. Although the  $T_{11}^0$  remains mixed with the  $S_{11}$  state, the occupation of one of the two split-off triplet states can block the



current flow through the system. The situation for  $\Delta_{\text{LR}} \sim 0$  is more complicated due to a three-way competition between the exchange interaction and nuclear and external magnetic fields. In contrast to the previous case, increasing  $B_{\text{ext}}$  from 0 to  $\sqrt{2}t/g\mu_{\text{B}}$  gives an increase of singlet-triplet mixing, as illustrated in Fig. 3.4a. Theoretical calculations of the nuclear-spin mediated current flow, obtained from a master equation approach, are discussed in [14, 19]. This approach can be extended by incorporating the ESR Hamiltonian to calculate the current through the system when an oscillating magnetic field is applied [20].

### 3.4 Relaxation and decoherence

Here, we will briefly discuss a basic theoretical framework to evaluate two types of information loss of a quantum two-level system representing a qubit. The first is energy relaxation where the qubit relaxes from the excited state to the ground state and energy is transferred to the environment. The second is decoherence where the qubit loses phase information but the energy is preserved.

The basic theory we discuss here is appropriate only for evaluating the general cases of relaxation and decoherence, but it does not describe microscopic processes or more complex dynamics when the environment has a long memory. In general, a single quantum system coupled to its environment can reveal very rich and non-classical dynamics, for example when a single spin is coupled to a spin bath.

In order to study how fluctuations in the environment affect a qubit, it is convenient to write the qubit Hamiltonian as:

$$H = -\frac{1}{2}[\Delta E \sigma_z + \delta h_z(t) \sigma_z + \delta h_x(t) \sigma_x + \delta h_y(t) \sigma_y], \quad (3.6)$$

where  $\Delta E$  is the energy splitting of the qubit and  $\delta h_{x,y,z}(t)$  are fluctuations in the  $x, y, z$ -direction that couple to the qubit. These fluctuations can have any source like the electromagnetic environment of an electronic circuit, moving charges in a substrate, magnetic field fluctuations of a superconducting magnet, fluctuations of an electrostatic trap, electric field fluctuations from phonons or magnetic dipole fluctuations of the nuclear spins. As we will see below, it is useful to express these fluctuations in the form of a noise spectral density.

Energy relaxation is the process where the qubit relaxes from the excited state to the ground state due to a process that couples the two qubit states (Fermi's golden rule). In Eq. (3.6), the  $x, y$ -components of  $\delta h$  couple the two qubit states, but for energy conservation arguments, only the  $\Delta E/\hbar$  frequency component of the noise spectrum contributes to relaxation. For example, an electron spin in a static magnetic field can undergo transitions from spin up to spin down due to

magnetic field fluctuations in the  $x, y$ -direction at a frequency that matches the Larmor precession. In the case of weak coupling between qubit and environment, relaxation is initially exponential in time with a typical timescale:

$$1/T_1 = S_x(\Delta E/\hbar) + S_y(\Delta E/\hbar) \quad (3.7)$$

This expression has been derived phenomenologically in the context of NMR (see e.g. [21, 22]) but it has also been derived by integration of the qubit time dynamics over different noise paths [23].

The loss of phase information, also referred to as decoherence, is due to the longitudinal fluctuations  $h_z$ . A qubit in a superposition state undergoes due to  $h_z$  a precession in the  $xy$ -plane of the Bloch-sphere, which can be seen as a loss of phase coherence if the value of  $h_z$  is unknown. In contrast to relaxation where only one frequency component of the noise spectrum contributes, a wide range of frequency components of  $S_z(\omega)$  contributes to the loss of phase coherence (see below for a more precise definition).

Experimentally, the coherence decay during free evolution can be measured via a Ramsey sequence performed on a qubit eigenstate; e.g.  $|0\rangle$ . The coherence decay of a qubit in a superposition of  $|0\rangle$  and  $|1\rangle$  can also be represented as the decay of the off-diagonal elements of the qubit density matrix  $\rho_{ij}$  and reads [37]:

$$\rho_{12}(\tau) \propto e^{-(\tau/T_2^*)^2}, \text{ with } 1/T_2^* = \int S_z(\omega) d\omega = \sigma. \quad (3.8)$$

This is the result of averaging the qubit precession in the  $xy$ -plane with rate  $h_{x,y}$  over the distribution of  $\delta h_z$ , which we have taken Gaussian in this case with spread  $\sigma$ . This expression for  $T_2^*$  is only valid when  $S_z(\omega) \cong 0$  for  $\omega > 1/T_2^*$ . In that case, the time-dependent fluctuations of  $h_z$  are quasi-static compared to the precession rate due to  $h_z$ . Interestingly, due to high frequency components of  $S_z(\omega)$ ,  $T_2^*$  can increase because from the perspective of the spin, the fast fluctuations average to a static effective field. This effect is called motional narrowing, which we will not further address here. The loss of spin coherence that is caused by the zero frequency component of  $S_z(\omega)$  is often referred to as dephasing or inhomogeneous broadening. These terms were used in traditional NMR experiments on ensembles of spins. Then, each spin experiences a different  $\delta h$  and therefore, the coherence decay is an average effect of the  $\delta h$  distribution. For single qubit experiments, dephasing can still occur when coherence measurements are averaged over long times. Therefore, the dephasing time does not characterize the coherence of the qubit well.

An improved characterization of the qubit coherence is provided by a Hahn echo decay time. Namely, dephasing is reversible by a Hahn echo, which is a qubit

$\pi$ -rotation in the xy-plane of the Bloch-sphere. This will reverse completely the dynamics caused by  $S_z(0)$ , but higher frequency components still contribute to a (echo) coherence decay.

Finally, we remark that the effect of  $\delta h_z$  on the coherence is quite different for a driven qubit. In that case,  $S_z(0)$  and the driving frequency  $\omega_d$  component of the noise power spectrum  $S_z(\omega_d)$  contribute to the coherence decay [24]. This implies that driving the qubit faster results in a longer decay time, provided that  $S_z(\omega)$  is smaller for larger  $\omega$ , which is often the case. In chapter 8, we discuss an experiment where  $S_z(\omega_d)$  is zero, i.e.  $1/\omega_d$  is much shorter than the correlation time of the environment. In that case, the decay of the driven oscillations is only due to  $S_z(0)$  and follows a power law instead of the usual exponential decay [25].

As we will see below, relaxation of an electron spin in a GaAs quantum dot is dominated by electric field fluctuations from phonons which couple to the electron spin via the spin-orbit interaction (SOI). The associated effective field fluctuations point in the longitudinal direction only (see next section) with a more significant contribution at higher frequencies. Therefore, this mechanism contributes mainly to spin relaxation. In contrast, a fluctuating effective field due to the interaction with the nuclear spins points in all three directions, and contains mostly low-frequency components. Therefore, the contribution from the nuclei to spin relaxation is very small, but instead, the nuclei do cause very rapid spin dephasing (see section 3.6).

## 3.5 Spin-orbit interaction

An electron moving in a static but non-homogeneous electric field “sees” in its rest frame a time-varying electric field, which induces a magnetic field. In turn, this magnetic field couples to the magnetic moment of the electron. This coupling between the electron spin and its orbital momentum in space gives rise to the well-known fine splitting in atomic spectra. The spin-orbit interaction (SOI) was originally introduced as a relativistic correction to the Hamiltonian of the Schrödinger equation:  $H_{\text{SO}} = \frac{\hbar}{4m_0^2c^2}(\nabla V) \times \mathbf{p} \cdot \boldsymbol{\sigma}$ , where  $m_0$  is the free electron mass,  $c$  is the speed of light,  $V$  the potential landscape,  $p$  the electron momentum, and  $\sigma$  the Pauli matrices.

In semiconductors, the SOI is also present because the moving electrons (and holes) experience an internal field from the crystal potential landscape. In 2DEGs formed in III-V semiconductors, we can distinguish two sources for the SOI. The first is due to an asymmetric crystal potential. This is present in III-V semiconductors that crystallize in the zinc-blende structure, which does not have

inversion symmetry (in contrast to silicon). This effect was investigated theoretically by Dresselhaus [26], and the Hamiltonian in two dimensions reads:  $H_D = \beta(-p_x\sigma_x + p_y\sigma_y) + \mathcal{O}(|p^3|)$ , with the  $|p^3|$  term much smaller than the linear-momentum terms due to strong confinement in the z-direction. Here,  $\beta$  depends on material properties and the confinement in the z-direction, and  $x, y$  point along the crystallographic directions [100],[010].

The second source giving rise to SOI is the asymmetry of the confining potential in the z-direction. This type of SOI is known as Rashba SOI [27] with Hamiltonian  $H_R = \alpha(-p_y\sigma_x + p_x\sigma_y)$ . Although the average electric field acting on the electron is zero, the Rashba SOI is non-zero due to mixing of the conduction band with the valence band. For that reason the strength  $\alpha$  of the Rashba SOI depends not only on the shape of the confining potential, but also on the crystal composition in the quantum well, and is largest for narrow gap III-V semiconductors, such as InAs and InGaAs.

Besides externally applied electric fields, several sources of uncontrolled fluctuating electric fields are present in semiconductor quantum dots, like fluctuations of the gate potentials [28], background charge fluctuations [28], noise in an adjacent point contact [29] or lattice phonons [30]. The latter is the dominant source for spin relaxation, which is extensively studied in theory and experiments. Because the Zeeman energy  $E_z$  (for fields below 12 T) is much smaller than the typical orbital level spacing  $\hbar\omega$ , this relaxation time can be extraordinary long, especially when approaching zero field. This can be understood from the fact that virtual transitions to the excited orbital are necessary to flip the spin. An elaborate calculation of the spin relaxation rate includes the phonon density of states ( $\sim E_z^2$ ) [31] and the electric field amplitude of piezo-electric or deformation phonons respectively:  $\propto E_z^{\pm 1/2}$ . This gives  $1/T_1 \propto (N(E_z)+1)E_z^5/(\hbar\omega_0)^4$  for piezo-electric phonons and  $1/T_1 \propto (N(E_z)+1)E_z^7/(\hbar\omega_0)^6$  for deformation phonons [33, 32]. Here,  $N(E_z) = (e^{E_z/kT} - 1)^{-1}$  is the Bose occupation number for the phonons. Experimentally measured relaxation times between Zeeman sublevels range from 120  $\mu s$  at 14 T to a value exceeding a second at 1 T [34, 35, 36].

## 3.6 Interaction with the nuclear spin bath

### 3.6.1 Hyperfine interaction

In all III-V semiconducting materials such as GaAs, the nuclei have non-zero spin. The magnetic coupling between the electron and nuclear dipole moments

$\mu_n$  and  $\mu_e$  is described by the Hamiltonian

$$H = \frac{\mu_e \cdot \mu_n}{r^3} - \frac{3(\mu_e \cdot \mathbf{r})(\mu_n \cdot \mathbf{r})}{r^5}, \quad (3.9)$$

where  $\mathbf{r}$  is the vector from the nucleus to the electron. Provided that the magnetic moments are sufficiently far apart (for any state of nonzero angular momentum, like p and d-states), the interaction is evaluated straightforwardly by averaging over the electron wavefunction. However, for s-states (like conduction band electrons), the wavefunction is non-zero at the nucleus and the large electrostatic potential energy requires evaluation of the relativistic theory. Solving the Dirac equation for the s-state results in the so-called Fermi contact hyperfine interaction between the electron spin  $\mathbf{S}$  and nuclear spin  $\mathbf{I}$  [22]. We give the contact hyperfine Hamiltonian after averaging over the electron wavefunction  $\psi(\mathbf{r})$ :

$$H_F = \frac{8\pi}{3} \frac{\mu_0}{4\pi} g_0 \mu_B \gamma_n \hbar \mathbf{I} \cdot \mathbf{S} |\psi(0)|^2, \quad (3.10)$$

with  $\mu_B$  the Bohr magneton,  $g_0$  the free-electron g factor,  $\gamma_n$  the nuclear gyro-magnetic ratio, and  $|\psi(0)|^2$  the value of the electronic wave function  $\psi(\mathbf{r})$  at the position of the nucleus.

When an electron spin interacts with more than one nuclear spin (like in the solid-state environment), we sum over the contributions from the nuclear spins in different unit cells [22, 37]:

$$H_{HF} = \sum A_i \mathbf{I}_i \cdot \mathbf{S}, \quad (3.11)$$

where we introduced the hyperfine constant  $A_i = \nu A |\psi(r_i)|^2$ , with  $\nu$  the volume of a crystal unit cell containing one nuclear spin, and  $A$  is the average hyperfine coupling constant. In GaAs  $A \sim 90 \mu\text{eV}$  [17], which is weighted by the natural abundances of the three isotopes  $^{69}\text{Ga}$ ,  $^{71}\text{Ga}$  and  $^{75}\text{As}$  (of respectively 1, 0.6 and 0.4). We note that  $A$  is independent of  $N$ , which implies that the hyperfine energy of one electron interacting with one nucleus is the same as one electron interacting with one million nuclei, provided that they point in the same direction. Furthermore,  $A \propto 1/Z^3$  because  $|\psi(0)|^2 \sim 1/Z^3$  for hydrogenic s-type wavefunctions and assuming an unscreened potential from the nucleus.

The contact hyperfine interaction is exactly zero for p or d-type orbitals because  $\psi(0) = 0$ . For these orbitals, the anisotropic hyperfine interaction is important, which is the case for example for confined GaAs hole spins. For s-type

---

The effective g-factor takes into account the spin interaction of the electron with the crystal field that varies slowly in space. This is different for the hyperfine field created by the nuclei where the free electron g-factor must be used

orbitals, the anisotropic hyperfine interaction is exactly zero because the angular integral vanishes. In GaAs, the conduction band is not completely s-type and for that reason the anisotropic hyperfine interaction is not exactly zero. Still, it is small relative to the isotropic contact hyperfine interaction.

### 3.6.2 Spin dephasing due to the nuclear field

The effects of the hyperfine interaction can be very complex, as the nuclear spins can affect the electron spin, giving rise to relaxation and/or decoherence. In turn, the electron spin affects the nuclear spins, giving rise to a so-called Knight field (effective field felt by the nuclei) and electron-mediated interactions between distant nuclear pairs. In this section, we will discuss how the nuclear spins affects the coherence of the electron spin, and in the next section, we will address the nuclear dynamics mediated by the electron.

From the perspective of the electron, it is, under certain conditions, allowed (when quantum fluctuations of  $H_{HF}$  can be neglected [38]) to replace the operator  $\sum A_i \mathbf{I}_i$  with a classical magnetic field  $\mathbf{B}_N$ , also called Overhauser field. When all nuclear spins are fully polarized,  $|\mathbf{B}_N| \sim 5$  T, independent of  $N$ . However, in thermal equilibrium with typical temperatures ( $\geq 10$  mK) and magnetic fields ( $\leq 12$  T), the thermal energy  $kT$  dominates the nuclear Zeeman energy (described by  $H_N$ ) and  $H_{HF}$ . In that case, according to the central-limit theorem we can write the density matrix of the thermal nuclear spin state as

$$\rho_N \cong e^{-H_N/kT} = \sum_J P_J |J\rangle \langle J|, \quad (3.12)$$

where  $|J\rangle$  is an eigenstate of  $\hat{H}_N$ . The average effective nuclear field of this thermal nuclear spin state is zero, but the distribution is Gaussian in all three direction with spread  $\sigma_N = A/\sqrt{N} \sim 5$  mT for  $N = 10^6$  [33, 39]. This is a typical number of nuclei overlapping with the wavefunction of the confined electron. The nuclear field distribution is commonly seen as a statistical nuclear field  $B_{N,stat}$  which fluctuates around zero with spread  $\sigma$ . The statistical nuclear field distribution has been measured in both optical [40, 41] and electrical dots [42, 18]; all were in the range of a few mT. We remark that this statistical nuclear field is much stronger for electrons localized in dots or bound to impurities than for free electrons in a 2DEG which overlap with a much larger number of nuclei.

The statistical nuclear field forms an important dephasing source, because it can point in the direction of the external field and the electron Larmor precession time around a typical nuclear field  $1/g\mu_B B_{N,stat}$  can be quite fast. The coherence decay is reflected in an average precession about a Gaussian distributed

nuclear field:  $\int_{-\infty}^{\infty} \frac{1}{\sqrt{2\pi}\sigma} e^{(-B_{N,z}^2/2\sigma^2)} \cos(g\mu_b B_{N,z}t/\hbar) dB_{N,z} = e^{-(t/T_2^*)^2}$ , with  $T_2^* = \hbar/g\mu_b\sigma \sim 5$  ns [39, 43] (assuming  $\sigma = 5$  mT).

There are several ways to suppress this dephasing source. First of all, one can perform a Hahn echo. Next, polarizing the nuclear system by a fraction  $p$  suppresses the field distribution by a factor  $1/\sqrt{N(1-p^2)}$  [44, 15]. However, a very large, and therefore difficult to realize, polarization of 99.99% is needed to enhance  $T_2^*$  by a factor of 100. Perhaps, a more feasible proposal is to reduce the nuclear field uncertainty by performing measurements of the nuclear field in the  $z$ -direction [45, 46, 47, 48].

Finally, we remark that (similar to the SOI) the effective nuclear field depends on the position of the electron. This implies that an applied electric field at the frequency of the electron spin splitting together with the transverse nuclear field  $B_{N,x,y}$  can induce spin transitions [49]. Similar, uncontrolled field fluctuations, like phonons [50, 51, 52, 53] can lead to spin relaxation, but this process is relatively weak, and the expected relaxation time due to the nuclear field is on the order of a second.

### 3.6.3 Spin decoherence due to nuclear dynamics

The electron spin dynamics due to the statistical nuclear field can be reversed by a Hahn echo technique (see section 3.4) to the extent that the nuclear field is static. However, the spin-echo coherence time  $T_{2,\text{echo}}$  can still be limited by fluctuations of the nuclear field due to the hyperfine interaction (as we will see below), and the dipole interaction between neighboring nuclear spins.

In order to study the dynamics of the electron-nuclear system, we write the hyperfine interaction Hamiltonian in the following way:

$$H = \sum_i A_i (\sigma_z I_{z,i} + \sigma_+ I_{i-} + \sigma_- I_{i+}). \quad (3.13)$$

The last two terms represent electron-nuclear flips-flops that cause fluctuations of the nuclear field. However, due to the difference in Zeeman energy between electron and nuclear spin, this process is not energy conserving and therefore very inefficient for  $B_{\text{ext}} \gg B_{\text{stat}}$ . However, virtual processes such as  $A_i A_j I_{i+} I_{j-} \sigma_+ \sigma_- + \dots$  preserve the electron spin polarization and thus have only a small energy cost ( $\sim A_i - A_j$ ). This energy mismatch of the electron Zeeman energy is allowed for a very short time, similar to an electron tunneling process. While the rate of direct electron-nuclear flip-flops is reduced efficiently with  $1/B_z^2$ , the rate of the first order virtual processes scale with  $1/B_z$  and therefore, these are much harder to suppress. The virtual processes will lead to a long-range coupling between the

nuclear spins changing the effective nuclear field  $\sum A_i I_{i,z}$  and therefore also the electron spin coherence (like discussed in section 3.4). We note that this process is similar to the long-range RKKY interaction between nuclear spins in metals.

Calculating the dynamics due to the hyperfine-mediated nuclear-nuclear flip-flop is a complex many body problem, especially for inhomogeneous  $A_i$  which suppresses this process due to the energy cost  $A_i - A_j$  of a flip-flop. Furthermore, because the nuclear dynamics are not independent of the electron spin, the coupled electron-nuclear system can lead to coherence decay characteristics different than the usual exponential decay. These so-called non-Markovian dynamics are extensively discussed in [15]. In general, the predicted coherence time due to this process is in the range 1-100  $\mu s$  [15, 33, 54, 55, 56] for magnetic fields below 3 T. Interestingly, some theories predict that the hyperfine-mediated dynamics are reversible by a Hahn echo at sufficiently high field ( $>100$  mT) [54, 55, 56]. This would imply that a Hahn echo can not only reverse the spin dynamics due to the environment, but that even the dynamics of the spin environment can be reversed via the electron spin itself!

A second process governing the nuclear dynamics is the dipole-dipole interaction between neighboring nuclei, which is given by the secular approximation (valid for Zeeman energies larger than the interaction strength  $D$ ):

$$H_{i,j} = D(I_i^+ I_j^- + I_i^- I_j^+ - 4I_i^z I_j^z)/2, \quad (3.14)$$

with  $D \sim 1/100\mu s$  [57]. The first two terms give rise to flip-flops of nuclear pairs which changes  $B_{N,z}$  and therefore affects the electron spin coherence. The timescale of the drift in  $B_{N,z}$  is difficult to evaluate due to a combination of complications. First of all, the flip-flop rate is suppressed when  $A_i - A_{i+1} > D$ , causing an energy mismatch [56]. This so-called Knight gradient is stronger in the z-direction (quantum well confinement  $\sim 5$  nm) than x,y-direction (quantum dot confinement  $\sim 30$  nm). It is expected that the drift in  $B_{N,z}$  due to the dipole interaction has a timescale of 1-100 sec, depending sensitively on the dot size. This timescale is much longer than  $1/D$  due to the Knight gradient, but even without Knight gradient long diffusion times are expected because many flip-flops are needed to diffuse nuclear spins to the edge of the quantum dot.

The contribution from the dipole-dipole interaction to the electron coherence time is estimated theoretically at  $\sim 10$ -100  $\mu s$  [16, 58, 55, 59], much faster than the  $B_{N,z}$  drift time. We remark that the nuclear dipole-dipole contribution to  $T_2$  is independent of  $B_{ext}$  and longer for larger dots and thicker quantum wells because then,  $A_i$  is more homogeneous [58]. Furthermore, the drift of  $B_{N,z}$  is governed only by flip-flops from nuclear pairs of the same species. Namely, different species have different gyromagnetic ratios (due to the difference in nuclear mass), resulting in



an energy mismatch.

## References

- [1] L.P. Kouwenhoven, D.G. Austing, and S. Tarucha, Rep. Prog. Phys. **64** (6), 701 (2001).
- [2] L.P. Kouwenhoven, C.M. Marcus, P.L. McEuen, S. Tarucha, R.M. Westervelt, and N.S. Wingreen, in *Mesoscopic Electron Transport*, edited by L.L. Sohn, L.P. Kouwenhoven and G. Schön, (Kluwer, Series E **345**, 1997), p.105-214.
- [3] See e.g. R. Hanson, I. T. Vink, D. P. DiVincenzo, L. M. K. Vandersypen, J. M. Elzerman, L. H. Willems van Beveren, and L.P. Kouwenhoven, to be published in the Proceedings of the XXXIXth Rencontres de Moriond (La Thuile, 2004) “Quantum information and decoherence in nanosystems”; cond-mat/0407793.
- [4] N.W. Ashcroft and N.D. Mermin, *Solid state physics* (Brooks/Cole 1976).
- [5] S. Tarucha, D.G. Austing, Y. Tokura, W.G. van der Wiel and L.P. Kouwenhoven, Phys. Rev. Lett. **84**, 2485 (2000).
- [6] S. Tarucha, D.G. Austing, T. Honda, R.J. van der Hage and L.P. Kouwenhoven, Phys. Rev. Lett. **77**, 3613 (1996) .
- [7] V.N. Golovach and D. Loss, Europhys. Lett. **62**, 83 (2003).
- [8] G. Burkard, D. Loss, and D. P. DiVincenzo, Phys. Rev. B **59**, 2070 (1999).
- [9] J.M. Martinis, M.H. Devoret and J. Clarke, Phys. Rev. B **35**, 4682 (1987).
- [10] K. Bladh *et al.*, Rev. Sci. Instr. **74**,1323 (2003).
- [11] J.H. Davies, *The physics of low-dimensional semiconductors* (Cambridge University Press, 1998).
- [12] L. P. Kouwenhoven, D. G. Austing and S. Tarucha, Rep. Prog. Phys. **64** (6), 701 (2001).
- [13] L. H. Willems van Beveren, R. Hanson, I. T. Vink, F. H. L. Koppens, L. P. Kouwenhoven and L. M. K. Vandersypen, New Journal of Physics **7**, 182 (2005).
- [14] O. N. Jouravlev and Y. V. Nazarov, Phys. Rev. Lett. **96**, 176804 (2006).
- [15] W. A. Coish and D. Loss, Phys. Rev. B. **70**, 195340 (2004).
- [16] R. de Sousa and S. Das Sarma, Phys. Rev. B **67**, 33301 (2003).

- [17] D. Paget, G. Lampel, B. Sapoval, and V. I. Safarov, Phys. Rev. B **15**, 5780 (1977).
- [18] F. H. L. Koppens, J. A. Folk, J. M. Elzerman, R. Hanson, L. H. W. van Beveren, I. T. Vink, H. P. Tranitz, W. Wegscheider, L. P. Kouwenhoven, and L. M. K. Vandersypen, Science **309**, 1346 (2005).
- [19] J. Inarrea, *et al.*, Arxiv:cond-mat/0609323 (2006)
- [20] F. H. L. Koppens, C. Buizert, I. T. Vink, K. C. Nowack, T. Meunier, L. P. Kouwenhoven, and L. M. K. Vandersypen, Journal of Applied Physics **101**, 081706 (2007)
- [21] F. Bloch, Phys. Rev. **70**, 460 (1946).
- [22] A. Abragam, The Principles of Nuclear Magnetism, Clarendon, 1961.
- [23] [51] E.B. Davies. Quantum theory of open systems. IMA, 1976.
- [24] E. Geva, The Journal of Chemical Physics **102**, 8541 (1995).
- [25] F. H. L. Koppens, D. Klauser, W. A. Coish, K. C. Nowack, L. P. Kouwenhoven, D. Loss, and L. M. K. Vandersypen, Physical Review Letters **99**, 106803 (2007).
- [26] G. Dresselhaus, Phys. Rev. **100**, 580 (1955).
- [27] E. I. Rashba, Sov. Phys. Solid State **2**, 1109 (1960).
- [28] F. Marquardt and V. A. Abalmassov, Phys. Rev. B **71**, 165325 (2005).
- [29] Massoud Borhani, Vitaly N. Golovach, and Daniel Loss, Phys. Rev. B **73**, 155311 (2006).
- [30] V. N. Golovach, A.V. Khaetskii, and D. Loss, Phys. Rev. Lett. **93**, 016601 (2004).
- [31] N. W. Ashcroft and N. D. Mermin, Solid State Physics, Saunders, New York, 1974.
- [32] A. V. Khaetskii and Y. V. Nazarov, Phys. Rev. B **64**, 125316 (2001).
- [33] A. V. Khaetskii, D. Loss, and L. Glazman, Phys. Rev. Lett. **88**, 186802 (2002).
- [34] J. M. Elzerman, R. Hanson, L. H. W. van Beveren, B. Witkamp, L. M. K. Vandersypen, and L. P. Kouwenhoven, Nature **430**, 431 (2004).
- [35] M. Kroutvar, Y. Ducommun, D. Heiss, M. Bichler, D. Schuh, G. Abstreiter, and J. J. Finley, Nature **432**, 81 (2004).

- [36] S. Amasha, K. MacLean, I. Radu, D. M. Zumbuhl, M. A. Kastner, M. P. Hanson, and A. C. Gossard, cond-mat/0607110 (2006).
- [37] C. P. Slichter. Principles of Magnetic Resonance, 3rd ed. Springer-Verlag, Berlin, 1990.
- [38] W. A. Coish, Daniel Loss, E. A. Yuzbashyan, and B. L. Altshuler, Journal of Applied Physics **101**, 081715 (2007).
- [39] I. A. Merkulov, A. L. Efros, and M. Rosen, Phys. Rev. B **65**, 205309 (2002).
- [40] P. F. Braun, X. Marie, L. Lombez, B. Urbaszek, T. Amand, P. Renucci, V. K. Kalevich, K. V. Kavokin, O. Krebs, P. Voisin, and Y. Masumoto, Phys. Rev. Lett. **94**, 116601 (2005).
- [41] M. V. G. Dutt, J. Cheng, B. Li, X. D. Xu, X. Q. Li, P. R. Berman, D. G. Steel, A. S. Bracker, D. Gammon, S. E. Economou, R. B. Liu, and L. J. Sham, Phys. Rev. Lett. **94**, 227403 (2005).
- [42] A. C. Johnson, J. R. Petta, J. M. Taylor, A. Yacoby, M. D. Lukin, C. M. Marcus, M. P. Hanson, and A. C. Gossard, Nature **435**, 925 (2005).
- [43] A. V. Khaetskii, D. Loss, and L. Glazman, Phys. Rev. B **67**, 195329 (2003).
- [44] J. Schliemann, A. V. Khaetskii, and D. Loss, Phys. Rev. B **66**, 245303 (2002).
- [45] D. Klauser, W. A. Coish, and D. Loss, Phys. Rev. B **73**, 205302 (2006).
- [46] D. Stepanenko, G. Burkard, G. Giedke, and A. Imamoglu, Phys. Rev. Lett. **96**, 136401 (2006).
- [47] O. Cakir and T. Takagahara, Arxiv preprint cond-mat/0609217 (2006).
- [48] G. Giedke, J. M. Taylor, D. DAlessandro, M. D. Lukin, and A. Imamoglu, Phys. Rev. A **74**, 32316 (2006).
- [49] EA Laird, C. Barthel, EI Rashba, CM Marcus, MP Hanson, and AC Gossard, arXiv: cond-mat/0707.0557 (2007).
- [50] S. I. Erlingsson, Y. V. Nazarov, and V. I. Falko, Phys. Rev. B **64**, 195306 (2001).
- [51] S. I. Erlingsson and Y. V. Nazarov, Phys. Rev. B **66**, 155327 (2002).
- [52] S. I. Erlingsson and Y. V. Nazarov, Phys. Rev. B **70**, 205327 (2004).
- [53] V. A. Abalmassov and F. Marquardt, Phys. Rev. B **70**, 75313 (2004).
- [54] N. Shenvi and K. Rogerio de Sousa, Phys. Rev. B **71**, 224411 (2005).
- [55] W. Yao, R. B. Liu, and L. J. Sham, Phys. Rev. B **74**, 195301 (2006).
- [56] C. Deng and X. Hu, Phys. Rev. B **73**, 241303 (2006).

- [57] R. G. Shulman, B. J. Wyluda, and H. J. Hrostowski, Phys. Rev. **109**, 808 (1958).
- [58] R. de Sousa and S. Das Sarma, Phys. Rev. B **68**, 115322 (2003).
- [59] W. M. Witzel and S. Das Sarma, Physical Review B **74**, 35322 (2006).

## Chapter 4

# Single-shot read-out of two-electron spin states using spin-dependent tunnel rates

We present a method for reading out the spin state of confined electrons in a quantum dot that is, unlike previously used read-out, robust against charge noise and can still be used when the electron temperature exceeds the energy splitting between the states. The spin dependence of the tunnel rates is used to correlate the spin states to different charge states. A subsequent fast measurement of the charge on the dot then reveals the original spin state. We experimentally demonstrate the method by performing read-out of the two-electron spin states, achieving a single-shot visibility of more than 80%. We find very long triplet-to-singlet relaxation times (up to several milliseconds), with an in-plane magnetic field dependence consistent with spin-orbit coupling, in combination with phonons, as the dominant source of relaxation. Additionally, we perform repeated measurements on the spin states with short read-out pulses. This allows us to study the evolution of the spins states between measurements and correlate their outcomes. Finally, we exploit both the spin-dependent tunnel rates and the high singlet-triplet energy splitting to increase the measurement fidelity to 97.5%.

---

Parts of this chapter have been published in *Physical Review Letters* **94**, 196802 (2005), *Physical Review B* **74**, 195303 (2006) and *Physica Status Solidi (b)* **243**, 3855 (2006).

## 4.1 Read-out of electron spin states

The magnetic moment associated with the electron spin is tiny and therefore hard to measure directly. However, by correlating the spin states to different charge states and subsequently measuring the charge on the dot, the spin state can be determined [1]. Such a spin-to-charge conversion can be achieved by positioning the spin levels around the electrochemical potential of the reservoir  $\mu_{res}$  as depicted in Fig. 4.1a, such that one electron can tunnel off the dot from the spin excited state,  $|ES\rangle$ , whereas tunneling from the ground state,  $|GS\rangle$ , is energetically forbidden. By combining this scheme with a fast (40 kHz bandwidth) measurement of the charge dynamics, we have recently performed read-out of the spin orientation of a single electron, with a single-shot visibility up to 65% [2]. A conceptually similar scheme has also allowed single-shot read-out of a superconducting charge qubit [3]. However, this energy-selective read-out (E-RO) has three drawbacks: (i) E-RO requires an energy splitting of the spin states larger than the thermal energy of the electrons in the reservoir. Thus, for a single spin the read-out is only effective at very low electron temperature and high magnetic fields (8 T and higher in Ref. [2]). Also, interesting effects occurring close to degeneracy, e.g. near the singlet-triplet crossing for two electrons [4], can not be probed. (ii) Since the E-RO relies on precise positioning of the spin levels with respect to the reservoir, it is very sensitive to fluctuations in the electrostatic potential. Background charge fluctuations [5], active even in today's most stable devices, can easily push the levels out of the read-out configuration. (iii) High-frequency noise can spoil the E-RO by inducing photon-assisted tunneling from the spin ground state to the reservoir. Since the QPC is a source of shot noise, this limits the current through the QPC and thereby the bandwidth of the charge detection [6]. A different read-out method is desired that does not suffer from these constraints.

### 4.1.1 Spin read-out scheme using spin-dependent tunnel rates

In this section, we present a spin read-out scheme where spin-to-charge conversion is achieved by exploiting the difference in *tunnel rates* of the different spin states to the reservoir [24]. We outline the concept of this tunnel-rate selective read-out (TR-RO) in Fig. 4.1b. Assume that the tunnel rate from the spin excited state  $|ES\rangle$  to the reservoir,  $\Gamma_{ES}$ , is much higher than the tunnel rate from  $|GS\rangle$ ,  $\Gamma_{GS}$ , i.e.  $\Gamma_{ES} \gg \Gamma_{GS}$ . Then, we can read out the spin state as follows. At time  $t=0$ , we position the levels of both  $|ES\rangle$  and  $|GS\rangle$  far above the electrochemical potential

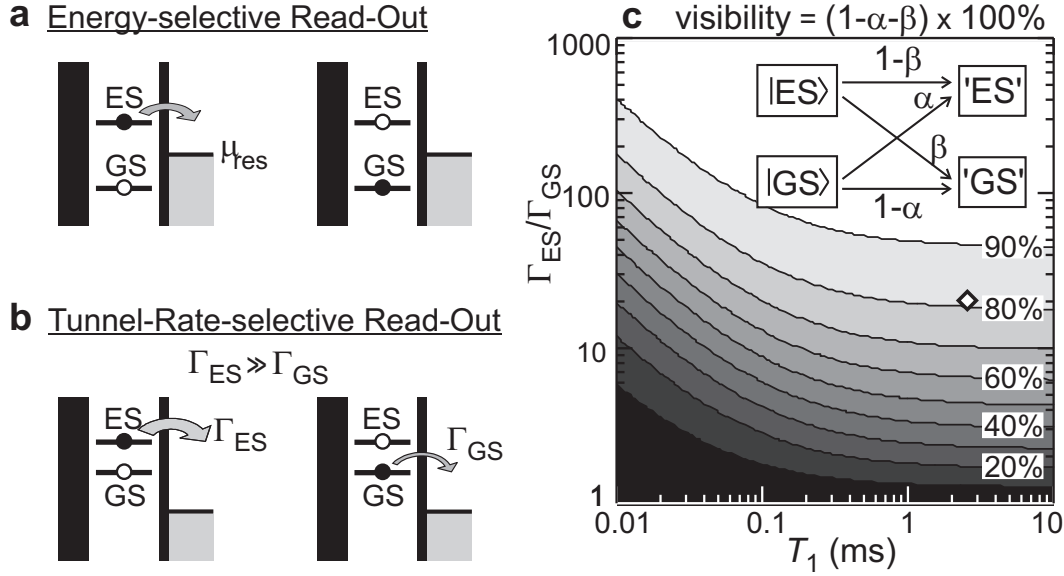


**Figure 4.1:** (a-b) Energy diagrams explaining two schemes for spin-to-charge conversion. (a) Energy-selective read-out (E-RO). Tunneling is energetically allowed from  $|ES\rangle$  (left diagram), but not from  $|GS\rangle$  (right diagram). (b) Tunnel rate-selective read-out (TR-RO). One electron is allowed to tunnel off the dot, regardless of the spin state, but the tunnel rate depends strongly on the spin state:  $\Gamma_{ES} \gg \Gamma_{GS}$ . If a charge measurement after a time  $\tau$ , where  $\Gamma_{GS}^{-1} \gg \tau \gg \Gamma_{ES}^{-1}$ , indicates that one electron has (not) tunneled, the state is declared  $|'ES'\rangle$  ( $|'GS'\rangle$ ). (c) Visibility of the TR-RO as a function of spin relaxation time  $T_1$  and the ratio  $\Gamma_{ES}/\Gamma_{GS}$ , for  $\Gamma_{GS} = 2.5$  kHz. The diamond corresponds to the read-out parameters of Fig. 4.2e. Inset: definition of the error rates  $\alpha$  and  $\beta$ . If the initial state is  $|GS\rangle$ , there is a probability  $\alpha$  that the measurement gives the wrong outcome, i.e.  $|'ES'\rangle$  ( $\beta$  is defined similarly).

of the reservoir  $\mu_{res}$ , so that one electron is energetically allowed to tunnel off the dot regardless of the spin state. Then, at a time  $t = \tau$ , where  $\Gamma_{GS}^{-1} \gg \tau \gg \Gamma_{ES}^{-1}$ , an electron will have tunneled off the dot with a very high probability if the state was  $|ES\rangle$ , but most likely no tunneling will have occurred if the state was  $|GS\rangle$ . Thus, the spin information is converted to charge information, and a measurement of the number of electrons on the dot reveals the original spin state.

A major advantage of this TR-RO scheme is that it does not rely on a large energy splitting between the spin states. Furthermore, it is robust against background charge fluctuations, since these cause only a small variation in the tunnel rates (of order  $10^{-3}$  in Ref. [5]). Finally, photon-assisted tunneling is not important since here tunneling is energetically allowed regardless of the initial spin state. Thus, we see that TR-RO can overcome the limitations of E-RO.

### 4.1.2 Measurement visibility of the read-out

We first analyze the fidelity of the TR-RO theoretically using the error rates  $\alpha$  and  $\beta$  as defined in the diagram of Fig. 4.1c (inset). Here,  $\alpha$  is the probability that one electron has tunneled even though the initial state was  $|GS\rangle$ , and  $\beta$  the probability that no tunneling has occurred even though the initial state was  $|ES\rangle$ . The charge measurement itself is assumed to be perfect, and spin relaxation from  $|ES\rangle$  to  $|GS\rangle$  is modeled by a rate  $1/T_1$ . We find analytically

$$\alpha = 1 - e^{-\Gamma_{GS}\cdot\tau}, \quad (4.1)$$

$$\beta = \frac{(1/T_1)e^{-\Gamma_{GS}\cdot\tau} + (\Gamma_{ES} - \Gamma_{GS})e^{-(\Gamma_{ES} + 1/T_1)\cdot\tau}}{\Gamma_{ES} + 1/T_1 - \Gamma_{GS}}, \quad (4.2)$$

where  $\tau$  is the time at which we measure the number of electrons  $N$  [8]. The visibility of the read-out is  $1 - \alpha - \beta$ .

The optimal value for the read-out time for given values of  $T_1$  and the ratio  $\Gamma_T/\Gamma_S$ ,  $\tau_{max}$ , is found by solving  $d(\text{visibility})/d\tau = 0$  for  $\tau$ . We find

$$\tau_{max} = \frac{1}{\Gamma_{ES} + 1/T_1 - \Gamma_{GS}} \ln \left( \frac{\Gamma_{ES} + 1/T_1}{\Gamma_{GS}} \right). \quad (4.3)$$

Inserting this expression into Eq.(4.1) and Eq.(4.2) yields the maximum visibility.

In Fig. 4.1c we plot the visibility for  $\tau = \tau_{max}$  as a function of  $T_1$  and the ratio of the tunnel rates  $\Gamma_{ES}/\Gamma_{GS}$ . (Here,  $\Gamma_{GS}$  is chosen to be 2.5 kHz, which is well within the bandwidth of our charge detection set up [6].) We see that for  $\Gamma_{ES}/\Gamma_{GS} = 10$  and  $T_1 = 0.5$  ms, the visibility is 65%, equal to the visibility obtained with E-RO in Ref. [2] for the same  $T_1$ . For  $\Gamma_{ES}/\Gamma_{GS} > 60$  and  $T_1 = 0.5$  ms, the visibility of TR-RO exceeds 90%.

The TR-RO can be used in a similar way if  $\Gamma_{ES}$  is much *lower* than  $\Gamma_{GS}$ . The visibility for this case can be calculated simply by replacing  $\alpha$  and  $\beta$  in Eqs.(4.1)-(4.2) with  $1 - \alpha$  and  $1 - \beta$  respectively. Significant differences with the values in Fig. 4.1c arise only in the limit  $T_1 \ll \Gamma_{ES}^{-1}$ .

The main ingredient necessary for TR-RO is a spin dependence in the tunnel rates. For a single electron, this spin dependence can be obtained in the Quantum Hall regime, where a high spin-selectivity is induced by the spatial separation of spin-resolved edge channels [9, 10]. TR-RO can also be used for read-out of a two-electron dot, where the electrons are either in the spin-singlet ground state, denoted by  $|S\rangle$ , or in a spin-triplet state, denoted by  $|T\rangle$ . In  $|S\rangle$ , the two electrons both occupy the lowest orbital, but in  $|T\rangle$  the electrons are both divided amongst the lowest and the first excited orbital. Since the wave function in this excited orbital has more weight near the edge of the dot [11], the coupling to the reservoir



is stronger than for the lowest orbital. Therefore, the tunnel rate from a triplet state to the reservoir  $\Gamma_T$  is much larger than the rate from the singlet state  $\Gamma_S$ , i.e.  $\Gamma_T \gg \Gamma_S$  [13]. We use this spin-dependence in the following to experimentally demonstrate TR-RO for two electrons.

### 4.1.3 Single-shot read-out of the two-electron spin states

A quantum dot (white dotted circle in Fig. 4.2a) and a QPC are defined in a two-dimensional electron gas (2DEG) with an electron density of  $4 \cdot 10^{15} \text{ m}^{-2}$ , located 60 nm below the surface of a GaAs/AlGaAs heterostructure from Sumitomo Electric, by applying negative voltages to gates  $L$ ,  $M$ ,  $T$  and  $Q$ . Gate  $P$  is used to apply fast voltage pulses. We completely pinch off the tunnel barrier between gates  $L$  and  $T$ , so that the dot is only coupled to the reservoir on the right. The conductance of the QPC is tuned to about  $e^2/h$ , making it very sensitive to the number of electrons on the dot. A voltage bias of 0.8 mV induces a current through the QPC,  $I_{QPC}$ , of about 30 nA.

We tune the dot to the  $N = 1 \leftrightarrow 2$  transition in a small parallel field  $B_{//}$  of 0.02 T. Here, the energy difference between  $|T\rangle$  and the ground state  $|S\rangle$ ,  $E_{ST}$ , is about 1 meV. From measurements of the tunnel rates [12], we estimate the ratio  $\Gamma_T/\Gamma_S$  to be on the order of 20. A similar ratio was found previously in transport measurements on a different device [13]. As can be seen in Fig. 4.1c, for  $T_1 > 1 \text{ ms}$  this permits a read-out visibility  $> 80\%$ .

We implement the TR-RO by applying voltage pulses as depicted in Fig. 4.2b to gate  $P$ . Figure 4.2c shows the expected response of  $I_{QPC}$  to the pulse, together with the level diagrams in the three different stages. Before the pulse starts, there is one electron on the dot. Then, the pulse pulls the levels down so that a second electron can tunnel onto the dot ( $N = 1 \rightarrow 2$ ), forming either a singlet or a triplet state with the first electron. The probability that a triplet state is formed is given by  $3\Gamma_T/(\Gamma_S + 3\Gamma_T)$ , where the factor of 3 is due to the degeneracy of the triplets. After a variable waiting time  $t_{wait}$ , the pulse ends and the read-out process is initiated, during which one electron can leave the dot again. The rate for tunneling off depends on the two-electron state, resulting in the desired spin-to-charge conversion. The QPC is used to detect the number of electrons on the dot. Due to the direct capacitive coupling of gate  $P$  to the QPC channel,  $\Delta I_{QPC}$  follows the pulse shape. Tunneling of an electron on or off the dot gives an additional step in  $\Delta I_{QPC}$  [2, 6, 14], as indicated by the arrows in Fig. 4.2c.

Now,  $\Gamma_S$  is tuned to 2.5 kHz, and  $\Gamma_T$  is therefore  $\approx 50 \text{ kHz}$ . In order to achieve a good signal-to-noise ratio in  $I_{QPC}$ , the signal is sent through an external 20 kHz low-pass filter. As a result, many of the tunnel events from  $|T\rangle$  will not

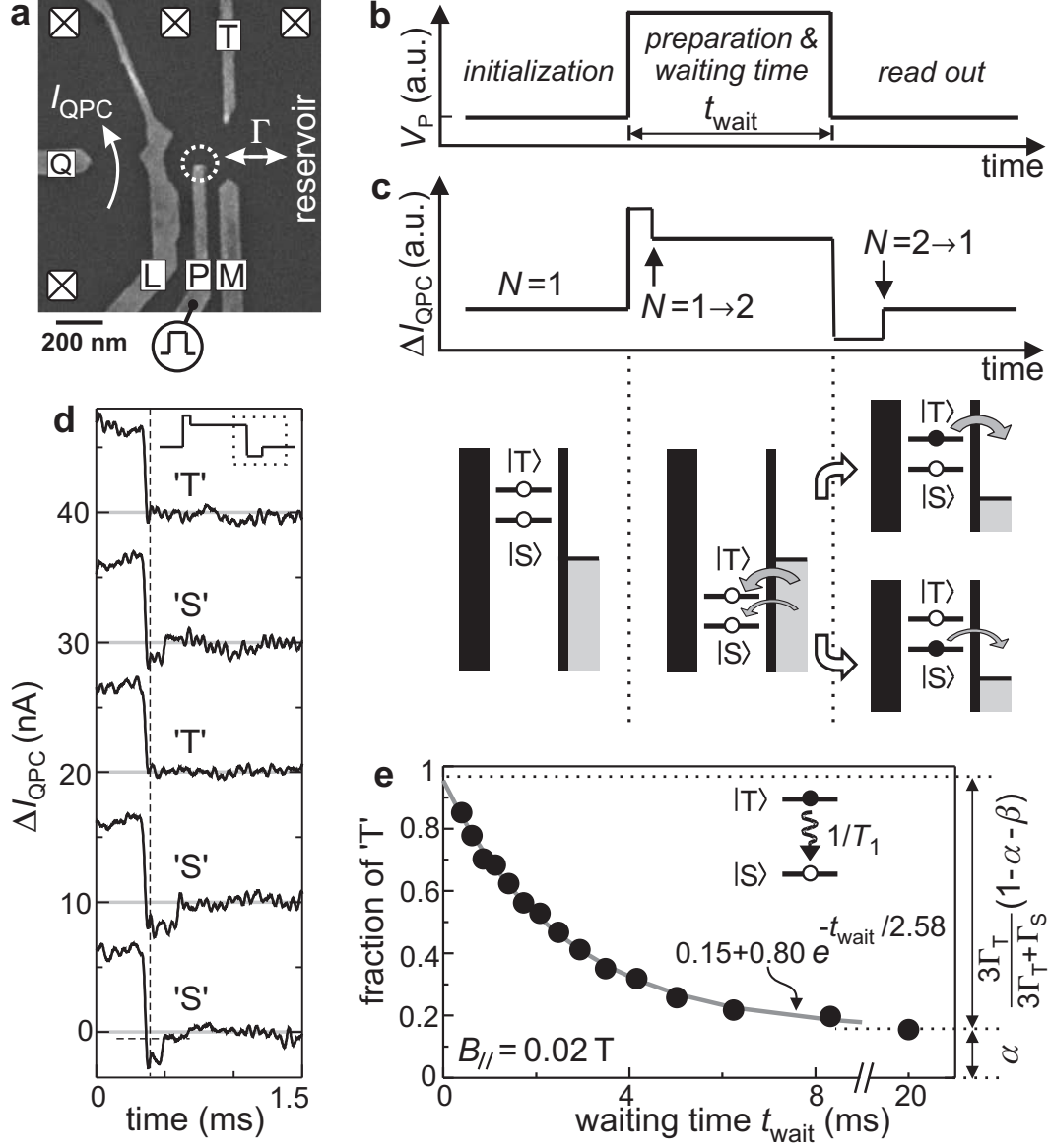


**Figure 4.2:** Single-shot read-out of  $N=2$  spin states. (a) Scanning electron micrograph of a device as used in the experiments. (b) Pulse waveform applied to gate  $P$ . (c) Response of the QPC-current to the waveform of (b). Energy diagrams indicate the positions of the levels during the three stages. In the final stage, spin is converted to charge information due to the difference in tunnel rates for states  $|S\rangle$  and  $|T\rangle$ . (d) Real-time traces of  $\Delta I_{QPC}$  during the last part of the waveform (dashed box in the inset), for  $t_{wait} = 0.8$  ms. At the vertical dashed line,  $N$  is determined by comparison with a threshold (horizontal dashed line in bottom trace) and the spin state is declared 'T' or 'S' accordingly. (e) Fraction of 'T' as a function of waiting time at  $B_{//} = 0.02$  T, showing a single-exponential decay with a time constant  $T_1$  of 2.58 ms.

be resolved, but the tunneling from  $|S\rangle$  should be clearly visible.

Figure 4.2d shows several traces of  $\Delta I_{QPC}$ , from the last part (300  $\mu$ s) of the pulse to the end of the read-out stage (see inset), for a waiting time of 0.8 ms. In some traces, there are clear steps in  $\Delta I_{QPC}$ , due to an electron tunneling off the dot. In other traces, the tunneling occurs faster than the filter bandwidth. In order to discriminate between  $|S\rangle$  and  $|T\rangle$ , we first choose a read-out time  $\tau$  (indicated by a vertical dashed line in Fig. 4.2d) and measure the number of electrons on the dot at that time by comparing  $\Delta I_{QPC}$  to a threshold value (as indicated by the horizontal dashed line in the bottom trace of Fig. 4.2d). If  $\Delta I_{QPC}$  is below the threshold, it means  $N = 2$  and we declare the state ' $S$ '. If  $\Delta I_{QPC}$  is above the threshold, it follows that  $N = 1$  and the state is declared ' $T$ '. Our method for determining the optimal threshold value and read-out time is explained below.

To verify that ' $T$ ' and ' $S$ ' indeed correspond to the spin states  $|T\rangle$  and  $|S\rangle$ , we change the relative occupation probabilities by varying the waiting time. The probability that the electrons are in  $|T\rangle$ ,  $P_T$ , decays exponentially with the waiting time:  $P_T(t) = P_T(0) e^{-t_{wait}/T_1}$ . Therefore, as we make the waiting time longer, we should observe an exponential decay of the fraction of traces that are declared ' $T$ '.

We take 625 traces similar to those in Fig. 4.2d for each of 15 different waiting times. Note that the two-electron state is formed on a timescale (of order  $1/\Gamma_T$ ) much shorter than the shortest  $t_{wait}$  used (400  $\mu$ s). To find the optimal read-out parameters, we scan a wide range of read-out times and threshold values using a computer program. For each combination of these two parameters, the program determines the fraction of traces declared ' $T$ ' for each of the waiting times, and fits the resulting data with a single exponential decay  $A e^{-t_{wait}/T_1} + \alpha$ . The prefactor  $A$  is given by  $3\Gamma_T/(\Gamma_S + 3\Gamma_T) \times (1 - \alpha - \beta)$ . We see that  $A$  is proportional to the read-out visibility, and therefore the optimal read-out parameters can be determined simply by searching for the highest value of  $A$ . Here, we find the optimal values to be -0.4 nA for the threshold and 70  $\mu$ s for  $\tau$  (corresponding to  $t = 370$   $\mu$ s in Fig. 4.2d), and use these in the following.

In Fig. 4.2e, we plot the fraction of traces declared ' $T$ ' as a function of  $t_{wait}$ . We see that the fraction of ' $T$ ' decays exponentially, showing that we can indeed read out the two-electron spin states. A fit to the data yields a triplet-to-singlet relaxation time  $T_1 = (2.58 \pm 0.09)$  ms, which is more than an order of magnitude longer than the lower bound found in Ref. [15]. As indicated on the right side of Fig. 4.2e, we can also extract  $\alpha$  and  $\beta$  from the data. We find  $\alpha = 0.15$  and  $\beta = 0.04$  (taking  $\Gamma_T/\Gamma_S = 20$ ). The single-shot visibility is thus 81%. These numbers agree well with the values predicted by the model ( $\alpha = 0.14$ ,  $\beta = 0.05$ ,

visibility= 81%), as indicated by the diamond in Fig. 4.1c. Note that, since the visibility is insensitive to  $\tau$  near the optimal value, it is not significantly reduced by the finite bandwidth of the charge measurement.

As an extra check of the read-out, we have also applied a modified pulse where during the preparation only the singlet state is energetically accessible. Here, the read-out should ideally always yield 'S', and therefore the measured probability for finding 'T' directly gives us  $\alpha$ . We find a fraction of 'T' of 0.16, consistent with the value of  $\alpha$  obtained from the fit. This again confirms the validity of the read-out method.

#### 4.1.4 Magnetic field dependence of the triplet-to-singlet relaxation

We further study the relaxation between triplet and singlet states by repeating the measurement of Fig. 4.2e at different magnetic fields  $B_{//}$ . Figure 4.3a shows the decay of the fraction of 'T', normalized to the fraction of 'T' at  $t_{wait} = 0$ , on a logarithmic scale. The data follow a single-exponential decay at all fields. Figure 4.3b shows the relaxation rate  $1/T_1$  as a function of  $B_{//}$ . The dominant relaxation mechanisms for large values of  $E_{ST}$  are believed to originate from the spin-orbit interaction [4, 16]. Ref. [16] predicts a  $B$ -independent rate  $\Gamma_2$  that determines the low- $B$  relaxation, and a Zeeman energy-related rate  $\Gamma_5$ , proportional to  $B^2$ , that dominates at higher  $B$  (we adopt the notation of Ref. [16]).

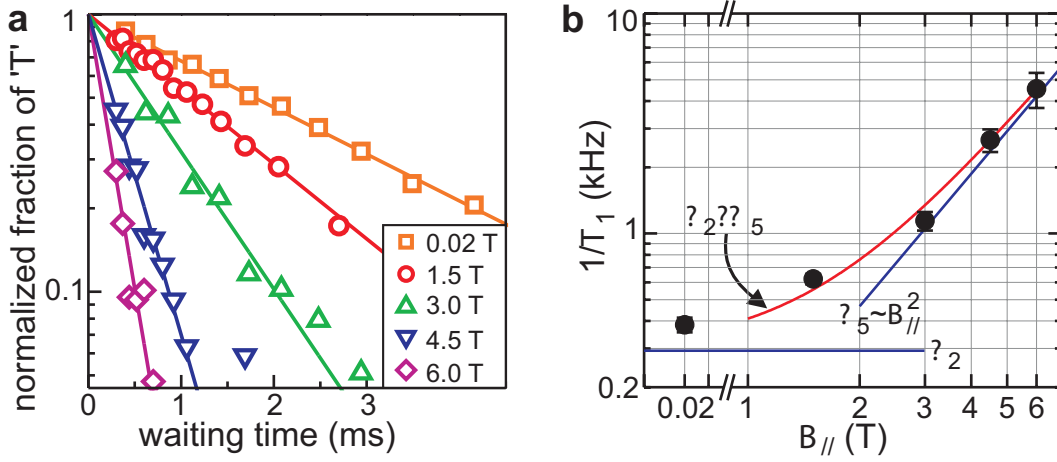


**Figure 4.3:** Triplet-to-singlet relaxation as a function of  $B_{//}$ . (a) Normalized fraction of 'T' vs.  $t_{wait}$  for different values of  $B_{//}$ . (b) Triplet-to-singlet relaxation rate  $1/T_1$  as a function of  $B_{//}$ . The data is fit by a combination of a  $B_{//}$ -independent rate  $\Gamma_2$  and a rate  $\Gamma_5 \propto B_{//}^2$  (see text).

Although the theory of Ref. [16] is based on single-spin flips, it can explain the two-electron relaxation data well. A fit to the data yields  $\Gamma_2 = (0.29 \pm 0.09)$  kHz and  $\Gamma_5 = (0.11 \pm 0.005) \cdot B_{//}^2$  kHz, consistent with the prefactors found in Ref. [16].

#### 4.1.5 Read-out of nearly degenerate states

Finally, we show that the TR-RO can still be used when  $|S\rangle$  and  $|T\rangle$  are almost degenerate. By mounting the device under a 45 degree angle with respect to the magnetic field axis, we can tune the singlet-triplet energy difference  $E_{ST}$  through zero [11]. In Fig. 4.4a we plot  $E_{ST}$  as a function of  $B$ , extracted from pulse spectroscopy measurements [12]. In these measurements, transitions are broadened both by the electron temperature in the reservoir and by fluctuations in the dot potential. We model these two effects by one effective electron temperature  $T_{eff}$ . For  $E_{ST}$  smaller than about  $3.5 kT_{eff}$ , the energy splitting can not be resolved. As in previous transport and pulse spectroscopy measurements, we find here  $3.5 kT_{eff} \approx 60 \mu\text{eV}$  (see inset of Fig. 4.4a), and therefore it is impossible to use the E-RO method beyond  $B \approx 3.9$  T. From extrapolation of the data, we find that the singlet-triplet ground state transition occurs at  $(4.25 \pm 0.05)$  T.

We tune  $B$  to 4.15 T (see inset of Fig. 4.4a), so that we are very close to the degeneracy point, but still certain that  $|S\rangle$  is the ground state. Figure 4.4b shows the result of the read-out measurement at this field. Again, an exponential decay of the fraction of ' $T$ ' is observed, with a  $T_1$  of  $(0.31 \pm 0.07)$  ms. This demonstrates that even when the energy splitting  $E_{ST}$  is too small to resolve, we

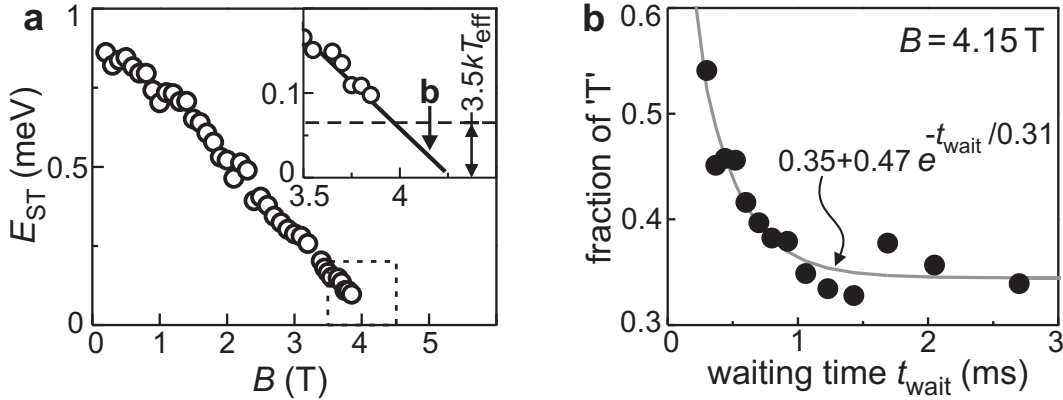


**Figure 4.4:** Single-shot read-out of nearly degenerate states. (a) Singlet-triplet energy difference  $E_{ST}$  as a function of magnetic field  $B$ , applied under a 45 degree angle with the 2DEG. Inset: zoom-in of the region inside the dashed square. For  $B > 3.9$  T,  $E_{ST}$  is smaller than the effective electron temperature. (b) Single-shot read-out at  $B = 4.15$  T. This field value is indicated with 'b' in the inset of (a).

can still read out the spin states using TR-RO.

In chapter 5 we will use this to probe the singlet-triplet relaxation time  $T_1$  over a broad range of energy splittings  $E_{ST}$  in order to study the influence of phonons in this relaxation process.

## 4.2 Repeated measurements

In this section we will demonstrate our ability to perform repeated single-shot measurements. An attractive feature of this read-out scheme is that it allows one to study the time evolution between two successive measurements. Furthermore the proposed technique could allow the implementation of weak, partial-collapse or non-destructive measurements [18].

### 4.2.1 Short read-out pulses

The fact that  $\Gamma_T$  can be tuned to be very high (higher than the measurement bandwidth) whereas  $\Gamma_S$  can then still be slow enough to be observed allows us to reduce the length of the read-out pulse  $\tau_m$  from  $\tau_m \gg \Gamma_S^{-1}$  (as used in section 4.1) to  $\Gamma_T^{-1} \ll \tau_m \ll \Gamma_S^{-1}$ .

In the experiment we discuss in this section (section 4.2),  $\Gamma_T^{-1} \approx 5 \mu s$ ,  $\tau_m = 20 \mu s$ , and  $\Gamma_{S,out}^{-1} = 100 \mu s$  (for the singlet, we observe that the time to tunnel in is different from the time to tunnel out:  $\Gamma_{S,in}^{-1} \approx 1000 \mu s$  [19]). If the dot is in the singlet state, most of the time no electron tunnels out during the read-out stage of the pulse since  $\tau_m$  is small compared to  $\Gamma_S^{-1}$ , even though tunneling would be energetically allowed. In the case of the triplet state, an electron will tunnel off the dot after the pulse is applied, in a time  $\Gamma_T^{-1}$  much smaller than  $\tau_m$ . In this case, an electron tunnels back into the dot after the read-out pulse, and will occupy the triplet state with high probability since  $\Gamma_T \gg \Gamma_S$ .

The actual measurement takes place through the occurrence or absence of a tunnel process during the read-out stage. For a superposition input state, this is when the "projection" of the wave function would take place. When the initial state is a singlet state, the dot remains in the singlet state all along; when the initial state is a triplet state, the dot is reinitialized through a tunnel event right after the read-out pulse.

The data shown here (section 4.2) have been obtained using a device with a similar design as in Fig. 4.1a but fabricated on a different heterostructure. In this particular heterostructure, the two-dimensional electron gas (2DEG) was located 90 nm below the surface and has an electron density of  $1.3 \cdot 10^{15} \text{ m}^{-2}$ . All measurements are performed at zero magnetic field. We tune the dot to the

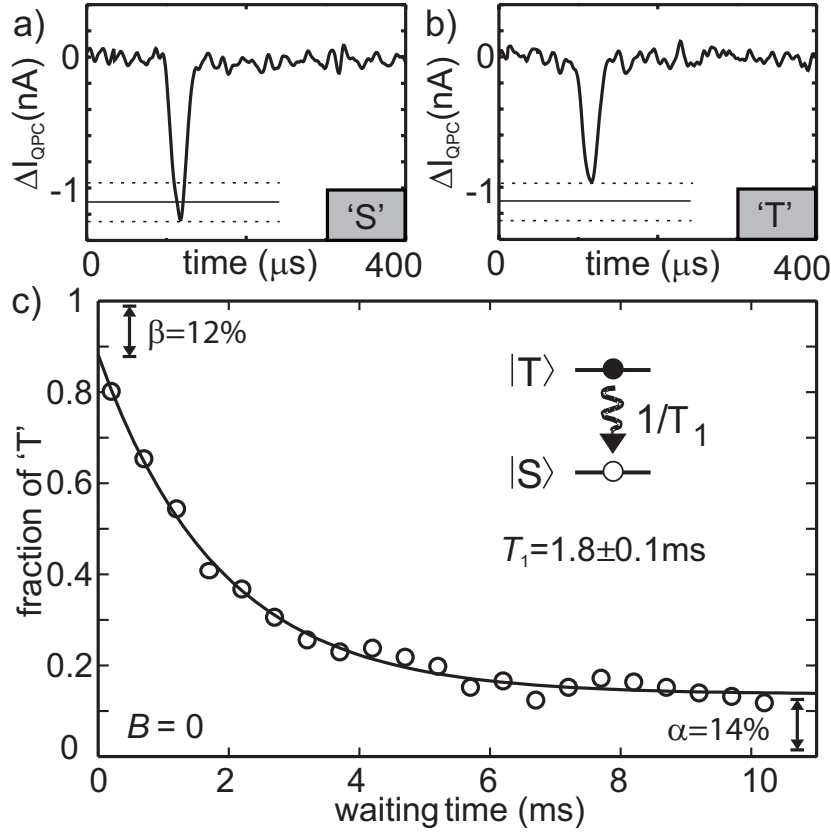


**Figure 4.5:** Typical QPC response in a 400  $\mu$ s interval surrounded by the dashed rectangle in the inset of (c). In the case the pulse response goes below the threshold we assume that no electron has tunneled of the dot and we declare the state in the dot to be singlet (a) whereas in the case the current stays above the threshold we assume an electron tunneled out and the state is declared triplet (b). The reference of the time axis is taken 100  $\mu$ s before the short read-out pulse is applied. The solid horizontal line indicates the position of the threshold. (c) The probability for detecting a triplet state as a function of the waiting time. Each point is an average over 500 single-shot experiments. The solid line is an exponential fit to the data, yielding a relaxation time  $T_1 = 1.8 \pm 0.1$  ms. The measurement errors  $\alpha$  and  $\beta$  (see text) are indicated. Inset: Voltage pulses applied to gate 'P' (see Fig. 4.2) for this relaxation measurement.

few-electron regime and completely pinch off the tunnel barrier between gates  $L$  and  $T$ , so that the dot is only coupled to the right reservoir [12]. A voltage bias of 0.7 mV induces a current through the QPC,  $I_{QPC}$ , of about 30 nA when it is set to a conductance of about  $e^2/h$ . Tunneling of an electron on or off the dot gives steps in  $I_{QPC}$  of 300 pA [6, 14] and we observe them in a measurement bandwidth of 60 kHz.

### 4.2.2 Single measurement

First we demonstrate that these short read-out pulses correctly read out the spin states by measuring relaxation from the triplet to the singlet state and comparing the result to those obtained using the read-out scheme of section 4.1. The short read-out pulse measurement scheme is illustrated in the inset of Fig. 4.5c. The starting point of this pulse scheme is a dot with one electron in the ground state (initialization stage). In the second stage of the pulse, the singlet and triplet electrochemical potentials are below the Fermi energy and a second electron tunnels into the dot. Since  $\Gamma_T \gg \Gamma_S$ , most likely a triplet state will be formed, on a timescale of  $\Gamma_T^{-1}$ . The short measurement pulse is applied after a waiting time that we vary. Due to the direct capacitive coupling of gate  $P$  to the QPC channel,  $\Delta I_{QPC}$  follows the pulse shape. The precise amplitude of the QPC pulse response directly reflects the charge state of the dot throughout the read-out pulse. If the two electrons remain in the dot, the QPC signal goes below a predefined threshold, and we conclude that the dot was in the singlet state (outcome ' $S$ ', see Fig. 4.5a). Otherwise, if one electron tunnels out in a time shorter than the pulse response time, the QPC pulse response stays above the threshold and we declare that the dot was in the triplet state (outcome ' $T$ ', see Fig. 4.5b) [21].

As expected, we observe an exponential decay of the triplet population as a function of the waiting time, yielding a singlet-triplet relaxation time,  $T_1 = 1.8 \pm 0.1$  ms. The measurement errors are  $\alpha = 0.14$  and  $\beta = 0.12$ , where  $\alpha$  ( $\beta$ ) is again defined as the probability for the measurement to return triplet (singlet) if the actual state is singlet (triplet). We observe the same values (within error bars) when we repeat the experiment using the read-out scheme with long read-out pulses as described in section 4.1. In both cases, measurement errors are completely explained by the two different tunnel rates (see section 4.1). The resulting measurement fidelity,  $1 - (\alpha + \beta)/2$ , is 87%. It is worth noticing that in this new read-out scheme the measurement time,  $t_{meas} \simeq \tau = 20 \mu s$ , is much shorter than  $T_1$  ( $T_1/t_{meas} \simeq 90$ ).

### 4.2.3 Repeated measurements

We will now perform two successive measurements and study the correlations between the measurement outcomes. From these repeated measurements we get confirmation that the system indeed reinitializes in the triplet state and we can obtain the singlet-triplet relaxation time as well as the rate to tunnel out of the singlet state. We program a second read-out pulse  $60 \mu s$  after the end of the first



pulse and record the probability for each of the four combined outcomes, ' $SS'$ ', ' $TT'$ ', ' $ST'$ ', ' $TS'$ ' (Fig.4.6a). In order to accurately characterize the measurement, we first do this with singlet initial states (prepared by waiting 20 ms for complete relaxation), and then again with mostly triplet initial states (prepared by letting the second electron tunnel in 200  $\mu$ s before the first measurement [22]). A clear correlation between consecutive measurement outcomes is observed (Fig. 4.6b), both for singlet and triplet initial states. When we average over  $S$  or  $T$  initial states (i.e. when we have no a-priori knowledge of the spin state), we find, from the correlation data and the known values of  $\alpha$  and  $\beta$ , an 85% (73%) conditional probability for outcome ' $T'$ ' (' $S'$ ') in the second measurement given that the first measurement outcome was ' $T'$ ' (' $S'$ ') [23].

The degree to which post-measurement state corresponds to the measurement outcome is quantified via the probability for obtaining a  $S$  or  $T$  post measurement state (60  $\mu$ s after the end of the first pulse) conditional on the measurement outcome. From the correlation data and the known values of  $\alpha$  and  $\beta$ , we extract a 97% (84%) conditional probability  $P(T|T')$  ( $P(S|S')$ ), again assuming no a-priori knowledge of the initial state [23]. For a triplet outcome, one electron tunneled out during the read-out pulse, and another electron tunneled back in after the pulse. A triplet state is formed with near certainty in this reinitialization process. Since  $\Gamma_T/\Gamma_{S,in} \approx 200$ , the probability to form a triplet is  $3\Gamma_T/(3\Gamma_T + \Gamma_S)=99.8\%$  (see section 4.1). However the triplet state can relax to the singlet during the 60  $\mu$ s between the two measurements. This occurs with a probability of 3%, which explains the observed conditional probability  $P(T|T')$ . The conditional probability  $P(S|S')$  can be found as  $1 - P(T, S')/P(S')$ .  $P(S')$  is simply  $((1 - \alpha) + \beta)/2$  (averaged over  $S$  and  $T$  initial states). There are two main contributions to  $P(T, S')$ . First, for  $\beta = 12\%$  of the triplet initial states, both electrons remain on the dot. In this case, a singlet outcome is declared but the post-measurement state is almost always a triplet. Second, for singlet initial states, a singlet outcome is obtained with probability  $1 - \alpha = 86\%$ . For 5% of those cases, one electron nevertheless tunneled out and the post-measurement state is a triplet [23]. All measured probabilities can thus be explained by the statistics of the tunnel events using the spin-dependent tunnel rates.

#### 4.2.4 Varying the time between measurements and the measurement time

An attractive feature of this read-out scheme is that it allows one to study the (non-coherent) time evolution of the two-electron spin states between two successive measurements. As a proof of principle, we let the spin evolve under

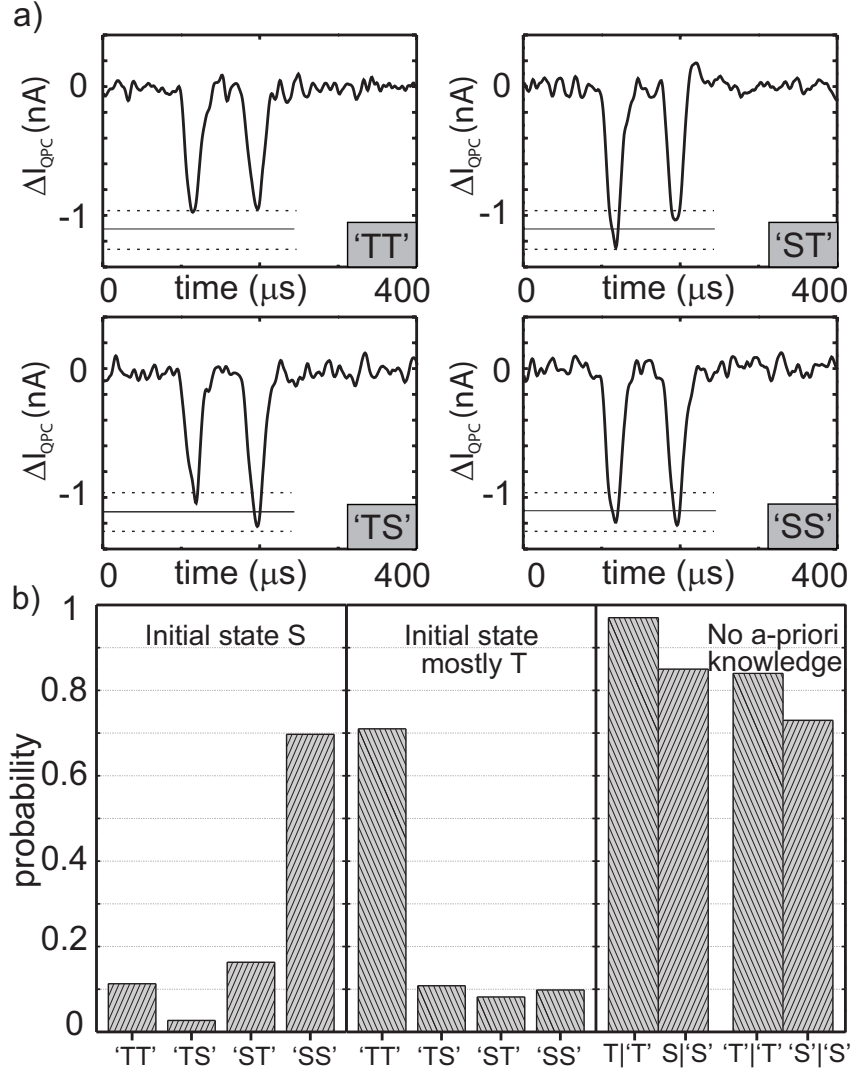


**Figure 4.6:** (a) Typical QPC response for two consecutive measurements in the case of 'SS', 'TT', 'ST' and 'TS'. The threshold is the same for the two non-destructive measurement pulses. The pulse width is 20  $\mu\text{s}$  and the delay between the two measurement pulses is 60  $\mu\text{s}$ . (b) The recorded probabilities for each of these four events over 3000 runs, with the singlet (first graph) and mostly the triplet (second graph) as the initial state. In the third graph, conditional probabilities  $P(T|T')$  or  $P(S|S')$  that the state after the first measurement corresponds to the outcome of the first measurement and conditional probabilities  $P('T'|T')$  or  $P('S'|S')$  that the second measurement gives the same outcome as the first one are presented. They are extracted from the two previous graphs and the known  $\alpha$  and  $\beta$  with no a-priori knowledge of the initial state.

relaxation for a controlled time in between two measurements. The singlet state is not affected by relaxation, so we initialize the dot (mostly, as before) in the

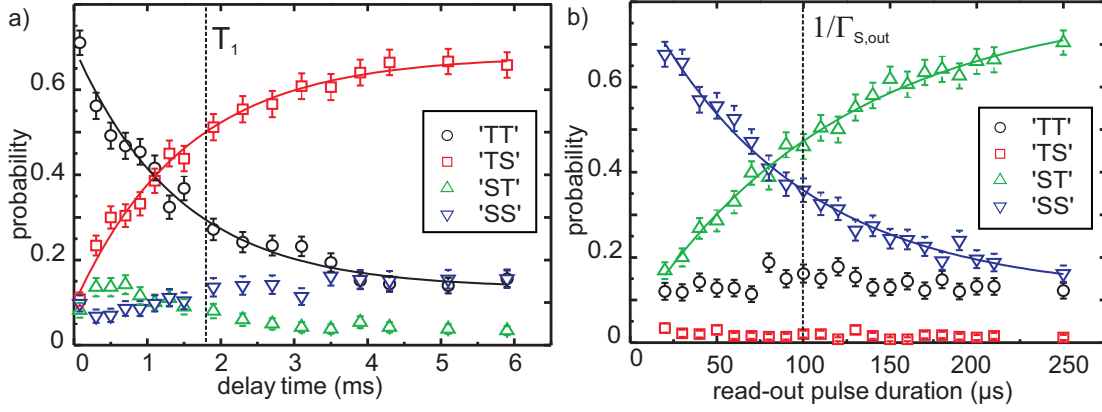


**Figure 4.7:** The probabilities for the two consecutive measurement outcomes as a function of (a) the measurement delay and (b) the measurement pulse duration. In (b) we initialize in the singlet state since for triplet initial states, the post-measurement state doesn't depend on the pulse duration. The solid lines are exponential fits to the data.

triplet state. In figure 4.7a), the probabilities for the four possible outcomes are recorded as a function of the waiting time. We notice that '*TT*' and '*TS*' respectively decay and increase exponentially, with a time constant  $1.5 \pm 0.3$  ms, within the error bars of the relaxation time obtained from Fig. 4.5c. Finally, we remark that if  $\tau_m \gg \Gamma_{S,out}^{-1}, \Gamma_T^{-1}$ , one electron will always tunnel off the dot during the read-out pulse irrespective of the state of the dot. When the levels are pulsed below the Fermi-level of the reservoir, the dot will be reinitialized and the post-measurement state will always be a triplet state. We can vary the duration of the pulse in order to make the transition from non-destructive to destructive read-out. Here we initialize in the singlet state, since for triplet initial states, the post-measurement state doesn't change with  $\tau_m$ . Figure 4.7b summarizes the results. The four different curves correspond to each combination of measurement outcomes as a function of the duration of the pulse. As expected, the '*TS*' and '*TT*' statistics are steady, while the '*SS*' and '*ST*' probabilities decay respectively increase exponentially with a time constant  $105 \pm 10$   $\mu$ s, within the error bars of the evaluation of  $\Gamma_{S,out}^{-1}$ .

In conclusion, we demonstrate our ability to implement a measurement scheme with short read-out pulses for distinguishing the two-electron singlet state from triplet states in a single quantum dot. Repeated measurements give the same results and the post-measurement state corresponds to the measurement outcome. All the imperfections in the correlations observed in the experiments are explained by the ratio between the singlet and triplet tunnel rates, and the relaxation rate

from triplet to singlet.

### 4.3 High-fidelity measurements of two-electron spin states

In section 4.1 we discussed the drawbacks of the energy-selective read-out (E-RO) scheme (as used in Ref. [2]). When performing E-RO of two-electron spin states, these drawbacks are not overcome but turn out to be of less importance. In this section we will demonstrate that the measurement fidelity of the E-RO for two-electron spin states has a very high fidelity of 93%, which is increased to 97.5% when the tunnel rate of the excited spin state is higher than the tunnel rate of the ground state ( $\Gamma_{ES} \gg \Gamma_{GS}$ ).

The first drawback (i) is that the E-RO requires an energy splitting of the spin states larger than the thermal energy of the electrons in the reservoir. For read-out of a single spin this means that we need to apply a large magnetic field to obtain a large enough energy splitting (approximately 6 Tesla for a 150  $\mu\text{eV}$  energy splitting). When we are interested in reading out the spin state of a two-electron system, the relevant energy splitting is the singlet-triplet splitting  $E_{ST}$  ( $\approx 500 \mu\text{eV}$  at zero field). Therefore we don't need to apply large magnetic field. Since this splitting is several times larger than the electron temperature the read-out does not require an accurate alignment with respect to the Fermi level of the lead anymore and is therefore less susceptible to fluctuations in the electrostatic potential (drawback (ii)). Furthermore, since the excited state is far above the Fermi level of the lead while the ground state is far below it, the read-out of the two-electron spin states suffers less from high-frequency noise (drawback (iii)) than the read-out of a single electron spin.

If we consider the fidelity of the E-RO, we see it can again be characterized by two parameters,  $\alpha$  and  $\beta$  [2]. Here, the parameter  $\alpha$  corresponds to the probability that the QPC current exceeds the threshold even though the electron was actually in the ground spin state (GS), for instance due to thermally activated tunneling or electrical noise (similar to 'dark counts' in a photon detector). The parameter  $\beta$  corresponds to the probability that the QPC-current stays below the threshold even though the electron was actually in the excited spin state (ES) at the start of the read-out stage. There are two processes that contribute to this error. First, an electron in the excited spin state can relax to the ground spin state before spin-to-charge conversion takes place. This occurs with probability  $\beta_1 = 1/(1 + T_1\Gamma_{ES})$ . Second, if the electron in the excited spin state does tunnel off the dot but is replaced by an electron in the ground spin state faster than the

measurement bandwidth of the setup (about  $8 \mu\text{s}$  in Refs. [2, 6]), the resulting step in the QPC current is too small to be detected. The probability that a step is missed,  $\beta_2$ , depends on the value of the threshold. From these observations it becomes clear that a large difference in tunnel rate between the ground and the excited state will increase the fidelity of the read-out. If  $\Gamma_{ES} \gg \Gamma_{GS}$ , an electron in the excited spin state will tunnel off the dot very fast, reducing the probability to relax to the ground spin state ( $\beta_1$ ). The length of the step in the QPC current however is not determined by how fast the electron in the ES tunnels off the dot ( $\Gamma_{ES}$ ) but by the time it takes an electron from the lead to occupy the GS ( $\Gamma_{GS}$ ). Here, we use the fact that tunneling into the dot is slower than the measurement bandwidth as well as the fact that the tunnel rate for the excited state is faster than the relaxation time  $T_1$  to obtain a very high measurement fidelity. Note that this only works when  $\Gamma_{ES} \gg \Gamma_{GS}$ . In section 4.3.2 we show that in the two-electron case the E-RO measurement fidelity is 93% which is increased to 97.5% when the tunnel rate of the excited state is higher than the tunnel rate of the ground state.

#### 4.3.1 Energy-selective read-out of the two-electron spin states with spin-dependent tunnel rates

For the read-out of the two-electron spin states we use the same scheme as used in Ref. [2]. In this scheme, the spin-to-charge conversion is achieved by positioning the spin levels around the electrochemical potential of the reservoir  $\mu_{res}$  as depicted in Fig. 4.1a, such that one electron can tunnel off the dot from the spin excited states, the triplet states  $|T\rangle$ , whereas tunneling from the ground (singlet) state,  $|S\rangle$ , is energetically forbidden. If a triplet state is occupied, the electron will almost always leave the dot before the spins have a chance to relax to the singlet state, since the tunnel rate from the triplet state is very fast. After one electron has left the dot, another electron can tunnel into the dot again, into the singlet state (the triplet is not energetically accessible). The tunnel rate to the singlet state is very slow, much slower than the charge measurement time in the experiment. The expected steps in the charge detection signal (indicating that the dot contains temporarily only one electron instead of two) will thus be clearly visible.

This experiment has been performed on the same device as used in section 4.2.1. In this experiment, we find the ratio of the tunnel rates from the triplet state ( $\Gamma_T$ ) and the singlet state ( $\Gamma_S$ ) to be  $\Gamma_T/\Gamma_S \sim 17$ .

In order to determine the visibility, we measure relaxation from the triplet to the singlet state. The protocol is illustrated in Fig. 4.8a-b. The starting point is

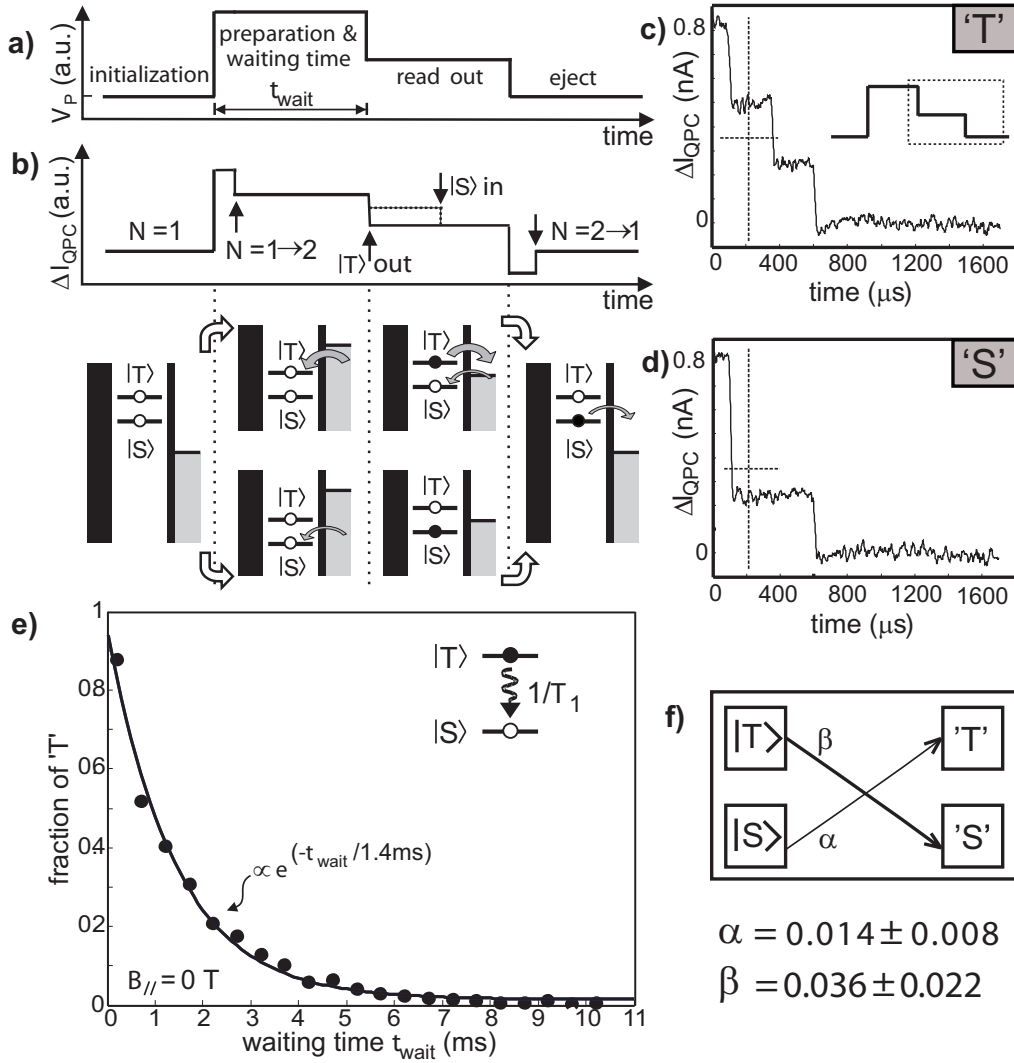


**Figure 4.8:** (a) Pulse waveform applied to gate  $P$ . (b) Response of the QPC-current to the waveform of (a). Energy diagrams indicate the positions of the levels during the four stages. In the third stage, spin is converted to charge information due to the difference in energy between the states  $|S\rangle$  and  $|T\rangle$ . (c-d) Real-time traces of  $\Delta I_{QPC}$  during the readout and ejection stages of the waveform in (a). At the vertical dashed lines (in the read-out stage), the charge state of the dot is determined by comparison with a threshold (horizontal dashed lines) and the spin state is declared  $'T'$  (c) or  $'S'$  (d) accordingly. (e) Fraction of  $'T'$  as a function of waiting time  $t_{wait}$  at  $B_{//} = 0$  T, showing a single-exponential decay with a time constant  $T_1$  of  $1.4 \pm 0.1$  ms. (f) The error rate  $\alpha$  ( $\beta$ ) is defined as the probability for the measurement to return triplet  $'T'$  (singlet  $'S'$ ) if the actual state is singlet  $|S\rangle$  (triplet  $|T\rangle$ ). The values of  $\alpha$  and  $\beta$  are obtained from the fit in (e).

a dot with one electron in the ground state. A first pulse is applied to gate ' $P$ ' to move the singlet and the triplet electrochemical potentials below the Fermi energy of the lead and a second electron tunnels into the dot. In this situation, the ratio  $\Gamma_T/\Gamma_S$  is higher than 17 and we observe that only the triplet state will be formed (perfect initialization in the excited state with an estimated error below 0.5%). After a waiting time that we vary, we pulse the electrochemical potential of the triplet state above the Fermi energy while the electrochemical potential of the singlet is still below. If the system is in the triplet state, an electron will tunnel off the dot on a timescale  $1/\Gamma_T \sim 5 \mu\text{s}$  (faster than the measurement bandwidth) and another electron will tunnel on the dot to form a singlet on a timescale  $1/\Gamma_S$  (slower than the measurement bandwidth and measured to be 7.8 kHz). If the system is in the singlet state, tunneling is energetically forbidden and the system remains in the singlet state.

Again we see that  $\Delta I_{QPC}$  follows the pulse shape due to the direct capacitive coupling of gate  $P$  to the QPC, (see Fig. 4.8b). As a consequence of the tunneling events in case the dot was initialized in a triplet state, a step in the QPC response occurs during the read-out stage of the pulse. If  $\Delta I_{QPC}$  goes above a predefined threshold during this read-out stage we conclude that the state was triplet (labeling it 'T', see Fig. 4.8c). If  $\Delta I_{QPC}$  remains below the threshold we conclude that the state was singlet (labeling it 'S', see Fig. 4.8d). For each waiting time, we record 500 individual traces and we extract the probability for detecting a triplet state. As expected, we observe an exponential decay of the triplet population as a function of the waiting time, giving a relaxation time,  $T_1 = 1.4 \pm 0.1 \text{ ms}$  (see Fig. 4.8e).

### 4.3.2 Measurement fidelity of the read-out

From the experimentally observed relaxation (Fig. 4.8e) we can extract the measurement errors  $\alpha$  and  $\beta$  as defined in Fig. 4.8f [2]. We find  $\alpha = 0.014$  and  $\beta = 0.036$ .

The error-rate  $\alpha$  is mainly explained by thermally activated tunneling from the singlet. This process is suppressed in the experiment since the energy splitting between the singlet and the reservoir,  $450 \mu\text{eV}$ , is substantially larger than the electron temperature ( $20 \mu\text{eV}$ ). Two mechanisms are necessary to evaluate  $\beta$ . Some errors occur when a triplet relaxes to a singlet before an electron tunnels off the dot. The probability  $\beta_1 = 1/(1 + T_1\Gamma_T)$  of such a process is 0.5% in the present experimental setup. The dominant error process is tunneling into the dot on a timescale faster than the charge measurement time. The probability of this error process is  $\beta_2 = 1 - e^{-\Gamma_S t_R} \sim 4\%$ . The total error rate  $\beta$  is related to  $\beta_1$  and

$\beta_2$  via  $(1 - \beta) \approx (1 - \beta_1)(1 - \beta_2) + \alpha\beta_1$ , where the last term accounts for the case when a triplet relaxes to the singlet, but there is nevertheless a step in  $\Delta I_{QPC}$  due to the dark-count mechanism [2].

We achieve a fidelity  $1 - (\alpha + \beta)/2 = 97.5\%$  for this read-out of the two-electron spin states in a single quantum dot. If the two spin states would have the same tunneling rate, an optimal fidelity equal to 93 % can be expected in the present measurement setup with an optimal tunnel rate of 17 kHz. The difference in tunnel rates between the two spin states significantly improves the spin measurement fidelity.

We would like to stress again that this high fidelity can only be achieved when the energy splitting  $E_{ST} \gg k_B T$ , the tunnel rates satisfy  $\Gamma_T/\Gamma_S \gg 1$  and  $\Gamma_S$  is smaller than the measurement bandwidth. Note that  $\Gamma_S/\Gamma_T \gg 1$  will decrease the measurement fidelity! These requirements make this scheme neither suitable for read-out of nearly degenerate two-electron spin states (see chapter 5) nor for single-spin read-out, since  $\Gamma_\uparrow \ll \Gamma_\downarrow$  has not yet been observed [28, 29]. The fidelity for single-shot read-out of a *single* spin can therefore only be increased by increasing the measurement bandwidth of the charge sensing setup. One approach to achieve a high measurement bandwidth is discussed in chapter 6 where a high electron mobility transistor (HEMT) is used as a cryogenic pre-amplification stage.

## 4.4 Summary

In this chapter we have presented a method for reading out the spin state of two electrons in a quantum dot. It is, unlike previously used read-out techniques, robust against charge noise and can still be used when the electron temperature exceeds the energy splitting between the states. The spin dependence of the tunnel rates is used to correlate the spin states to different charge states of the quantum dot. A subsequent fast measurement of the charge on the dot then reveals the original spin state. We have experimentally demonstrated the method by performing read-out of the two-electron spin states, achieving a single-shot visibility of more than 80%. We find very long triplet-to-singlet relaxation times (up to several milliseconds), with an in-plane magnetic field dependence consistent with spin-orbit coupling as the dominant source of relaxation. Additionally, we perform repeated measurements on the spin states with short read-out pulses. We show that these short pulses correctly read out the spin state and that these short read-out pulses, together with fast reinitialization, allows us to study the evolution of the spins states between measurements and correlate their outcomes.



Finally, we have shown that the large singlet-triplet splitting results in a high fidelity of 93% for the Energy-Selective Read-out. When the tunnel rates of these states satisfy  $\Gamma_T \gg \Gamma_S$ , the measurement fidelity increases to 97.5%.

We thank V. Golovach, S.I. Erlingsson and D. Loss for useful discussions, Raymond Schouten and Bram van der Enden for technical support. This work was supported by FOM, NWO, the DARPA-QUIST program, the ONR and the EU-RTN network on spintronics.

The work in this chapter has been done in collaboration with J. M. Elzerman, R. Hanson, F. H. L. Koppens, W. J. M. Naber, T. Meunier, K-J Tielrooij, L. H. Willems van Beveren, L. P. Kouwenhoven and L. M. K. Vandersypen.

## References

- [1] D. Loss and D.P. DiVincenzo, Phys. Rev. A **57**, 120 (1998).
- [2] J.M. Elzerman *et al.*, Nature **430**, 431 (2004).
- [3] O. Astafiev *et al.*, Phys. Rev. B **69**, 180507(R) (2004).
- [4] V. Golovach *et al.*, in preparation.
- [5] S.W. Jung *et al.*, Appl. Phys. Lett. **85**, 768 (2004).
- [6] L. M. K. Vandersypen *et al.*, Appl. Phys. Lett. **85**, 4394 (2004).
- [7] Similarly, spin-dependent tunneling to a second dot can be used, see H.A. Engel *et al.*, Phys. Rev. Lett. **93**, 106804 (2004).
- [8] The probability  $\beta$  that no tunnel event has occurred at  $t = \tau$ , even though the initial state was  $|ES\rangle$ , is the sum of  $\beta_1$ , the probability that the state is  $|ES\rangle$ , and  $\beta_2$ , the probability that the state is  $|GS\rangle$ . These are given by:

$$\begin{aligned}\beta_1 &= e^{-(\Gamma_{ES} + 1/T_1) \cdot \tau}, \\ \beta_2 &= \int_0^\tau P_{rel}(t) \cdot P_{GS}(\tau - t) dt.\end{aligned}$$

Here,  $P_{rel}(t) dt$  is the probability that  $|ES\rangle$  relaxes to  $|GS\rangle$  within the time interval  $[t, t + dt]$ , and  $P_{GS}(\tau - t)$  is the probability that no tunneling has taken place from  $|GS\rangle$  during a time  $\tau - t$ :

$$\begin{aligned}P_{rel}(t) &= 1/T_1 e^{-(1/T_1 + \Gamma_{ES}) \cdot t} \\ P_{GS}(\tau - t) &= e^{-\Gamma_{GS} \cdot (\tau - t)}.\end{aligned}$$

- [9] M. Ciorga *et al.*, Phys. Rev. B **61**, R16315 (2000).
- [10] M. Ciorga *et al.*, Appl. Phys. Lett. **80**, 2177 (2002).
- [11] L. P. Kouwenhoven, D. G. Austing, and S. Tarucha, Rep. Prog. Phys. **64** (6), 701 (2001).
- [12] J. M. Elzerman *et al.*, Appl. Phys. Lett. **84**, 4617 (2004).
- [13] R. Hanson *et al.*, Proceedings of the XXXIXth Rencontres de Moriond (La Thuile, 2004) ‘Quantum information and decoherence in nanosystems’.
- [14] R. Schleser *et al.*, Appl. Phys. Lett. **85**, 2005 (2004).
- [15] T. Fujisawa *et al.*, Nature **419**, 278 (2002).
- [16] A.V. Khaetskii and Y.V. Nazarov, Phys. Rev. B **61**, 12639 (2000).
- [17] M. Field *et al.*, Phys. Rev. Lett. **70**, 1311 (1993).
- [18] N. Katz *et al.*, Science **312**, 1498 (2006).
- [19] A possible explanation could be that the pulse not only shifts the dot potential but also distorts it, thereby changing the orbitals.
- [20] D. Leibfried, R. Blatt, C. Monroe, and D. Wineland, Rev. Mod. Phys. **75**, 281 (2003).
- [21] When the QPC signal went below the threshold and a ‘*S*’ outcome is declared, there is still some probability,  $\sigma$ , that one electron tunneled out during the pulse (after a time longer than the pulse response time).
- [22] The ratio of *T* and *S* tunnel rates *into* the dot is  $\approx 200$ , but 10% of the triplets relax to singlet in the short time between injection and read-out (200  $\mu$ s).
- [23] Full details of the statistics of all processes are available as supplementary material.
- [24] Hans-Andreas Engel *et al.*, Phys. Rev. Lett. **93**, 106804 (2004).
- [25] A. C. Johnson *et al.*, Nature **435**, 925 (2005).
- [26] F. H. L. Koppens *et al.*, Science **309**, 1346 (2005).
- [27] J. R. Petta *et al.*, Science **309**, 2180 (2005).
- [28] S. Amasha *et al.*, Phys. Rev. B **78**, 041306 (2008).
- [29] R. Hanson, I.T. Vink *et al.*, Proceedings of the 39th Rencontres de Moriond: Quantum Information and Decoherence in Nanosystems (La Thuile, Italy), D. C. Glattli, M. Sanqueur and J. Tran Thanh Van (eds.), pp. 145-150 (2005).

## Chapter 5

# Experimental signature of phonon-mediated spin relaxation

In this chapter, we study the relaxation of spin states of two electrons confined in a single quantum dot. We observe an experimental signature of the role of the phonons in spin relaxation between triplet and singlet states in a two-electron quantum dot. Using both the external magnetic field and the electrostatic confinement potential, we change the singlet-triplet energy splitting from 1.3 meV to zero and observe that the spin relaxation time depends non-monotonously on the energy splitting. A simple theoretical model is derived to capture the underlying physical mechanism. The present experiment confirms that spin-flip energy is dissipated in the phonon bath.

---

This chapter has been published in Physical Review Letters **98**, 126601 (2007).

## 5.1 Introduction

Relaxation properties of a quantum system are strongly affected by the reservoir where energy is dissipated. This has been seen clearly for electron spins embedded in nanostructures. Spin relaxation times  $T_1$  up to a few ns have been observed for free electrons in a two dimensional electron gas (2DEG) where energy is easily given to the motion [1]. In quantum dots, the discrete orbital energy level spectrum imposes other energy transfer mechanisms. Near zero magnetic field, the electron spin can directly flip-flop with the surrounding nuclear spins, inducing short  $T_1$ 's of the order of  $\mu\text{s}$  [2]. When a small magnetic field is applied, direct spin exchange with nuclei is suppressed. Lattice vibrations, i.e. phonons, are expected to become the dominant reservoir in which spin-flip energy can be dissipated. This dissipative mechanism is inefficient and very long spin relaxation times follow [2, 3, 4, 5, 6].

For spin relaxation involving phonons, two interactions are important. The spin-orbit interaction provides the essential coupling between different spin states and electronic orbitals. This coupling enables the electron-phonon interaction to mix the spin states, and subsequently dissipate the energy, released upon relaxation. [7, 8, 9]. Energy conservation requires that the phonon energy corresponds to the energy separation between the excited and the ground spin state. Changing the energy separation affects the efficiency of the electron spin relaxation in two ways. First, since the phonon density of states increases with energy, the relaxation rate is expected to increase with energy as well. Furthermore, since the electron-phonon interaction is highly dependent on the matching between the size of the dot and the phonon wavelength [10, 11], we expect a suppression of relaxation for very large and for very small phonon wavelengths in comparison to the dot size. Mapping the relaxation time  $T_1$  as a function of the energy splitting between the two spin states will provide insight in both the electron-phonon interaction and the spin-orbit coupling as well as an understanding of the limitations on  $T_1$ . This is of particular relevance in the context of both spintronic and spin-based quantum information processing devices [12].

In this chapter, we study the spin relaxation time from triplet to singlet states for different energy separations in a single quantum dot containing two electrons. Singlet and triplet states have respectively two electrons in the lowest orbital and two electrons distributed over both the lowest and the first excited orbital. In the experiment, the energy splitting  $\Delta E_{ST}$  between these two-electron spin states could be tuned from 0.9 meV to zero with a perpendicular magnetic field and from 0.8 meV to 1.3 meV by deforming the dot potential [13, 14].

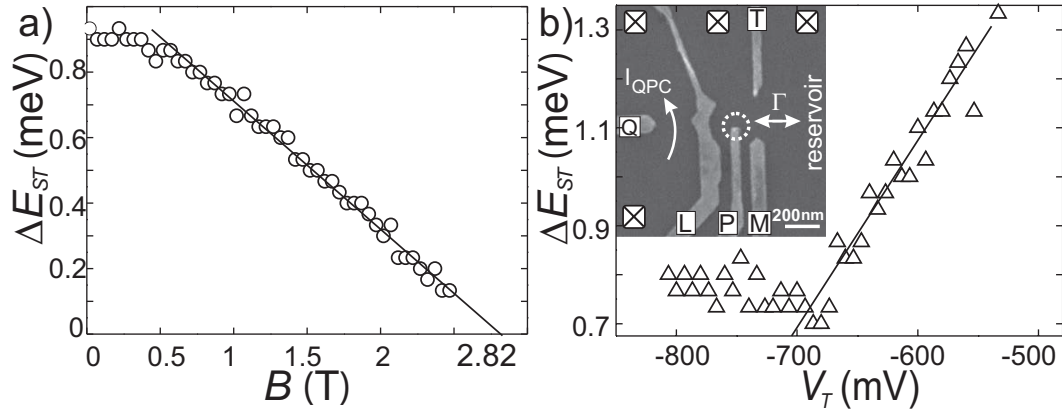


**Figure 5.1:** (a) Dependence of the energy splitting  $\Delta E_{ST}$  on total magnetic field  $B$ . (b) Dependence of the energy splitting  $\Delta E_{ST}$  on the voltage  $V_T$  applied on gate 'T' at  $B=0$ . Inset: Scanning electronic micrograph showing the sample design. The 2DEG, located 90 nm below the surface of a GaAs/AlGaAs heterostructure, has an electron density of  $1.3 \cdot 10^{15} \text{ m}^{-2}$ . By applying negative voltages to gates  $L$ ,  $M$ ,  $T$  and  $Q$  we define a quantum dot (white dotted circle) and a QPC. Gate  $P$  is used to apply fast voltage pulses that rapidly change the electrochemical potentials of the dot. We tune the dot to the few-electron regime, and completely pinch off the tunnel barrier between gates  $L$  and  $T$ , so that it is only coupled to one electron reservoir at a time. A voltage bias of 0.7 mV induces a current through the QPC,  $I_{QPC}$ , of about 30 nA. Tunneling of an electron on or off the dot gives steps in  $I_{QPC}$  of 300 pA. The QPC measurement bandwidth is 100 kHz.

## 5.2 Device and characterization

All the experiments are performed in a dilution refrigerator with a quantum dot and a quantum point contact (QPC) defined in a 2DEG (see inset of Fig. 5.1b). The conductance of the QPC is tuned to about  $e^2/h$ , making it very sensitive to the charge on the dot [19]. The sample is mounted at an angle  $\phi = 68^\circ \pm 5^\circ$  with respect to the direction of the magnetic field  $B$  where  $\phi$  is derived from Shubnikov-deHaas oscillations. The magnetic field component perpendicular to the 2DEG is equal to  $B \cos \phi$  ( $\sim 0.38 B$ ). The electron temperature was measured to be 180 mK from the width of the Coulomb peaks. The lattice temperature was 50 mK.

## 5.3 Determination of the singlet-triplet splitting

We extract experimentally the energy splitting  $\Delta E_{ST}$  between the singlet and the triplet states as a function of both magnetic field  $B$  and the confinement

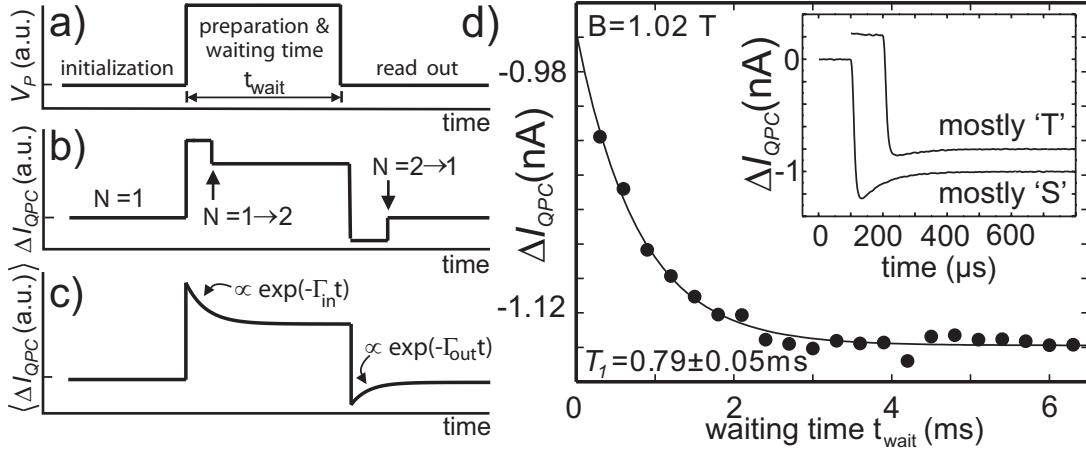


**Figure 5.2:** (a) Voltage pulses applied to gate ' $P$ ' for the relaxation measurement. The starting point is a dot with one electron in the ground state (initialization). During the pulse, the singlet and triplet electrochemical potentials are below the Fermi energy and a second electron tunnels into the dot. Due to the difference in tunnel rates, most likely a triplet state will be formed. We allow relaxation to occur during a waiting time that we vary. After the pulse, both electrochemical potentials are moved back above the Fermi energy and an electron tunnels out. This last step allows us to read-out the spin state. (b) Schematic of the  $\Delta I_{QPC}$  induced by the voltage pulse on gate ' $P$ '. If the state was singlet, a step from a slow tunneling event is added to the QPC response just after the read-out pulse. If the state was triplet, the tunneling event is too fast to be observed. (c) After averaging over many single traces, a dip is observed and its amplitude is proportional to the probability of having singlet present in the dot. (d) Relaxation curve obtained for  $B = 1.02$  T constructed by plotting the dip amplitude of the averaged traces at a pre-defined time after the read-out pulse. The relaxation time,  $T_1 = 0.79 \pm 0.05$  ms, is extracted from an exponential fit to the data (all the data are taken with a 100 kHz low-pass filter). Inset: curve resulting from the averaging over 500 individual traces for the longest waiting time (20 ms) and for the shortest waiting time (300  $\mu\text{s}$ ), offset by 100  $\mu\text{s}$  and 0.2 nA for clarity.

potential using a pulse spectroscopy technique [16]. The dependence of  $\Delta E_{ST}$  on  $B$  is presented in Fig. 5.1a. Up to 0.4 T,  $\Delta E_{ST}$  does not vary significantly with magnetic field which we relate to the elliptic nature of the dot at zero magnetic field [20]. For  $B$  larger than 0.4 T,  $\Delta E_{ST}$  decreases, to a good approximation, linearly with magnetic field. For energy separations below 100  $\mu\text{eV}$ , the thermal broadening of the reservoir prevents us to measure  $\Delta E_{ST}$ . From extrapolation of the data, we can determine the magnetic field needed for singlet and triplet energy levels to cross:  $2.82 \pm 0.07$  T.

## 5.4 Singlet-triplet relaxation time as a function of their energy splitting

We measure the relaxation time for varying  $\Delta E_{ST}$ . To be able to measure  $T_1$  close to the degeneracy point, we use a tunnel-rate selective read-out procedure (TRRO) [6] (see Fig. 5.2). The measured spin relaxation time  $T_1$  as a function of  $B$  is presented in Fig. 5.3. The shape of the  $T_1$  dependence on magnetic field exhibits a striking non-monotonous behavior. From 0.4 T to  $\sim 2$  T, corresponding to a decrease in the energy splitting from 0.9 meV to 0.2 meV, the relaxation time first decreases, reaching a minimum of 180  $\mu$ s. In between 2 T and the degeneracy point (2.82 T),  $T_1$  increases whereas the energy splitting continues to decrease.

As a complementary study, we change  $\Delta E_{ST}$  in a different way by controlling the electrostatic potential of the dot via the voltage  $V_T$  applied to gate 'T' and again look at  $T_1$ . The dependence of  $\Delta E_{ST}$  on  $V_T$  is presented in Fig. 5.1b. With this second experimental knob,  $\Delta E_{ST}$  can be varied from 0.8 meV to 1.3 meV. We interpret the change in the observed energy splitting as a consequence of a change in the dot ellipticity. A more positive  $V_T$  implies a more circular dot and a larger energy splitting. We observe that  $T_1$  further increases with  $\Delta E_{ST}$  as  $V_T$  is varied at  $B = 0$  T (see the inset of Fig. 5.3). The maximum energy splitting reached at -530 mV, 1.3 meV, corresponds to a maximum of  $T_1 = 2.3$  ms. With both experimental knobs, we observe that when  $\Delta E_{ST}$  is constant,  $T_1$  is constant too (respectively for  $V_T < -700$  mV and  $B < 0.4$  T). These observations clearly indicate that the most important parameter for the variation in the triplet-singlet relaxation time is their energy separation.

The observed minimum in  $T_1$  is precisely what one would expect for energy relaxation mediated by the electron-phonon interaction [8, 11]. Indeed, the energy splitting  $\Delta E_{ST}$  determines the relevant acoustic phonon energy (acoustic phonons are the only available phonons for the explored energy range). At  $B \sim 2$  T,  $\Delta E_{ST} \sim 0.3$  meV, the associated half-wavelength, approximately 30 nm (the group velocity for acoustic phonons  $c_s \sim 4000$  m/s), is comparable to the expected size of the dot and therefore the coupling of the electrons in the dot to phonons is strongest (see Eq. (5.3) and below). For energy separations smaller (larger) than 0.3 meV, the phonon wavelength is larger (smaller) than the size of the dot, the coupling to the orbitals becomes smaller and  $T_1$  increases. Taken together, all these observations strongly suggest that the phonon bath is the dominant reservoir for dissipating the spin-flip energy during relaxation.

## 5.5 A simple model for the phonon mediated relaxation

In order to get more insight in the role of the phonon wavelength, we present a simplified model of the energy relaxation process between triplet and singlet as a function of their energy splitting  $\Delta E_{ST}$ . A more detailed derivation can be found in Appendix A. From Fermi's golden rule, the relaxation rate between the triplet and the singlet states with energy separation  $\Delta E_{ST}$  is proportional to their coupling strength through electron-phonon interaction and to the phonon density of states at the energy  $\Delta E_{ST}$  [11]. To obtain a simple analytical expression, we assume that the only effect of the perpendicular magnetic field and the modification of the potential landscape (and the corresponding change in the Coulomb interaction between the electrons) is to change the energy splitting. Especially, their effects on the spatial distribution of the wavefunctions are neglected and we neglect the Zeeman energy. Furthermore, we restrict the state space of the analysis to  $|T_{-}\rangle$ ,  $|T_{+}\rangle$ ,  $|T_0\rangle$  and  $|S\rangle$  constructed from the lowest energy orbital and the first excited orbital (even though the contributions to triplet-singlet relaxation from higher orbitals can in fact be important [21]). In the notation  $|T_{-}\rangle$ ,  $|T_{+}\rangle$ ,  $|T_0\rangle$  and  $|S\rangle$ , both the orbital part (assuming Fock-Darwin states) and the spin part are present. Finally, we also neglect higher order (e.g. two-phonon) processes, which are important at small magnetic field [22].

In contrast to the one electron case, where virtual transitions to higher orbitals are required [7, 9], here the spin-orbit interaction admixes the first excited states  $|T_{\pm}\rangle$  with the ground state  $|S\rangle$  directly, since the higher orbital is already involved. Due to the selection rules of the spin-orbit interaction, it does not couple  $|T_0\rangle$  and  $|S\rangle$  in lowest order [23]. As a consequence, the spin relaxation time of  $|T_0\rangle$  can be much longer than  $|T_{\pm}\rangle$  [24]. However, we do not observe any signature of a slowly relaxing component in the experiment. Since the spin-orbit coupling strength  $M_{SO}$  is small in comparison with  $\Delta E_{ST}$  (in the range accessed in the experiment), we can approximate the new eigenstates of the system as:

$$|S'\rangle = |S\rangle - \frac{M_{SO}}{\Delta E_{ST}}(|T_{+}\rangle + |T_{-}\rangle) \quad (5.1)$$

$$|T'_{\pm}\rangle = |T_{\pm}\rangle + \frac{M_{SO}}{\Delta E_{ST}}|S\rangle \quad (5.2)$$

In general,  $M_{SO}$  is dependent on the magnetic field, but to simplify the discussion, we neglect this dependence [21, 22]. Since the electron-phonon interaction preserves the spin, the coupling between  $|T'_{\pm}\rangle$  and  $|S'\rangle$  has the following form:



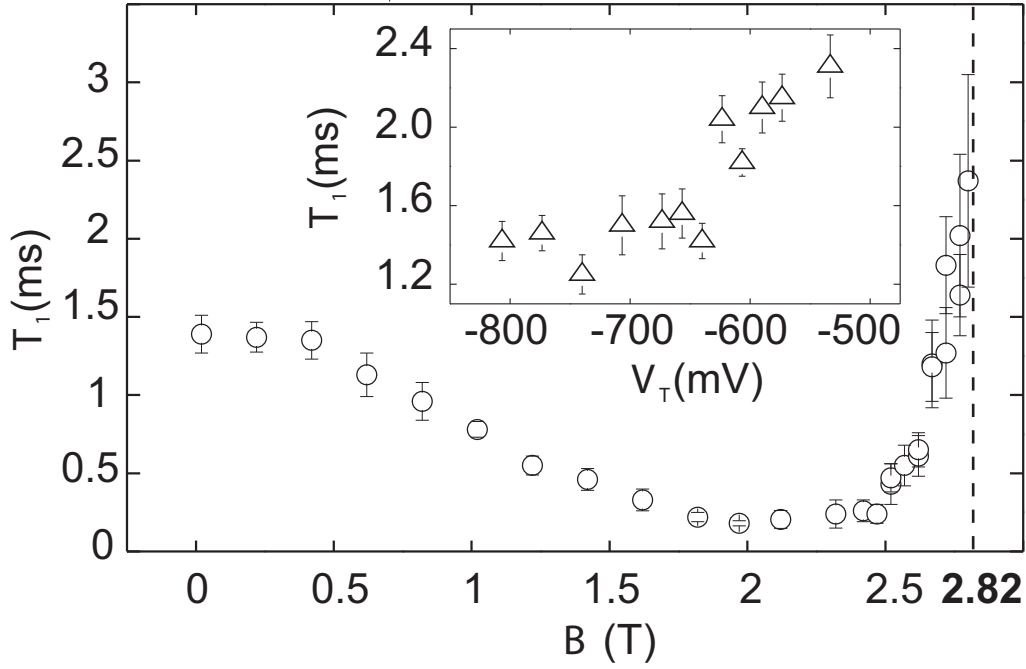


**Figure 5.3:** The spin relaxation time  $T_1$  as a function of the total magnetic field. The magnetic field where singlet and triplet states are degenerate is indicated by the dashed line. A minimum in  $T_1$  is observed around 2.2 T. The error bars represent 70% confidence intervals. For energy separations close to degeneracy, the sensitivity of the measurement is reduced and the uncertainty in  $T_1$  increases. Inset: dependence of the relaxation time  $T_1$  on  $V_T$  at  $B = 0$  T.

$$\langle T'_\pm | H_{e,p} | S' \rangle = \frac{M_{SO}}{\Delta E_{ST}} (\langle S | H_{e,p} | S \rangle - \langle T_\pm | H_{e,p} | T_\pm \rangle) \quad (5.3)$$

where  $H_{e,p} \sim e^{i\mathbf{q}\cdot\mathbf{r}_1} + e^{i\mathbf{q}\cdot\mathbf{r}_2}$  is the interaction Hamiltonian between electrons and phonons,  $\mathbf{q}$  the phonon wavevector and  $\mathbf{r}_i$  the positions of the electrons. One can then interpret the coupling between  $|T'_\pm\rangle$  and  $|S'\rangle$  as the difference of the electron-phonon interaction strength for the corresponding unperturbed states  $|T_\pm\rangle$  and  $|S\rangle$ . If the phonon wavelength is much larger than the dot size, the coupling to the phonons is the same for both states and the two terms will cancel. If the phonon wavelength is much shorter than the dot size, the coupling is small for each state separately.

To provide a quantitative comparison to the data, we need to model the electron-phonon interaction. Following [8, 11], we assume bulk-like 3D phonons. For the energy separations discussed in our experiment, only acoustic phonons are relevant. The Hamiltonian  $H_{e,p}$  has then the following expression:

$$H_{e,p} = \sum_{j,\mathbf{q}} \frac{F_z(q_z)}{\sqrt{2\rho q c_j/\hbar}} (e^{iq_{\parallel}r_1} + e^{iq_{\parallel}r_2}) (e\beta_{j,\mathbf{q}} - iq\Xi_{j,\mathbf{q}}) \quad (5.4)$$

where  $(\mathbf{q}, j)$  denotes an acoustic phonon with wave vector  $\mathbf{q} = (\mathbf{q}_{\parallel}, q_z)$ ,  $j$  the phonon branch index and  $\rho = 5300 \text{ kg/m}^3$  is the density of lattice atoms. The factor  $F_z(q_z)$  depends on the quantum well geometry and is assumed to be 1 in our model [11]. The speed of sound for longitudinal and transverse phonons are respectively  $c_l = 4730 \text{ m/s}$  and  $c_t = 3350 \text{ m/s}$ . We consider both piezo-electric and deformation potential types of electron-phonon interaction. In the considered crystal, the deformation potential interaction is non-zero only for longitudinal phonons (with a coupling strength  $\Xi = 6.7 \text{ eV}$ ). In contrast, all phonon polarizations  $j$  are important for piezo-electric coupling. The coupling strength depends on  $\theta$ , defined as the angle between the wavevector and the growth axis, and varies for different polarizations as  $e\beta_{j,\mathbf{q}} = A_j(\theta)e\beta$  where  $e\beta = 1.4 \times 10^9 \text{ eV/m}$  [8, 25]. Due to the different dependence on  $q$  for both mechanisms ( $\sqrt{q}$  for deformation potential interaction,  $1/\sqrt{q}$  for piezo-electric interaction), the piezo-electric (the deformation potential) coupling between electrons and phonons is dominant for energy separations below (above)  $0.6 \text{ meV}$ . From direct application of Fermi's golden rule, we derive the following analytical expression for the spin relaxation rate  $1/T_1$ :

$$\begin{aligned} 1/T_1 = & \frac{M_{SO}^2 \alpha^4}{32\pi\rho\hbar^6} \left( \frac{\Xi^2 \Delta E_{ST}^5}{\hbar^2 c_l^9} \int_0^{\pi/2} d\theta \sin^5 \theta e^{-\frac{\Delta E_{ST}^2 \alpha^2 \sin^2 \theta}{2\hbar^2 c_l^2}} \right. \\ & \left. + \sum_{j=l,t} \frac{e^2 \beta^2 \Delta E_{ST}^3}{c_j^7} \int_0^{\pi/2} d\theta |A_j(\theta)|^2 \sin^5 \theta e^{-\frac{\Delta E_{ST}^2 \alpha^2 \sin^2 \theta}{2\hbar^2 c_j^2}} \right) \end{aligned} \quad (5.5)$$

where  $\alpha$  is the dot radius (in our model  $\alpha$  is independent of  $\Delta E_{ST}$  and is estimated to be  $23 \text{ nm}$ , from the measured single particle level spacing). This simple model reproduces the most important feature in the measurements, which is that the coupling to the phonons vanishes for large and small energy separations and is strongest when the phonon wavelength matches the dot size (see Fig. 5.4).

## 5.6 Discussion

The spin-orbit strength  $M_{SO}$  appears in the expression of  $1/T_1$  only as a scaling factor. With a value  $M_{SO} = 0.4 \text{ } \mu\text{eV}$  (corresponding to a spin-orbit length equal

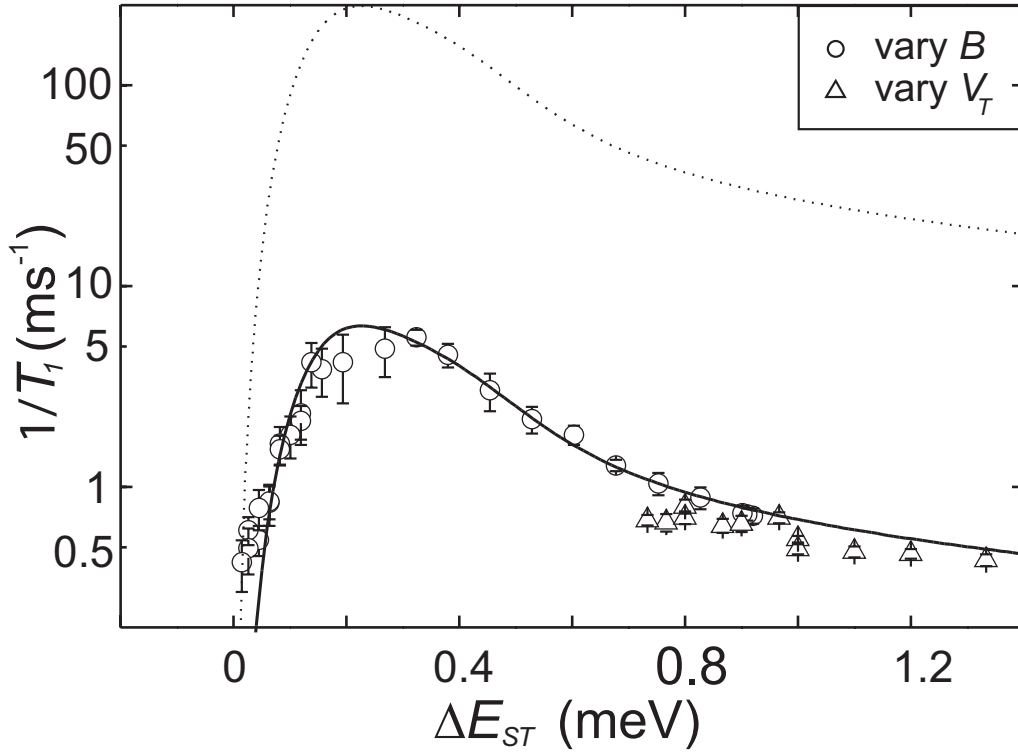


**Figure 5.4:** Relaxation rate as a function of the energy splitting  $\Delta E_{ST}$  deduced from the experimental data. The circles and the triangles correspond to the experiment where we vary respectively the magnetic field and the dot potential. The solid (dotted) line is the curve for  $M_{SO} = 0.37 \mu\text{eV}$  ( $M_{SO} = 2.31 \mu\text{eV}$ ) obtained from the simplified model.

to  $\hbar/2\alpha m^* M_{SO} \approx 50 \mu\text{m}$ ), the model reproduces the peak amplitude of the data quite well (Fig. 5.4, solid line). However, this value for  $M_{SO}$  is about six times smaller than the values reported in [26, 27] (the dotted line in Fig. 5.4 corresponds to the relaxation rate using this value of  $M_{SO}$  in the model). The discrepancy could be the result of the exclusion of higher orbitals and the magnetic field dependence of  $M_{SO}$  in our model [21, 22]. Again, we emphasize that both curves have a maximum corresponding to a phonon wavelength matching the dot size.

For single electron spin states, comparable variations of  $T_1$  with the energy splitting are expected although direct spin-orbit coupling between Zeeman sub-levels of the same orbital is zero. To maximize the relaxation time of electron spin qubits, one needs then to choose an energy separation between the spin states such that the corresponding phonon wavelength is different from the dot size. To complete our study of spin relaxation, it will be interesting to rotate the sample with respect to the magnetic field since the spin-orbit coupling strength depends

on the angle between the crystallographic axis and the magnetic field [7, 8, 28].

We thank V. Golovach and D. Loss for drawing our attention to the role of the phonon wavelength in spin relaxation and for useful discussions; R.N. Schouten, B. van der Enden and W. den Braver for technical assistance. Supported by the Dutch Organization for Fundamental Research on Matter (FOM), the Netherlands Organization for Scientific Research (NWO), the DARPA QUIST program and a E.U. Marie-Curie fellowship (for T. Meunier).

This work has been performed in close collaboration with R. Hanson, F. H. L. Koppens, T. Meunier, K-J. Tielrooij, H. P. Tranitz, W. Wegscheider, L. H. Willems van Beveren, L. P. Kouwenhoven and L. M. K. Vandersypen.

## References

- [1] Y. Ohno *et al.*, Phys. Rev. Lett. **83**, 4196 (1998).
- [2] A. C. Johnson *et al.*, Nature **435**, 925 (2005).
- [3] T. Fujisawa *et al.*, Nature **419**, 278 (2002).
- [4] J.M. Elzerman *et al.*, Nature **430**, 431 (2004).
- [5] M. Kroutvar *et al.*, Nature **432**, 81 (2004).
- [6] R. Hanson *et al.*, Phys. Rev. Lett. **94**, 196802 (2005).
- [7] A.V. Khaetskii and Y.V. Nazarov, Phys. Rev. B **61**, 12639 (2000).
- [8] V.N. Golovach, A.V. Khaetskii, D. Loss, Phys. Rev. Lett. **93**, 016601 (2004)
- [9] D. V. Bulaev and D. Loss, Phys. Rev. B **71**, 205324 (2005)
- [10] T. Fujisawa *et al.*, Science **282**, 932 (1998).
- [11] U. Bockelmann, Phys. Rev. B **50**, 17271 (1994)
- [12] D. Loss and D.P. DiVincenzo, Phys. Rev. A **57**, 120 (1998).
- [13] L. P. Kouwenhoven, D. G. Austing, and S. Tarucha, Rep. Prog. Phys. **64** (6), 701 (2001).
- [14] Jordan Kyriakidis *et al.*, Phys. Rev. B **66**, 035320 (2002)
- [15] M. Ciorga *et al.*, Phys. Rev. B **61**, R16315 (2000)
- [16] J. M. Elzerman *et al.*, Appl. Phys. Lett. **84**, 4617 (2004).
- [17] R. Schleser *et al.*, Appl. Phys. Lett. **85**, 2005 (2004).

- [18] L.M.K. Vandersypen *et al.*, Appl. Phys. Lett. **85**, 4394 (2004).
- [19] M. Field *et al.*, Phys. Rev. Lett. **70**, 1311 (1993).
- [20] D. G. Austing *et al.*, Phys. Rev. B **60**, 11514 (1999)
- [21] V.N. Golovach, A.V. Khaetskii, D. Loss, preprint.
- [22] P. San-Jose *et al.*, Phys. Rev. Lett., **97**, 076803, (2006)
- [23] S. Dickmann and P. Hawrylak, JETP Lett., **77**, 30 (2003)
- [24] S. Sasaki *et al.*, Phys. Rev. Lett. **95**, 056803 (2005).
- [25] For longitudinal phonons, the piezo-electric constant  $A_l(\theta) = 3\sqrt{2}/4 \sin^2(\theta) \cos \theta$ .  
For the two transverse polarizations,  $A_{t1}(\theta) = \sqrt{2}/4 \sin 2\theta$  and  $A_{t2}(\theta) = \sqrt{2}/4 (3 \cos^2 \theta - 1) \sin \theta$ .
- [26] D. M. Zumbuhl *et al.*, Phys. Rev. Lett. **89**, 276803 (2002)
- [27] S. Amasha *et al.*, cond-mat/0607110
- [28] V.I. Fal'ko, B.L. Altshuler, and O. Tsyplatyev, Phys. Rev. Lett. **95**, 076603 (2005)



## Chapter 6

# A cryogenic amplifier for fast real-time detection of single-electron tunneling

In this chapter, we employ a cryogenic High Electron Mobility Transistor (HEMT) amplifier to increase the bandwidth of a charge detection setup with a quantum point contact (QPC) charge sensor. The HEMT is operating at 1K and the circuit has a bandwidth of 1 MHz. The noise contribution of the HEMT at high frequencies is only a few times higher than that of the QPC shot noise. We use this setup to monitor single-electron tunneling to and from an adjacent quantum dot and we measure fluctuations in the dot occupation as short as 400 nanoseconds, 20 times faster than in previous work.

---

Parts of this chapter have been published in Applied Physics Letters **91**, 123512 (2007).

## 6.1 Introduction

The conventional method for studying quantum dot properties electrically is to measure electron transport through the dot [1]. An alternative approach is to measure the current through a quantum point contact (QPC) located next to the dot, which is sensitive to the charge dynamics of the quantum dot [4, 5, 3, 2, 6]. This technique is very versatile and has also been used to probe the excited state spectrum of a quantum dot [7, 8], perform single-shot read-out of electron spin states [9, 10] and observe coherent electron spin dynamics in quantum dots [11].

Until now, current fluctuations through such a QPC charge sensor have always been measured using room temperature (RT) electronics. This limits the measurement bandwidth to several tens of kHz [4], because of the low-pass (LP) filter formed by the capacitance of the measurement wires to ground and the input impedance of the RT amplifier. However, increasing this bandwidth is crucial in order to study (real-time) fast electron and nuclear spin dynamics [12] as well as to increase the single-shot spin readout fidelity [9]. One way to increase the bandwidth is to embed the QPC in a resonant circuit and measure its damping [13, 14], analogous to the operation of the RF-SET [15]. In theory such an "RF-QPC" allows for single-shot charge detection within a few tens of nanoseconds [16]. However, this technique requires RF-modulation and is experimentally rather involved.

In this chapter, we explore a much simpler approach to increasing the bandwidth, which uses a HEMT operated in DC as a cryogenic pre-amplifier [17]. Compared to a RT amplifier, a cryogenic amplifier can be mounted much closer to the sample, which significantly reduces the capacitance of the measurement wire. The use of a HEMT has the additional advantage that the noise level at cryogenic temperatures is very low (especially at high frequencies), so a better charge sensitivity can be obtained.

## 6.2 Charge detection setup

We start this section by explaining how a HEMT can be used to detect current fluctuations through a QPC charge sensor. This is followed by a discussion on how the HEMT is biased and how a properly biased HEMT amplifies AC-signals on its gate. Finally we measure the bandwidth of the circuit and analyze the various noise contributions.



### 6.2.1 Probing current fluctuations with a HEMT

The current through a HEMT is strongly dependent on the voltage difference between its gate and its source terminal. This makes a HEMT a suitable device to probe voltage fluctuations. However, we are interested in probing fluctuations of a current. To do so we will connect the HEMT in the following way. The gate of the HEMT is connected to the right lead of the QPC, which is also connected to ground via resistor  $R_c$  (Fig. 6.1a). A bias voltage,  $V_{sd}$ , is applied to the left lead of the QPC and a current  $I_{qpc}$  will flow which depends on the QPC conductance  $G_{qpc}$ . The voltage over  $R_c$  is a measure for this current and is probed via the HEMT. Fluctuations of  $G_{qpc}$  result in fluctuations of  $I_{qpc}$ , which we will label  $\Delta I_{qpc}$ . These generate fluctuations in the voltage on the HEMT gate,  $V_G$ , with respect to the voltage on its source,  $V_S$ . The modulation of  $V_{GS} = V_G - V_S$  results in a modulation of the HEMT drain current,  $I_D$ , through the HEMT channel. This current modulation is measured by an AC-coupled "fast" IV-converter at RT and digitized using a digital oscilloscope (LeCroy WaveRunner 6030A).

### 6.2.2 DC-biasing of the HEMT

We use a commercially available HEMT (Agilent ATF 35143) with a 400  $\mu\text{m}$  gate length and a threshold voltage  $V_T \approx 0.4$  V. To bias the HEMT we have a single knob " $I_D$ " that effectively sets the HEMT drain current. The voltage on the gate of the HEMT,  $V_G$ , is determined by the DC current through the QPC,  $I_{qpc}$ , and the resistor  $R_c$ , and is approximately 100  $\mu\text{V}$ . The source is connected to ground via a 1k $\Omega$  resistor ( $R_S$ ) which sets the gate-source voltage at  $V_{GS} = V_G - V_S \approx -V_S = -I_D R_S$ , since  $V_G \approx 100$   $\mu\text{V}$ , which is three orders of magnitude smaller than  $I_D R_S$  for the appropriate DC bias settings. This  $V_{GS}$  determines both the transconductance,  $g_m$ , and the drain-source voltage  $V_{DS}$ . In Fig. 6.1b we plot the drain current as a function of drain-source voltage for this particular circuit. Note that the non-zero slope in the saturation region indicates that the HEMT does not behave as a ideal current source but still has a finite output impedance. We operate the HEMT at  $I_D \approx 400$   $\mu\text{A}$  which results in a power dissipation in the HEMT of  $P_{HEMT} = V_{DS} I_D \approx 30$   $\mu\text{W}$ , see inset of Fig. 6.1b. The open dots in Fig. 6.1b indicate the HEMT operation point in this experiment. This operation point lies just in the saturation region of the HEMT. This point is chosen such that the HEMT has sufficient gain (the gain doesn't increase more than 5% at higher  $I_D$ ) and has a small power dissipation (30  $\mu\text{W}$ ). This low dissipation allows the HEMT to be mounted on the 1K-stage of the dilution refrigerator. The resistor  $R_S$  dissipates much more ( $P_{R_S} = I_D^2 R_S \sim 190$

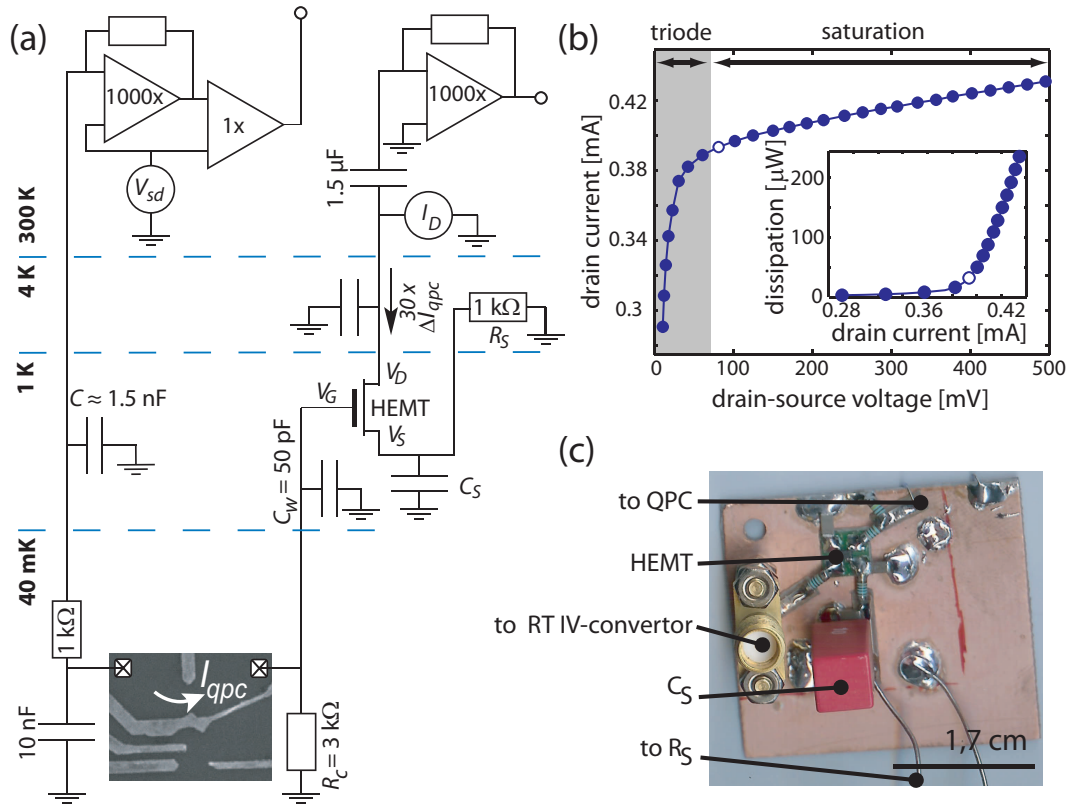


**Figure 6.1:** (a) Simplified schematic of the experimental setup.  $R_c$  converts fluctuations in  $I_{qpc}$  into voltage fluctuations on the HEMT gate. Through its transconductance the HEMT converts these fluctuations into current fluctuations which are amplified by an additional amplification stage at room temperature.  $R_c$  and  $C_w$  form a 1 MHz LP-filter. (b) Drain current as a function of drain-source voltage. Inset: HEMT power dissipation as a function of drain current. Both curves have been measured at 4K. The open dots indicate the used DC bias settings of the HEMT for fast charge detection ( $I_D \approx 400 \mu\text{A}$  and  $P_{HEMT} \approx 30 \mu\text{W}$ ). (c) Photograph of the HEMT circuit board. The main components and connection points are labelled.

$\mu\text{W}$ ) and is therefore not mounted on the same circuit board as the HEMT but on the 4K-stage of the setup.

### 6.2.3 Amplifying AC-signals

The transconductance  $g_m$  of the HEMT relates the drain current  $I_D$  through the HEMT to its gate-source voltage  $V_{GS}$  as  $I_D = -g_m V_{GS}$ . When this HEMT is appropriately DC biased,  $g_m = 10$  mA/V. This implies  $\Delta I_D \approx -30 \Delta I_{qpc}$ , using  $R_c = 3$  k $\Omega$ . The source of the HEMT is connected to ground by a resistor ( $R_S = 1.1$  k $\Omega$ ) and a capacitor ( $C_S = 4.7$   $\mu$ F) in parallel. The capacitor is used to hold the source of the HEMT at a fixed DC bias voltage. Furthermore, for AC signals with  $f \gg 1/(2\pi R_S C_S) \approx 30$  Hz, the HEMT gain exceeds its DC value and will increase for frequencies up to 3 kHz, determined by  $C_S // Z_{in}$ , where  $Z_{in} = 100 \Omega$  is the input impedance of the RT IV-converter. For higher frequencies the gain is measured to be constant up to 8 MHz.

### 6.2.4 Other parts of the setup

In addition to the HEMT,  $I_{qpc}$  can also be measured *simultaneously* from DC to 100 Hz using a "slow" IV-converter at RT which is connected to the left lead of the QPC. We refer to this measured current as the time averaged current.

As depicted in Fig. 6.1a, we introduced a capacitor to ground on the node where we connect the RT IV-converter to the QPC. Its purpose is twofold: (i) It filters out high frequency noise coming either from the RT IV-converter or coupling into the measurement wire radiatively. (ii) It also effectively 'grounds' the left lead of the QPC for high frequency signals, ensuring that the high-frequency signals propagate towards the HEMT. The value of the capacitor (10 nF) is a trade-off between a series of requirements: (i) the capacitance should ideally be very high in order to create an effective ground for frequencies higher than a few tens of kHz. (ii) Since this capacitance amplifies the input voltage noise of the RT amplifier at high frequencies, the capacitance should be small to have a large measurement bandwidth [4]. (iii) Furthermore, we want to calibrate the gain of the HEMT circuitry by modulating the QPC bias voltage  $V_{qpc}$ , thereby modulating the gate of the HEMT with a known amplitude. The chosen value of 10 nF is a good compromise. We can still modulate the HEMT gate at a few tens of kHz and it ensures that fast fluctuations in the QPC-current will generate voltage fluctuations on the gate of the HEMT of maximal amplitude (since  $10$  nF  $\ll 3$  k $\Omega$  at 100 kHz).

Additionally, we included a resistor in series with the QPC on its left lead. Its value of 1 k $\Omega$  is chosen since (i) 1 k $\Omega$  is much larger than the impedance of the measurement wire, helping to attenuate interference signals (1 k $\Omega$   $\parallel$  10 nF forms a 17 kHz LP-filter) and (ii) 1 k $\Omega$  is of the same order as the input impedance of

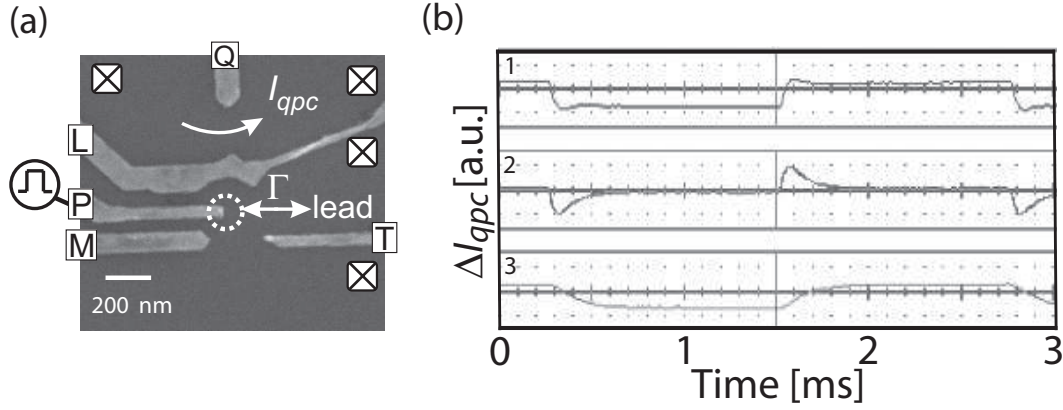


**Figure 6.2:** (a) Scanning Electron Micrograph of a similar device as used in the experiment. The dot (dashed circle) and QPC are defined in a 2DEG formed at a GaAs/AlGaAs interface 90 nm below the surface, with an electron density of  $1.3 \times 10^{15} \text{ m}^{-2}$  by applying negative voltages to gates  $L$ ,  $M$ ,  $T$  and  $Q$ . Fast voltage pulses can be applied to gate  $P$ . The crosses represent Ohmic contacts. (b) Response to a voltage pulse applied to gate  $P$ . Trace 1 shows the total response to a voltage pulse when  $G_{qpc} \approx \frac{e^2}{h}$ . When the QPC is pinched-off, there is still a response due to crosstalk between the pulse line and the HEMT gate-wire (trace 2), providing a measure for the bandwidth of the readout circuit from the HEMT gate up to RT ( $\sim 8 \text{ MHz}$ ). Subtracting trace 2 from 1 reveals the signal from the QPC (trace 3) with a rise time of 285 ns, corresponding to a bandwidth of 1 MHz.

the "slow" RT IV-converter and much smaller than the typical QPC resistance ( $\approx 25 \text{ k}\Omega$ ), yielding a sufficiently high signal-to-noise ratio for measurements of the DC-current.

Both the 10 nF capacitor and the 3 k $\Omega$  resistor  $R_c$  are mounted on the coldfinger of the dilution refrigerator, very close to the device, to minimize the area of the (ac-)current loop (ground  $\rightarrow$  10 nF  $\rightarrow$  QPC  $\rightarrow$  3 k $\Omega$   $\rightarrow$  ground) which in turn minimizes the interference due to the pick-up of magnetic flux.

The quantum dot and the QPC are defined in a two-dimensional electron gas (2DEG) by applying negative voltages to metal surface gates (labeled  $L$ ,  $M$ ,  $T$  and  $Q$  in Fig 6.2a). Gate  $L$  completely separates the QPC source and drain electrically from the leads of the dot. The experiment is performed in a dilution refrigerator with a base temperature of 40 mK and with zero externally applied magnetic field.

## 6.3 Determination of the bandwidth

First, we characterize the bandwidth of the setup. The bandwidth ( $BW$ ) is expected to be limited by the resistor  $R_c$  and the capacitance,  $C_w$ , of the measurement wire connecting the right lead of the QPC to the HEMT gate ( $BW = (2\pi R_c C_w)^{-1}$ ). The HEMT is mounted on the 1K-stage, since this has sufficient cooling power to dissipate the heat generated by the HEMT in operation. The value for  $C_w$  is then a tradeoff between two requirements: a low capacitance and sufficient thermal anchoring of the wire. The value of  $R_c$  is also a tradeoff: increasing the value of  $R_c$  increases the amplitude of the voltage fluctuations on the HEMT gate ( $v_{GS} = \Delta I_{qpc} R_c$ ) but reduces the bandwidth of the setup (for a given value of  $C_w$ ). Our aim is to detect single-electron tunneling on a sub-microsecond timescale. The value for  $R_c$  was chosen by assuming  $\Delta I_{qpc} \approx 400$  pA and an equivalent input referred voltage noise of  $0.4$  nV/ $\sqrt{\text{Hz}}$ . This was determined in a separate cooldown to 4K without the device being connected to the HEMT gate. When we choose  $R_c = 3$  k $\Omega$ , we obtain a SNR  $\approx 3$  and a bandwidth of 1 MHz. Experimentally we determine the bandwidth by measuring the QPC response to fast voltage pulses applied to gate  $P$ . The measured rise times are 285 ns, yielding a bandwidth of 1 MHz, in excellent agreement with the designed bandwidth (Fig. 6.2b).

## 6.4 Sources of noise

The next step is a characterization of the noise contributions. The first contribution we will address is the current noise originating from the HEMT. This was examined in a separate cooldown (to 4K) without the device attached to the gate of the HEMT. Finally we will discuss the HEMT voltage noise as well as the QPC shot noise contributions. We choose to compare signal and noise at the gate of the HEMT. Noise we measure at the output will therefore be converted to values as if the origin was a noise source on the HEMT gate and will be referred to as the equivalent input referred voltage noise.

### 6.4.1 HEMT current noise

Current noise from a HEMT is expected to be very small but very important to be quantified since the presence of a current noise source will cause a current which will directly flow to the device. In order to measure a current noise contribution we assemble a circuit board which we cool down to 4K, see Fig. 6.3a. We connect

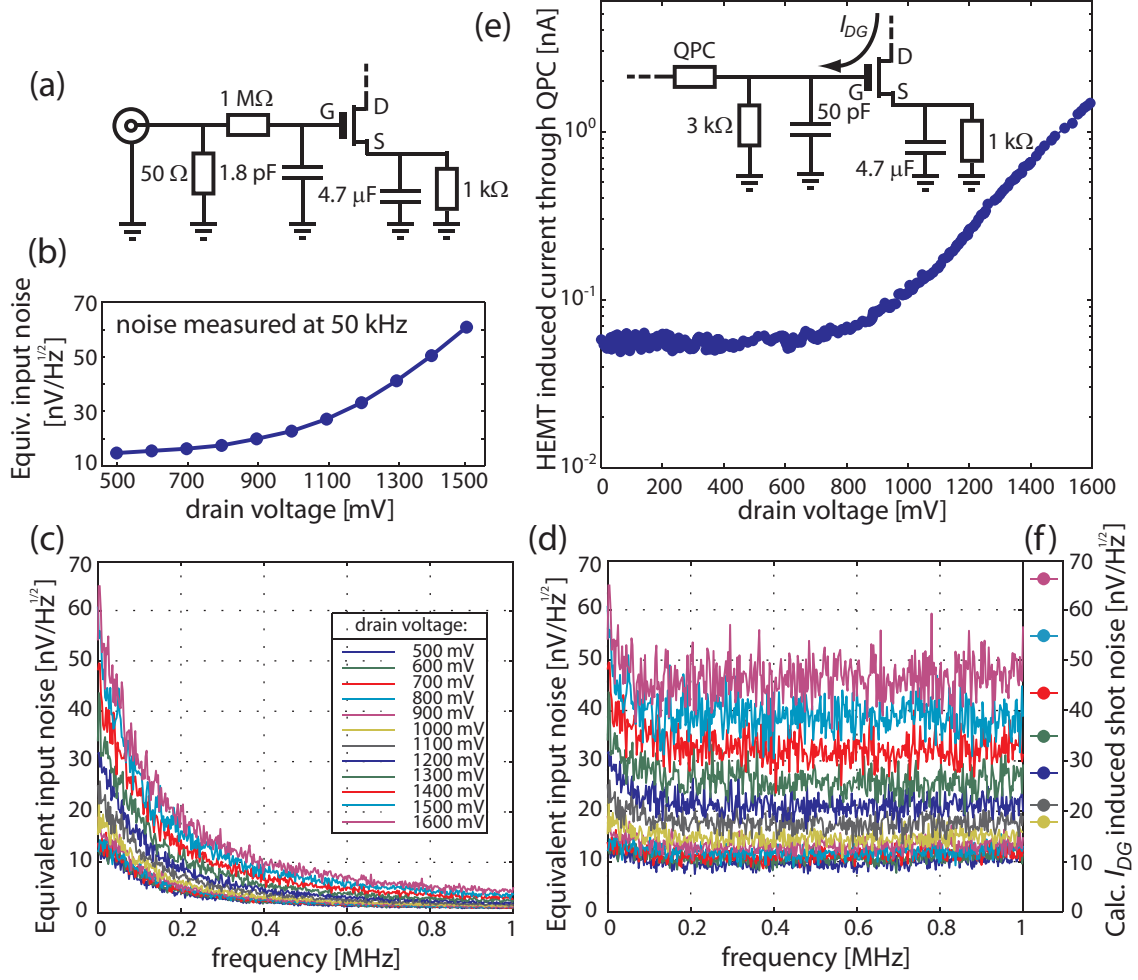


**Figure 6.3:** (a) Schematic of the test circuit for the 4K measurements of the HEMT current noise. The 1 M $\Omega$  resistor and the 1.8 pF HEMT input (stray) capacitance form a low-pass filter, reducing the bandwidth to  $\sim 90$  kHz. (b) Equivalent input referred voltage noise as a function of the HEMT drain current. The measured values are determined at 50 kHz. (c) Equivalent input referred voltage noise measured in a range from 100 Hz to 1 MHz for different values of the drain voltage. The small bandwidth causes the apparent reduction of the noise at higher frequencies. (d) The same spectra as in (c) are plotted after correcting for the amplitude reduction by the 90 kHz RC low-pass filter. (e) HEMT induced current through the QPC, measured in the configuration shown in the inset (and in 6.1a). For  $V_D > 800$  mV we measure a current through the QPC, originating at the HEMT side of the QPC, with an exponential dependence on  $V_D$ . (f) The calculated voltage fluctuations, generated by the shot noise of  $I_{DG}$ , at the HEMT gate in the configuration of (a), using the drain-gate leakage currents from (e).

a 1 M $\Omega$  resistor to the gate of the HEMT. The 1 M $\Omega$  resistor is chosen to be large

enough to generate a measurable voltage (higher than its own thermal noise at 4K) even if the amplitude of the current noise is small, and it is small enough to allow the current noise to be measured in an appreciable bandwidth. This bandwidth is  $\sim 90$  kHz due to the  $1\text{ M}\Omega$  resistor and the  $1.8\text{ pF}$  HEMT input (stray) capacitance. The  $50\text{ }\Omega$  coaxial connection allows the gate to be modulated with a known amplitude to determine the HEMT gain each bias setting. When measuring the equivalent input referred voltage noise we expect to see at least  $15\text{ nV}/\sqrt{\text{Hz}}$  (thermal noise of  $1\text{ M}\Omega$  at 4K). This is exactly what is observed for low drain voltages  $V_D$ . However, as shown in Fig. 6.3b, the measured noise increases with increasing  $V_D$ . The reported values are determined at  $50\text{ kHz}$ , well within the bandwidth of the circuit. To verify whether this noise source has a frequency dependency, we measure the equivalent input referred voltage noise in a  $1\text{ MHz}$  bandwidth. In Fig. 6.3c these spectra are plotted for different values of  $V_D$ . At low frequencies, we see values of the noise in agreement with Fig. 6.3b. At high frequencies however, the noise spectral density goes down dramatically. This is due to the small bandwidth of the testing circuit ( $\sim 90\text{ kHz}$ ). When we take the frequency dependent transfer function into account, we see that up to  $1\text{ MHz}$  the HEMT current noise has a white spectrum (Fig. 6.3d).

The fact that the current noise spectrum is frequency independent leads to the assumption that the microscopic origin of the current noise is shot noise. The HEMT is specified to have a typical leakage current from its drain to its gate terminal of tens of  $\mu\text{A}$  at RT (which is DC bias dependent). Electrons tunneling from drain to gate will generate a shot noise  $S_{DG} = 2e\langle I_{DG} \rangle$ . We test this hypothesis by measuring the drain-gate leakage current  $I_{DG}$  as a function of the drain voltage  $V_D$ . We determine  $I_{DG}$  using the QPC. The HEMT is again connected as in Fig. 6.1a (see also the inset of Fig. 6.3e). We apply zero bias over the QPC ( $V_{qpc} = 0$ ) and measure the current through the QPC as a function of the HEMT drain voltage  $V_D$ . Figure 6.3e shows that for  $V_D > 800\text{ mV}$  we observe a current which increases with increasing  $V_D$ . Both the direction of this current and its exponential dependence on  $V_D$  confirm that this current is due to electrons tunneling from the HEMT drain to its gate terminal. This measured QPC current can be translated into a drain-gate leakage current  $I_{DG}$ . To compare these results to the measured spectra in Fig. 6.3d, we calculate the equivalent voltage noise on the HEMT gate as a result of the shot noise ( $\sqrt{S_{DG}} \cdot 1\text{M}\Omega$ ), and plot it in Fig. 6.3f. We see a good agreement and conclude that the microscopic origin of the measured shot noise is indeed the shot noise generated by the drain-gate leakage current of the HEMT.

From the current noise measurements we conclude that, for the HEMT DC

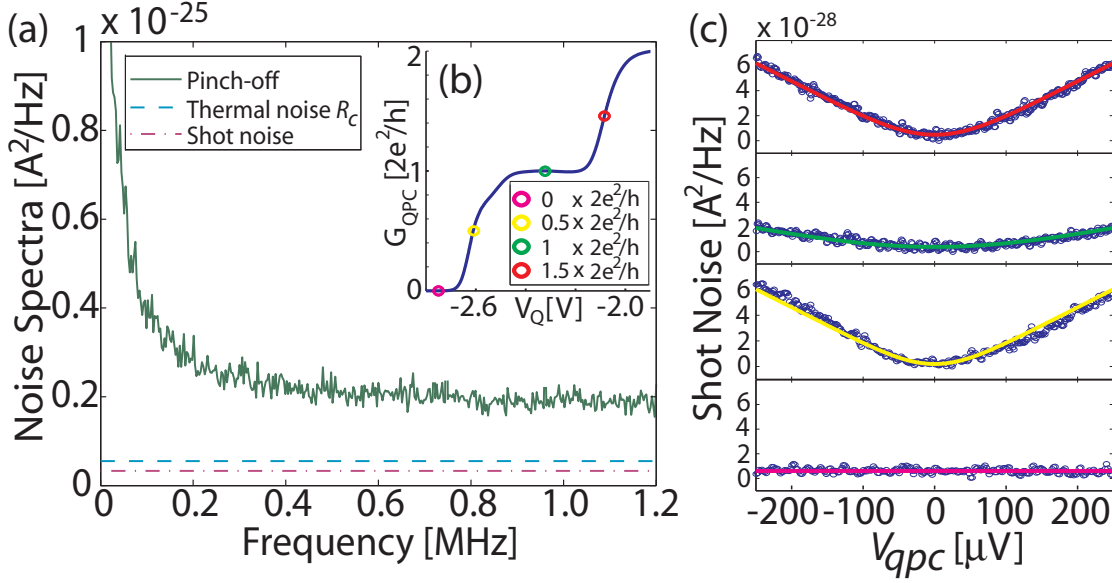


**Figure 6.4:** (a) Noise spectra of the setup including the cryogenic HEMT amplifier. The measured spectrum is taken for the QPC in pinch-off, thereby excluding shot noise and noise coming from the other side of the QPC. The calculated noise contributions from the QPC shot noise and the thermal noise of  $R_c$  are plotted for reference (dash-dotted and dashed line respectively). (b) QPC conductance as a function of the voltage on gate Q. (c) Measurements of the QPC shot noise power measured at the QPC conductances indicated by the colored markers in (b). Solid lines are fits to Eq. (7.2).

bias settings used for fast charge detection ( $I_D \approx 400 \mu\text{A}$ ), the current noise contribution is smaller than  $1/2 \sqrt{S_J^{1\text{M}\Omega}/R} \approx 7 \text{ fA}/\sqrt{\text{Hz}}$ , where  $S_J^{1\text{M}\Omega}$  denotes the spectral density of the thermal noise generated by the  $1\text{M}\Omega$  resistor.

When we translate this to the situation where we have the HEMT connected to our device as in Fig. 6.1a, the HEMT current noise will result in voltage fluctuations on the HEMT gate of  $\sim 20 \text{ pV}/\sqrt{\text{Hz}}$  and a total injected current of  $\sim 0.8 \text{ pA}$  from the HEMT into the QPC. Both effects are negligible.

### 6.4.2 HEMT voltage noise

Since the contributions from the HEMT current noise are small, we will only be interested in the voltage noise of the HEMT and the contribution of the shot noise from the QPC. To determine the HEMT voltage noise we measure in the configuration shown in Fig. 6.1a and pinch of the QPC, thereby excluding shot noise and noise from the other side of the QPC channel, and measure the total noise spectral density. We plot this as an equivalent input referred noise in Fig.



6.4a. A characteristic  $1/f$  contribution is present up to 200 kHz. For frequencies above 200 kHz, the spectrum is approximately flat, saturating at  $0.2 \times 10^{-25} \text{ A}^2/\text{Hz}$  ( $= 0.4 \text{ nV}/\sqrt{\text{Hz}}$ ).

### 6.4.3 QPC shot noise

This measured value for the HEMT voltage noise is very close to the voltage fluctuations generated by the QPC shot noise (calculated to be  $S_I = 0.17 \text{ nV}/\sqrt{\text{Hz}}$ , for 1 mV bias over the QPC [4]). We test this by a *direct* measurement of the QPC shot noise. We measure the rms voltage after band-pass filtering the output of the "fast" RT IV-converter (bandwidth from 500 kHz to 1 MHz). In Fig. 6.4b we show the QPC conductance  $G_{qpc}$  as a function of the voltage on gate Q, determined from the time averaged current. The colored markers indicate the QPC conductances ( $G_{qpc} = n \frac{e^2}{h}$ ,  $n = 0, 1, 2, 3$ ) at which the shot noise was measured as a function of bias over the QPC,  $V_{qpc}$ , see Fig. 6.4c.  $V_{qpc}$  is varied by changing  $V_{sd}$ , applied by the "slow" RT IV-converter. We verified that the QPC was in its linear regime for the entire range of  $V_{qpc}$ . The total shot noise spectral density  $S_I$  can be expressed as [18, 19]

$$S_I = \frac{2e^2}{h} \sum_i \mathcal{N}_i \left[ eV_{qpc} \coth \left( \frac{eV_{qpc}}{2k_B T_e} \right) - 2k_B T_e \right] \quad (6.1)$$

where  $\mathcal{N}_i = T_i (1 - T_i)$  with  $T_i$  the QPC transmission coefficient of mode  $i$ ,  $V_{qpc}$  the bias over the QPC,  $k_B$  the Boltzmann constant and  $T_e$  the electron temperature. The solid lines in Fig. 6.4c are fits to Eq. (7.2) yielding  $\mathcal{N} = 0.234, 0.090, 0.229$  and 0 from top to bottom, in agreement with the QPC conductances. The measurements prove that the input referred voltage noise is indeed very close to the shot noise limit in this setup. From the fits we also extract the electron temperature  $T_e = 255 \text{ mK}$ , consistent with the value obtained from the width of Coulomb peaks ( $T_e = 267 \text{ mK}$ ).

## 6.5 Measurement of real-time tunneling of single electrons

The noise measurements show that the noise from the HEMT is in agreement with our initial estimation. We therefore expect to have sufficient SNR to detect single-electron tunnel events. To test this experimentally, the dot is tuned to be near the  $0 \leftrightarrow 1$  electron transition by adjusting the voltages on gates  $L$ ,  $M$  and  $T$ , and to be isolated from the bottom lead [7]. The dot remains coupled

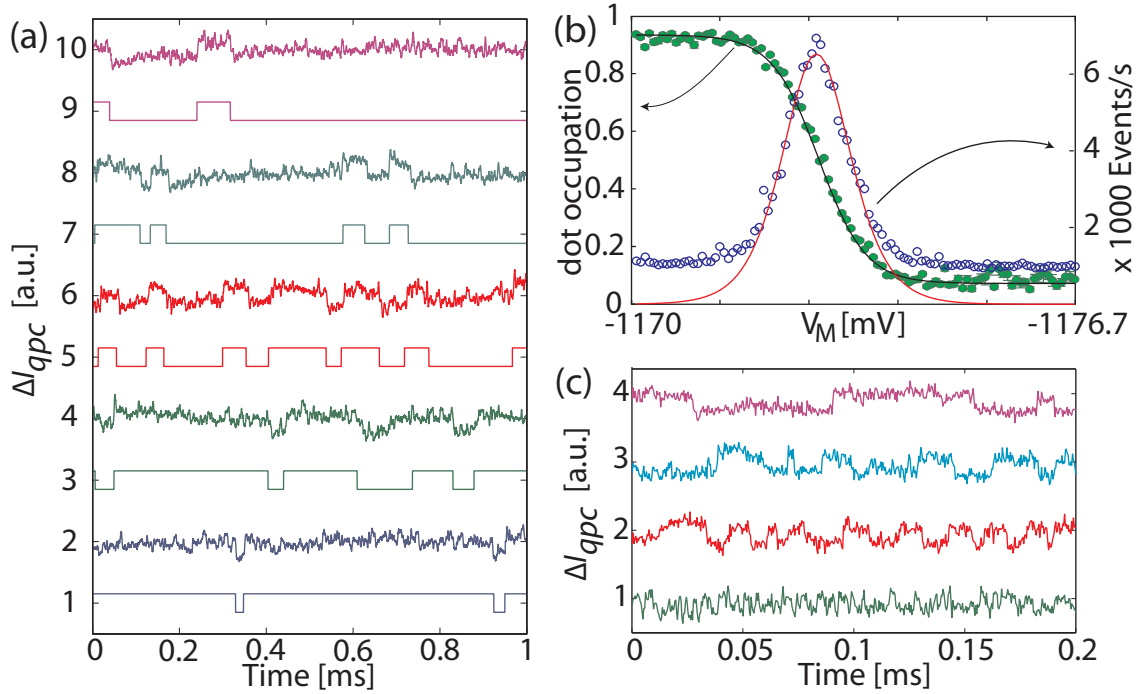


**Figure 6.5:** (a) Measured QPC current when increasing the dot potential from top to bottom. The result of our flank detection routine is plotted below each measured trace. An additional band-pass filter (200 Hz - 200 kHz) was used for this measurement. (b) Dot occupation extracted from the same data as (a) as a function of  $V_M$ . From the same data we extract the number of tunnel events per second as a function of  $V_M$  from which we can extract the tunnel rate. The solid curves are fits to the data using the Fermi distribution function  $f(\mu)$  (black curve) and  $\Gamma \times f(\mu) [1 - f(\mu)]$  yielding  $\Gamma = 26.1$  kHz (red curve). (c) The tunnel rate  $\Gamma$  is increased from top to bottom by decreasing the negative voltage on gate  $T$ . Here, the signal was band-pass filtered from 3 kHz to 1 MHz. The shortest detectable events are on the order of 400 ns.

to the other lead with a tunable tunnel rate,  $\Gamma$ . An electron is now allowed to tunnel back and forth between the dot and the lead and the QPC current should therefore exhibit a random telegraph signal (RTS). The QPC conductance is set again at approximately  $e^2/h$ .

In order to maximize  $\Delta I_{qpc}$ , we want to apply the highest possible bias,  $V_{qpc}$ . However, for  $V_{qpc} > 0.65$  mV, we observe a severe change in the dot occupation, most probably due to intradot excitations to the first orbital excited state [20]. We therefore restrict ourselves to QPC bias voltages below 0.65 mV. This reduces  $\Delta I_{qpc}$  to 320 pA, resulting in a lower SNR. Measurements of the RTS are shown in Fig. 6.5. To verify that the measured RTS originates from electron tunnel events between the dot and the lead, we varied two control parameters, as in

[4]: (1) the dot electrochemical potential  $\mu$  relative to the Fermi level of the lead  $\mu_F$  and (2) the tunnel barrier between the dot and the lead. The dot potential is changed by changing the voltage on gate  $M$ . The dot occupation probability  $P$  depends on  $\mu - \mu_F$  and the temperature broadening of the lead so it should directly reflect the Fermi-Dirac distribution of electronic states in the lead. We infer the dot occupation from the measured average time the electron spends on (off) the dot,  $\tau_{on(off)}$ , as  $P = \tau_{off}/\tau_{on} + \tau_{off}$ , [5]. However, since both the HEMT and the RT IV-converter AC-coupled, signals from the QPC are high-pass filtered (1.2 kHz cut-off). We can therefore not use a simple threshold detection scheme [9] but instead detect the flanks of the steps in  $\Delta I_{qpc}$  to obtain the single-electron tunneling statistics. In Fig. 6.5b the average dot occupation is plotted versus

the voltage on gate  $M$  ( $V_M$ ). At  $V_M = -1172.8$  mV,  $\mu$  is aligned with  $\mu_F$ . The solid black line is a fit to the Fermi-Dirac distribution function  $f(\mu)$  yielding an electron temperature  $T_e = 275$  mK. The average times  $\tau_{on/off}$  also allow the determination of the tunnel rate  $\Gamma$ . The Fermi distribution and the tunnel rate  $\Gamma$  determine the average number of tunnel events per second as  $r_e = 1/(\tau_{on} + \tau_{off}) = \Gamma \times f(\mu) [1 - f(\mu)]$ . This is also plotted in Fig. 6.5b. The fit to this data yields  $\Gamma = 26.1$  kHz (solid red line) [21]. The tunnel rate  $\Gamma$  can be varied via the voltage on gate  $T$  (Fig. 6.5c). The shortest detectable events are on the order of 400 ns. The charge sensitivity reached is  $4.4 \times 10^{-4} e/\sqrt{\text{Hz}}$  in the range 200 kHz - 1 MHz, only 3.8 times larger than the shot noise limit in this setup with  $V_{qpc} = 0.65$  mV.

## 6.6 Conclusion and recommendations

We have demonstrated that a HEMT can be used as a cryogenic amplifier to increase the measurement bandwidth of a QPC charge detection setup. The bandwidth of the setup is 1 MHz and the input referred voltage noise is measured to be  $0.4 \text{ nV}/\sqrt{\text{Hz}}$  above  $\sim 200$  kHz, which is close to the QPC shot noise limit. This allows us to detect fluctuations in the dot occupation as short as 400 ns, 20 times faster than previously achieved using a QPC as a charge sensor. The signal-to-noise ratio can be increased in several ways. The signal can be increased by changing the design of the gate structure in order to optimize the coupling between the dot and the QPC [22, 23]. A lower amplifier noise (both  $1/f$  and baseline) could be obtained by using a HEMT with a larger gate area. This will be investigated in chapter 7. The bandwidth could be further increased by placing the HEMT even closer to the sample (since the dissipation in the HEMT is low enough), which would reduce the capacitance even more.

We thank F.H.L. Koppens, J. Love, T. Meunier, K.C. Nowack, J.H. Plantenberg, R.J. Schoelkopf, G.A. Steele, H.P. Tranitz and L.H. Willems van Beveren for help and discussions, A. van der Enden and R.G. Roeleveld for technical support, and L.P. Kouwenhoven for supplying infrastructure. This work is supported by the 'Stichting voor Fundamenteel Onderzoek der Materie (FOM)' and the 'Nederlandse Organisatie voor Wetenschappelijk Onderzoek (NWO)'.

This work has been performed in close collaboration with T. Nooitgedagt, R. N. Schouten, W. Wegscheider and L. M. K. Vandersypen.

## References

- [1] L. P. Kouwenhoven, D. G. Austing and S. Tarucha, Few-electron quantum dots, Rep. Prog. Phys. **64**, 701 (2001).
- [2] T. Fujisawa, R. Tomita, T. Hayashi and Y. Hirayama, Science **314**, 1634 (2006).
- [3] S. Gustavsson, R. Leturcq, B. Simovic, R. Schleser, T. Ihn, P. Studerus, K. Ensslin, D. C. Driscoll and A. C. Gossard, Phys. Rev. Lett. **96**, 076605 (2006).
- [4] L.M.K. Vandersypen, J. M. Elzerman, R. N. Schouten, L. H. Willems van Beveren, R. Hanson and L. P. Kouwenhoven, Appl. Phys. Lett. **85**, 4394 (2004).
- [5] R. Schleser, E. Ruh, T. Ihn, K. Ensslin, D. C. Driscoll and A. C. Gossard, Appl. Phys. Lett. **85**, 2005 (2004).
- [6] J. R. Petta, A. C. Johnson, C. M. Marcus, M. P. Hanson, A. C. Gossard, Phys. Rev. Lett. **93**, 186802 (2004).
- [7] J. M. Elzerman, R. Hanson, L. H. W. van Beveren, L. M. K. Vandersypen and L. P. Kouwenhoven, Appl. Phys. Lett. **84**, 4617 (2004).
- [8] A. C. Johnson, C. M. Marcus, M. P. Hanson, and A. C. Gossard, Phys. Rev. B **71**, 115333 (2005).
- [9] J. M. Elzerman, R. Hanson, L. H. Willems van Beveren, B. Witkamp, L. M. K. Vandersypen and L. P. Kouwenhoven, Nature **430**, 431 (2004).
- [10] R. Hanson, L. H. Willems van Beveren, I. T. Vink, J. M. Elzerman, W. J. M. Naber, F.H. L. Koppens, L. P. Kouwenhoven and L. M. K. Vandersypen, Phys. Rev. Lett. **94**, 196802 (2005).

- [11] J. R. Petta, A. C. Johnson, J. M. Taylor, E. A. Laird, A. Yacoby, M. D. Lukin, C. M. Marcus, M. P. Hanson and A. C. Gossard, *Science* **309**, 2180 (2005).
- [12] R. Hanson, L. P. Kouwenhoven, J. R. Petta, S. Tarucha and L. M. K. Vandersypen, *Reviews of Modern Physics* **79**, 1217 (2007)
- [13] D. J. Reilly, C. M. Marcus, M. P. Hanson and A. C. Gossard, arXiv:0707.2946v1 (2007).
- [14] M. Thalakulam, W. W. Xue, F. Pan, Z. Ji, J. Stettenheim, L. Pfeiffer, K. W. West, A. J. Rimberg, arXiv:0708.0861v1 (2007).
- [15] R. J. Schoelkopf, P. Wahlgren, A. A. Kozhevnikov, P. Delsing and D. E. Prober, *Science* **280**, 1238 (1998).
- [16] R. J. Schoelkopf, private communication.
- [17] A. T. Lee, *Rev. Sci. Instrum.* **60**, 3315 (1989).
- [18] Ya. M. Blanter and M. Büttiker, *Phys. Rep.* **336**, 1 (2000).
- [19] L. DiCarlo, Y. Zhang, D. T. McClure, D. J. Reilly, C. M. Marcus, L. N. Pfeiffer, K. W. West, *Phys. Rev. Lett.* **97**, 036810 (2006).
- [20] E. Onac, F. Balestro, L. H. Willems van Beveren, U. Hartmann, Y. V. Nazarov and L. P. Kouwenhoven, *Phys. Rev. Lett.* **96**, 176601 (2006).
- [21] For every trace without a tunnel event, the total length of the trace (1 ms) is assigned to  $\tau_{on/off}$ . This results in a baseline of 1000 events/s instead of 0. To determine  $\Gamma$ , we fit to a subset of the data with a sufficient number of tunnel events.
- [22] L.-X. Zhang, J. P. Leburton, R. Hanson and L. P. Kouwenhoven, *Appl. Phys. Lett.* **85**, 2628 (2004).
- [23] S. Amasha, K. MacLean, Iuliana P. Radu, D. M. Zumbhl, M. A. Kastner, M. P. Hanson and A. C. Gossard, *Phys. Rev. Lett.* **100**, 046803 (2008).



## Chapter 7

# Improving the cryogenic charge detection setup

As has been demonstrated in chapter 6, a HEMT used as a cryogenic pre-amplifier can dramatically increase the bandwidth of a charge detector setup with a quantum point contact charge sensor. However, making use of the full (DC - 1 MHz) bandwidth turned out to be nearly impossible due to a small signal-to-noise ratio. Lower amplifier noise is believed to be achievable by using a HEMT with a larger gate area. In this chapter, we study the performance of different commercially available high electron mobility transistors (HEMTs). We characterize HEMTs with three different gate lengths (400, 1600 and 6400  $\mu\text{m}$ ) at room temperature and cryogenic temperatures. We identify the best HEMT to use as a cryogenic pre-amplifier for single-shot spin read-out experiments and propose an improved charge detection setup.

## 7.1 Introduction

Using a cryogenic HEMT amplifier we have been able to increase the bandwidth of a charge detection setup with a quantum point contact (QPC) charge sensor up to 1 MHz (see chapter 6, [1]). Even though the equivalent input referred voltage noise was only  $0.4 \text{ nV}/\sqrt{\text{Hz}}$ , the noise was barely low enough to allow real-time detection of single-electron tunneling to and from a proximal quantum dot in a 1 MHz bandwidth. If we want to use this setup to perform single-spin read-out, as in Ref. [2], with a read-out fidelity exceeding 99%, the signal-to-noise ratio (SNR) has to be increased. The reason that this high fidelity cannot be obtained with the present cryogenic setup is that even though we reduced the errors we make due to a small bandwidth [2], we increase the number of "dark counts" due to the low SNR. The SNR can be increased by (i) increasing the signal and/or (ii) reducing the noise.

The signal of interest is the change of the QPC current,  $\Delta I_{qpc}$ , corresponding to an electron entering or leaving the adjacent quantum dot. It has, in our current samples, a maximum amplitude of  $\sim 400 \text{ pA}$ . The height of this step depends on the coupling between the quantum dot and the QPC. It might be possible to increase this coupling by modifying the sample design [3, 4] but this is beyond the scope of this chapter. For now we will assume  $\Delta I_{qpc}$  to be fixed. The signal at the input of our cryogenic amplifier is not only determined by  $\Delta I_{qpc}$  but also by the resistor  $R_c$ , which converts  $\Delta I_{qpc}$  into a modulation of the voltage on the gate of the HEMT (see chapter 6 and [1]). Increasing the resistor value will increase the signal amplitude. However, at the same time this will also reduce the electronic bandwidth (for a fixed wire capacitance  $C_w$ ).

The equivalent input referred noise of a given HEMT depends on the DC biasing, transconductance, ambient temperature and type of HEMT. In this chapter we explore to what extent we can improve the cryogenic charge detection setup by using different (DC biasing of the) HEMTs. The HEMTs we use are listed in table 7.5.1.

## 7.2 HEMT amplifier test circuit

In order to measure the properties of all three HEMTs we design a circuit which is suitable for biasing the HEMT at arbitrary dissipations, and to determine the HEMT gain and noise spectrum at room temperature (RT) and cryogenic temperatures. This circuit is shown in Fig. 7.1 and explained in the caption. The design is somewhat different from the design in chapter 6 since now the source terminal is connected to ground (not the gate) and we have the ability



Name	Gate length	Type
<b>Agilent ATF35143</b>	400 $\mu\text{m}$	n-channel depletion
<b>Agilent ATF33143</b>	1600 $\mu\text{m}$	n-channel depletion
<b>Agilent ATF511P8</b>	6400 $\mu\text{m}$	n-channel enhancement

**Table 7.1:** HEMTs used in this chapter. All HEMTs are commercially available and purchased from Agilent. The ATF35143 (400  $\mu\text{m}$ ) and ATF33143 (1600  $\mu\text{m}$ ) have, except for their gate length, a similar design. In order to pinch off their source-drain channel, negative gate voltages have to be applied with respect to their source. The ATF511P8 (6400  $\mu\text{m}$ ) is already pinched off without applied gate-source voltages. In order to open up the channel positive gate-source voltages are required.

to bias 2 terminals of the transistor instead of one. This allows us to set the HEMT to have an arbitrary dissipation and optimize the bias settings for a fixed dissipation to obtain maximum gain, see section 7.3. The left part of the circuit is mounted on the same circuit board as on which the HEMT is placed and can be cooled down to 77K and 4K. The right part of the circuit remains at RT.

## 7.3 Biasing the HEMT

As mentioned in section 7.1, we characterize the HEMT at several fixed dissipations at three temperatures: RT, 77 K and 4 K.

### 7.3.1 Different HEMT dissipations

Since we aim at using the HEMT as a cryogenic pre-amplifier, the dissipation is an important parameter to know and to control. The cooling power of the dilution refrigerators, in which the HEMTs will be mounted, are specified to be 300 (400)  $\mu\text{W}$  at 100 mK for the Oxford Kelvinox 300 (400HA). We require the HEMT dissipation to be less than this when mounted on the dilution unit. When the HEMT is placed on the 4K-stage, higher dissipations are allowed. We will characterize the HEMTs for three different dissipations: 100  $\mu\text{W}$ , 10  $\mu\text{W}$  and 1  $\mu\text{W}$  (or 1 mW for the ATF511P8 (6400  $\mu\text{m}$  gate length)).

The dissipation of the HEMT is given by  $P_{HEMT} = V_{DS}I_D$ , where the drain-source voltage  $V_{DS}$  ( $= V_D - V_S$ ) and the drain current  $I_D$  are set by controlling the drain bias voltage and the gate-source voltage  $V_{GS}$  ( $= V_G - V_S$ ).

Examples of the DC bias settings are shown in Fig. 7.2 where the RT data

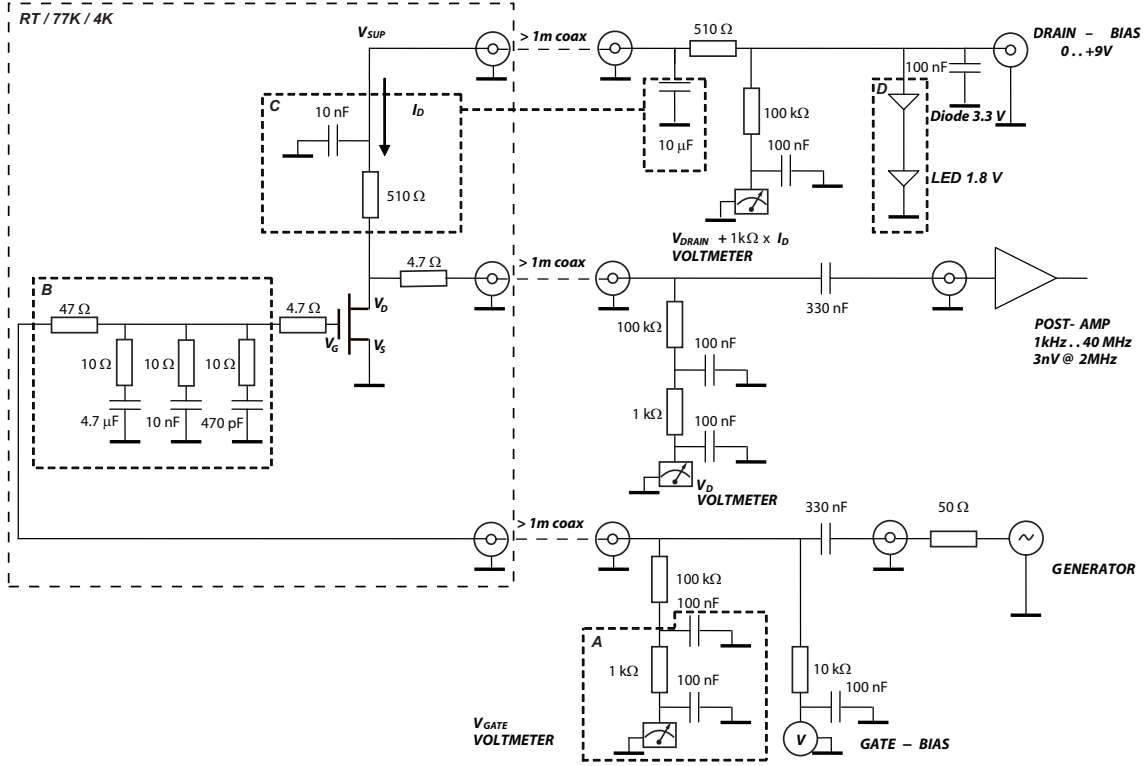


**Figure 7.1:** Schematic of the experimental setup. The left part of the circuit, indicated by the dashed box, is mounted on a single circuit board, which is measured at room temperature, 77K and 4K. The rest of the circuit remains at room temperature. Since the gate of the HEMT is biased in the test circuit we have to make sure to avoid that noise or interference, originating from the biasing circuitry, arrives at the gate. The low-pass filters (labelled A) reduce the noise from the voltmeter that measures  $V_G$ . Similar filtering is applied to the drain terminal. The resistors and capacitors directly connected to the gate form an attenuator of 26 dB that attenuates signals above  $\sim 10$  kHz (labelled B in Fig. 7.1). Oscillating voltages from the AC-coupled frequency generator are added to the DC bias voltage and modulate the gate voltage with a known amplitude. To keep the node ' $V_{SUP}$ ' at a constant DC voltage, we need the components labelled C in Fig. 7.1. Finally, a diode (1.8V) and a LED (3.3V) (labelled A in Fig. 7.1) limit the bias voltage to a range smaller than the specified breakdown voltage for the HEMTs. The oscillating drain voltages are amplified by an AC-coupled RT post-amplifier.

of the ATF35143 ( $400 \mu\text{m}$ ) is displayed. In Fig. 7.2a we have plotted the HEMT operation points  $\{V_{DS}, I_D\}$ , with drain current  $I_D$  and source-drain voltage  $V_{SD}$ , at which we characterize the HEMT. Along the solid and dashed lines the dis-

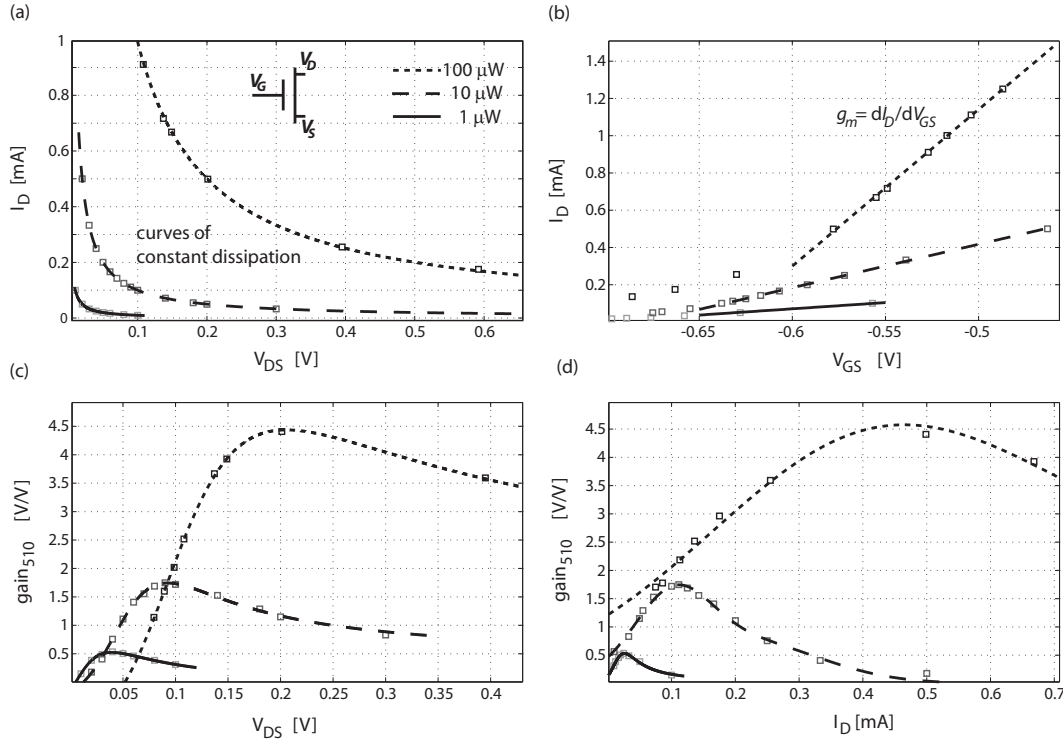


**Figure 7.2:** The ATF35143 biased at RT for 1  $\mu$ W, 10  $\mu$ W and 100  $\mu$ W. (a) HEMT operation points.  $I_D$  and  $V_{DS}$  are chosen such that the dissipation of the HEMT is constant. The solid and dashed lines are curves of constant dissipation. (b)  $I_D$  as function of  $V_{GS}$  for the three different dissipations. The slopes of the lines represent the transconductance, which increases with increasing dissipation. (c) AC voltage gain ( $V_{out}/V_G$ ) as function of  $V_{DS}$ . The voltage gain depends on the value of the resistor attached to the HEMT drain terminal (510  $\Omega$ ). We therefore adopt the name  $gain_{510}$ . For higher dissipation the gain increases significantly. (d) Voltage gain now plotted as function of  $I_D$ .

sipation is constant. The transconductance of the HEMT  $g_m$  is the parameter that relates the change in  $V_{GS}$  to a change in  $I_D$ . We can extract its value from fits through the data in Fig. 7.2b, where the dashed/solid lines mark constant dissipation. We see that  $g_m \approx 8$  mA/V at a dissipation of 100  $\mu$ W and decreases roughly by an order of magnitude when we go to a dissipation of 1  $\mu$ W. The AC voltage gain decreases, as expected, by same order of magnitude as  $g_m$  if the dissipation is reduced from 100  $\mu$ W to 1  $\mu$ W (Fig. 7.2c,d). The small deviation ( $\sim 10\%$ ) is most likely due to the finite HEMT output impedance (see section 7.4).

The HEMT biasing and performance also depend on the ambient temperature. This is illustrated in Fig. 7.3 where the ATF35143 is biased at a 100  $\mu$ W dissipa-

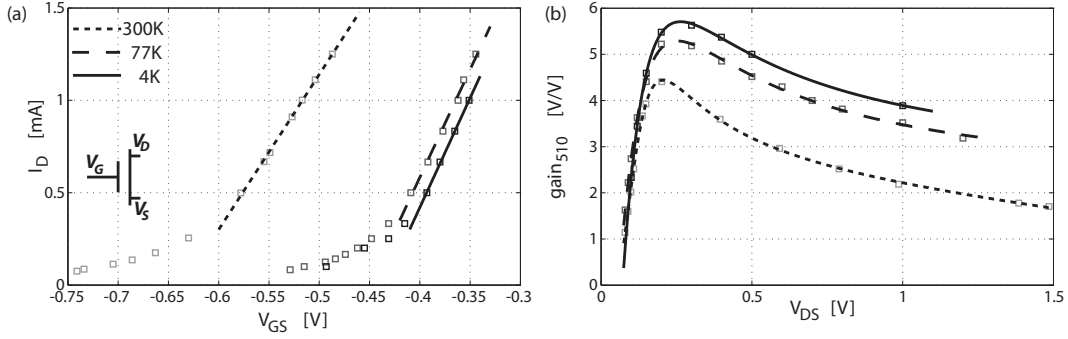


**Figure 7.3:** The ATF35143 biased at 4K, 77K and RT at a fixed dissipation of 100  $\mu$ W. (a)  $I_D$  as a function of  $V_{GS}$ . The transconductance  $g_m$  increases slightly with decreasing temperatures. Note the large shift in  $V_{GS}$  with decreasing temperatures. (b) AC voltage gain as a function of  $V_{DS}$ . The gain does not significantly increase when cooling the HEMT down to 4 K. This behavior is consistent with the small increase in  $g_m$  as observed in (a).

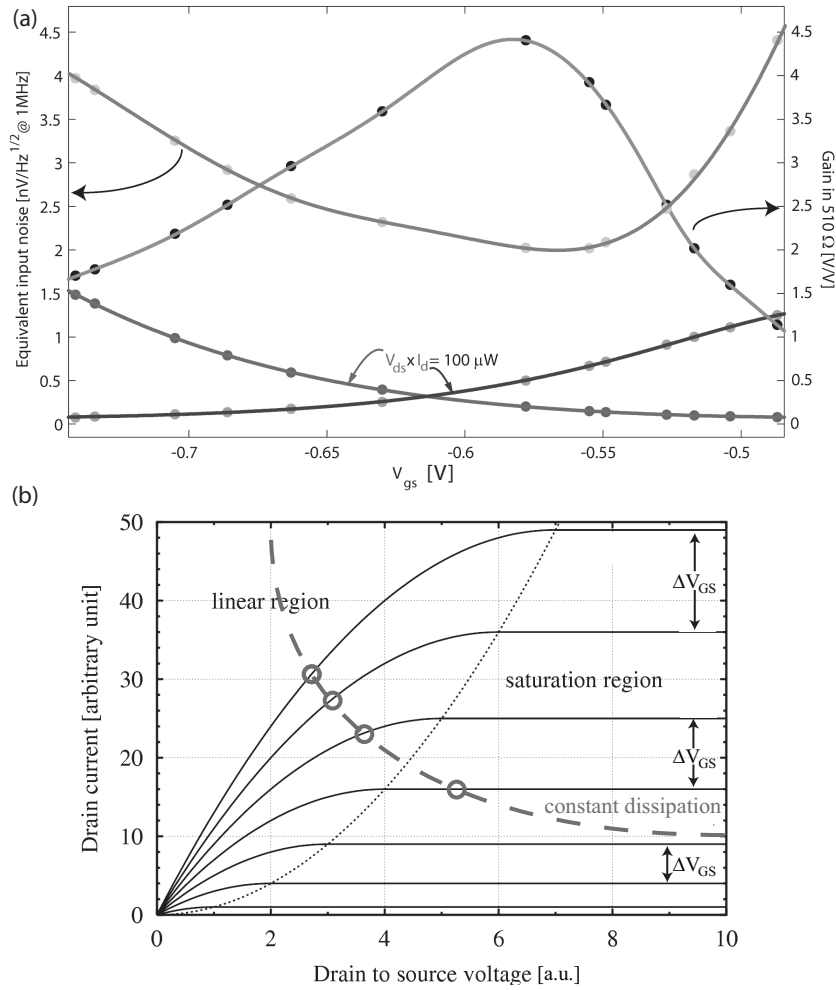
tion at different temperatures. The required values for  $I_D$  and  $V_{SD}$  obviously do not change but we observe a dramatic shift in the values for  $V_{GS}$  towards more positive voltages (Fig. 7.3a). This shift is observed for all HEMTs and turns out to limit our parameter space at cryogenic temperatures for the ATF511P8 (6400  $\mu$ m). The required positive voltages to set this HEMT at a dissipation of 1 mW are dangerously close to its specified breakdown voltages.

Figure 7.3a also shows that cooling down to 4 K increases  $g_m$  by 25% to 10 mA/V (see chapter 6). A similar increase in voltage gain is seen in Fig. 7.3b.

### 7.3.2 Optimal DC bias point

In section 7.3.1 we have seen that for a fixed dissipation we have a large set of  $\{V_{DS}, I_D\}$  to choose from. In this section we will determine the optimal bias point for our application. Generally one would like to have a high gain pre-amplification stage in order to put less restraints on the noise specifications of the post-amplifier. In other words, a high gain results in a low equivalent input referred noise, for a given noise source at the output of the pre-amplifier. We illustrate the determination of the optimal bias point by measurements on the ATF35143 (400  $\mu$ m) biased at 100  $\mu$ W dissipation at RT.

We measure for each bias point the (voltage) gain of the HEMT and observe that the gain exhibits a maximum around  $V_{GS} = -0.57$  V (Fig. 7.4a). To verify whether we indeed have the lowest input referred noise we measure the output noise density (measured at 1 MHz) and convert this to an input referred voltage



**Figure 7.4:** The ATF25143 biased at  $100 \mu\text{W}$  at RT. (a) A minimum in the equivalent input referred noise is observed around maximum voltage gain. Note that the curves of  $V_{DS}$  and  $I_D$  don't have a corresponding axis. (b) Example of a characteristic HEMT bias curve. The dashed line represents a curve of constant dissipation which results in HEMT operation points indicated by the circles. When the drain-source voltage is reduced the operation points move from the saturation region into the triode (linear) region.

noise at the gate of the HEMT by dividing the measured noise by the (constant) gain of the RT amplifier and the (varying) voltage gain of the HEMT. This equivalent input referred voltage noise is also plotted in Fig. 7.4a. We see indeed that the input referred noise is minimal at the bias point where we have maximal gain. The dominant noise source in this measurement is the thermal noise of the  $510 \Omega$  drain resistor ( $3 \text{ nV}/\sqrt{\text{Hz}}$ ) and the thermal noise of the HEMT channel resistance ( $\sim 780 \Omega$ ,  $3.6 \text{ nV}/\sqrt{\text{Hz}}$ ).

The fact that the gain exhibits a peak deserves a little more explanation. Since we choose to operate the HEMT at a fixed dissipation, with decreasing  $V_{GS}$  we move towards bias points with a higher transconductance and the gain increases. For even smaller  $V_{GS}$  the gain decreases again, even though the transconductance increases. This is due to the fact that for these bias points we operate the HEMT outside its saturation region and the HEMT output impedance becomes finite. Therefore, when the HEMT output impedance  $R_H$  becomes comparable to the load resistance  $R_L$ , part of the signal at the drain terminal goes through the HEMT instead of the load resistor which is observed as a reduction of the gain. A possibility to overcome this problem is to connect an active load (e.g. an operational amplifier) to the HEMT drain terminal. Since the opamp input impedance is tunable (by changing its gain) it is possible to operate the HEMT in the triode region, where the transconductance is higher, and still satisfy  $R_H \gg R_L$ . Another advantage will be that the HEMT will be operated at smaller values of  $V_{DS}$  for which the drain-gate leakage current and the resulting current noise is strongly suppressed (see chapter 6).

We continue here with a passive load, the 510  $\Omega$  resistor  $R_L$ , and bias all HEMTs to have maximum gain, thereby minimizing the equivalent input referred voltage noise and maximizing the SNR.

## 7.4 Transconductance and output impedance

So far we have used AC signals only to study the DC bias settings of the HEMTs and we have learned how to bias the HEMTs to have a certain dissipation and a maximum SNR. In this section we proceed to examine AC performance of the HEMTs. We again apply an oscillating voltage with known amplitude to the gate of the HEMT and measure the voltage on its output. This gives a direct measurement of the AC voltage gain of the HEMT circuit. However, this is not a intrinsic property of the HEMT since the voltage gain also depends on the drain load resistor ( $R_L = 510 \Omega$ , see Fig. 7.1) and the unknown HEMT output impedance. A measurement of the circuit bandwidth allows us to directly determine the transconductance and the output impedance. In the inset of Fig. 7.5 the equivalent circuit of the HEMT (plus load) is sketched for AC signals. The HEMT is a voltage controlled current source with a current of  $\Delta I_D = -g_m \Delta V_{GS}$ . If the HEMT was an ideal current source, its output impedance  $R_H$  would be infinite. In practice it turns out that the HEMT is by far not an ideal current source (for our DC bias settings) and  $R_H$  can be of the same order as our load resistance  $R_L = 510 \Omega$ . The effective impedance  $R_H // R_L$  and the capacitance of

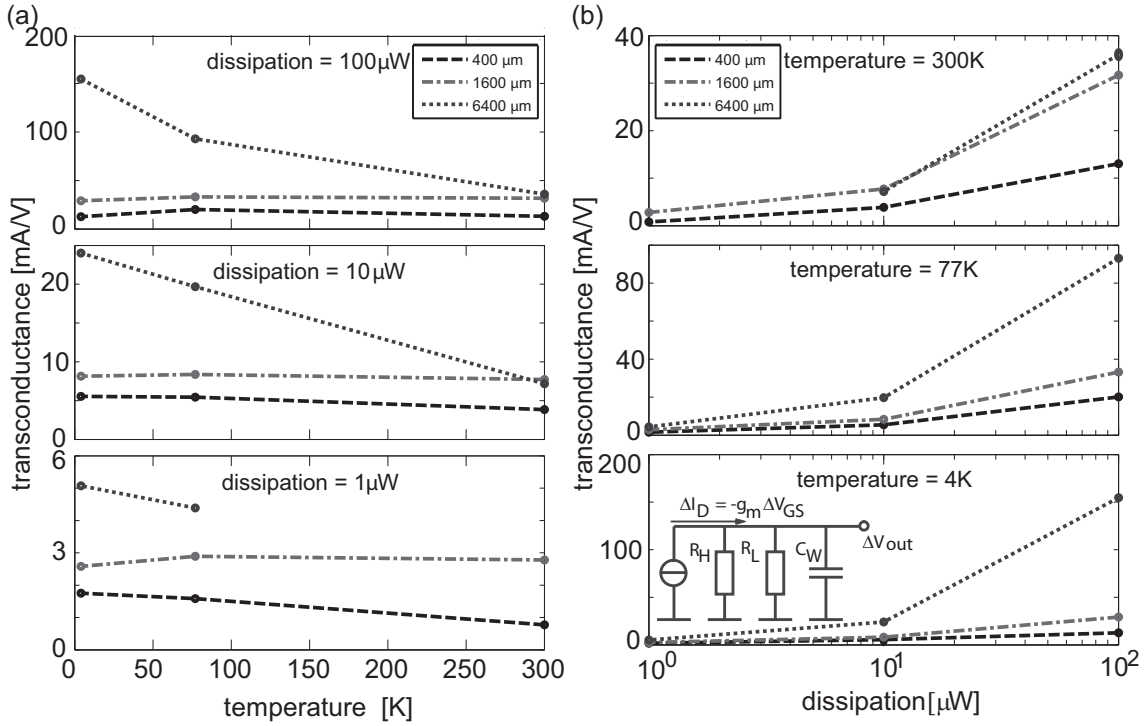


**Figure 7.5:** Transconductance of the three different HEMTs determined at three dissipations and three temperatures. (a) The transconductances are displayed as a function of temperature for different dissipations. (b) The transconductances are displayed as a function dissipation for different temperatures.

the coaxial cable to the RT post-amplifier ( $C_W \approx 100$  pF) form a low-pass filter which determines the bandwidth of the circuit.

Since we know both  $R_L$  and  $C_W$ , a measurement of the bandwidth yields  $R_H$ . Once both  $R_H$  and  $R_L$  are known, the HEMT voltage gain can be translated into the transconductance. The bandwidth of the setup is measured for different HEMTs by a spectrum analyzer (Hewlett Packard 4195A) running in network mode. Results of these measurements are summarized in Fig. 7.5. We see that for all HEMTs the transconductance increases with increasing dissipation. The transconductance of the ATF511P8 (6400  $\mu\text{m}$ ) increases with decreasing temperature but the temperature dependence of the smaller HEMTs is not that clear.

## 7.5 HEMT voltage noise spectra

Up to here we have investigated at which operation point the highest signal and lowest equivalent input noise can be expected considering only the noise at high

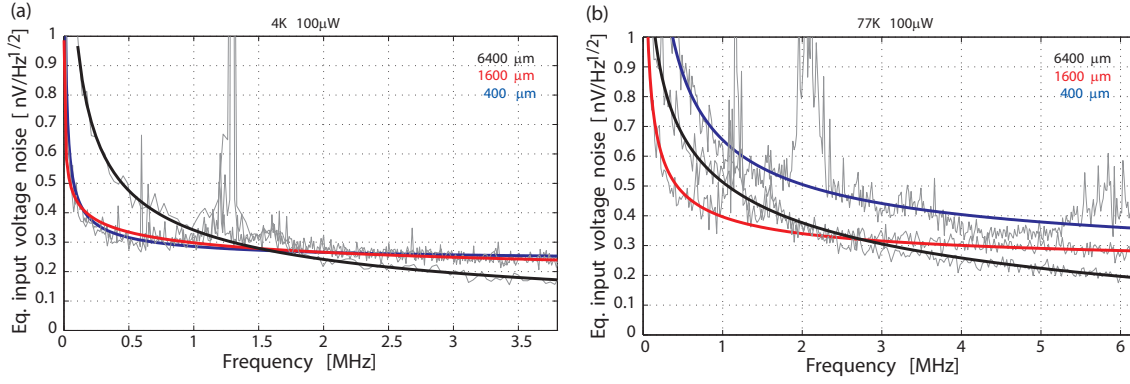


**Figure 7.6:** (a) Equivalent input referred voltage noise spectra of the three HEMTs measured at 4K. For high frequencies, the noise density of the 6400  $\mu\text{m}$  HEMT is significantly lower than the contributions of the 400 and 1600  $\mu\text{m}$  HEMTs. However below 1.5 MHz (our region of interest) the noise density of the 6400  $\mu\text{m}$  HEMT is considerably higher. (b) Equivalent input referred voltage noise spectra of the three HEMTs measured at 77K. Again for high frequencies the largest HEMT has the lowest noise density, but below 2.5 MHz its noise contribution will be higher than the 1600  $\mu\text{m}$  HEMT. The spikes in the spectra are generated by ground loops that were removed at a later stage.

frequencies (1 MHz) where the HEMT noise is approximately frequency independent. However, since our aim is to measure in the full bandwidth from 1 kHz - 1 MHz, we are interested in both high and low frequency noise contributions of the HEMTs and the expected noise needs a more detailed study. We start by examining the noise contributions at high frequencies. For this, noise spectra are measured within the bandwidths determined in section 7.4 using the same spectrum analyzer. After dividing these spectra by the total gain of the circuit, we obtain the equivalent input referred voltage noise of the HEMT. The spectra of the three HEMTs at 4K (77K) are plotted in Fig. 7.6a (b). For the spectra taken at 4K we see that at frequencies higher than 1.5 MHz, the noise density of the 6400  $\mu\text{m}$  HEMT is significantly lower than the contributions of the 400 and 1600  $\mu\text{m}$  HEMTs (Fig. 7.6). However our region of interest is from 1 kHz - 1MHz. In this regime the noise density of the 6400  $\mu\text{m}$  HEMT is considerably higher. At 77K the spectra look somewhat different but again for high frequencies the largest HEMT has the lowest noise density. Below 2.5 MHz we see that its noise contribution is higher than the 1600  $\mu\text{m}$  HEMT. The spikes in the spectra are generated by ground loops that were removed at a later stage.

Since the low frequency (1/f) components of the HEMT noise spectra contribute



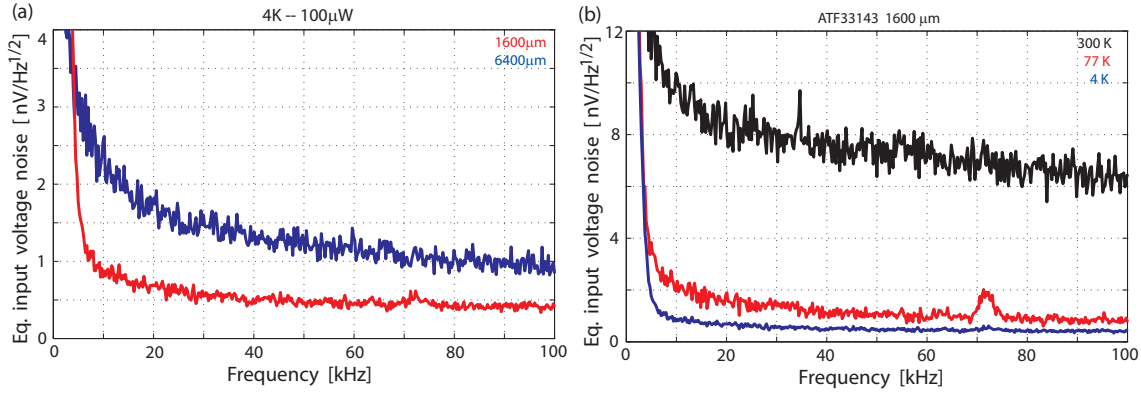


**Figure 7.7:** (a) Spectra for the 1600  $\mu\text{m}$  and the 6400  $\mu\text{m}$  HEMTs at 4K in a frequency range of 1 - 100 kHz. The equivalent input referred voltage noise of the 6400  $\mu\text{m}$  HEMT is much higher than that of the 1600  $\mu\text{m}$  HEMT. (b) Spectra of the 1600  $\mu\text{m}$  HEMT demonstrating the dramatic decrease in noise with decreasing temperature.

considerably to the total integrated noise in a bandwidth from 1 kHz - 1 MHz, an accurate measurement of the spectra for low frequencies is essential. In Fig. 7.7a the 4K spectra are plotted for the 1600  $\mu\text{m}$  and the 6400  $\mu\text{m}$  HEMTs in a frequency range of 1 - 100 kHz. It is clear that the total integrated noise of the 6400  $\mu\text{m}$  HEMT is much higher than that of the 1600  $\mu\text{m}$  HEMT. Figure 7.7b shows that the equivalent input referred voltage noise of the 1600  $\mu\text{m}$  HEMT decreases dramatically with decreasing temperature.

### 7.5.1 Most suitable HEMT

From these spectra we conclude that for an application with a bandwidth from DC to 1 MHz the 6400  $\mu\text{m}$  HEMT has a higher noise contribution than both the 400 and the 1600  $\mu\text{m}$  HEMTs. Based on its high equivalent input noise we exclude the 6400  $\mu\text{m}$  HEMT for our application. Based on their noise characteristics there is not a clear difference between the 400 and the 1600  $\mu\text{m}$  HEMTs. We therefore base our decision on two other parameters: the input capacitance  $C_{in}$  and transconductance  $g_m$  of the HEMTs at 100  $\mu\text{W}$  and 4K. The input capacitance of the ATF33143 (1600  $\mu\text{m}$ ) is 4 times larger than the input capacitance of the ATF35143 (400  $\mu\text{m}$ ). However, we have to compare the HEMT input impedance to the 50 pF wire capacitance which leads us to conclude that the contributions of both HEMTs to the total signal bandwidth are negligible. The remaining criterion is the transconductance. The transconductance of the ATF33143 (1600  $\mu\text{m}$ ), operated at 100  $\mu\text{W}$  at 4K, is 29.2 mA/V. This is more than a factor of 2 higher than the transconductance of the ATF35143 (400  $\mu\text{m}$ ), operated at the

Name	Gate length	$C_{in}$	$g_m$
ATF35143	400 $\mu\text{m}$	0.4 pF	12.7 mA/V
ATF33143	1600 $\mu\text{m}$	1.6 pF	29.2 mA/V

**Table 7.2:** Overview of the essential HEMT properties of the HEMTs with the lowest equivalent input noise in a DC - 1 MHz bandwidth.

same conditions (12.7 mA/V). Using a HEMT with a high transconductance puts less restraints on the specifications of the post-amplification stage. We therefore choose to proceed with the ATF33143 (1600  $\mu\text{m}$ ).

## 7.6 Improvements of the charge detection setup

The rest of this chapter discusses the possible modifications to the setup that increase the SNR for the application we have in mind: high fidelity single-shot read-out of an individual electron spin. This means that we would like to be able to detect steps in the QPC current as short as 1  $\mu\text{s}$  in a trace of approximately 100  $\mu\text{s}$ , preferably in a DC - 1 MHz bandwidth.

### 7.6.1 Signal amplitude

We start with modifications which increase the amplitude of the signal which arrives at the HEMT gate. We assume the step in the QPC current to be a parameter with a fixed amplitude of 400 pA. The amplitude of the corresponding voltage step on the gate of the HEMT depends on the value of the resistor  $R_c$  (see chapter 6). When we assume that the resistance of the QPC is  $R_{QPC} = 25 \text{ k}\Omega$ , the maximum amplitude of this voltage step is  $\sim 5 \text{ }\mu\text{V}$  for  $R_c = 25 \text{ k}\Omega$ . Together with the wire capacitance  $C_w$  the resistor  $R_c$  forms a low-pass filter, which cut-off frequency depends on the choice of the value of  $R_c$ , assuming the wire capacitance  $C_w$  remains  $\sim 50 \text{ pF}$  as in chapter 6. The gain  $G_{RC}$  of this RC network is given by:

$$G_{RC}(f) = \frac{(R_{QPC} // R_c)}{\sqrt{1 + (2\pi f R_c C_w)^2}}. \quad (7.1)$$

In Fig. 7.8a we plot  $G_{RC}$  for  $R_c = 3 \text{ k}\Omega$  (dashed line) and  $25 \text{ k}\Omega$  (solid line). The gain is multiplied by  $\Delta I_{QPC}$  to obtain a measure for the maximum amplitude of the voltage step:  $5 \text{ }\mu\text{V}$  for  $R_c = 25 \text{ k}\Omega$ . It becomes clear from Fig. 7.8a

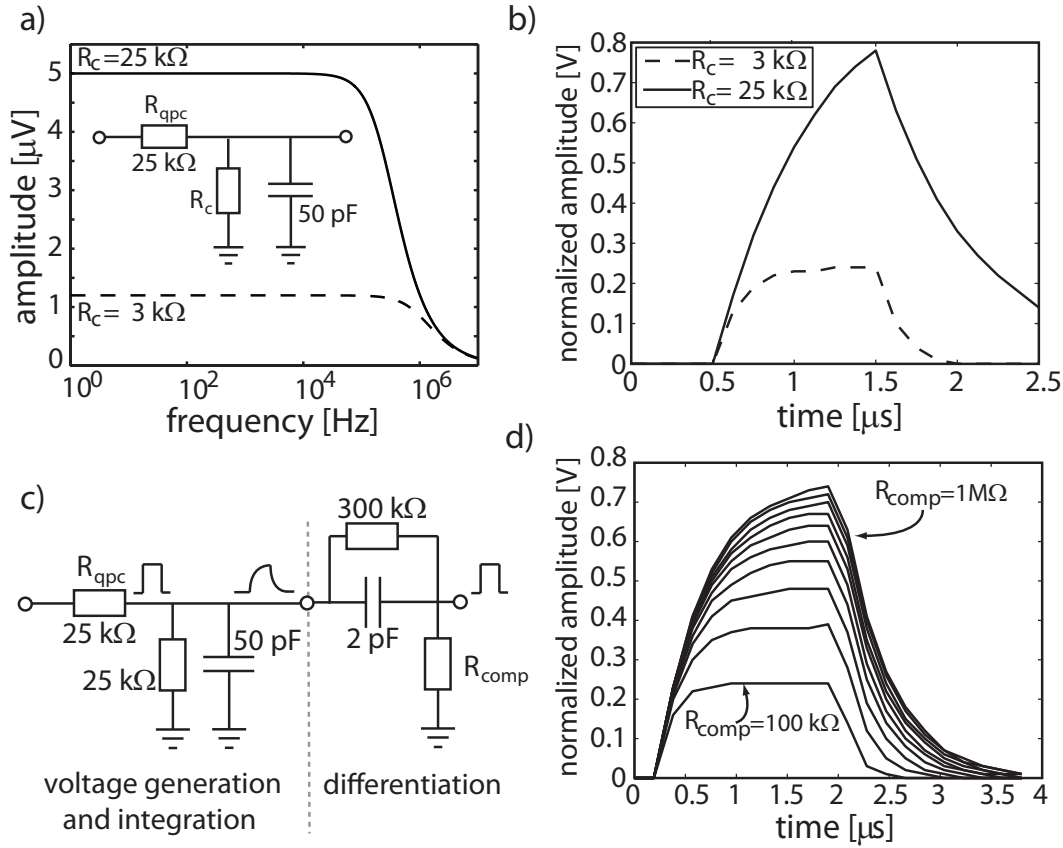


**Figure 7.8:** The influence of the circuit on the pulse shape arriving at the HEMT gate. (a) The gain of the low pass RC-filter (inset) for the two relevant values of  $R_c$ :  $3\text{ k}\Omega$  (dashed line) and  $25\text{ k}\Omega$  (solid line). We see that all amplitudes of the Fourier components in the range from DC - 1 MHz are increased when we replace the  $3\text{ k}\Omega$  by  $25\text{ k}\Omega$ . (b) The distortion of the pulse shape for  $R_c = 3\text{ k}\Omega$  (dashed line) and  $R_c = 25\text{ k}\Omega$  (solid line) for a  $1\text{ }\mu\text{s}$  step at the input. Important to note is that even though the cut-off frequency of the LP-filter with  $R_c = 25\text{ k}\Omega$  is lower, the amplitude at the output rises faster than of the filter using  $R_c = 3\text{ k}\Omega$ . (c) Electrical scheme of a compensating (differentiating) network to restore the pulse shape. This differentiator stage can be implemented after amplification of the signal, even at room temperature. By changing the value of resistor  $R_{\text{comp}}$  we can change the electronic bandwidth and thereby the pulse shape. (d) Simulations of the pulse shape at the output when changing  $R_{\text{comp}}$  from  $1\text{ M}\Omega$  (curve with highest amplitude) to  $100\text{ k}\Omega$  (curve with smallest amplitude) in steps of  $100\text{ k}\Omega$ . For  $R_{\text{comp}} = 100\text{ k}\Omega$ , we retrieve the same pulse shape as when using  $R_c = 3\text{ k}\Omega$  without a compensating network.

that in a bandwidth from DC - 1 MHz all Fourier components will have a larger amplitude for  $R_c = 25\text{ k}\Omega$ . By increasing the value from  $R_c = 3\text{ k}\Omega$  to  $R_c = 25\text{ k}\Omega$ , the amplitude of the signal (at frequencies  $f \ll 1/(2\pi R_c C_w)$ ) increases

by approximately a factor 4. The idea behind this approach is to give more weight to the components at low frequencies, which is exactly the regime where the HEMT has the highest noise contributions (see Fig. 7.9a). The disadvantage of choosing  $R_c = 25 \text{ k}\Omega$  is that the signal bandwidth will be reduced by a factor 4 compared to the situation when  $R_c = 3 \text{ k}\Omega$ ,  $\sim 250 \text{ kHz}$  instead of  $1 \text{ MHz}$ . On first sight this may seem disastrous for the detection of fast pulses. Indeed it will take this circuit 4 times longer for to reach its maximum amplitude. But since this amplitude is also higher than before, it turns out that the amplitude of the output voltage of the RC-network increases faster with  $R_c = 25 \text{ k}\Omega$  than with  $R_c = 3 \text{ k}\Omega$ , independent of the length of the step. This is illustrated in Fig. 7.8b. A potential disadvantage of choosing  $R_c = 25 \text{ k}\Omega$  is that the pulse shape will be distorted since the signal is effectively integrated. When desired, the pulse shape can be restored by adding a differentiating network to the output of the integrating stage. This differentiating network can be used after amplification of the signal, even at RT. An example of such a compensation network is given in Fig. 7.8c. The timescale of the resistor and capacitor in parallel has to match the timescale of the original integrating network (here  $250 \text{ kHz}$ ) and the resistor  $R_{comp}$  is a (RT) knob which determines (i) the low frequency gain and (ii) the cut-off frequency of the high-pass (HP) filter formed with the capacitor. In Fig. 7.8d the influence of resistor  $R_{comp}$  on the pulse shape (and bandwidth) is illustrated. For now, we choose  $R_c$  to be  $25 \text{ k}\Omega$  and proceed with determining the SNR of this setup.

### 7.6.2 Noise contributions

When we replace the  $R_c = 3 \text{ k}\Omega$  by a  $25 \text{ k}\Omega$  resistor we increase the thermal noise generated by the circuitry attached to the gate of the HEMT. The thermal noise of  $R_{QPC} // R_c$  at a temperature of  $T = 50 \text{ mK}$  will be  $\sqrt{4k_B T (R_{QPC} // R_c)} \approx 0.18 \text{ nV}/\sqrt{\text{Hz}}$  which is still smaller than the equivalent voltage noise of the HEMT in the frequency range of interest (see Fig. 7.9a,b). Another source of noise is the shot noise of the QPC. The total shot noise spectral density  $S_I$  can be expressed as

$$S_I = \frac{2e^2}{h} \sum_i \mathcal{N}_i \left[ eV_{qpc} \coth \left( \frac{eV_{qpc}}{2k_B T_e} \right) - 2k_B T_e \right], \quad (7.2)$$

where  $\mathcal{N}_i = T_i (1 - T_i)$  with  $T_i$  the QPC transmission coefficient of mode  $i$ ,  $V_{qpc}$  the bias over the QPC,  $k_B$  the Boltzmann constant and  $T_e$  the electron temperature [5, 6]. We choose to operate the QPC at a conductance of  $e^2/h$  which corresponds to  $T_i = 1/2$ , yielding  $\mathcal{N}_i = 1/4$  and apply a bias over the QPC of  $V_{qpc}$

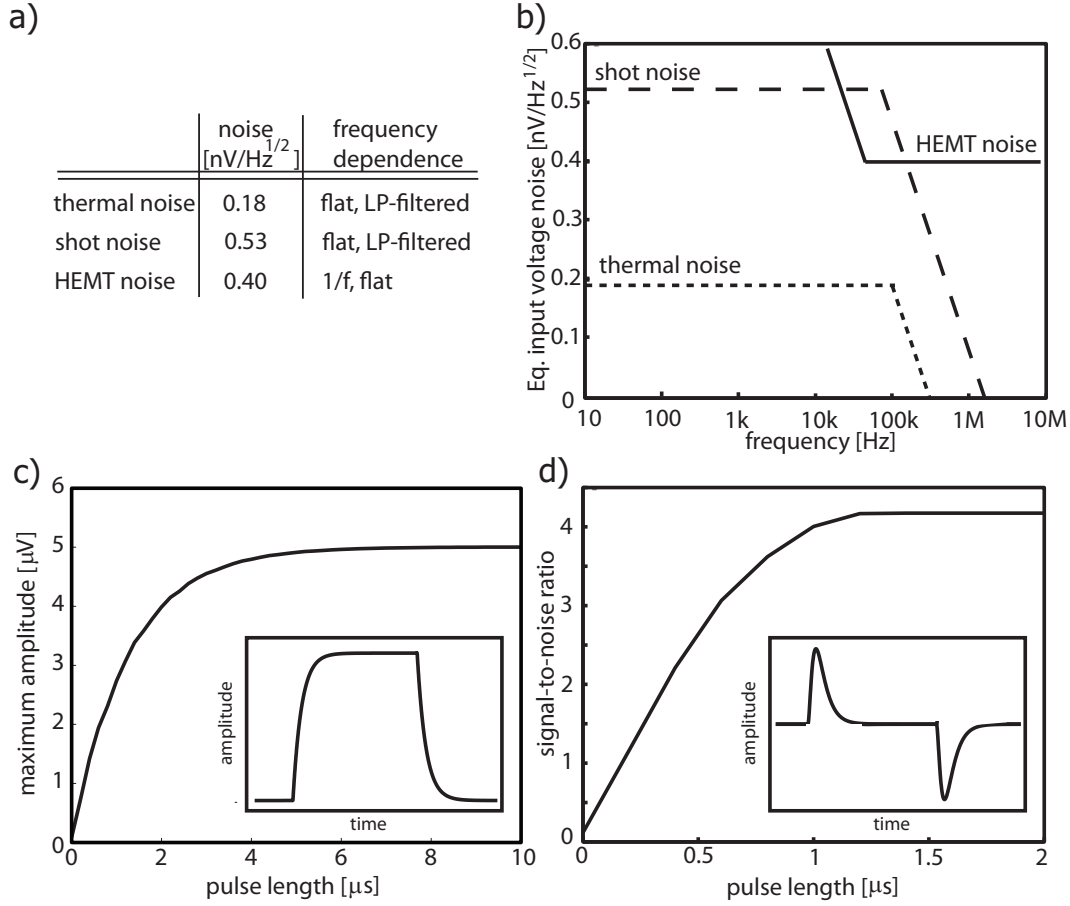


**Figure 7.9:** (a) Summary of the important sources of noise, their values and frequency dependence. (b) Illustrations of the noise spectra for the important sources of noise. Both the thermal noise and the shot noise are LP-filtered before arriving at the HEMT gate. The HEMT has a large  $1/f$  contribution and is flat for high frequencies. (c) Maximum voltage at the HEMT gate as a function of the pulse duration for  $R_c = 25$  k $\Omega$  and  $C_w = 50$  pF. The pulse shape is shown in the inset. (d) SNR determined for the flank detection protocol. The noise has been integrated from 500 kHz to the sampling rate (1 MHz), where the HEMT is the dominant noise source. The pulse shape after (effective) high pass filtering is plotted in the inset. We estimate that in this setup it possible to achieve a sufficiently high SNR to perform fast detection of single electron tunneling events.

$= 600$   $\mu$ V. We estimate a shot noise contribution of  $v_{sn} = \sqrt{S_I(R_{QPC}/R_c)} = 0.53$  nV/ $\sqrt{\text{Hz}}$ . We have schematically depicted these sources of noise in Fig. 7.9b. We see that in the frequency interval from  $\sim 50$  kHz to  $\sim 200$  kHz the shot noise is the dominant source of noise. In the range of 500 kHz to 1 MHz, both the shot noise and the thermal noise contribute less than 10% to the total noise and the

HEMT noise is dominant.

### 7.6.3 Signal-to-noise ratio

To determine a SNR it is important to know how the steps in the current will be detected. In a noisy environment which has a pronounced  $1/f$  spectrum it is very hard to use an amplitude threshold. This is because low frequency noise contributions will distort the baseline of a time trace, especially for long traces. A better alternative to detect steps in the current is to detect the flanks of these steps (see chapter 6). In the simplest flank detection scheme one examines segments of a time trace with a length of (a few times) the rise time of the circuit and determines whether an increase of the signal is due to an actual step in the signal or due to noise. When the first segment has been analyzed we go on to the next, etcetera. This can be thought of as effectively high-pass filtering the signal with a cut-off frequency equal to  $1/(\text{rise time})$ .

We assume a flank detection will be used to detect the steps in the signal and we calculate the SNR below. Since the signal from the QPC is low-pass filtered the amplitude of the signal at the gate of the HEMT depends on the length of the step. In Fig. 7.9c the residual amplitude of a  $5 \mu\text{V}$  step after the low-pass filter as a function of the pulse length is plotted. We see that the amplitude of steps shorter than  $\sim 6 \mu\text{s}$  is drastically reduced. When we look at the noise of the setup we see that for frequencies higher than 500 kHz, both the shot noise and the thermal noise contribute less than 10% to the total noise and we consider the HEMT as the dominant noise source. We choose the length of the 'compare intervals' to be of the order of  $1/500 \text{ kHz}$  and a sampling rate of 1 MS/s and therefore have to integrate the HEMT noise from 500 kHz to 1 MHz. Since a flank detecting scheme is in essence a threshold detection scheme for the high-pass filtered signal, we have to compare the noise to the amplitude of the high-pass filtered step. Such a pulse shape is illustrated in the inset of Fig. 7.9d. Comparing the integrated noise (rms) to the resulting amplitude of the pulse provides a measure for the SNR. This is plotted in Fig. 7.9d as a function of the pulse length. We see that for pulses longer than  $1.5 \mu\text{s}$  we obtain a SNR of approximately 4. This is almost a factor of 2 better than the simulations for  $R_c = 3 \text{ k}\Omega$ , used in the chapter 6.

## 7.7 Conclusions

We have characterized three different HEMTs at three different temperatures and dissipations. We have determined that the optimal bias point of these HEMTs

is the operation point where the AC voltage gain is maximal since at this setting the equivalent input referred voltage noise of the HEMT is also minimal. Based on the equivalent input referred voltage noise, the input capacitance and the transconductance we conclude that the ATF33143 (1600  $\mu\text{m}$ ) HEMT is the most suitable HEMT for our application. Finally we propose modifications to the setup which will increase the SNR for the detection of steps in the QPC current in an experiment aimed at high fidelity single-shot read-out of an individual electron spin.

This work has been done in collaboration with R. P. Rewat, R. N. Schouten and L. M. K. Vandersypen.

We thank P.C. de Groot, C.J.P.M. Harmans, K.C. Nowack and especially G.A. Steele for help and discussions.

## References

- [1] I. T. Vink, T. Nooitgedagt, R. N. Schouten, W. Wegscheider and L. M. K. Vandersypen, *Appl. Phys. Lett.* **91**, 123512 (2007).
- [2] J. M. Elzerman, R. Hanson, L. H. W. van Beveren, B. Witkamp, L. M. K. Vandersypen, and L. P. Kouwenhoven, *Nature*, **430**, 431 (2004).
- [3] L.-X. Zhang, J. P. Leburton, R. Hanson and L. P. Kouwenhoven, *Appl. Phys. Lett.* **85**, 2628 (2004).
- [4] S. Amasha, K. MacLean, Iuliana P. Radu, D. M. Zumbhl, M. A. Kastner, M. P. Hanson and A. C. Gossard, *Phys. Rev. Lett.* **100**, 046803 (2008).
- [5] Ya. M. Blanter and M. Büttiker, *Phys. Rep.* **336**, 1 (2000).
- [6] L. DiCarlo, Y. Zhang, D. T. McClure, D. J. Reilly, C. M. Marcus, L. N. Pfeiffer, K. W. West, *Phys. Rev. Lett.* **97**, 036810 (2006).





## Chapter 8

# Driven coherent oscillations of a single electron spin in a quantum dot

The ability to control the quantum state of a single electron spin in a quantum dot is at the heart of recent developments towards a scalable spin-based quantum computer. In combination with the recently demonstrated exchange gate between two neighboring spins, driven coherent single spin rotations would permit universal quantum operations. Here, we report the experimental realization of single electron spin rotations in a double quantum dot. First, we apply a continuous-wave oscillating magnetic field, generated on-chip, and observe electron spin resonance in spin-dependent transport measurements through the two dots. Next, we coherently control the quantum state of the electron spin by applying short bursts of the oscillating magnetic field and observe about eight oscillations of the spin state (so-called Rabi oscillations) during a microsecond burst. These results demonstrate the feasibility of operating single-electron spins in a quantum dot as quantum bits.

---

This chapter has been published in Nature **442**, 766-771 (2006).

## 8.1 Introduction

The use of quantum mechanical superposition states and entanglement in a computer can theoretically solve important mathematical and physical problems much faster than classical computers [1, 2]. However, the realization of such a quantum computer represents a formidable challenge, because it requires fast and precise control of fragile quantum states. The prospects for accurate quantum control in a scalable system are thus being explored in a rich variety of physical systems, ranging from nuclear magnetic resonance and ion traps to superconducting devices [3].

Electron spin states were identified early on as an attractive realization of a quantum bit [4], because they are relatively robust against decoherence (uncontrolled interactions with the environment). Advances in the field of semiconductor quantum dots have made this system very fruitful as a host for the electron spin. Since Loss and DiVincenzo's proposal [5] on electron spin qubits in quantum dots in 1998, many of the elements necessary for quantum computation have been realized experimentally. It is now routine to isolate with certainty a single electron in each of two coupled quantum dots [6, 7, 34, 9]. The spin of this electron can be reliably initialized to the ground state, spin-up, via optical pumping [10] or by thermal equilibration at sufficiently low temperatures and strong static magnetic fields (for example,  $T = 100$  mK and  $B_{\text{ext}} = 1$  T). The spin states are also very long-lived, with relaxation times of the order of milliseconds [40, 12, 13]. Furthermore, a lower bound on the spin coherence time exceeding 1 s was established, using spin-echo techniques on a two-electron system [14]. These long relaxation and coherence times are possible in part because the magnetic moment of a single electron spin is so weak. On the other hand, this property makes read-out and manipulation of single spins particularly challenging. By combining spin-to-charge conversion with real-time single-charge detection [15, 16, 17], it has nevertheless been possible to accomplish single-shot read-out of spin states in a quantum dot [13, 18].

The next major achievement was the observation of the coherent exchange of two electron spins in a double dot system, controlled by fast electrical switching of the tunnel coupling between the two quantum dots [14]. Finally, free evolution of a single electron spin about a static magnetic field (Larmor precession) has been observed, via optical pump-probe experiments [19, 20]. The only missing ingredient for universal quantum computation with spins in dots remained the demonstration of driven coherent spin rotations (Rabi oscillations) of a single electron spin.

The most commonly used technique for inducing spin flips is electron spin

resonance (ESR) [21]. ESR is the physical process whereby electron spins are rotated by an oscillating magnetic field  $B_{\text{ac}}$  (with frequency  $f_{\text{ac}}$ ) that is resonant with the spin precession frequency in an external magnetic field  $B_{\text{ext}}$ , oriented perpendicularly to  $B_{\text{ac}}$  ( $hf_{\text{ac}} = g\mu_{\text{B}}B_{\text{ext}}$ , with  $\mu_{\text{B}}$  the Bohr magneton and  $g$  the electron spin  $g$ -factor). Magnetic resonance of a single electron spin in a solid has been reported in a few specific cases [22, 23, 24], but has never been realized in semiconductor quantum dots. Detecting ESR in a single quantum dot is conceptually simple [25], but experimentally difficult to realize, as it requires a strong, high-frequency magnetic field at low temperature, while accompanying alternating electric fields must be minimized. Alternative schemes for driven rotations of a spin in a dot have been proposed, based on optical excitation [26] or electrical control [27, 28, 29] but this is perhaps even more challenging and has not been accomplished either.

Here, we demonstrate the ability to control the spin state of a single electron confined in a double quantum dot via ESR. In a double dot system, spin-flips can be detected through the transition of an electron from one dot to the other [35, 31] rather than between a dot and a reservoir, as would be the case for a single dot. This has the advantage that there is no need for the electron spin Zeeman splitting (used in a single dot for spin-selective tunneling) to exceed the temperature of the electron reservoirs ( $\sim 100$  mK; the phonon temperature was  $\sim 40$  mK). The experiment can thus be performed at a smaller static magnetic field, and consequently with lower, technically less demanding, excitation frequencies. Furthermore, by applying a large bias voltage across the double dot, the spin detection can be made much less sensitive to electric fields than is possible in the single-dot case (electric fields can cause photon-assisted tunneling; see Section 8.9.2). Finally, in a double dot, single-spin operations can in future experiments be combined with two-qubit operations to realize universal quantum gates [5], and with spin read-out to demonstrate entanglement [32, 33].

## 8.2 Device and ESR detection concept

Two coupled semiconductor quantum dots are defined by surface gates (Fig. 8.1a) on top of a two-dimensional electron gas. By applying the appropriate negative voltages to the gates the dots can be tuned to the few-electron regime [34]. The oscillating magnetic field that drives the spin transitions is generated by applying a radio-frequency (RF) signal to an on-chip coplanar stripline (CPS) which is terminated in a narrow wire, positioned near the dots and separated from the surface gates by a 100-nm-thick dielectric (Fig. 8.1b). The current through the wire generates an oscillating magnetic field  $B_{\text{ac}}$  at the dots, perpendicular to

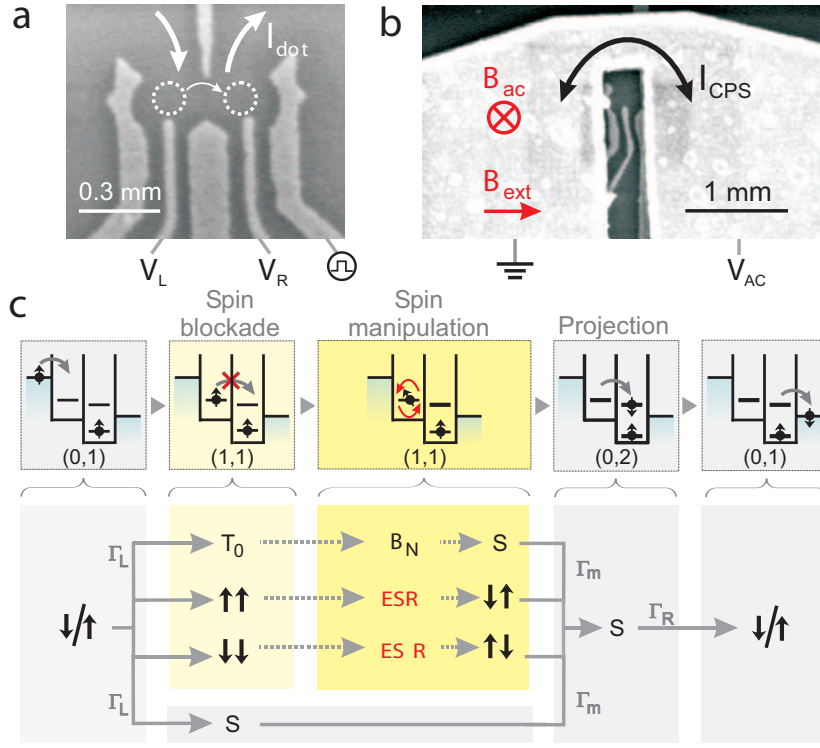


**Figure 8.1:** Device and ESR detection scheme. (a) Scanning electron microscope (SEM) image of a device with the same gate pattern as used in the experiment. The Ti/Au gates are deposited on top of a GaAs/AlGaAs heterostructure containing a two-dimensional electron gas 90 nm below the surface. White arrows indicate current flow through the two coupled dots (dotted circles). The right side gate is fitted with a homemade bias-tee (rise time 150 ps) to allow fast pulsing of the dot levels. (b) SEM image of a device similar to the one used in the experiment. The termination of the coplanar stripline is visible on top of the gates. The gold stripline has a thickness of 400 nm and is designed to have a  $50 \, \Omega$  characteristic impedance,  $Z_0$ , up to the shorted termination. It is separated from the gate electrodes by a 100-nm-thick dielectric (Calixerene). (c) Diagrams illustrating the transport cycle in the spin blockade regime. This cycle can be described via the occupations  $(m, n)$  of the left and right dots as  $(0, 1) \rightarrow (1, 1) \rightarrow (0, 2) \rightarrow (0, 1)$ . When an electron enters the left dot (with rate  $\Gamma_L$ ) starting from  $(0, 1)$ , the two-electron system that is formed can be either a singlet  $S(1, 1)$  or a triplet  $T(1, 1)$ . From  $S(1, 1)$ , further current flow is possible via a transition to  $S(0, 2)$  (with rate  $\Gamma_m$ ). When the system is in  $T(1, 1)$ , current is blocked unless this state is coupled to  $S(1, 1)$ . For  $T_0$ , this coupling is provided by the inhomogeneous nuclear field  $B_N$ . For  $T_+$  or  $T_-$ , ESR causes a transition to  $\uparrow\downarrow$  or  $\downarrow\uparrow$ , which contains a  $S(1, 1)$  component and a  $T_0$  component (which is in turn coupled to  $S(1, 1)$  by the nuclear field).

the static external field  $B_{\text{ext}}$  and slightly stronger in the left dot than in the right dot. To detect the ESR-induced spin rotations, we use electrical transport measurements through the two dots in series in the spin blockade regime where current flow depends on the relative spin state of the electrons in the two dots [35, 36]. In brief, the device is operated so that current is blocked owing to spin blockade, but this blockade is lifted if the ESR condition ( $\hbar f_{\text{ac}} = g\mu_B B_{\text{ext}}$ ) is

satisfied.

This spin blockade regime is accessed by tuning the gate voltages such that one electron always resides in the right dot, and a second electron can tunnel from the left reservoir to the left dot (Fig. 8.1c and Section 3.2.1). If this electron forms a double-dot singlet state with the electron in the right dot ( $S = \uparrow\downarrow - \downarrow\uparrow$ ; normalization omitted for brevity), it is possible for the left electron to move to the right dot, and then to the right lead (leaving behind an electron in the right dot with spin  $\uparrow$  or spin  $\downarrow$ ), since the right dot singlet state is energetically accessible. If, however, the two electrons form a double-dot triplet state, the left electron cannot move to the right dot because the right dot's triplet state is much higher in energy. The electron also cannot move back to the lead and therefore further current flow is blocked as soon as any of the (double-dot) triplet states is formed.

### 8.3 Role of the nuclear spin bath for ESR detection

In fact, the situation is more complex, because each of the two spins experiences a randomly oriented and fluctuating effective nuclear field of  $\sim 1\text{--}3$  mT [37, 38]. This nuclear field,  $B_N$ , arises from the hyperfine interaction of the electron spins with the Ga and As nuclear spins in the host material, and is in general different in the two dots, with a difference of  $\delta B_N$ . At zero external field and for sufficiently small double dot singlet-triplet splitting (see chapter 9 and Fig. 8.9d), the inhomogeneous component of the nuclear field causes all three triplet states ( $T_0$ ,  $T_+$  and  $T_-$ ) to be admixed with the singlet  $S$  (for example,  $T_0 = \uparrow\downarrow + \downarrow\uparrow$  evolves into  $S = \uparrow\downarrow - \downarrow\uparrow$  due to  $\Delta B_{N,z}$ , and  $T_+ = \uparrow\uparrow$  and  $T_- = \downarrow\downarrow$  evolve into  $S$  owing to  $B_{N,x,y}$ ). As a result, spin blockade is lifted. For  $B_{\text{ext}} \gg \sqrt{\langle B_N^2 \rangle}$ , however, the  $T_+$  and  $T_-$  states split off in energy, which makes hyperfine-induced admixing between  $T_{\pm}$  and  $S$  ineffective ( $T_0$  and  $S$  remain admixed; see Fig. 8.2a). Here spin blockade does occur, whenever a state with parallel spins ( $\uparrow\uparrow$  or  $\downarrow\downarrow$ ) becomes occupied.

ESR is then detected as follows (see Fig. 8.1c). An oscillating magnetic field resonant with the Zeeman splitting can flip the spin in the left or the right dot. Starting from  $\uparrow\uparrow$  or  $\downarrow\downarrow$ , the spin state then changes to  $\uparrow\downarrow$  (or  $\downarrow\uparrow$ ). If both spins are flipped, transitions occur between  $\uparrow\uparrow$  and  $\downarrow\downarrow$  via the intermediate state  $\frac{\uparrow\pm\downarrow}{\sqrt{2}} \frac{\downarrow\pm\uparrow}{\sqrt{2}}$ . In both cases, states with anti-parallel spins ( $S_z = 0$ ) are created owing to ESR. Expressed in the singlet-triplet measurement basis,  $\uparrow\downarrow$  or  $\downarrow\uparrow$  is a superposition of the  $T_0$  and  $S$  state ( $\uparrow\downarrow = T_0 + S$ ). For the singlet component of this state, the left

electron can transition immediately to the right dot and from there to the right lead. The  $T_0$  component first evolves into a singlet due to the nuclear field and then the left electron can move to the right dot as well. Thus whenever the spins are anti-parallel, one electron charge moves through the dots. If such transitions from parallel to anti-parallel spins are induced repeatedly at a sufficiently high rate, a measurable current flows through the two dots.

## 8.4 ESR spectroscopy

The resonant ESR response is clearly observed in the transport measurements as a function of magnetic field (Figs. 8.2a,b and 8.9), where satellite peaks develop at the resonant field  $B_{\text{ext}} = \pm \hbar f_{\text{ac}} / g \mu_B$  when the RF source is turned on (the zero-field peak arises from the inhomogeneous nuclear field, which admixes all the triplets with the singlet (see chapter 9 and refs [38, 39]). The key signature of ESR is the linear dependence of the satellite peak location on the RF frequency, which is clearly seen in the data of Fig. 8.2c, where the RF frequency is varied from 10 to 750 MHz. From a linear fit through the top of the peaks we obtain a  $g$ -factor with modulus  $0.35 \pm 0.01$ , which lies within the range of reported values for confined electron spins in GaAs quantum dots [40, 41, 42, 43]. We also verified explicitly that the resonance we observe is magnetic in origin and not caused by the electric field that the CPS generates as well; negligible response was observed when RF power is applied to the right side gate, generating mostly a RF electric field (see Fig. 8.2d).

The amplitude of the peaks in Fig. 8.2b increases linearly with RF power ( $\sim B_{\text{ac}}^2$ ) before saturation occurs, as predicted [25] (Fig. 8.2b, inset). The ESR satellite peak is expected to be broadened by either the excitation amplitude  $B_{\text{ac}}$  or incoherent processes, like cotunneling, inelastic transitions (to the  $S(0,2)$  state) or the statistical fluctuations in the nuclear field, whichever of the four has the largest contribution. No dependence of the width on RF power was found within the experimentally accessible range ( $B_{\text{ac}} < 2$  mT). Furthermore, we suspect that the broadening is not dominated by cotunneling or inelastic transitions because the corresponding rates are smaller than the observed broadening (see Fig. 8.9).

---

A very faint line is still present at the same position as the ESR response in Fig. 8.2c. This response could be due to the small magnetic field generated by the current in the gate, which is capacitively coupled to its environment. It could also be due to the coupling of the electric field to the electron spin, through Rashba or Dresselhaus spin-orbit interaction [28]. A final possibility is that spins are flipped when the electron wave function is moved back-and-forth in the inhomogeneous nuclear field [29]. In any case, it is clear that in our experiment, all these mechanisms are much less efficient than magnetic excitation via the CPS.

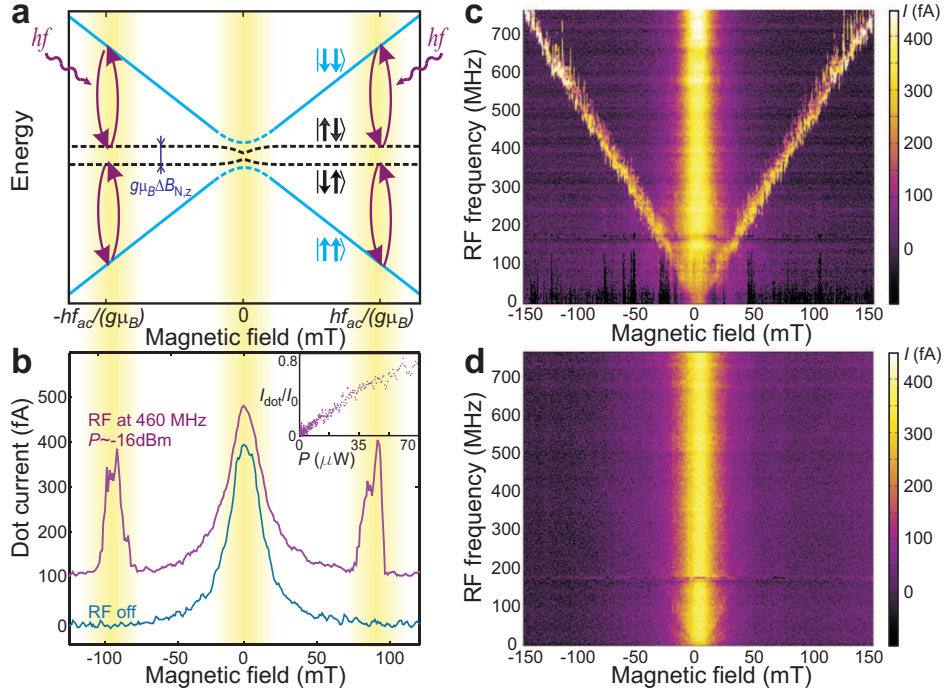


**Figure 8.2:** ESR spin state spectroscopy. (a) Energy diagram showing the relevant eigenstates of two electron spins in a double-dot, subject to an external magnetic field and nuclear fields. Because  $B_{N,z}$  is in general different in the two dots, the energy for  $\uparrow\downarrow$  and  $\downarrow\uparrow$  is different. ESR turns the spin states  $\uparrow\uparrow$  and  $\downarrow\downarrow$  into  $\uparrow\downarrow$  or  $\downarrow\uparrow$ , depending on the nuclear fields in the two dots. The yellow bands denote the ranges in  $B_{\text{ext}}$  where spin blockade is lifted (by the nuclear field or ESR) and current will flow through the dots. (b) Current measured through the double-dot in the spin blockade regime, with (red trace, offset by 100 fA for clarity) and without (blue trace) a RF magnetic field. Satellite peaks appear as the external magnetic field is swept through the spin resonance condition. Each measurement point is averaged for one second, and is therefore expected to represent an average response over many nuclear configurations. The RF power  $P$  applied to the CPS is estimated from the power applied to the coax line and the attenuation in the lines. Inset, satellite peak height versus RF power ( $f = 408$  MHz,  $B_{\text{ext}} = 70$  mT, taken at slightly different gate voltage settings). The current is normalized to the current at  $B_{\text{ext}} = 0$  ( $=I_0$ ). Unwanted electric field effects are reduced by applying a compensating signal to the right side gate with opposite phase as the signal on the stripline (see section 8.9.2). This allowed us to obtain this curve up to relatively high RF powers. (c) Current through the dots when sweeping the RF frequency and stepping the magnetic field. The ESR satellite peak is already visible at a small magnetic field of 20 mT and RF excitation of 100 MHz, and its location evolves linearly in field when increasing the frequency. For higher frequencies the satellite peak is broadened asymmetrically for certain sweeps, visible as vertical stripes. This broadening is time dependent, hysteretic in sweep direction, and changes with the dot level alignment. The horizontal line at 180 MHz is due to a resonance in the transmission line inside the dilution refrigerator. (d) Similar data as in (c), but now with the RF signal applied to the right side gate instead of to the ESR stripline. The amplitude of the RF signal (-50 dBm at the gate) was chosen such that the electric field is equally strong as in the ESR measurements of (c) (determined from the measured PAT rate).

The observed ESR peaks are steeper on the flanks and broader than expected from the nuclear field fluctuations. In many cases, the peak width and position

are even hysteretic in the sweep direction, suggesting that the resonance condition is shifted during the field sweep. We speculate that dynamic nuclear polarization due to feedback of the electron transport on the nuclear spins plays a central part here [39, 44, 45, 46].

## 8.5 Coherent Rabi oscillations

Following the observation of magnetically induced spin flips, we next test whether we can also coherently rotate the spin by applying RF bursts with variable length. In contrast to the continuous-wave experiment, where detection and spin rotation occur at the same time, we pulse the system into Coulomb blockade during the spin manipulation. This eliminates decoherence induced by tunnel events from the left to the right dot during the spin rotations. The experiment consists of three stages (Fig. 8.3): initialization through spin blockade in a statistical mixture of  $\uparrow\uparrow$  and  $\downarrow\downarrow$ , manipulation by a RF burst in Coulomb blockade, and detection by pulsing back for projection (onto  $S(0,2)$ ) and tunneling to the lead. When one of the electrons is rotated over  $(2n + 1)\pi$  (with integer  $n$ ), the two-electron state evolves to  $\uparrow\downarrow$  (or  $\downarrow\uparrow$ ), giving a maximum contribution to the current (as before, when the two spins are anti-parallel, one electron charge moves through the dots). However, no electron flow is expected after rotations of  $2n\pi$ , where one would find two parallel spins in the two dots after the RF burst.

We observe that the dot current oscillates periodically with the RF burst

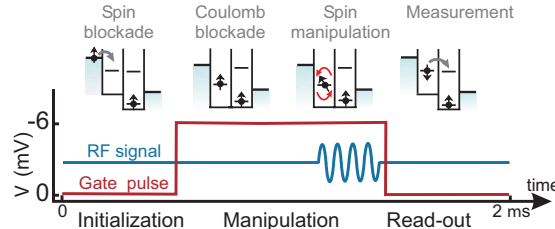


**Figure 8.3:** The control cycle for coherent manipulation of the electron spin. During the 'initialization' stage the double-dot is tuned in the spin blockade regime. Electrons will move from left to right until the system is blocked with two parallel spins (either  $\uparrow\uparrow$  or  $\downarrow\downarrow$ ; in the figure only the  $\uparrow\uparrow$  case is shown). For the 'manipulation' stage, the right dot potential is pulsed up so none of the levels in the right dot are accessible (Coulomb blockade), and a RF burst with a variable duration is applied. 'Read-out' of the spin state at the end of the manipulation stage is done by pulsing the right dot potential back; electron tunneling to the right lead will then take place only if the spins were anti-parallel. The duration of the read-out and initialization stages combined was  $1 \mu s$ , long enough ( $1 \mu s \gg 1/\Gamma_L, 1/\Gamma_M, 1/\Gamma_R$ ) to have parallel spins in the dots at the end of the initialization stage with near certainty (this is checked by signal saturation when the pulse duration is prolonged). The duration of the manipulation stage is also held fixed at  $1 s$  to keep the number of pulses per second constant. The RF burst is applied just before the read-out stage starts.



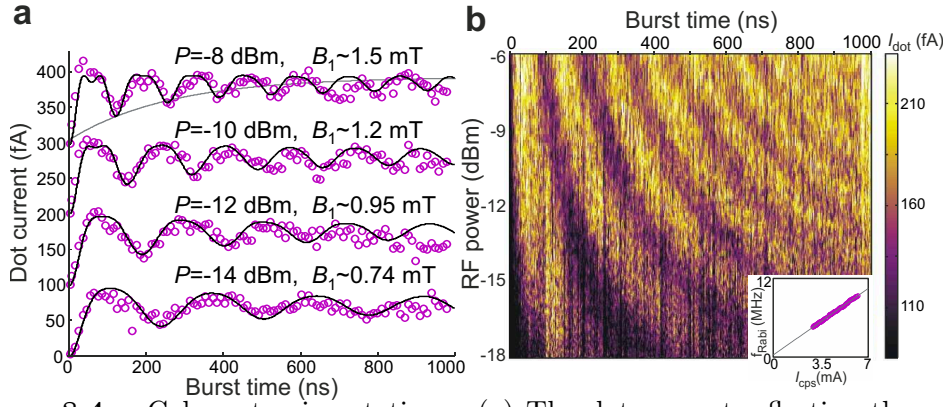


**Figure 8.4:** Coherent spin rotations. (a) The dot current-reflecting the spin state at the end of the RF burst-oscillates as a function of RF burst length (curves offset by 100 fA for clarity). The frequency of  $B_{ac}$  is set at the spin resonance frequency of 200 MHz ( $B_{ext} = 41$  mT). The period of the oscillation increases and is more strongly damped for decreasing RF power. The RF power  $P$  applied to the CPS is estimated from the power applied to the coax line and the attenuation in the lines and RF switch. From  $P$ , the stripline current is calculated via the relation  $P = \frac{1}{2}(\frac{I_{CPS}}{2})^2 Z_0$  assuming perfect reflection of the RF wave at the short. Each measurement point is averaged over 15 s. We correct for a current offset which is measured with the RF frequency off-resonance (280 MHz). The solid lines are obtained from numerical computation of the time evolution, as discussed in the text. The grey line corresponds to an exponentially damped envelope. (b) The oscillating dot current (represented in colorscale) is displayed over a wide range of RF powers (the sweep axis) and burst durations. The dependence of the Rabi frequency  $f_{Rabi}$  on RF power is shown in the inset.  $f_{Rabi}$  is extracted from a sinusoidal fit with the current oscillations from 10 to 500 ns for RF powers ranging from -12.5 dBm up to -6 dBm.

length (Fig. 8.4). This oscillation indicates that we performed driven, coherent electron spin rotations, or Rabi oscillations. A key characteristic of the Rabi process is a linear dependence of the Rabi frequency on the RF burst amplitude,  $B_{ac}$  ( $f_{Rabi} = g\mu_B B_1/h$  with  $B_1 = B_{ac}/2$  due to the rotating wave approximation). We verify this by extracting the Rabi frequency from a fit of the current oscillations of Fig. 8.4b with a sinusoid, which gives the expected linear behavior (Fig. 8.4b, inset). From the fit we obtain  $B_{ac} = 0.59$  mT for a stripline current  $I_{CPS}$  of  $\sim 1$  mA, which agrees well with predictions from numerical finite element simulations. The maximum  $B_1$  we could reach in the experiment before electric field effects hindered the measurement was 1.9 mT, corresponding to  $\pi/2$  rotations of only 27 ns (that is, a Rabi period of 108 ns, see Fig. 8.4b). If the accompanying electric fields from the stripline excitation could be reduced in future experiments (for example, by improving the impedance matching from coax to CPS), considerably faster Rabi flopping should be attainable.

The oscillations in Fig. 8.4b remain visible throughout the entire measurement range, up to 1  $\mu$ s. This is striking, because the Rabi period of  $\sim 100$  ns is much longer than the time-averaged coherence time  $T_2^*$  of 10-20 ns (refs [14, 19, 37, 38])

caused by the nuclear field fluctuations. The slow damping of the oscillations is only possible because the nuclear field fluctuates very slowly compared to the timescale of spin rotations and because other mechanisms, such as the spin-orbit interaction, disturb the electron spin coherence only on even longer timescales [13, 47, 48]. We also note that the decay is not exponential (grey line in Fig. 8.4a), which is related to the fact that the correlation time of the nuclear bath is longer than the Rabi period [49, 50].

## 8.6 Theoretical model

To understand better the amplitudes and decay times of the oscillations, we model the time evolution of the spins throughout the burst duration. The model uses a Hamiltonian that includes the Zeeman splitting for the two spins and the RF field, which we take to be of equal amplitude in both dots ( $\mathbf{S}_L$  and  $\mathbf{S}_R$  refer to the electron spins in the left and right dot respectively):

$$H = g\mu_B(\mathbf{B}_{\text{ext}} + \mathbf{B}_{L,N}) \cdot \mathbf{S}_L + g\mu_B(\mathbf{B}_{\text{ext}} + \mathbf{B}_{R,N}) \cdot \mathbf{S}_R + g\mu_B \cos(\omega t) \mathbf{B}_{\text{ac}} \cdot (\mathbf{S}_L + \mathbf{S}_R)$$

where  $\mathbf{B}_{L,N}$  and  $\mathbf{B}_{R,N}$  correspond to a single frozen configuration of the nuclear field in the left and right dot. This is justified because the electron spin dynamics is much faster than the dynamics of the nuclear system. From the resulting time evolution operator and assuming that the initial state is a statistical mixture of  $\uparrow\uparrow$  and  $\downarrow\downarrow$ , we can numerically obtain the probability for having anti-parallel spins after the RF burst. This is also the probability that the left electron tunnels to the right dot during the read-out stage.

In the current measurements of Fig. 8.4a, each data point is averaged over 15 s, which presumably represents an average over many nuclear configurations. We include this averaging over different nuclear configurations in the model by taking 2,000 samples from a Gaussian distribution of nuclear fields (with standard deviation  $\sigma = \sqrt{\langle B_N^2 \rangle}$ ), and computing the probability that an electron tunnels out after the RF burst. When the electron tunnels, one or more additional electrons, say  $m$ , may subsequently tunnel through before  $\uparrow\uparrow$  or  $\downarrow\downarrow$  is formed and the current is blocked again. Taking  $m$  and  $\sigma$  as fitting parameters, we find good agreement with the data for  $m = 1.5$  and  $\sigma = 2.2$  mT (solid black lines in Fig. 8.4a). This value for  $\sigma$  is comparable to that found in refs [37, 38]. The value found for  $m$  is different from what we would expect from a simple picture where all four spin states are formed with equal probability during the initialization stage, which would give  $m = 1$ . We do not understand this discrepancy, but it could be due to different tunnel rates for  $\uparrow$  and  $\downarrow$  or more subtle details in the transport cycle that we have neglected in the model.

## 8.7 Time evolution of the spin states during RF bursts

We now discuss in more detail the time evolution of the two spins during a RF burst. The resonance condition in each dot depends on the effective nuclear field, which needs to be added vectorially to  $B_{\text{ext}}$ . Through their continuous reorientation, the nuclear spins will bring the respective electron spins in the two dots on and off resonance as time progresses. When a RF burst is applied to two spins initially in  $|\uparrow\uparrow\rangle$ , and is on-resonance with the right spin only, the spins evolve as:

$$|\uparrow\rangle|\uparrow\rangle \rightarrow |\uparrow\rangle \frac{|\uparrow\rangle + |\downarrow\rangle}{\sqrt{2}} \rightarrow |\downarrow\rangle|\uparrow\rangle \rightarrow \frac{|\uparrow\rangle - |\downarrow\rangle}{\sqrt{2}} \rightarrow |\uparrow\rangle|\uparrow\rangle$$

When the RF burst is on-resonance with both spins, the time evolution is:

$$|\uparrow\rangle|\uparrow\rangle \rightarrow \frac{|\uparrow\rangle + |\downarrow\rangle}{\sqrt{2}} \frac{|\uparrow\rangle + |\downarrow\rangle}{\sqrt{2}} \rightarrow |\downarrow\rangle|\downarrow\rangle \rightarrow \frac{|\uparrow\rangle - |\downarrow\rangle}{\sqrt{2}} \frac{|\uparrow\rangle - |\downarrow\rangle}{\sqrt{2}} \rightarrow |\uparrow\rangle|\uparrow\rangle$$

In both cases, the RF causes transitions between the  $\uparrow$  and  $\downarrow$  states of single spin-half particles. When the RF is on-resonance with both spins, such single-spin rotations take place for both spins simultaneously. Because the current through the dots is proportional to the  $S_z = 0$  probability ( $|\uparrow\downarrow\rangle$  or  $|\downarrow\uparrow\rangle$ ), we see that when both spins are excited simultaneously, the current through the dots will oscillate twice as fast as when only one spin is excited, but with only half the amplitude.

In the experiment, the excitation is on-resonance with only one spin at a time for most of the frozen nuclear configurations (Fig. 8.5). Only at the highest powers ( $B_1/\sqrt{\langle B_N^2 \rangle} > 1$ ), both spins may be excited simultaneously (but independently) and a small double Rabi frequency contribution is expected, although it could not be observed, owing to the measurement noise.

## 8.8 Quantum gate fidelity

We can estimate the angle over which the electron spins are rotated in the Bloch sphere based on our knowledge of  $B_1$  and the nuclear field fluctuations in the  $z$ -direction, again using the Hamiltonian  $H$ . For the maximum ratio of  $\sqrt{\langle B_N^2 \rangle} = B_1/(\sigma/\sqrt{3}) = 1.5$  reached in the present experiment, we achieve an average tip angle of  $131^\circ$  for an intended  $180^\circ$  rotation, corresponding to a fidelity of 73% (Fig. 8.5). Apart from using a stronger  $B_1$ , the tip angle can be increased considerably by taking advantage of the long timescale of the nuclear field fluctuations. First, application of composite pulses, widely used in nuclear

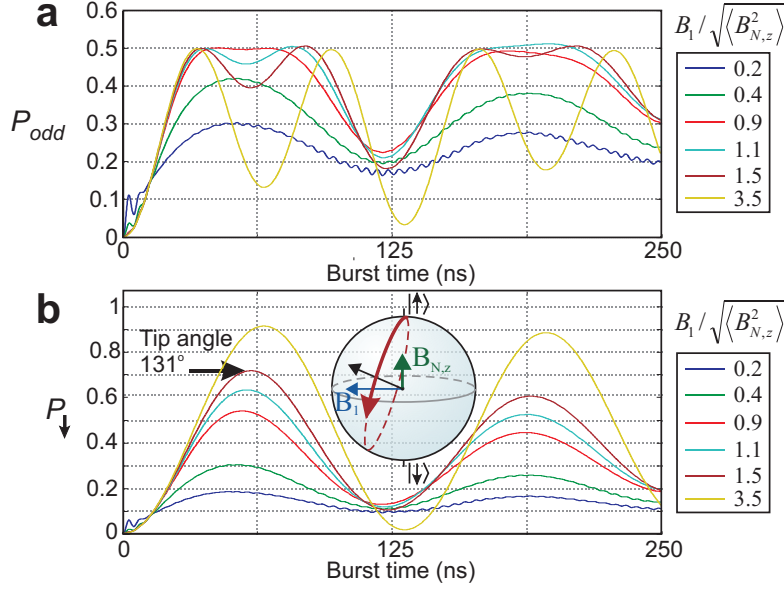


**Figure 8.5:** Time evolution of the spin states. (a) Probability for the two spins to be in  $\uparrow\downarrow$  or  $\downarrow\uparrow$  ( $S_z=0$ ) at the end of a RF burst, with initial state  $\uparrow\uparrow$ , computed using the Hamiltonian  $H$  presented in the main text, for six different values of  $\sigma_{N,z} = \langle B_N^2 \rangle^{1/2}$  (fixed  $B_1=1.5$  mT,  $B_{\text{ext}}=40$  mT, each of the traces is averaged over 2000 static nuclear configurations). As expected, the oscillation contains a single frequency for  $B_1$  small compared to  $\sigma_{N,z}$ , corresponding to the Rabi oscillation of a single spin. The oscillation develops a second frequency component, twice as fast as the first, when  $B_1/\sigma_{N,z} > 1$ . For  $B_1/\sigma_{N,z} > 4$  the double frequency component is dominant, reflecting the simultaneous Rabi oscillation of the two spins. (b) Probability for one of the spins to be  $\downarrow$  at the end of a RF burst. The spin state evolution is computed as in a. This oscillation represents the Rabi oscillation of one spin by itself. For increasing  $B_1$ , the maximum angle over which the spin is rotated in the Bloch sphere increases as well. In the experiment, this angle could not be measured directly, because the current measurement constitutes a two-spin measurement, not a single-spin measurement. We can, however, extract the tip angle from  $P_{\downarrow}$ .

magnetic resonance to compensate for resonance off-sets [51], can greatly improve the quality of the rotations. A second solution comprises a measurement of the nuclear field (nuclear state narrowing [52, 53, 54]), so that the uncertainty in the nuclear field is reduced, and accurate rotations can be realized for as long as the nuclear field remains constant.

In future experiments, controllable addressing of the spins in the two dots separately can be achieved through a gradient in either the static or the oscillating magnetic field. Such gradient fields can be created relatively easily using a ferromagnet or an asymmetric stripline. Alternatively, the resonance frequency of the spins can be selectively shifted using local  $g$ -factor engineering [55, 56]. The single spin rotations reported here, in combination with single-shot spin read-out [13, 18] and the tunable exchange coupling in double dots [14], offers many new

opportunities, such as measuring the violation of Bell's inequalities or the implementation of simple quantum algorithms.

This work has been performed in collaboration with C. Buizert, F. H. L. Koppens, L. P. Kouwenhoven, T. Meunier, K. C. Nowack, K. J. Tielrooij and L. M. K. Vandersypen.

We thank W. Coish, J. Elzerman, D. Klauser, A. Lupascu, D. Loss and in particular J. Folk for discussions; R. Schouten, B. van der Enden and W. den Braver for technical assistance; The International Research Centre for Telecommunication and Radar at the Delft University of Technology for assistance with the stripline simulations. Supported by the Dutch Organization for Fundamental Research on Matter (FOM), the Netherlands Organization for Scientific Research (NWO) and the Defense Advanced Research Projects Agency Quantum Information Science and Technology programme.

## 8.9 Additional material

### 8.9.1 Generation of the oscillating magnetic field

The oscillating field is generated by applying RF signals to an on-chip coplanar stripline (CPS) which is terminated by a narrow wire that shorts the two planes. The CPS is designed to maximize the amplitude of the oscillating field at the location of the dots. More details about the CPS can be found in Fig. 8.6.

### 8.9.2 Photon assisted tunneling due to electric fields

The coplanar stripline is designed to maximize the ratio between the RF magnetic field and electric field. Nevertheless, a small RF electric field will unavoidably be generated. High frequency electric fields can excite an electron to higher lying orbitals in the dot or in the reservoir. In this process, one or more photons are absorbed to match the excitation energy. Such so-called photon-assisted tunneling (PAT) processes [57, 58] can lift spin blockade and overwhelm the ESR signal. In this section we will discuss two different kinds of PAT processes that can lift spin blockade (Figs. 8.7a,b). The first is PAT through the interdot barrier. Electrons blocked in any of the three  $T(1,1)$  states can tunnel to the  $T(0,2)$  state if the energy difference between these states corresponds to an integer multiple of the photon energy  $hf$ . This will lead to sideband resonances running parallel to the  $T(0,2)$  line with a spacing  $hf$ . In the classical limit, where  $hf$  is much smaller

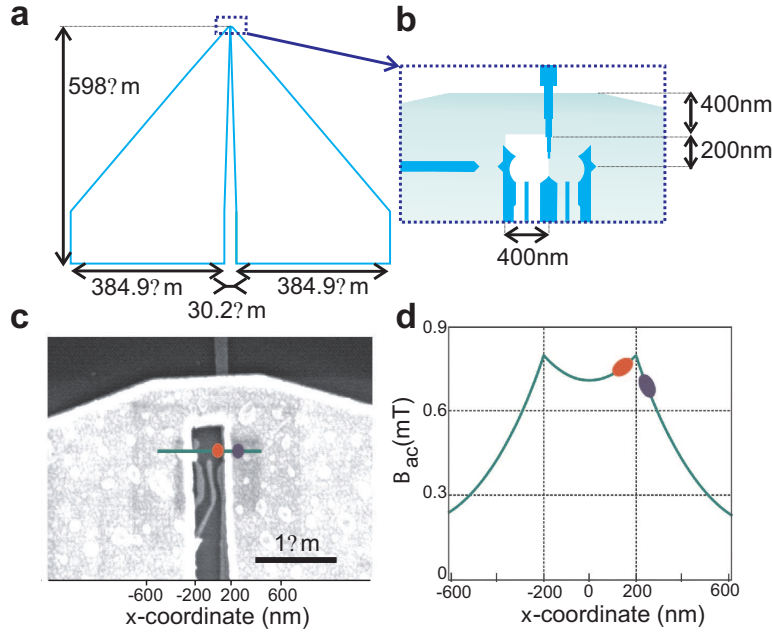


**Figure 8.6:** (a) Schematic diagram of the on-chip coplanar stripline. The CPS is terminated by a narrow wire that shorts the two planes. The wire effectively acts as a shorted termination of the  $50\ \Omega$  transmission line and therefore the current will exhibit an anti-node at the wire. (b) Schematic diagram showing the termination of the stripline and the position of the surface gates that define the double quantum dot. The design is optimized to maximize  $B_{ac}$  at the location of the dots. (c) SEM image of a device similar to the one used in the experiment of chapter 8. The termination of the CPS is visible as well as part of the surface gates that define the dots. The estimated locations of the two quantum dots are indicated in red and blue. (d) Amplitude of the oscillating magnetic field perpendicular to the plane, 200 nm below the CPS, along the green line in (c) ( $P=-22\ \text{dBm}$ ,  $f=200\ \text{MHz}$ ), computed numerically using CST Microwave Studio. This program solves the integral form of Maxwell's equations with the finite difference time domain method for a discretised spatial domain. In the simulation, an ideal waveguide source is connected to the CPS, through which a quasi-TEM wave will propagate. The approximate x-coordinates of the dots are indicated in light and dark gray. Based on these simulation results, we expect a field of  $B_{ac} \sim 0.7\ \text{mT}$  for a  $-22\ \text{dBm}$  excitation (corresponding to  $I_{cps} \sim 1\ \text{mA}$ ) at 200 MHz. Furthermore, we expect the fields in the two dots to differ from each other by no more than 20%.

than the line width of the states  $\hbar\Gamma$  ( $\Gamma$  is the tunnel rate), the individual sidebands cannot be resolved. Instead the  $T(0,2)$  line is broadened. We can quantify how efficient PAT is in lifting spin blockade using ref. [57]. The basic idea is that an AC voltage drop  $V = V_{ac} \cos(2\pi ft)$  across a tunnel barrier modifies the tunnel rate through the barrier as  $\Gamma(\tilde{E}) = \sum_{n=-\infty}^{n=\infty} J_n^2 \Gamma(E + n\hbar f)$ . Here  $\Gamma(E)$  and  $\Gamma(\tilde{E})$  are the tunnel rates at energy  $E$  with and without an AC voltage, respectively;  $J_n^2(\alpha)$  is the square of the  $n$ th order Bessel function evaluated at  $\alpha = (eV_{ac})/\hbar f$ , which describes the probability that an electron absorbs or emits  $n$  photons of energy  $\hbar f$  ( $-e$  is the electron charge). The energy splitting between the  $S(0,2)$  and

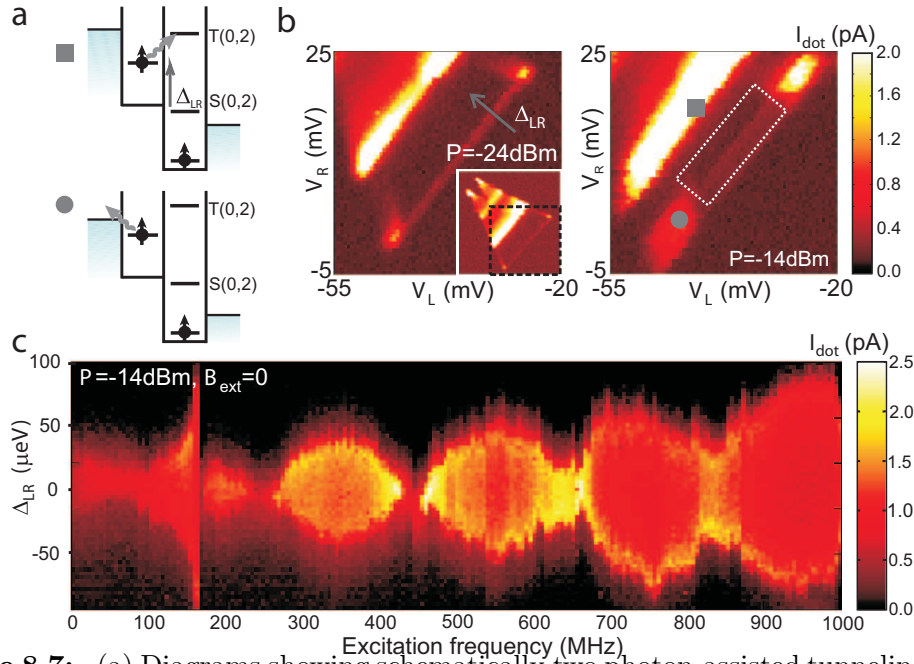


**Figure 8.7:** (a) Diagrams showing schematically two photon-assisted tunneling (PAT) processes. Top: excitation from T(1,1) to T(0,2). Bottom: excitation from T(1,1) to the left reservoir. (b) The current measured through the double dot under forward bias is plotted in grayscale, as a function of the gate voltages controlling the left and right dot potential (RF power -24 dBm and -14 dBm applied to the CPS and  $B_{\text{ext}} = 100$  mT). The effect of the two PAT processes on the measured current is visible as current enhancement in the areas around the yellow circle and blue square. ESR detection in the experiments discussed in the main text has been performed in the area enclosed by the white dotted lines where the PAT rates are smaller than the measurement noise ( $\sim 10$ -100 fA). (c) Current as a function of CPS excitation frequency and  $\Delta_{LR}$  (energy difference between S(1,1) and S(0,2) state, see also a and b) with an RF signal applied both to the right side gate (time-delayed and 34 dB attenuated) and the CPS ( $B_{\text{ext}} = 0$ ). The amplitude of the total electric field, reflected in the broadening of the current peak along the vertical axis, shows constructive and destructive interference as a function of frequency.

T(0,2) states is typically  $\sim 410$  eV, and the energy difference between the T(1,1) and the T(0,2) state will be of the same order. Since we can keep the Zeeman splitting small in this double dot measurement, the excitation frequency can be kept small too. Typically,  $f = 200$  MHz in the present experiment. The single-photon energy is then  $hf = 0.8 \mu\text{eV}$ . PAT processes from T(1,1) to T(0,2) thus require  $n = 500$  photons, and will therefore be very inefficient. Such 500-photon processes only occur with a reasonable probability,  $J_n^2(\alpha) > 0.05$ , if  $\alpha > n - 1 \sim 500$ . So only when the amplitude of the oscillating voltage across the central barrier exceeds roughly  $400 \mu\text{V}$ , spin blockade is lifted due to PAT from the T(1,1) to the T(0,2) state. In the continuous-wave experiment this occurs for RF powers larger than -12 dBm. The second PAT process occurs through the outer barriers. The electron blocked in the left dot can be excited to the left reservoir



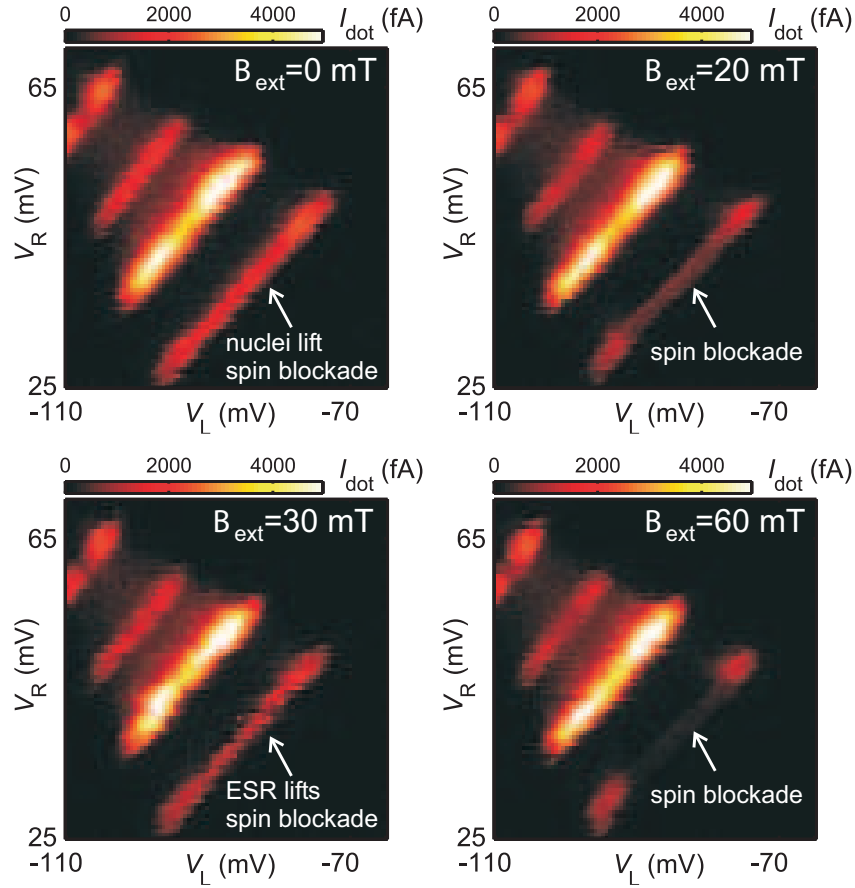


**Figure 8.8:** Current through the double quantum dot under forward bias ( $1400 \mu\text{eV}$ ) as a function of  $V_L$  and  $V_R$  with RF power  $-14 \text{ dBm}$  and frequency  $200 \text{ MHz}$  applied to the CPS. At zero external field, the nuclear field admixes all three triplets with the singlet, and spin blockade is lifted. At  $B_{\text{ext}}=20, 60 \text{ mT}$ , transport is blocked by spin blockade, but at  $B_{\text{ext}}=35 \text{ mT}$  spin blockade is lifted by ESR.

if the Fermi level of this reservoir lies within  $nhf$  in energy from the  $T(1,1)$  electrochemical potential (Fig. 8.7a). Subsequently, another electron with possibly a different spin state can tunnel from the left reservoir into the dot. Effectively this process can thus flip the spin by electron exchange with the reservoir. Similarly, the electron in the right dot can be excited to the right reservoir. The data presented in Figs. 8.2 and 8.4 are taken with a large bias voltage of  $1.4 \text{ mV}$  applied across the double dot, and with the relevant levels in the left and right dots far separated in energy from the Fermi level in the corresponding reservoir. In this way, PAT processes to the reservoirs were minimized. We point out that a third process, namely photon-assisted tunneling from the  $S(1,1)$  state to the  $S(0,2)$  state, does not disturb ESR detection. This process only broadens the ESR peak on the gate axis (defined by  $\Delta_{\text{LR}}$ , see Figs. 8.7a,b). Even though PAT can thus be easily recognized and minimized in double dot measurements, PAT



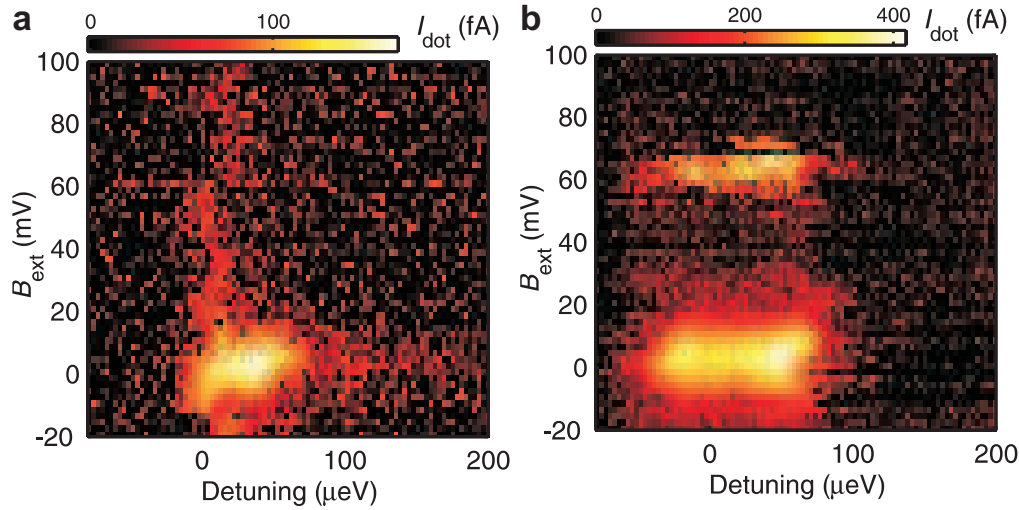


**Figure 8.9:** (a) Current through the double quantum dot under forward bias (1400  $\mu\text{eV}$ ) as a function of field and detuning between the S(1,1) and S(0,2) chemical potential. No splitting of the leakage current peak on the field axis at zero detuning can be observed. This indicates that the energy splitting  $J$  between S(1,1) and T(1,1) is smaller than  $\langle B_N^2 \rangle^{0.5}$ . This gives an upper bound for the tunnel coupling  $t$  ( $=J/\sqrt{2}$  at zero detuning) and inelastic transitions  $\Gamma_{\text{in}}$  from the S(1,1) state to the S(0,2) state:  $t, h\Gamma_{\text{in}} < g\mu_B \langle B_N^2 \rangle^{1/2}$ . (b) Similar measurement as in (a), but now with RF power -13 dBm and frequency 300 MHz applied to the CPS. Spin blockade is lifted around  $B_{\text{ext}} = hf/g\mu_B$ , where the resonance condition is matched. The extra broadening of the leakage current peak on the detuning axis is due to the (unwanted) oscillating electric field, see Fig. 8.7.

rates still became excessive at higher RF powers. This imposed a limitation on the power we could apply to the CPS, and thus on the amplitude of Bac we could produce in the experiment (before heating of the sample or the mixing chamber became a limitation). We therefore developed a method to reduce the PAT rates via interference between two signals. Hereby we split the RF signal at the output of the source, send one branch directly to the CPS and send the other branch to the right side gate of the dot. The latter signal is delayed through an additional coax of length  $L$  and properly attenuated such that for specific RF frequencies  $f = (n + \frac{1}{2})c/\Delta L$ , the electric field generated by the CPS interferes destructively with the electric field created by the side gate (Fig. 8.7c). At the frequencies that correspond to nodes in the interference pattern, it is possible to apply about 6 dB more RF power than is possible without PAT cancellation. Only the data in the inset of Fig. 8.2b are obtained with PAT reduction. For the pulsed experiments, the PAT rate to the T(0,2) state is smaller than in the continuous-wave

experiments, because the right dot levels are pulsed to a higher energy (thereby increasing the energy difference between  $T(0,2)$  and  $T(1,1)$ ) when the microwaves are applied.

### 8.9.3 Lifting spin blockade by nuclear spins or ESR: additional figures

Two figures are added to illustrate how two different mechanisms can lift spin blockade: the randomly fluctuating nuclear field and ESR. Fig. 8.8 shows the current through the double quantum dot. Spin blockade results in a suppression of the current at the baseline of the triangle. Spin blockade can be lifted by the nuclei at zero magnetic field or by ESR when the resonance condition is met at finite field. How this lifting of the spin blockade depends on the detuning of the  $S(1,1)$  and  $S(0,2)$  electrochemical potentials and the external magnetic field is displayed in 8.9 for (a) microwaves off and (b) microwaves on.

## References

- [1] M. A. Nielsen and I. L. Chuang, Quantum Computation and Quantum Information, Cambridge Univ. Press, Cambridge (2000).
- [2] P.W. Shor, Foundations of Computer Science, 1994 Proceedings., 35th Annual Symposium on ,124, (1994).
- [3] P. Zoller *et al.*, The European Physical Journal D-Atomic, Molecular and Optical Physics, 36, 203 (2005)
- [4] D. P. DiVincenzo, Progress of Physics **48**, 771, (2000).
- [5] D. Loss and D. P. DiVincenzo, Phys. Rev. A, **57**, 120 (1998)
- [6] D. G. Austing *et al.*, Physica B, **249**, 206, (1998)
- [7] M. Ciorga *et al.*, Phys. Rev. B **61**, R16315 (2000).
- [8] J. M. Elzerman *et al.*, Phys. Rev. B, **67**, 161308,(2003)
- [9] M. Bayer *et al.* Coupling and Entangling of Quantum States in Quantum Dot Molecules,(2001)
- [10] M. Atature *et al.*, Science **312**, 551 (2006)
- [11] R. Hanson, *et al.*, Phys. Rev. Lett. **91**, 196802 (2003)
- [12] T. Fujisawa *et al.*, Nature **278**, 419, (2002).
- [13] J. M. Elzerman, *et al.*, Nature **430**, 431 (2004)

- [14] J. R. Petta *et al.* Science **309**, 2180 (2005)
- [15] R. Schleser *et al.* Appl. Phys. Lett. **85**, 2005 (2004).
- [16] L. M. K. Vandersypen, *et al.* Appl. Phys. Lett. **85**, 4394, (2004).
- [17] W. Lu, *et al.* Nature **423**, 6938,422 (2003)
- [18] R. Hanson, *et al.* Phys. Rev. Lett. **94**, 196802 (2005)
- [19] M. V. G. Dutt, *et al.* Phys. Rev. Lett. **94**, 227403 (2005)
- [20] A. Greulich, *et al.* Phys. Rev. Lett. **96**, 227401 (2006)
- [21] C. P. Poole, Electron Spin Resonance, 2nd ed., Wiley, New York, 1983
- [22] M. Xiao, *et al.* Nature **430**, 435, (2004).
- [23] F. Jelezko, *et al.* Phys. Rev. Lett. **92**, 076401, (2004)
- [24] D. Rugar, *et al.* Nature **430**, 329, (2004).
- [25] H.-A. Engel and D. Loss, Phys. Rev. Lett. **86**, 4648, (2001).
- [26] A. Imamoglu, *et al.*, Phys. Rev. Lett. **83**, 4204, (1999)
- [27] Y. Kato, *et al.* Nature **427**, 50 (2003).
- [28] V. N. Golovach, *et al.*, Phys. Rev. Lett. **74**, 165319 (2006)
- [29] Y. Tokura, *et al.*, Phys. Rev. Lett. **96**, 047202, (2006)
- [30] K. Ono, *et al.*, Science **297**, 1313, (2002)
- [31] H.-A. Engel, *et al.*, Phys. Rev. Lett. **93**, 106804 (2004).
- [32] M. Blaauboer and D. P. DiVincenzo, Phys. Rev. Lett. **95**, 160402 (2005).
- [33] H. -A. Engel and D. Loss, Science **309**, 586 (2005)
- [34] J. M. Elzerman, *et al.*, Phys. Rev. B. **67**, 161308 (2003)
- [35] K. Ono, *et al.* Science **297**, 1313 (2002)
- [36] A. C. Johnson, *et al.* Phys. Rev. B. **72**, 165308 (2005)
- [37] A. C. Johnson, *et al.*, Nature **435**, 925, (2005).
- [38] F. H. L. Koppens, *et al.*, Science **309**, 1346 (2005)
- [39] O. N. Jouravlev and Y. V. Nazarov, Phys. Rev. Lett. **96**, 176804 (2006)
- [40] R. Hanson, *et al.*, Phys. Rev. Lett. **91**, 196802 (2003).
- [41] R. M. Potok, *et al.*, Phys. Rev. Lett. **91**, 16802 (2003)
- [42] L. H. Willems van Beveren, *et al.*, New Journal of Physics **7**, 182 (2005).
- [43] A. Kogan, *et al.*, Phys. Rev. Lett. **93**, 166602 (2004)

- [44] K. Ono, *et al.*, Phys. Rev. Lett. **92**, 256803 (2004)
- [45] M. S. Rudner and L. S. Levitov, Arxiv:cond-mat/0609409 (2006)
- [46] J. Inarrea, *et al.*, Arxiv:cond-mat/0609323 (2006)
- [47] M. Kroutvar, *et al.*, Nature **432**, 81, (2004)
- [48] V. N. Golovach, *et al.* Phys. Rev. Lett. **93**, 016601 (2004)
- [49] W. A. Coish and D. Loss, Phys. Rev. B. **70**, 195340 (2004)
- [50] F. H. L. Koppens, *et al.* arXiv:cond-mat/0703640 (2007)
- [51] L. M. K. Vandersypen and I. L. Chuang, Rev. Mod. Phys. **76**, 1037 (2004).
- [52] D. Klauser, *et al.*, Phys. Rev. B. **73**, 205302 (2006)
- [53] G. Giedke, *et al.*, Phys. Rev. A **74**, 32316 (2006)
- [54] D. Stepanenko, *et al.* Phys. Rev. Lett. **96**, 136401 (2006)
- [55] G. Salis, *et al.*, Nature **414**, 619 (2001).
- [56] H. W. Jiang and E. Yablonovitch, Phys. Rev. B **64**, 041307 (2001)
- [57] T. H. Stoof and Y. V. Nazarov, Phys. Rev. B **53**, 1050 (1996)
- [58] T. H. Oosterkamp, *et al.*, Nature **395**, 1998

## Chapter 9

# Locking electron spins into resonance by electron-nuclear feedback

In this chapter, we study the interaction between the electron spins and the bath of nuclear spins of the host lattice. We use magnetically driven spin resonance to control the electron spin and observe strong electron-nuclear feedback, which allows us to indirectly manipulate the nuclear spins. One experimental signature of this feedback is the locking of the electron spin system onto resonance with the RF frequency. Once the electron spin is locked on resonance, this resonance condition remains fulfilled even when the external magnetic field or the microwave frequency is changed. This is due to a dynamical build up of nuclear polarization which generally counteract the external magnetic field. After polarization we can dynamically depolarize the nuclear spins as well. At finite nuclear polarizations, the electron spin remains locked on resonance on timescales exceeding minutes. Locking of the electron spin system into resonance suggests that the nuclear polarization exhibits stable configurations where fluctuations of the nuclear distribution are reduced.

---

This chapter is in preparation for submission.

## 9.1 Introduction

The coherent control over a single electron spin such as demonstrated in chapter 8 opens up ways to study the environment with which the electron spin interacts. Improving the knowledge of the interaction of the electron with its environment is essential for using electron spins in solid state quantum information processing. From studying the driven Rabi oscillations both theoretically and experimentally, the observed non-exponential decay of these oscillations was understood by taking into account the interactions of the electron spin with the nuclear spin bath. Due to the long correlation time of this bath the decay of the Rabi oscillations follows a power law and the oscillations are shifted in phase by a universal value of  $\sim \pi/4$  [1]. Furthermore, the ability to rotate the electron spin over an arbitrary angle allows for the implementation of spin-echo techniques. When the electron spin is rotated into the transverse plane, it dephases in approximately 40 ns due to the Larmor precession about a random effective nuclear field. If this nuclear field changes slowly compared to the timescale of the electron spin dynamics, this dephasing can be reversed by applying a spin-echo pulse. The results in Ref. [2] show that a spin-echo pulse can extend the coherence time to about  $0.5 \mu\text{s}$  (at 70 mT). Times up to  $1 \mu\text{s}$  have been obtained by performing spin-echo pulses on a qubit encoded in the two-electron  $S$  and  $T_0$  state [3]. This allows the implementation of more involved qubit operations such as a CNOT gate or small algorithms. However reversing the spin dephasing by spin-echo techniques comes at the expense of (many) additional pulses. Extending  $T_2^*$  by preparing the nuclear environment in a state where fluctuations are reduced considerably reduces the burden of using complex pulse sequences or large field gradients. Another big advantage of nuclear state preparation is the increased accuracy of the qubit gate operations.

Many approaches have been proposed for nuclear state preparation such as complete nuclear polarization [4], narrowing of the nuclear distribution [4, 5, 6, 7], and the use of control pulses to decouple the coherent evolution of the electron spin from the nuclear spin dynamics [8, 9, 10]. Most of these proposals have not been implemented experimentally, although a suppression of nuclear fluctuations in ensembles of self-assembled quantum dots has been achieved by synchronizing the precessing spins using a series of laser pulses [11]. And recently a suppression of the spin dephasing by a factor  $\sim 70$  was demonstrated by using a gate voltage controlled electron-nuclear flip-flop pumping cycle to prepare a nuclear state [12].

In this chapter we study electron-nuclear spin interaction in gate-defined GaAs quantum dots. We use magnetically driven spin resonance to control the electron spin and observe strong electron-nuclear feedback, which allows us to indirectly

manipulate the nuclear spins. One experimental signature of this feedback is the locking of the electron spin system onto resonance with the RF frequency. Once the electron spin is locked on resonance, this resonance condition remains fulfilled even when the external magnetic field or the microwave frequency is changed. This is due to a dynamical build up of nuclear polarization which generally counteract the external magnetic field. After polarization we can dynamically depolarize the nuclear spins as well. At finite nuclear polarizations, the electron spin remains locked on resonance on timescales exceeding minutes. Locking of the electron spin system on resonance suggests that the nuclear polarization exhibits stable configurations where fluctuations of the nuclear distribution are suppressed. The ability to prepare a nuclear spin state with reduced fluctuations will help to significantly extend the dephasing time of the electron spin.

## 9.2 Reverse dynamic nuclear spin polarization

The measurements in this chapter are performed on the same device as used in chapter 8. The double quantum dot is tuned to the Pauli spin blockade regime but at a higher electron number than the (1,1) – (0,2) transition. Even though the exact electron number is not known we adopt the (1,1) / (0,2) terminology in the rest of this chapter. We perform magnetic ESR by applying RF excitation to a coplanar stripline (CPS) which is terminated close to the dots, generating an oscillating magnetic field.

As observed in chapter 8, the electron spin resonance (ESR) satellite peak at high excitation frequencies is asymmetrically broadened for certain sweeps. Furthermore, this broadening is time dependent, depends on sweep direction and the detuning of the dot levels. When the tunnel coupling between the dots is increased as well as the tunnel rates to the reservoirs this effect becomes more pronounced.

This phenomenon is illustrated in Fig. 9.1. We perform CW ESR spectroscopy by sweeping the RF frequency for different values of the external magnetic field. In Fig. 9.1a spectroscopic data is shown where we sweep the RF frequency  $f$  from low to high frequencies for different values of the external magnetic field  $B_0$ . We measure the current through the double quantum dot in the spin blockade regime and observe a current around zero field, where the randomly fluctuating nuclear fields lift spin blockade, as well as two satellite current peaks at the point where the ESR condition is met ( $hf = g\mu_B B_0$ ) and their location evolves linearly in frequency when changing the magnetic field (see chapter 8).

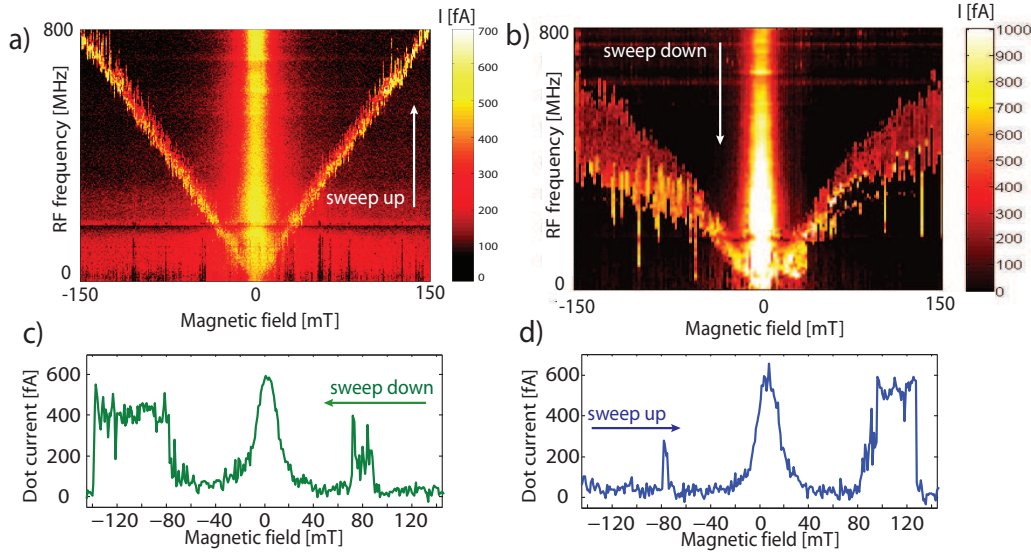


**Figure 9.1:** Reverse dynamic nuclear spin polarization. (a) CW ESR spectroscopic data as presented in chapter 8. (b) Frequency sweeps in a regime where the tunnel coupling is higher than in (a). We observe a build up of nuclear spin polarization *counteracting* the externally applied magnetic field. (c) Magnetic field sweep from positive to negative fields and (d) a magnetic field sweep in the opposite direction. Again we observe a dynamical build up of nuclear spin polarization resulting in an effective field opposing the external magnetic field.

When we reverse the sweep direction of the frequency we see strikingly different behaviour. Instead of a resonant peak, the current jumps up at the spin resonance frequency and *remains* high over a certain range of lower frequencies (Fig. 9.1b). This implies that the electron spin is still on resonance with the microwaves even though  $f < (g\mu_B B_0)/h$ . The electron spin can only be on resonance if there is an effective field  $B_{eff}$  that *counteracts* the external magnetic field  $B_0$  such that the spin resonance condition is still fulfilled:  $hf = g\mu_B(B_0 - B_{eff})$

Similar behaviour is observed when sweeping the magnetic field for a fixed RF frequency. In Fig. 9.1c the magnetic field is swept from positive to negative fields and in Fig. 9.1d in opposite direction. Both traces show that the effective field which is generated can only counteract  $B_0$ .

We explain this effective magnetic field sensed by the electron by the build up of a nuclear spin polarization. Building up this polarization is apparently much more efficient in the direction where its effective field counteracts the externally applied magnetic field. This polarization has a different sign than one would expect based on a mechanism involving hyperfine mediated spin relaxation [13] and hyperfine mediated inelastic interdot transitions.



### 9.3 Sweep rate and power dependence

We further investigate this effect by measuring its dependence on the sweep rate and the applied RF power. At this point it is important to mention that we proceed with sweeping the magnetic field instead of the RF frequency. The reason is that the generation of the oscillating magnetic field is accompanied by electric fields. These electric fields depend not only on the applied power but also on the excitation frequency. By sweeping the magnetic field we make sure that the electric fields are constant during the sweep.

We perform repeated field sweeps for different sweep rates at different RF power. A characteristic trace is shown in Fig. 9.2c, which shows two interesting features: (i) a sudden jump in the current at resonance instead of a slow increase, and (ii) a double step. The fact that the current suddenly jumps up indicates that some mechanism locks the electron spin on resonance when it approaches the resonance condition. This mechanism ensures that the spin remains locked on resonance even though the external field or RF frequency is changed, resulting in a build up of nuclear polarization. The origin of the second step remains unclear. The fact that the amplitude of the second step is approximately twice the amplitude of the first step might indicate that after the first step the spins in both dots are on resonance and after the second step only one.

We record the magnetic field values at which we jump on resonance, we observe the second step, and at which we lose spin resonance and the current drops back to zero. We plot them as a function of the applied power for different sweep rates in Fig. 9.2e-g. We observe that the maximum achievable nuclear polarization increases with increasing power. The specified powers are the powers applied to the CPS. The corresponding amplitude of the rotating field  $B_1$  are determined from the Rabi frequency and given in Fig. 9.2g.

Another interesting observation is that the length of the first plateau is generally larger for low sweep rates

### 9.4 Dragging the nuclear spin polarization

The measurements in section 9.3 indicate that there is a mechanism that locks the spin on resonance with the RF frequency. Here we study over what timescales the spin remains locked. We sweep the magnetic field through resonance with the RF excitation ( $f = 400$  MHz,  $B_0 = 75$  mT) and stop sweeping when we reach  $B_0 = 105$  mT. At that point we remain at 105 mT and continue measuring the current through the double dot for an arbitrary time. Note that 105 mT is sufficiently far from the zero-polarization resonance condition since the average

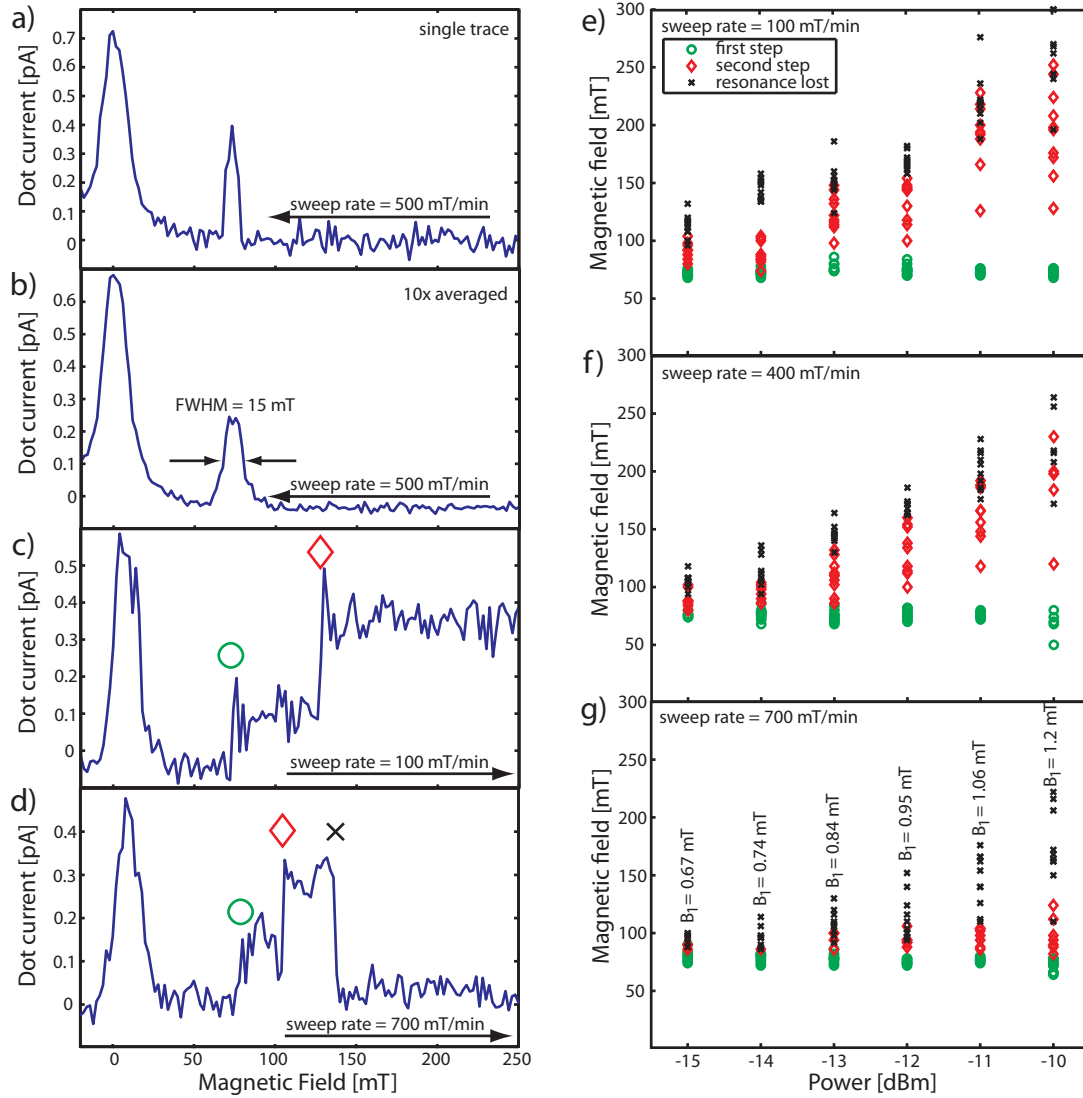


**Figure 9.2:** (a) A single magnetic field sweep from high to low field showing a small ESR satellite peak. (b) Same measurement as in (a) but 10 x averaged. The ESR peak has a FWHM of  $\sim 15$  mT. (c,d) Magnetic field sweeps from low to high field. When the field is swept through resonance the current jumps up (indicated by the green circle). A second step occurs at some higher field (indicated by the red diamond) and finally we lose the resonance (indicated by the black cross). (e-g) Sweeping the magnetic field for different sweep rates while keeping the microwave power constant. A clear trend for all sweep rates is that the maximum field at which we lose the resonance increases with increasing RF power. Another interesting feature is that the first plateau is generally larger for low sweep rates.

broadening of the spin resonance peak (without polarization) is approximately

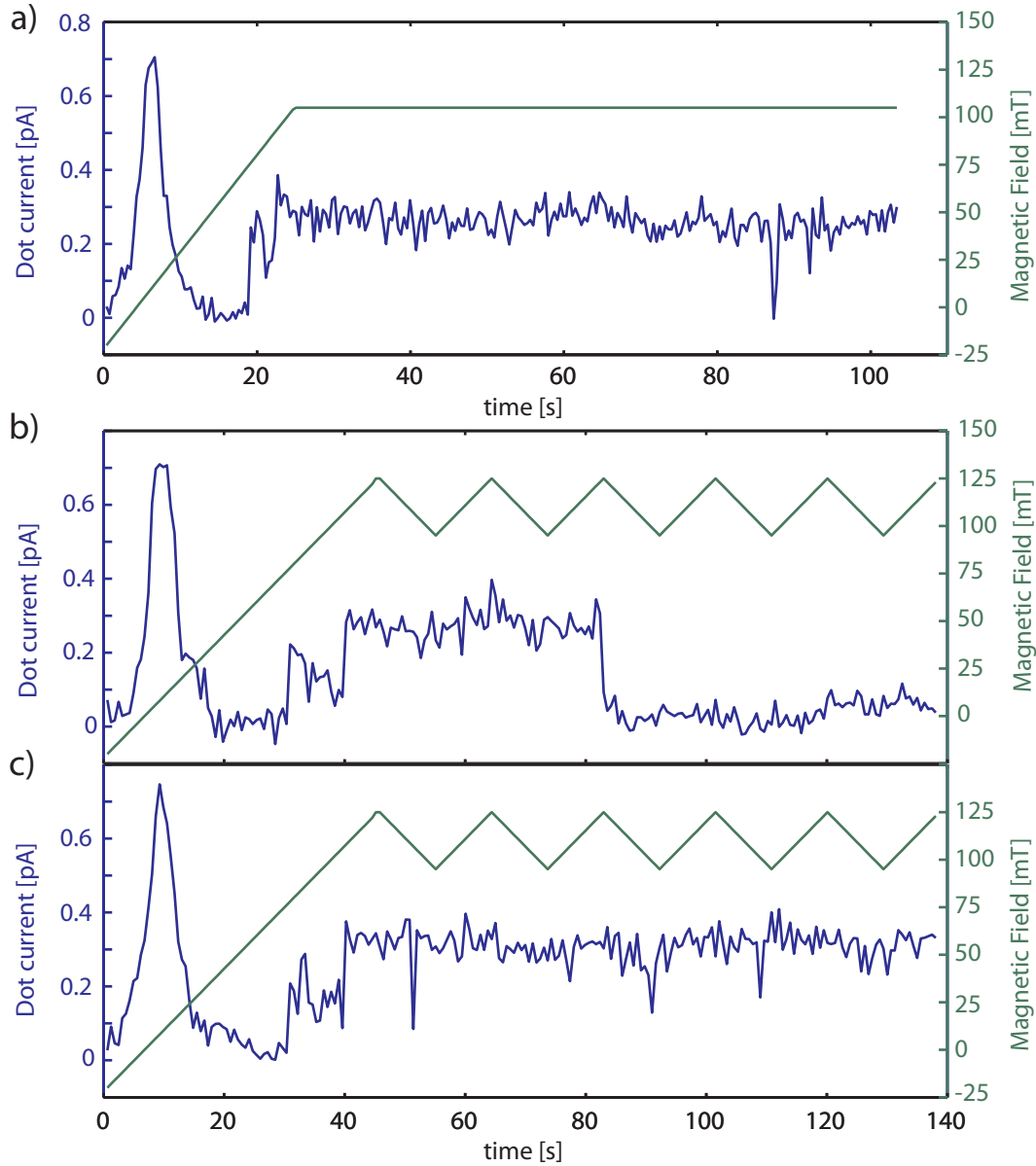


**Figure 9.3:** Dragging the nuclear polarization up and down. When we sweep the frequency from high to low frequencies, we hit the resonance the current jumps up. When we reverse the sweep direction we dynamically depolarize the nuclear spin system.

15 mT (see Fig. 9.2b).

A characteristic measurement is plotted in Fig 9.3a. The magnetic field (right y-axis) is swept from -20 mT to 105 mT in approximately 25 seconds and then remains 105 mT to the end of the measurement. The resulting current through the double dot (left y-axis) shows that when we sweep through resonance the

current jumps up (twice!) and remains high for well over a *minute*!

At this point we have demonstrated that there exists an electron-nuclear feedback mechanism which locks the electron spin on resonance. This mechanism can also be used to accurately set the nuclear spin polarization over a range of several hundred milliTesla. Starting from a finite polarization, this feedback also allows us to dynamically *depolarize* the nuclear spins. This is illustrated in Fig. 9.3b,c. We sweep the magnetic field up to 125 mT and then we sweep back and forth between 125 mT and 95 mT. The current again jumps up as we sweep through resonance and remains high independent of the sweep direction. In Fig. 9.3b the resonance is lost after approximately 1 minute, whereas in Fig. 9.3c the spin remains locked on resonance during the entire experiment (almost 2 minutes).

## 9.5 Spontaneous nuclear spin depolarization

Another timescale which is important in this process is the timescale on which the nuclear polarization is spontaneously depolarized (in contrast to dynamical depolarization), e.g. due to nuclear spin diffusion. In this section we present data on the spontaneous nuclear spin depolarization. This data was measured with the same device but in a different cooldown. The spin blockade transition in this experiment was known to be (1,1)–(0,2) transition.

We observe the build up of nuclear polarization only when we apply continuous microwave excitation to the system (independent of the electron number). If we apply bursts of microwaves of  $\sim 100$  ns and a duty cycle  $\ll 50\%$ , a dynamical nuclear polarization is not observed. This can be used to perform "microwave pump and probe" measurements. The idea is the following. The nuclear spin system is pumped using a frequency sweep of CW microwaves instead of a magnetic field sweep. When a finite (1-10%) nuclear polarization has been realized, we turn off the microwaves, step back to a higher frequency and immediately start to apply RF bursts. Note that when we stop pumping the nuclear system and switch to a pulsed mode, the horizontal axis becomes a time axis. The length of the bursts corresponds to a  $\pi$ -pulse and having a  $\ll 50\%$  duty cycle (Fig. 9.4a). Directly after we stop pumping, the current will be zero since we are off-resonance. However, after some time the nuclear polarization will have decayed to a value which corresponds to a nuclear field that makes the frequency at which we apply the RF bursts match the resonance condition, resulting in a peak in the current. This is shown in Fig. 9.4a. When we now plot the current as a function of the frequency at which we apply the MW bursts and the time, we observe an exponential decay of the nuclear polarization in time (Fig. 9.4b). The relaxation

rate of the polarization at short times is approximately 6 mT/s.

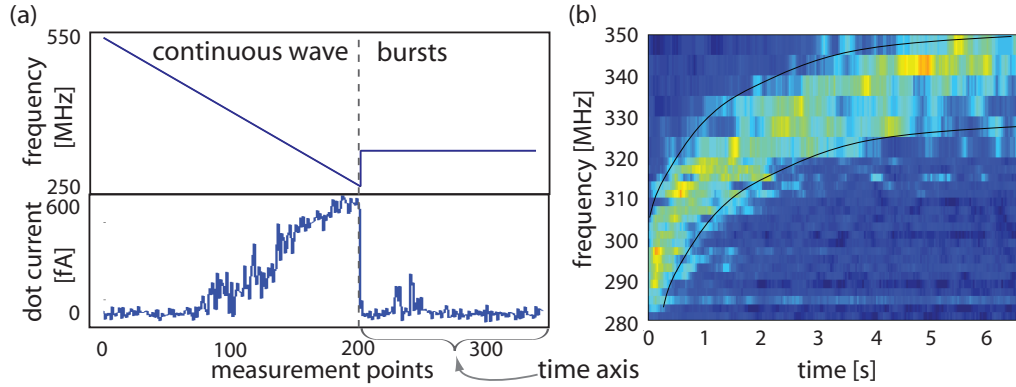


**Figure 9.4:** Microwave pump and probe measurements. (a) Illustration of the "pump and probe" cycle. First the frequency of the continuously applied microwaves is swept down. When the resonance condition is met the current jumps up and remains high due to the build up of nuclear polarization. At 250 MHz the continuous microwaves are turned off and off-resonant microwave bursts are applied. The measured current will remain zero until the nuclear spin bath has depolarized to a value that matches the resonance condition, resulting in a peak in the current. By varying the frequency of the applied microwave bursts the nuclear depolarization can be mapped out as a function of time (b).

## 9.6 Mechanisms for nuclear spin pumping

We observe that building up a nuclear polarization is much more efficient in the direction where its effective field acts *against* the externally applied magnetic field. This polarization has a different sign than the Overhauser type polarization, which involves hyperfine mediated electron spin relaxation [13]. ESR would create an electron spin-down population that can (partially) relax via electron-nuclear flip-flops, which results in an effective field that would add to the external field.

Recently, Rudner and Levitov proposed a mechanism to explain pumping in the reverse direction [14]. They considered electron spin-flips induced by electric fields [15], partially via flip-flopping with the nuclei. As long as the spin-up population is higher than spin-down, this results in a pumping direction opposite to hyperfine mediated electron spin relaxation. To ensure that the spin-up population is higher than the population of spin-down, weak driving of the electron spin system is assumed. If we would apply strong driving to the electron spin system, the resonance would be saturated and no reverse pumping occurs.

Very recently, Danon *et al.* have developed a theory which explains reverse pumping of the nuclear spins in the regime where the resonance is saturated [16]. They find that the pump rate increases close to resonance and exactly on resonance the pump rate exhibits a dip. This is due to the saturation of the resonance. Exactly at resonance, the rates for  $|\downarrow\uparrow\rangle \rightarrow |\uparrow\downarrow\rangle$  and  $|\uparrow\downarrow\rangle \rightarrow |\downarrow\uparrow\rangle$  are equal, where  $\{\uparrow, \downarrow\}$  denote the electron spin and  $\{\uparrow, \downarrow\}$  denote the nuclear spin. Since there is a finite polarization the number of up nuclei  $N_\uparrow$  is larger than the number of down nuclei  $N_\downarrow$  and therefore the process  $|\downarrow\uparrow\rangle \rightarrow |\uparrow\downarrow\rangle$  will have the highest rate and will effectively pump the nuclear spins in the opposite direction, resulting in a dip.

The model assumes a strong magnetic electron spin resonance field drives the spin states into saturation. The oscillating magnetic fields are accompanied by electric fields which modulate the hyperfine coupling constant [15, 14]. Furthermore, relaxation of the electron spin is included, which results in non-equal occupation probabilities of electron spin basis states, as well as a general term for nuclear spin relaxation.

If we plot the nuclear spin polarization rate  $dP/dt$  as a function of the polarization  $P = B_N/B_{max}$  we obtain a so-called pumping curve (see Fig. 9.5). The overall negative slope is due to a general nuclear spin relaxation term. The peak is due to the external driving and the dip is due to enhanced relaxation exactly at resonance. The important features are the three stable points in the nuclear polarization, indicated by the circles, one of which is located very close to resonance. The corresponding current through the double dot is high for the stable point close to resonance and lower for the stable point next to it.

In a double quantum dot the same behavior is found except for a higher number of stable points (up to nine) [16].

This model qualitatively explains many of the features observed in the experiment, such as the locking of the electron spin onto resonance due to the stable points in the nuclear polarization, nuclear spin pumping in the observed (reverse) direction with appreciable rates as well as the double step in the current. The latter might indeed be caused by switching from a stable nuclear configuration where both dots are resonant to a configuration where only one of the dots is resonant. However, further experiments and analysis are required to verify this model quantitatively as well as further analysis.

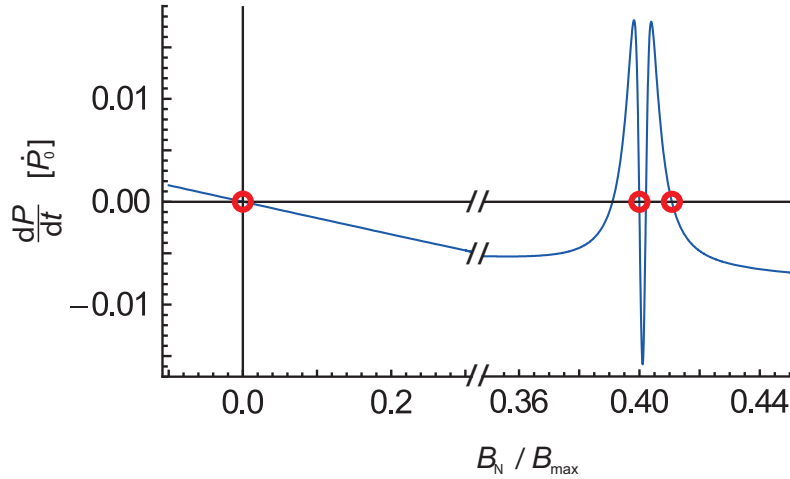


**Figure 9.5:** Nuclear spin pumping curve. The nuclear spin polarization rate for one dot ( $dP/dt$ ) as a function of its polarization  $P = B_N/B_{max}$  with the other dot far away from the resonance condition. The overall negative slope is due to nuclear spin relaxation. The peak is due to the external driving and the dip is due to enhanced relaxation exactly at resonance. Stable points in the nuclear spin polarization, indicated by circles, are found whenever the curve crosses the  $x$ -axis with a negative slope. (Figure courtesy of J. Danon and Yu. V Nazarov.)

## 9.7 Conclusion and recommendations

We use magnetically driven spin resonance to control the electron spin and observe strong electron-nuclear feedback which locks the electron spin onto resonance with the RF frequency. Once the electron spin is locked onto resonance, this resonance condition remains fulfilled even when the external magnetic field or the microwave frequency is changed. This is due to a dynamical build up of nuclear polarization which generally counteract the external magnetic field. An intriguing feature of this build up of polarization is the occurrence of a double step in the current. At a finite polarization, the electron spin can remain on resonance on the timescale of minutes. After polarization we can dynamically depolarize the nuclear spins as well. Locking of the electron spin system into resonance suggests that the nuclear polarization exhibits stable configurations where fluctuations of the nuclear distribution are reduced.

A recently developed model by Danon *et al.* qualitatively explains the observed phenomena but further research and analysis is required to verify this model quantitatively.

This work has been done in collaboration with J. Danon, F.H.L. Koppens, Yu.

V. Nazarov, K.C. Nowack and L. M. K. Vandersypen.

We thank S-C. Wang, L.R. Schreiber, F.R. Braakman, P.C. de Groot, G.A. Steele, for help and discussions, A. van der Enden, R.G. Roeleveld and R.N. Schouten for technical support, and L.P. Kouwenhoven for supplying infrastructure. This work is supported by the 'Stichting voor Fundamenteel Onderzoek der Materie (FOM)' and the 'Nederlandse Organisatie voor Wetenschappelijk Onderzoek (NWO)'.

## References

- [1] F. H. L. Koppens *et al*, Phys. Rev. Lett. **91**, 123512 (2007).
- [2] F. H. L. Koppens *et al*, Phys. Rev. Lett. **100**, 236802 (2008).
- [3] J. R. Petta *et al*, Science **309**, 2180 (2005).
- [4] A. Imamoglu *et al*, Phys. Rev. Lett. **91**, 017402 (2003).
- [5] D. Klauser, W. A. Coish, D. Loss, Phys. Rev. B **73**, 205302 (2006).
- [6] G. Giedke *et al*, Phys. Rev. A **74**, 032316 (2006).
- [7] D. Stepanenko *et al*, Phys. Rev. Lett. **96**, 136401 (2006).
- [8] K. Khodjasteh and D. A. Lidar, Phys. Rev. Lett. **95**, 180501 (2005).
- [9] W. Zhang *et al*, Phys. Rev. B **75**, 201302(R) (2007).
- [10] W. Yao, R.-B. Liu, L. J. Sham, Phys. Rev. Lett. **98**, 077602 (2007).
- [11] A. Greilich *et al*, Science **317**, 1896 (2007).
- [12] D. J. Reilly *et al*, Science **321**, 817 (2008).
- [13] J. Danon and Yu. V. Nazarov, Phys. Rev. Lett. **309**, 2180 (2005).
- [14] M. S. Rudner and L. S. Levitov, Phys. Rev. Lett. **99**, 246602 (2007).
- [15] E. A. Laird *et al*, Phys. Rev. Lett. **99**, 246601 (2007).
- [16] J. Danon *et al*, in preparation.



## Chapter 10

### Conclusions and future directions

In this chapter, we review the work presented in this thesis, together with the progress the community has made towards the implementation of qubits using electron spins in semiconductor quantum dots. We give suggestions to improve the existing read-out and manipulation techniques as well as ideas to improve the coherence properties of single spins confined in semiconductor quantum dots. These ideas and suggestions are put forward in the context of the physical implementation of an electron spin based scalable quantum computer.

## 10.1 Current status

This thesis focuses on using electron spins confined in semiconductor quantum dots as spin qubits [1] and contains the following experimental results:

- We can perform read-out of two-electron spin states. The observed relaxation times are long, up to milliseconds. When using a tunnel-rate-selective read-out method, we achieve a single-shot measurement fidelity of 90%. When we combine this with an energy-selective method we achieve a single-shot fidelity of 97.5% which would be 93% without spin dependent tunnel rates.
- The important role of phonons in the two-spin relaxation process has been confirmed. When the phonon wavelength matches the size of the dot the spin relaxation time increases by an order of magnitude.
- A novel approach to fast charge detection is introduced: a HEMT operated as a cryogenic pre-amplification stage. This approach to QPC-based charge sensing increases the bandwidth of the setup to 1 MHz and allows us to detect fluctuations in the quantum dot occupation as short as 400 ns.
- We can rotate a single electron spin via magnetic resonance about any arbitrary axis to any predefined superposition state with an accuracy of 75% for a  $\pi$ -rotation with initial state  $|\uparrow\rangle$ . The fastest  $\pi$ -rotation takes about 60 ns.
- Using a strong electron-nuclear feedback, caused by the hyperfine interaction between the electron spin and the nuclear spins, we can indirectly control the surrounding nuclear spins. This feedback results in locking the electron spin into resonance with the applied microwaves, which might indicate that the nuclear spin system exhibits stable configurations where fluctuations of the nuclear distribution are reduced.

These results in combination with other recent achievements in the field of spin qubits in quantum dots, including single-shot read-out of a single electron spin [2] and the demonstration of the SWAP-gate on two-electron spin states [3], illustrate that the field of electron spin based quantum bit has rapidly evolved. Furthermore, spin coherence times have been measured up to 0.5 - 1  $\mu$ s using spin-echo techniques [3, 4]. At this point, all the proof-of-principle experiments have been demonstrated for the list of basic ingredients necessary for encoding a logical quantum bit in an electron spin [5].

An important question is whether a quantum computer based on electron spins in quantum dots is feasible. In order to make scalable quantum computation with electron spins possible, the error per gate operation should be smaller than a certain threshold which allows for error correction. The value for this error threshold is often quoted to be  $10^{-4}$  assuming that classical, local information processing requires only a few time steps of the quantum computer [6, 7]. Furthermore, this threshold is only possible if long-distance communication can be realized or if spins can be shuttled with very low error. If only nearest-neighbor interactions are available, transport of quantum information is still possible but requires an even lower error threshold of  $10^{-6}$  [8].

The existing one and two-electron spin gates do not meet the required accuracy threshold but there is room for improvement, as will be discussed below.

With the existing techniques, further progress in the field of spin-based quantum information is already possible like the demonstration of the CNOT-gate or performing simple quantum algorithms. Furthermore, by combining the available techniques, experiments are possible that address fundamental quantum properties of spins in the solid-state environment. These include the demonstration of entanglement [9] and performing and reversing weak quantum measurements [10, 11].

## 10.2 Improvements and future directions

Here, we give suggestions for improving existing manipulation techniques and coherence properties of single spins confined in quantum dots. These future opportunities will be reviewed in the context of the basic requirements essential for building a scalable quantum computer based on electron spins in quantum dots.

### 10.2.1 Spin qubit read-out

Read-out determines the result at the end of the computation by measuring specific qubits. Many proposals exist for reading out the electron spin state on a quantum dot.

Single-shot read-out of a single electron spin state has been performed by converting spin-information into charge information via energy-selective tunneling with a fidelity of 82% [2]. This measurement fidelity was limited mostly by the  $\sim 40$  kHz bandwidth of the measurement setup as well as thermal excitation of electrons out of the quantum dot. By lowering the electron temperature below 100 mK, and especially by using faster charge detection (see chapter 6), the

fidelity of this energy-selective read-out (E-RO) technique can exceed 99% for a measurement bandwidth in 1 MHz (assuming  $T_1 = 1$  ms). It is important to note that the single-shot read-out using the energy-selective read-out technique only works at high magnetic fields (demonstrated only for  $B > 8$  T). This makes it difficult to combine with magnetic ESR. At low field, read-out techniques in the singlet-triplet basis are available, like spin-selective tunneling to the reservoir [12] or tunneling to a second quantum dot [13]. The latter can be used as well for read-out of single-spin (Zeeman) states, provided that a magnetic field gradient over the two dots is present. The disadvantage of this method is the required extra quantum dot.

The method presented in this thesis makes use of a difference in tunnel rate between the spin states (see chapter 4). In this case the fidelity is determined by the ratio of the tunnel rates of the ground and excited state,  $\Gamma_{ES}/\Gamma_{GS}$ . This tunnel-rate-selective read-out (TR-RO) method is used to read out the two-electron spin state, achieving a single-shot fidelity of >90% [12]. When both the energy-selective and tunnel-rate-selective methods are combined, the two-electron spin states can be read out with a single-shot measurement fidelity of 97.5%. This number can be increased by increasing the bandwidth of the setup and increasing the difference in tunnel rate between the two spin states.

When using a QPC as a charge sensor, it is important to note that the shot-noise generated by the QPC acts back on the qubit. This effect cannot be avoided. However, it is possible to use fast pulse techniques to pinch-off the QPC, effectively turning off the charge sensor as well as its backaction when the spins are being manipulated, initialized or stored. When read-out of the spin state is desired, the QPC can be quickly turned on again by a fast voltage pulse on the QPC gate.

### 10.2.2 Longer coherence times

The timescale on which the coherence is maintained, i.e. on which the evolution of the qubit state does not deviate from the desired route (set by the internal Hamiltonian plus the control fields), is denoted by  $T_2$ . Note that the coherence time merely reflects the lack of our knowledge about (the interaction of the qubit with) the environment or the inability to compensate for this interaction. Therefore, the coherence time can be extended by increasing the knowledge of or the control over (a part of) the environment. Also, decoherence mechanisms that are constant on a timescale much longer than the typical qubit operation time can be canceled out by spin-echo and composite pulses techniques, provided that the coherence time still allows a full rotation to be performed [14].

The most important environment for the electron spin coherence are the surrounding GaAs nuclear spins. The hyperfine interaction of the electron spin with these nuclear spins leads to an additional effective magnetic field  $h_z$ , the so-called Overhauser field. A static polarization just adds a constant offset to the external field and is thus a known change in precession frequency and has therefore no effect on the coherence. In contrast, the *fluctuations* in  $h_z$ , denoted by  $\delta h_z$ , cause uncertainty in the total effective magnetic field and can therefore lead to significant decoherence of the electron spin. The timescale on which the phase information is lost due to these nuclear field fluctuations has been measured to be 10-40 ns [3, 4]. By applying a spin-echo pulse one can undo the dephasing caused by fluctuations in the environment which are slower than the dynamics of the electron spin and the spin coherence time can be extended to 0.5 - 1  $\mu$ s [3, 4].

### Reducing the nuclear field fluctuations

This dephasing time can be extended through polarization of the nuclear spins. However, to extend the dephasing time by an order of magnitude, a polarization of above 99% is required, but the best result so far reached is only <90% in quantum dots [40]. Another and probably more promising approach is to prepare the nuclear spin system in a well-known and well-defined state before performing operations. Namely, a known nuclear field in the z-direction  $h_z$  is just an offset and a known dephasing will occur. Similar reasoning holds for the two-qubit operations if the difference  $\Delta h_z$  of  $h_z$  in the two dots is known. In principle, measuring the response when performing ESR on one spin or SWAP on two spins is a measurement of respectively  $h_z$  or  $\Delta h_z$  [15, 16, 17]. Performing these measurements in a clever way can lead to sufficient reduction of the  $h_z$  or  $\Delta h_z$  distribution to achieve so-called state narrowing of the nuclear spin bath. Another approach is to exploit feedback from the electron spin to the nuclear spin bath. By tuning the double quantum dot properly close to  $S/T_+$  and  $S/T_-$  degeneracies, spin can be transferred to the nuclear spin bath leading to dynamic nuclear polarization. This polarization process can be made self-limiting by balancing the polarization processes in the two directions. It is predicted that this type of feedback can reduce the fluctuations in the nuclear field significantly [18]. Another type of hyperfine induced feedback is present when we use continuous magnetic resonance and locks the electron spin into resonance with the microwaves (see chapter 9). This locking is also predicted to reduce the fluctuations of the nuclear spin in (one of the two) dots [19].

### Decoherence free subspace

Apart from using a single spin to encode the qubit, it is also possible to encode in

the two-electron singlet  $S$  and  $m_z = 0$  triplet state  $T_0$  [20]. These states are robust against nuclear-spin related dephasing, provided that the qubit splitting  $J$  is much larger than  $\delta h_z$ . This should be combined with a sufficiently high magnetic field to suppresses leakage to the  $T_{\pm}$  states. Both requirements can be realized easily. Single qubit rotations can in principle be performed via a magnetic field gradient and a phase-gate via the Heisenberg interaction [3]. Since now the qubit states involve different electronic orbitals, two-qubit operations can be realized by exploiting the capacitive coupling between two double quantum dots or by coupling the qubit to a resonant cavity mode [21]. One of the disadvantages of this qubit basis is dephasing due to fluctuations in the qubit splitting  $J$  caused by charge fluctuations. Another disadvantage is that  $2N$  quantum dots are required to encode  $N$  qubits.

### Other materials and systems

Most experiments with electron spins in quantum dots have so far been performed with III-V semiconductor materials such as GaAs, InAs or InP, in which all the atoms have non-zero nuclear spin. The only semiconductors that have stable isotopes without nuclear spin are the elemental ones: C, Si, and Ge. The spin decoherence time in these isotopically purified materials is expected to be limited by the spin-orbit interaction (SOI), and could therefore be very long. Namely, theory predicts that in leading order the spin-orbit limited decoherence time is similar as the relaxation time [22], which is in GaAs quantum dots beyond one second at 1 T [23]. Furthermore, the SOI is even weaker in Si and C than in GaAs. Experimental progress in developing C and Si quantum dot devices is significant, and includes the realization of gate-defined double quantum dots in carbon nanotubes [24, 25], Si/Ge 2DEGs [26] and Ge/Si nanowires [27]. Another promising host for the electron spin might be a single layer of graphene [28], but it is not yet clear whether gated dots can be defined in this structure.

Apart from gate-defined dots, alternatives for confining electrons are donors or impurities like nitrogen-vacancy centers in diamond (NV centers) or shallow donor states in Si. The coherence properties of these systems are very good. A spin decoherence time of 60 ms was reported in phosphorous donors of isotopically purified  $^{28}\text{Si}$  [29], and the longest decoherence time reported for NV centers was 0.5 ms (measured at room temperature!) [30]. Disadvantages of these systems are the lack of flexibility in tuning the potential landscape in-situ, and the long distance between the spins making it difficult to couple them. A solution to this is implantation of donors close to each other, and considerable progress is made with the implantation of phosphorous donors in Si [31] as well as NV centers in diamond [32, 33]. The major advantage of NV center qubits is the prospect

for long-distance spin interactions via photons. A completely different approach in overcoming spin decoherence is to use the nuclear spins as a storage medium for quantum information [34]. The decoherence time of the nuclear spins are expected to be very long. Coherent oscillations of a single nuclear spin were observed via the electron spin in a NV center [35] and more recently, quantum information was stored in one NV center nuclear spin [36].

### 10.2.3 Improving qubit gates

At this stage both a one-qubit gate (single spin rotation) as well as a two-qubit gate (SWAP-gate) have been demonstrated. These two gates constitute a universal set of quantum gates, i.e. every unitary operation on an arbitrary number of qubits can be decomposed into combinations of only these quantum gates, and therefore suffice to implement all possible quantum algorithms [37].

As mentioned in section 10.1, it is important for quantum computation that the quantum gates meet an accuracy threshold. To this end quantum operations must be fast and accurate.

#### One-qubit gate

The fastest demonstrated single qubit operation has been performed in 27 ns ( $\pi/2$ -rotation, see chapter 8) with an estimated accuracy of 75% for a  $\pi$ -rotation with initial state  $|\uparrow\rangle$ . The accuracy of this gate is limited by spin dephasing due to the nuclear field fluctuations. By reducing this nuclear field uncertainty a factor of ten (see section 10.2.2) the gate fidelity can exceed 99%. Faster rotations are required as well in order to achieve the error threshold. If we assume a decoherence time of 10  $\mu$ s, a spin flip should be performed in 1 ns. It is unlikely that this will be realized via magnetic resonance because an oscillating field of about 75 mT is required. Possibly, faster rotations can be realized via electric resonance if a very strong magnetic field gradient, perpendicular to the external field, can be applied [38]. An effective field gradient can in principle also be realized by polarizing the nuclear field in one of the two quantum dots and subsequently, rotate this nuclear field via a NMR pulse by  $\pi$ . The effect of NMR excitation signals applied to the nuclear spins in quantum dots has been observed ([39] and Delft, not published) as well as dot-selective polarization (see chapter 9). Furthermore, a nuclear field of 4 T obtained via dynamic nuclear polarization in the spin blockade regime has been reported in Ref. [40]. To estimate the required gradient, we use the numbers from Ref. [41], where hyperfine-mediated (but incoherent) electron spin resonance was observed. For a (random) nuclear field difference between the two dots of  $\sim 4$  mT, the estimated maximum Rabi

frequency was about 1.8 MHz. This implies that a  $\pi$ -rotation in 0.5 ns is possible with a 4 T field difference between the two dots. In dots where besides an electron also holes are confined, in principle very fast optical manipulation of the spin is possible with laser pulses only. Spin  $\pi/2$ -rotations in 5.1 ps were demonstrated in GaAs quantum wells [42] and recently picosecond-scale  $\pi$ -rotations of a single electron spin has been achieved in a GaAs quantum dot [43]. The mechanism for this process relies on the generation of an effective magnetic field by a below-bandgap laser pulse through the optical Stark effect [44]. Finally, we remark that single-spin rotations are not necessarily required for universal quantum computation with spins. In principle, with the Heisenberg interaction alone any quantum computer circuit can be implemented, at the expense of increasing the number of devices and the number of computational steps [45].

### Two-qubit gate

The two-qubit SWAP-gate has been performed in 180 ps [3], limited by the rise time of the fast voltage pulses, allowing for 7000 operations within the reported decoherence time of 1.2  $\mu$ s. Even shorter gate operation times down to 40 ps are in principle possible because a singlet-triplet splitting of 120  $\mu$ eV can be achieved. The fidelity of the SWAP-gate is limited by nuclear-spin [46] and charge-related dephasing [47]. The latter can be understood from the fact that the singlet-triplet splitting  $J$  depends on the level detuning  $\epsilon$  and tunnel coupling between the two dots; both are susceptible to charge noise. In order to achieve higher fidelity for the two-qubit gate, one should use higher  $J$  [46] and work in a regime where  $J$  is independent of  $\epsilon$  [48], or by further reduction of the charge noise [49].

### 10.2.4 Scalability

We will finally remark on the requirement of scalability. If we were to focus on studying decoherence and demonstrating basic quantum algorithms, a device containing about five to ten qubits is sufficient for the near future. Our present circuit can be extended to incorporate several more quantum dots, by making minor adjustments to the design of the surface gates. In fact, tunable GaAs triple quantum dots have already been reported [50, 51]. Note that the charge detection schemes offer a substantial advantage here, since these only require the dot to be coupled to a single reservoir.

In order to create a quantum computer consisting of, say, several hundreds of qubits, major revisions in the design and use of different fabrication techniques will be necessary. In order to build a quantum computer, consisting of thousands of qubits, it is probably not just sufficient to follow the same strategy. First



of all, expanding the quantum dot arrays in a second and maybe even a third dimension will be required. Secondly, communication between distant qubits via the Heisenberg interaction is practically difficult to realize, and also more time-consuming and susceptible to errors. To overcome this, channels or arrays of quantum dots can be developed to shuttle electrons [20]. Also, if spins can be coupled to photons, long-range interactions can be mediated via a cavity. An important practical difficulty in scaling will be the task of tuning all the quantum dots to the few-electron regime, which is very demanding for a large number of gates that do not couple only to one dot or barrier. A solution is to make clusters of a few coupled gate-defined quantum dots in combination with long-distance communication between these clusters by electron shuttling or photons.

### Communication between distant qubits

Communication between distant qubits in arrays of quantum dots is possible by performing multiple SWAP operations on pairs of electron spins. However, nearest-neighbor communication requires more than a factor  $10^2$  lower error threshold compared to qubit arrays where long-distance communication is possible [8, 37]. This communication channel could be provided by photons if the qubit can be coupled to photons. This is possible by exploiting the optical selection rules in optically accessible dots (such as dots defined in nanowires, self-assembled dots, or CdSe dots) via polarized laser and cavity fields [52, 53]. However, in gate-defined quantum dots holes are not confined, making optical access difficult. We note that the magnetic moment of the electron spin is coupled magnetically to a cavity photon but this coupling is very weak. A stronger coupling of the spin to a cavity mode can be achieved electrically, if in some way the electron charge is coupled to its spin. For example, one can use a delocalized state in a double quantum dot in combination with ESR that is resonant only in one dot [54]. When using the two-electron spin state  $S/T_0$  as a basis, the qubit is very strongly coupled to the electron orbital. This makes capacitive coupling between qubits possible [20, 21], or via a resonant cavity if a field gradient is present [55].

## 10.3 Conclusions

The field of spin-qubits in quantum dots is about six years old and has come a very long way in that time. All the proof-of-principle experiments have been demonstrated for the list of basic ingredients necessary for quantum computation.

At this stage the main challenges for quantum computation are to combine and improve existing (manipulation) schemes and techniques as well controlling

the disturbing environment like charge noise and the nuclear spins.

On the the other hand, one could explore the possibilities that other material systems have to offer or even combine systems like quantum dots and cavities to achieve long-distance communication.

Past experimental results and current theoretical understanding indicate that spin-based quantum computing may be possible. It remains an open question whether such a large scale quantum computer will ever be built. There are still countless hurdles on the road to a large scale quantum computer. But as new theoretical ideas and experimental techniques will be developed along the way, it is hard to tell how long and how difficult the journey will be. These new ideas and techniques will not only be extremely valuable for future research on a spin quantum computer, but at the same time will yield more interesting and exciting physics in many fields such as spin physics, material science and quantum optics.

## References

- [1] D. Loss and D.P. DiVincenzo, Phys. Rev. A **57**, 120 (1998).
- [2] J.M. Elzerman *et al.*, Nature **430**, 431 (2004).
- [3] J. R. Petta *et al.*, Science **309**, 2180 (2005).
- [4] F. H. L. Koppens *et al.*, Phys. Rev. Lett. **100**, 236802 (2008).
- [5] D. P. DiVincenzo, Fortschritte Der Physik-Progress of Physics **48**, 771 (2000).
- [6] D. Gottesman, PhD thesis, arXiv preprint quant-ph/9705052, 1997.
- [7] A. Steane, Phys. Rev. A **68**, 42322 (2003).
- [8] T. Szkopek *et al.*, IEEE Trans.Nano. **5**, 42 (2006).
- [9] M. Blaauboer and D. P. DiVincenzo, Phys. Rev. Lett. **95**, 160402 (2005).
- [10] A. N. Jordan *et al.*, arXiv preprint cond-mat/0706.0180 (2007).
- [11] A. Romito *et al.*, arXiv preprint cond-mat/0707.3695 (2007).
- [12] R. Hanson *et al.*, Phys. Rev. Lett. **94**, 196802 (2005).
- [13] H.-A. Engel *et al.*, Phys. Rev. Lett. **93**, 106804 (2004).
- [14] L. M. K. Vandersypen and I. L. Chuang, Rev. Mod. Phys. **76**, 1034 (2004).
- [15] D. Klauser *et al.*, Phys. Rev. B **73**, 205302 (2006).
- [16] D. Stepanenko *et al.*, Phys. Rev. Lett. **96**, 136401 (2006).
- [17] G. Giedke *et al.*, Phys. Rev. A **74**, 32316 (2006).

- [18] M. S. Rudner and L. Levitov, arXiv preprint cond-mat/0705.2177 (2007).
- [19] J. Danon and Yu. V. Nazarov, *private communication* (2008).
- [20] J. M. Taylor *et al.*, Nature Physics **1**, (2005).
- [21] D. Stepanenko and G. Burkard, Phys. Rev. B **75**, 085324 (2007).
- [22] V. N. Golovach *et al.*, Phys. Rev. Lett. **93**, 016601 (2004).
- [23] S. Amasha *et al.*, arXiv preprint cond-mat/0707.1656 (2007).
- [24] N. Mason *et al.*, Science **303**, 655 (2004).
- [25] S. Sapmaz *et al.*, Nano Letters **6**, 1350 (2006).
- [26] N. Shaji *et al.*, arXiv preprint cond-mat/0708.0794 (2007).
- [27] Y. Hu *et al.*, arXiv preprint cond-mat/0706.2271 (2007).
- [28] B. Trauzettel, *et al.*, Nature Physics **3**, 192 (2007).
- [29] A. Tyryshkin *et al.*, Phys. Rev. B **68**, 193207 (2003).
- [30] L. Childress *et al.*, Science **314**, 281 (2006).
- [31] V. Chan *et al.*, Journal of Applied Physics **100**, 106104 (2006).
- [32] J. Meijer *et al.*, Applied Physics Letters **87**, 261909 (2005).
- [33] T. Gaebel *et al.*, Nature Physics **2**, 408 (2006).
- [34] B. E. Kane, Nature **393**, 133 (1998).
- [35] F. Jelezko *et al.*, Phys. Rev. Lett. **92**, 076401 (2004).
- [36] M. Dutt *et al.*, Science **316**, 1312 (2007).
- [37] M.A. Nielsen, I.L. Chuang, *Quantum Computation and Quantum Information* (Cambridge U. Press, New York, 2000).
- [38] Y. Tokura *et al.*, Phys. Rev. Lett. **96**, 047202 (2006).
- [39] K. Ono *et al.*, Science **297**, 1313 (2002).
- [40] J. Baugh *et al.*, arXiv preprint cond-mat/0705.1104 (2007).
- [41] E. Laird *et al.*, arXiv preprint cond-mat/0707.0557 (2007).
- [42] J. Gupta *et al.*, Science **292**, 2458 (2001).
- [43] J. Berezovsky *et al.*, Science **320**, 349 (2008).
- [44] C. Cohen-Tannoudji and J. Dupont-Roc, Phys. Rev. A **5** (1972).
- [45] D. P. DiVincenzo *et al.*, Nature **408**, 339 (2000).
- [46] W. Coish and D. Loss, Phys. Rev. B **72**, 125337 (2005).

- [47] X. Hu and S. Das Sarma, Phys. Rev. Lett. **96**, 100501 (2006).
- [48] M. Stopa and C. M. Marcus, arXiv preprint cond-mat/0604008 (2006).
- [49] C. Buizert *et al.*, arXiv preprint cond-mat/0808.0465 (2008).
- [50] L. Gaudreau *et al.*, Phys. Rev. Lett. **97**, 36807 (2006).
- [51] D. Schröer *et al.*, Phys. Rev. B **76**, 075306 (2007).
- [52] A. Imamoglu *et al.*, Phys. Rev. Lett. **83**, 4204 (1999).
- [53] O. Gywat *et al.*, Phys. Rev. B **73**, 125336 (2006).
- [54] L. Childress *et al.*, Phys. Rev. A **69**, 042302 (2004).
- [55] G. Burkard and A. Imamoglu, Phys. Rev. B **74**, 41307 (2006).

# Appendix A

## Singlet-Triplet relaxation as a function of their energy splitting

In this appendix we will find an expression for the singlet-triplet relaxation time as a function of the energy splitting between these states. For this spin relaxation we basically need two ingredients. We need the spin states to be mixed and we need a reservoir to absorb the excess energy. Here we invoke the spin-orbit interaction to provide the essential mixing of the spin states and the electron-phonon interaction allows us to give the excess energy to the phonon bath.

### A.1 Spin-orbit interaction

To describe in what way the spin-orbit interaction couples the singlet and triplet states in our two electron system, we follow [1] by starting out treating the spin-orbit coupling for each spin as a first order perturbation. We take both the Dresselhaus and the Rashba type spin-orbit into account. The Dresselhaus and Rashba Hamiltonians for each of the spins read:

$$H_D^{(i)} = \beta(-\sigma_x^{(i)}\pi_x^{(i)} + \sigma_y^{(i)}\pi_y^{(i)}) \quad (\text{A.1})$$

$$H_R^{(i)} = \alpha(-\sigma_x^{(i)}\pi_y^{(i)} + \sigma_y^{(i)}\pi_x^{(i)}) \quad (\text{A.2})$$

where  $\sigma_\mu^{(i)}$  represent the Pauli spin matrices operating on spin  $i$  ( $i = 1, 2$ ) and  $\pi_\mu^{(i)}$  is the canonical momentum operator for spin  $i$ .

From the single particle picture, we construct the appropriate basis for our two electron system. We restrict the state space of our model to  $|T_-\rangle$ ,  $|T_+\rangle$ ,  $|T_0\rangle$  and  $|S\rangle$  constructed from the ground orbital and the first excited orbital (the excited singlet is not present in the model). In the notation  $|T_-\rangle$ ,  $|T_+\rangle$ ,  $|T_0\rangle$  and  $|S\rangle$  both the orbital part and the spin part are present. For the orbital part of the

wave functions we assume Fock-Darwin states  $|n, l\rangle$ ). In this basis, the spin-orbit Hamiltonian has the following matrix representation:

$$H_{SO} = \frac{1-\theta_h}{l} \begin{pmatrix} 0 & \alpha & 0 & i\beta \\ \alpha & 0 & 0 & 0 \\ 0 & 0 & 0 & 0 \\ -i\beta & 0 & 0 & 0 \end{pmatrix} \quad (\text{A.3})$$

with  $\theta_h = \frac{\omega_c}{2\omega_h}$  and  $l = \sqrt{\hbar/m\omega_h}$ , where  $\omega_h = \sqrt{\omega_0^2 + \omega_c^2/4}$ . From Eq. (A.3) we can see that in the leading order of the spin-orbit interaction  $\langle T_0 | H_{SO} | S \rangle = \langle T_0 | H_{SO} | T_{\pm} \rangle = 0$ . In the rest of the calculation, we will make the following approximations: (i) we will neglect the magnetic field dependence of the spin-orbit coupling strength, (ii) we assume that  $\beta$  and  $\alpha$  are approximately equal, and (iii) the spin-orbit matrix elements are real. Using first order perturbation we can then write the new eigenstates  $|S'\rangle$  and  $|T'_{\pm}\rangle$  as hybridized states:

$$|S'\rangle = |S\rangle - \frac{M_{SO}}{\Delta E_{ST}}(|T_+\rangle + |T_-\rangle) \quad (\text{A.4})$$

$$|T'_{\pm}\rangle = |T_{\pm}\rangle + \frac{M_{SO}}{\Delta E_{ST}}|S\rangle \quad (\text{A.5})$$

where  $\Delta E_{ST}$  is the splitting in energy between the triplet states and the singlet state and  $M_{SO}$  the spin-orbit coupling strength.

## A.2 Electron-phonon interaction

Following [2, 3], we assume that our spins interact with 3D bulklike acoustic phonons. The energy scales in our experiment (see chapter 5) are small enough to ignore the presence of optical phonons (i.e.  $\Delta E_{ST} \ll \hbar\omega_{opt}$ , where  $\hbar\omega_{opt}$  is the energy of an optical phonon). We assume the phonons obey the isotropic dispersion relation  $\omega_{s\mathbf{q}} = c_s |\mathbf{q}|$  where  $c_s$  is the velocity of propagation of phonon mode  $s\mathbf{q}$ .

When phonons of mode index  $s\mathbf{q}$  are present in a volume  $L^3$ , the total displacement  $\xi_{\mathbf{a},\alpha}$  of the atom labelled by  $\alpha$  in the unit cell numbered by the lattice vector  $\mathbf{a}$  is given by [4]:

$$\begin{aligned}
\xi_{\mathbf{a},\alpha} &= \sum_{s\mathbf{q}} b_{s\mathbf{q}} (\xi_{\mathbf{a},\alpha})_{s\mathbf{q}} + c.c. \\
&= \frac{1}{L^{3/2}} \sum_{s\mathbf{q}} b_{s\mathbf{q}} \sqrt{\frac{\hbar a_0^3}{2M\omega_{s\mathbf{q}}}} \mathbf{d}_{s\mathbf{q}}^\alpha e^{i\mathbf{q}\cdot\mathbf{a} - i\omega_{s\mathbf{q}}t} + c.c.
\end{aligned} \tag{A.6}$$

where  $(\xi_{\mathbf{a},\alpha})_{s\mathbf{q}}$  is the displacement caused by a single phonon with mode index  $s\mathbf{q}$ ,  $M$  is the mass of a unit cell and  $a_0^3$  its volume,  $b_{s\mathbf{q}}$  is the amplitude of phonon mode  $s\mathbf{q}$  which has a frequency  $\omega_{s,q}$  and  $\mathbf{d}_{s\mathbf{q}}^\alpha$  are dimensionless polarization vectors.

This displacement of the atoms changes the potential which is felt by the electrons. We take two contributions to the change in potential into account: (i) the piezoelectric potential and (ii) the deformation potential. The piezoelectric potential is caused by piezoelectric phonons, which generate an electric potential that directly interacts with the electrons. The deformation potential is due to (deformation potential) phonons which modify the periodic potential on a microscopic scale and interact with the electrons since they locally change the electronic band structure. The Hamiltonian of the interaction with a phonon mode  $s\mathbf{q}$  can be derived to be:

$$H_{e,p}^{s\mathbf{q}} = \sqrt{\frac{\hbar}{2\rho\omega_{s\mathbf{q}}L^3}} (e^{i\mathbf{q}\cdot\mathbf{r}_1} + e^{i\mathbf{q}\cdot\mathbf{r}_2}) (e\beta_{s\mathbf{q}} - iq\Xi_{s\mathbf{q}}) \tag{A.7}$$

with the deformation potential  $\Xi_{s\mathbf{q}} = 8.2$  eV, the effective piezoelectric modulus  $\beta_{s\mathbf{q}}$  gives a contribution  $e\beta_{s\mathbf{q}} = 1.2 \times 10^7$  eV/cm,  $\rho = M/a_0^3$  and  $\mathbf{r}_i$  denotes the position of electron  $i$ .

From this Hamiltonian it becomes clear that the piezoelectric coupling is proportional to  $1/\sqrt{q}$ , whereas the deformation potential coupling is proportional to  $\sqrt{q}$ . This is because the piezoelectric potential is proportional to the atomic displacement  $\xi_{\mathbf{a},\alpha}$  and the deformation potential is proportional to the deformation tensor  $u \propto \frac{\partial \xi_{\mathbf{a},\alpha}}{\partial x}$ .

The electron states are effectively coupled to each other via the phonon propagating term  $e^{i\mathbf{q}\cdot\mathbf{r}}$ . We can separate the spatial variables and integrate in the  $z$ -direction. The relevant matrix element then becomes

$$\langle f | e^{i\mathbf{q}\cdot\mathbf{r}} | i \rangle = \langle f | e^{i\mathbf{q}_\parallel \cdot \mathbf{r}} | i \rangle F_z(q_z L_z/2) \tag{A.8}$$

where the form factor  $F_z$  corresponds to the coupling with the degree of freedom of the dot in the  $z$ -direction. For a square well confinement  $F_z$  takes the form

$$F_z(L_z q_z/2) = \frac{\sin(L_z q_z/2)}{L_z q_z/2} \frac{1}{1 + (L_z q_z/2/\pi)^2} \tag{A.9}$$

with  $q_z = q_0 \cos(\theta)$ . After this integration the electron-phonon Hamiltonian looks like:

$$H_{e,p}^{s\mathbf{q}} = \sqrt{\frac{\hbar}{2\rho\omega_{s\mathbf{q}}L^3}} F_z(L_z q_0 \cos(\theta)/2)(e^{i\mathbf{q}_{\parallel}\cdot\mathbf{r}_1} + e^{i\mathbf{q}_{\parallel}\cdot\mathbf{r}_2})(e\beta_{s\mathbf{q}} - iq\Xi_{s\mathbf{q}}) \quad (\text{A.10})$$

where we decomposed the phonon wave vector as  $\mathbf{q} = (\mathbf{q}_{\parallel}, q \cos(\theta))$ .

### A.3 Transition rates

The relaxation rates from the triplet states to the singlet state can be calculated using the Fermi golden rule

$$\Gamma_{T_1} = \frac{2\pi}{\hbar} \int d^3q \left(\frac{L}{2\pi}\right)^3 |\langle T'_{\pm} | H_{e,p} | S' \rangle|^2 \delta(E_{T'_{\pm}} - E_{S'} + E_{ph}) \quad (\text{A.11})$$

which shows the important matrix elements to calculate:

$$\langle T'_{\pm} | H_{e,p} | S' \rangle = \frac{M_{SO}}{\Delta E} (\langle S | H_{e,p} | S \rangle - \langle T_{\pm} | H_{e,p} | T_{\pm} \rangle) \quad (\text{A.12})$$

This calculation consists only of the evaluation of  $\langle S | e^{i\mathbf{q}_{\parallel}\cdot\mathbf{r}} | S \rangle$  and  $\langle T_{\pm} | e^{i\mathbf{q}_{\parallel}\cdot\mathbf{r}} | T_{\pm} \rangle$ . For this we decompose the unperturbed singlet and triplet states into a spin part and an orbital part:

$$|S\rangle = |\Phi_S\rangle |n=0, l=0\rangle_1 |n=0, l=0\rangle_2 \quad (\text{A.13})$$

$$\begin{aligned} |T_{\pm}\rangle &= \frac{1}{\sqrt{2}} |\Phi_{T_{\pm}}\rangle (|n=0, l=1\rangle_1 |n=0, l=0\rangle_2 \\ &\quad + |n=0, l=0\rangle_1 |n=0, l=1\rangle_2) \end{aligned} \quad (\text{A.14})$$

where  $|\Phi_{S,T_{\pm}}\rangle$  denote the spin part and  $|n, l\rangle$  the orbital part of the wavefunction, assumed to be the Fock-Darwin states. Calculation of the matrix elements yield:

$$\langle 0, 0 | e^{i\mathbf{q}_{\parallel}\cdot\mathbf{r}} | 0, 0 \rangle = e^{-\alpha^2 q_0^2 \sin^2(\theta)/4} \quad (\text{A.15})$$

$$\langle 0, 1 | e^{i\mathbf{q}_{\parallel}\cdot\mathbf{r}} | 0, 1 \rangle = (1 - \alpha^2 q_0^2 \sin^2(\theta)/4) e^{-\alpha^2 q_0^2 \sin^2(\theta)/4} \quad (\text{A.16})$$

where  $\alpha = \sqrt{\hbar/m^*\omega}$  is the size of the lateral confinement potential. We will assume that this size is constant (to first order) when we change the singlet-triplet energy splitting in our experiment.

Now we have evaluated the relevant matrix elements of the electron-phonon coupling, we continue to calculate the singlet-triplet relaxation rate from Fermi's



golden rule:

$$\begin{aligned}
(1/T_1)_{s\mathbf{q}} &= \frac{q_0^2 L^3}{2\pi\hbar^2 c_s} \int_0^{\pi/2} d\theta \sin(\theta) |\langle T'_\pm | H_{e,p}^{s\mathbf{q}} | S' \rangle|^2 \\
&= \frac{q_0^2}{2\pi\rho\hbar^3 c_s^4} \frac{M_{SO}^2}{\Delta E_{ST}^2} (q_0 \Xi_{s\mathbf{q}}^2 + \frac{e^2 \beta_{s\mathbf{q}}^2}{q_0}) \frac{q_0^4 \alpha^4}{16} \int_0^{\pi/2} d\theta \sin^5(\theta) e^{-q_0^2 \sin^2(\theta) \alpha^2 / 2} \\
&= \frac{1}{2\pi\rho\hbar^3 c_s^4} M_{SO}^2 (q_0 \Xi_{s\mathbf{q}}^2 + \frac{e^2 \beta_{s\mathbf{q}}^2}{q_0}) \frac{q_0^4 \alpha^4}{16} \int_0^{\pi/2} d\theta \sin^5(\theta) e^{-q_0^2 \sin^2(\theta) \alpha^2 / 2} \\
&= \frac{M_{SO}^2 e^2 \beta_{s\mathbf{q}}^2}{32\pi\rho\hbar^3 c_s^4} \frac{\alpha^4}{\hbar^3 c_s^3} (\Delta E_{ST}^3 + \Delta E_{ST}^5 / \Lambda_{s\mathbf{q}}) \int_0^{\pi/2} d\theta \sin^5(\theta) e^{-\Delta E_{ST}^2 \alpha^2 \sin^2(\theta) / 2 \hbar^2 c_s^2}
\end{aligned} \tag{A.17}$$

with  $\Lambda_{s\mathbf{q}} = \hbar^2 c_s^2 e^2 \beta_{s\mathbf{q}}^2 / \Xi_{s\mathbf{q}}^2 = 0.26 \text{ meV}^2$ . From the fit of the relaxation curve, we obtain  $\frac{M_{SO}^2 e^2 \beta_{s\mathbf{q}}^2}{2\pi\rho\hbar^3 c_s^4} \frac{\alpha^4}{\hbar^3 c_s^3} = 2.10^6 \text{ meV}^{-3} \text{s}^{-1}$  and  $\frac{\alpha}{\hbar c_s} = 7.2 \text{ meV}^{-1}$ . We conclude that  $\alpha = 23.4 \text{ nm}$  and  $M_{SO} = 0.42 \text{ } \mu\text{eV}$ . From  $\alpha$  we deduce  $\hbar\omega_0 = 1.875 \text{ meV}$  which is a dot confinement energy in agreement with what we usually have.

As a conclusion, we remark a dependence on  $q^3$  of the relaxation rate induced by piezoelectric phonon ( $1/q$  for the coupling strength of piezoelectric phonon-electron interaction,  $q^2$  for the phonon density of states,  $1/q^2$  for the spin orbit interaction and  $q^4$  for the matching between wavelength and dot size in electron-phonon interaction. For deformation phonon, the coupling strength is proportional to  $q$ , leading to a relaxation rate in  $q^5$ .

We know take into account all possible phonon polarization and different speed of sound,  $c_l$  for longitudinal phonons and  $c_t$  for transverse phonons.

$$H_{e,p} = \sum_{s,\mathbf{q}} \frac{F_z(L_z q_0 \cos \theta / 2)}{\sqrt{2\rho q c_s / \hbar}} (e^{i\mathbf{q}_{\parallel} \cdot \mathbf{r}_1} + e^{i\mathbf{q}_{\parallel} \cdot \mathbf{r}_2}) (e\beta_{s,\mathbf{q}} - iq\Xi_{s,\mathbf{q}}) \tag{A.18}$$

The factor  $F_z(L_z q_0 \cos \theta / 2)$  depends on the type of quantum well and its characteristic distance  $L_z$ . From now on we consider it to be 1.

For deformation potential phonons, we see that only longitudinal phonons are relevant. So the contribution of these phonons will be:

$$1/T_{1,def} = \frac{M_{SO}^2 \Xi^2 \alpha^4}{32\pi\rho\hbar^6} \frac{\Delta E_{ST}^5}{\hbar^2 c_l^9} \int_0^{\pi/2} d\theta \sin^5(\theta) e^{-\Delta E_{ST}^2 \alpha^2 \sin^2(\theta) / 2 \hbar^2 c_l^2} \tag{A.19}$$

For piezoelectric phonons, all polarization are important. The different coupling constant  $\beta_{s\mathbf{q}}$  are  $\theta$  dependent due to the polarization. For the longitudinal and two transverse modes of the piezoelectric phonons we find the coupling con-

stants to be:

$$e\beta_l = \frac{3\sqrt{2}}{4}e\beta \sin^2(\theta) \cos(\theta) \quad (\text{A.20})$$

$$e\beta_{t1} = \frac{\sqrt{2}}{4}e\beta \sin(2\theta) \quad (\text{A.21})$$

$$e\beta_{t2} = \frac{\sqrt{2}}{4}e\beta(3\cos^2(\theta) - 1) \sin(\theta) \quad (\text{A.22})$$

which lead to three piezoelectric contributions to the relaxation time

$$1/T_{1,\text{piez},l} = 9\Upsilon_l \int_0^{\pi/2} d\theta \sin(\theta)^7 \cos^2\theta e^{-\frac{\Delta E_{ST}^2 \alpha^2 \sin(\theta)^2}{2\hbar^2 c_l^2}} \quad (\text{A.23})$$

$$1/T_{1,\text{piez},t1} = \Upsilon_t \int_0^{\pi/2} d\theta \sin(\theta)^5 \sin 2\theta^2 e^{-\frac{\Delta E_{ST}^2 \alpha^2 \sin(\theta)^2}{2\hbar^2 c_t^2}} \quad (\text{A.24})$$

$$1/T_{1,\text{piez},t2} = \Upsilon_t \int_0^{\pi/2} d\theta \sin(\theta)^5 (3\cos^2\theta - 1)^2 \sin\theta^2 e^{-\frac{\Delta E_{ST}^2 \alpha^2 \sin(\theta)^2}{2\hbar^2 c_t^2}} \quad (\text{A.25})$$

where  $\Upsilon_{l,t} = \frac{2}{16} \frac{M_{SO}^2 e^2 \beta^2 \alpha^4}{32\pi \rho \hbar^6 c_{l,t}^7} \Delta E_{ST}^3$ . By adding all the rates above we obtain the expression for the total singlet-triplet relaxation rate used in chapter 5 to fit the relaxation rate as a function of the singlet-triplet energy splitting:

$$\begin{aligned} 1/T_1 = & \frac{M_{SO}^2 \alpha^4}{32\pi \rho \hbar^6} \left( \frac{\Xi^2 \Delta E_{ST}^5}{\hbar^2 c_l^9} \int_0^{\pi/2} d\theta \sin^5(\theta) e^{-\frac{\Delta E_{ST}^2 \alpha^2 \sin^2(\theta)}{2\hbar^2 c_l^2}} \right. \\ & \left. + \sum_{j=l,t1,t2} \frac{e^2 \beta^2 \Delta E_{ST}^3}{c_j^7} \int_0^{\pi/2} d\theta |A_j(\theta)|^2 \sin^5(\theta) e^{-\frac{\Delta E_{ST}^2 \alpha^2 \sin^2(\theta)}{2\hbar^2 c_j^2}} \right) \end{aligned} \quad (\text{A.26})$$

where we've introduced  $A_s(\theta)e\beta = e\beta_{s\mathbf{q}}$ .

## References

- [1] M. Florescu and P. Hawrylak, Phys. Rev. B **73**, 045304 (2006).
- [2] V.N. Golovach, A.V. Khaetskii, D. Loss, Phys. Rev. Lett. **93**, 016601 (2004)
- [3] U. Bockelmann, Phys. Rev. B **50**, 17271 (1994)
- [4] V.F. Gantmakher and Y.B. Levinson, *Carrier scattering in Metals and Semiconductors* (North-Holland, Amsterdam, 1987)

# Summary

## Manipulation and Read-out of Spins in Quantum Dots

This thesis describes a series of experiments aimed at understanding and controlling the behavior of the spin degree of freedom of single electrons, confined in semiconductor quantum dots. This work is motivated by the prospects of using the electron spin as a quantum bit (qubit), the computational unit of a quantum computer. Here, the envisioned basis states (logical 0 and 1) of the qubit are the two possible orientations of the spin in a magnetic field: ‘spin-up’ (parallel to the field) and ‘spin-down’ (anti-parallel to the field). The research in this thesis is focused on manipulation and read-out of these spins as well as increasing our understanding of the interactions of the electron spin with its environment.

A quantum dot is an electrostatic trap for electrons in a semiconductor, which can contain a controllable number of electrons. This dot is coupled via tunnel barriers to reservoirs, with which electrons can be exchanged. The dot is also capacitively coupled to one or more gate electrodes that allow the number of electrons on the dot to be varied. Due to the small dot size (typically  $\sim 50$  nm), comparable to the Fermi wavelength of the electrons, it exhibits a discrete energy spectrum. The quantum dot devices studied in this work are defined in a two-dimensional electron gas (2DEG) of a GaAs/AlGaAs heterostructure, by applying negative voltages to metallic gate electrodes fabricated on top of the heterostructure.

There are two methods to probe the electronic properties of a quantum dot. The conventional approach is to look at the transport of electrons through the dot. A bias voltage is applied over the device, and the resulting current is measured. The dependence of the current on bias voltage and on the voltage that is applied to the surface gates provides detailed information on the energy level spectrum, electron (spin) states and the coupling of the different states to the reservoirs. Another approach is to measure the current through an external charge detector located next to the dot, e.g. a quantum point contact (QPC). A QPC is a narrow channel in the 2DEG, of which the conductance can be made very sensitive to

the electrostatic environment. By applying a bias voltage over the constriction, and measuring the resulting current, the QPC is operated as a sensor that is sensitive to the charge dynamics on the adjacent quantum dot. This technique is very versatile and can, in contrast to transport measurements, still be used when the tunnel coupling between the dot and the reservoirs is very weak.

In the first part of the thesis we focus on one of the key ingredients for a quantum computer: single-shot read-out of the spin states. The second part of the thesis covers another crucial step towards a small scale quantum computer: the coherent control of a single electron spin.

In order to read out spin states, we convert the spin information to charge information. This is done by using the spin-dependence of the tunnel rates, achieving a measurement visibility of more than 80%. We find that the relaxation can be very slow, with relaxation times up to milliseconds. We find a strong magnetic field dependence that hints at spin-orbit interaction as the dominant relaxation mechanism. Reducing the length of the read-out pulse together with fast reinitialization of the spin state allows us to perform repeated measurements, used to probe the evolution between two consecutive measurements. We demonstrate that, if we not only exploit spin-dependent tunnel rates but spin-dependent energies as well, the read-out fidelity increases to 97.5%.

One of the key advantages of the tunnel rate selective read-out is the ability to read out (nearly) degenerate spin states. We vary the singlet-triplet energy splitting over a wide range by changing the electric and magnetic confinement of the electrons, and measure the singlet-triplet relaxation time. The observed dependence on the energy splitting confirms that the spin-flip energy is dissipated in the phonon bath.

Then, a novel approach to ultra fast charge detection is introduced: a high electron mobility transistor (HEMT) operated as a cryogenic pre-amplification stage. This will increase the spin read-out fidelity and enable us to study real-time electron and nuclear dynamics on shorter timescales. We demonstrate that a cryogenic HEMT amplifier can be used to increase the bandwidth of a charge detection setup with a QPC charge sensor to 1 MHz. This setup allows us to detect fluctuations in the occupation of an adjacent quantum dot as short as 400 nanoseconds. The equivalent input noise of the HEMT turns out to limit the signal-to-noise ratio. We investigate whether we can decrease the noise by using different (biasing of the) HEMTs and propose ways to further improve this setup.

Coherent control over the electron spin is realized by combining a small oscillating magnetic field with a perpendicular larger static field. When the frequency of the oscillating field matches the (Larmor) precession frequency of the spin in the static field, the spin direction will spiral from spin-up to spin-down and again

back to spin-up. By applying bursts of the oscillating field, we rotate the spin to any pre-defined superposition state and subsequently read it out.

The electron spin is interacting with many surrounding nuclear spins of the host lattice via the hyperfine interaction. Therefore, the coherence properties of the electron spin depend on the dynamics of these nuclear spins. Since the hyperfine interaction works both ways, the nuclear spin dynamics depends in turn on the dynamics of the electron spin. This results in a strong electron-nuclear feedback which can be used to lock the electron spin into resonance with the applied microwaves. We use this locking to indirectly control the nuclear spins of the surrounding GaAs lattice, allowing us to dynamically polarize and depolarize the nuclear spins. A possible explanation for this locking is that the nuclear polarization exhibits stable configurations in which fluctuations of the nuclear spins are reduced. Reduction of the fluctuations of the nuclear spin bath is crucial for coherence enhancement of an electron spin in a GaAs environment.

Ivo Vink  
October 2008



# Samenvatting

## Manipulatie en Uitlezing van Spins in Quantum Dots

Dit proefschrift beschrijft een reeks experimenten, die tot doel hebben het gedrag van de spinvrijheidsgraad van enkele elektronen, opgesloten in een halfgeleider quantum dot, te begrijpen en onder controle te krijgen. De motivatie voor dit onderzoek is de mogelijke toepassing van de spin van een elektron als quantum bit (of qubit), de elementaire rekeneenheid van een quantum computer. De beoogde basistoestanden van de qubit (de logische 0 en 1) zijn de twee mogelijke richtingen van de spin in een magnetisch veld: 'spin-omhoog' (parallel aan het magnetische veld) en 'spin-omlaag' (antiparallel aan het magnetische veld). Het onderzoek in dit proefschrift richt zich op zowel het manipuleren en uitlezen van deze spintoestanden, als het vergroten van de kennis over de verschillende interacties van de elektronspin met zijn omgeving.

Een quantum dot kan worden beschouwd als een klein 'doosje' gevuld met een regelbaar aantal elektronen. Dit doosje is via tunnelbarrières gekoppeld aan reservoirs, waar elektronen mee kunnen worden uitgewisseld, en het is capacitief gekoppeld aan één of meer 'gate' elektroden waarmee het elektronenaantal op de dot gevarieerd kan worden. Vanwege de kleine afmetingen van de dot (typisch 50 nm), vergelijkbaar met de Fermi golflengte van de elektronen, vertoont de dot een discreet energiespectrum. De in dit werk bestudeerde quantum dots zijn gedefinieerd in een tweedimensionaal elektronengas (2DEG) van een GaAs/AlGaAs heterostructuur door negatieve spanningen aan te brengen op metalen elektroden bovenop de heterostructuur.

Er zijn twee manieren om de elektronische eigenschappen van een quantum dot te onderzoeken. De conventionele methode is het kijken naar het transport van elektronen door de dot. Een spanningsverschil wordt aangelegd over de structuur en de resulterende stroom wordt gemeten. De afhankelijkheid van die stroom van het aangelegde spanningsverschil en de spanning op de elektroden geeft gedetailleerde informatie over het spectrum van energieniveaus, elektron(spin)toestanden en de tunnelkoppeling van de verschillende toestanden naar

de reservoirs. Een andere aanpak is het meten van de stroom die loopt door een externe ladingsdetector die vlak naast de dot is geplaatst, bijvoorbeeld een quantum punt contact (QPC). Een QPC is een nauw kanaaltje in het 2DEG waarvan de geleiding erg gevoelig gemaakt kan worden voor de elektrostatistische omgeving. Door een spanningsverschil aan te leggen over het kanaaltje en de resulterende stroom te meten kan de QPC worden gebruikt als een sensor die gevoelig is voor de ladingdynamica op de naastgelegen quantum dot. Deze techniek is erg veelzijdig en kan, in tegenstelling tot transportmetingen, nog steeds worden gebruikt wanneer de tunnelkoppeling van de dot naar de reservoirs erg klein is.

In het eerste deel van het proefschrift concentreren we ons op één van de belangrijkste ingrediënten van een quantum computer: uitlezing van de spintoestand in een enkele meting. Het tweede deel van het proefschrift bestrijkt een andere cruciale stap richting een kleinschalige quantum computer: de coherente controle over een enkele elektronspin.

Om de spintoestanden uit te kunnen lezen converteren we de spininformatie in ladingsinformatie. Hiervoor gebruiken we het feit dat de tunnelfrequenties afhangen van de spintoestand, hetgeen resulteert in een nauwkeurigheid van een enkele meting boven de 80%. Voor deze spintoestanden wordt een zeer langzaam verval gevonden met vervaltijden tot aan milliseconden. De sterke magneetveldafhankelijkheid suggereert dat de spin-baan interactie het dominante vervalmechanisme is. Het verkorten van de uitleespuls samen met de snelle herinitialisatie van de spintoestand, stelt ons in staat om herhaaldelijk een meting te doen waarmee we de evolutie van de spintoestanden tussen twee opeenvolgende metingen kunnen bestuderen. Verder demonstreren we dat, als we niet alleen gebruik maken van de spinafhankelijkheid van de tunnelfrequenties maar ook van de spinafhankelijke energieën, de enkele-meting-nauwkeurigheid oploopt tot 97.5%.

Eén van de grote voordelen van de uitlezing die gebruik maakt van de spinafhankelijke tunnelfrequenties is de mogelijkheid om (bijna) ontaarde toestanden uit te kunnen lezen. We variëren het singlet-triplet energieverval over een groot gebied door zowel de elektrische als de magnetische opsluiting van de elektronen te veranderen en meten vervolgens de singlet-triplet vervaltijd. De waargenomen afhankelijkheid van het energieverval bevestigt dat de spin-flip energie door het phononbad wordt gedissipeerd.

Daarna introduceren we een nieuwe benadering van ultrasnelle ladingsdetectie: een hoge-elektron-mobiliteit-transistor (HEMT), gebruikt als een cryogene voorversterker. Dit zal de nauwkeurigheid van de spinuitlezing vergroten en ons in staat stellen om 'real-time' elektron- en nucleaire dynamica te bestuderen op kortere tijdschalen. We demonstreren dat een cryogene HEMT-versterker kan worden gebruikt om de bandbreedte van een ladingsdetectie opstelling met een



QPC te verhogen tot 1 MHz. Deze opstelling stelt ons in staat om fluctuaties in de bezetting van een naastgelegen quantum dot, vanaf 400 nanoseconden, te detecteren. Het blijkt dat de equivalente ingangsrui van de HEMT de signaal-rui verhouding limiteert. We onderzoeken of we de rui kunnen verminderen door verschillende (instelpunten van de) HEMTs te gebruiken en doen suggesties tot verdere verbetering van deze opstelling.

Coherente controle over de elektronspin is gerealiseerd door een klein oscillerend magnetisch veld te combineren met een groter statisch veld daar loodrecht op. Wanneer de frequentie van dit oscillerende veld overeenkomt met de (Larmor-) precessiefrequentie van de spin in het statische veld zal de spinrichting zich in een spiraalbaan bewegen van spin-omhoog naar spin-omlaag en weer terug naar spin-omhoog. Door het oscillerende veld gedurende een korte tijd aan te bieden kan de spin in iedere gewenste superpositietoestand worden gebracht en vervolgens worden uitgelezen.

De elektronspin heeft interactie met veel nucleaire spins in zijn directe omgeving via de hyperfijn interactie. De coherentie-eigenschappen van de elektronspin hangen daarom af van de dynamica van deze nucleaire spins. Aangezien de hyperfijn interactie twee kanten opwerkt, hangt de nucleaire spindynamica op haar beurt af van de dynamica van de elektronspin. Dit resulteert in een sterke elektron-nucleaire terugkoppeling die gebruikt kan worden om de elektronspin vast te houden op resonantie met de aangeboden microgolven. We gebruiken dat vasthouden om indirect de toestand van de nucleaire spins in het omringende GaAs rooster te controleren en het stelt ons in staat om de nucleaire spins dynamisch te polariseren en te depolariseren. Een mogelijke verklaring van dit vasthouden is dat de nucleaire spinpolarisatie stabiele punten heeft waarin fluctuaties van de nucleaire spins worden onderdrukt. Het onderdrukken van de fluctuaties in het nucleaire spinbad is cruciaal voor het verbeteren van de coherentie van een elektronspin in een GaAs omgeving.

Ivo Vink  
oktober 2008



# Curriculum Vitae

Ivo Timon Vink

- June 8, 1979    Born in Alkmaar, The Netherlands.
- 1991 – 1997    Grammar school at the Han Fortmann College, Heerhugowaard.
- 1997 – 2004    MSc Applied Physics (*Cum Laude*),  
Delft University of Technology.  
Graduate research in the group of prof. dr. ir. L. P. Kouwenhoven.  
”*Spin Filtering and Single-Spin Manipulation in Quantum Dots*”.
- 1999 – 2000    Board member of the student association of Applied Physics.
- 2004            Research at Yale University, Connecticut, USA  
under supervision of prof. dr. R. J. Schoelkopf.  
”*Proof of principle demonstration of a Radio-Frequency QPC*”.
- 2004            Research at IBM Almaden Research Center, California, USA  
under supervision of dr. D. M. Eigler and dr. A. J. Heinrich.  
”*Deposition of atomic layers of NaCl for STM spin-flip spectroscopy*”.
- 2004 – 2008    PhD research at Delft University of Technology  
under supervision of prof. dr. ir. L. M. K. Vandersypen and  
prof. dr. ir. L. P. Kouwenhoven.  
”*Manipulation and Read-out of Spins in Quantum Dots*”.



# List of publications

1. *Locking electron spins into resonance by electron-nuclear feedback*  
I. T. Vink, K. C. Nowack, F. H. L. Koppens, J. Danon, Yu. V. Nazarov and L. M. K. Vandersypen,  
*In preparation for submission.*
2. *Multiple nuclear polarization states in a double quantum dot*  
J. Danon, I. T. Vink, F. H. L. Koppens, K. C. Nowack, L. M. K. Vandersypen and Yu. V. Nazarov,  
*In preparation for submission.*
3. *In situ reduction of charge noise in GaAs/Al<sub>x</sub>Ga<sub>1-x</sub>As Schottky-gated devices*  
C. Buizert, F. H. L. Koppens, M. Pioro-Ladrière, H. P. Tranitz, I. T. Vink, S. Tarucha, W. Wegscheider and L. M. K. Vandersypen,  
*submitted to Phys. Rev. Lett.*
4. *A cryogenic amplifier for fast real-time detection of single-electron tunneling*  
I. T. Vink, T. Nooitgedagt, R.N. Schouten, W. Wegscheider and L. M. K. Vandersypen,  
Applied Physics Letters **91**, 123512 (2007)
5. *Experimental signature of phonon-mediated spin relaxation*  
T. Meunier, I. T. Vink, L. H. Willems van Beveren, K-J. Tielrooij, R. Hanson, F. H. L. Koppens, H. P. Tranitz, W. Wegscheider, L. P. Kouwenhoven and L. M. K. Vandersypen,  
Physical Review Letters **98**, 126601 (2007)
6. *Detection of single electron spin resonance in a double quantum dot*  
F. H. L. Koppens, C. Buizert, I. T. Vink, K. C. Nowack, T. Meunier, L. P. Kouwenhoven, and L. M. K. Vandersypen,  
Journal of Applied Physics **101**, 081706 (2007)
7. *Nondestructive measurement of electron spins in a quantum dot*  
T. Meunier, I. T. Vink, L. H. Willems van Beveren, F. H. L. Koppens, H. P. Tranitz, W. Wegscheider, L. P. Kouwenhoven, and L. M. K. Vandersypen,  
Physical Review B **74**, 195303 (2006)

8. *Driven coherent oscillations of a single electron spin in a quantum dot*  
F. H. L. Koppens, C. Buizert, K. J. Tielrooij, I. T. Vink, K. C. Nowack, T. Meunier, L. P. Kouwenhoven, and L. M. K. Vandersypen,  
*Nature* **442**, 766 (2006)
9. *Single-shot readout of electron spins in a semiconductor quantum dot*  
R. Hanson, L. H. Willems van Beveren, I. T. Vink, J. M. Elzerman, F. H. L. Koppens, L. P. Kouwenhoven and L. M. K. Vandersypen,  
*Physica E - low-dimensional systems and nanostructures*, **34**(1-2), 1-5. (2006).
10. *High fidelity measurement of singlet-triplet states in a quantum dot*  
T. Meunier, K-J. Tielrooij, I. T. Vink, F. H. L. Koppens, H. P. Tranitz, W. Wegscheider, L. P. Kouwenhoven and L. M. K. Vandersypen,  
*Physica status solidi b-basic research*, **243**, 3855-3858.(2006).
11. *Spin filling of a quantum dot derived from excited-state spectroscopy*  
L. H. Willems van Beveren, R. Hanson, I. T. Vink, J. M. Elzerman, F.H. L. Koppens, L. P. Kouwenhoven and L. M. K. Vandersypen,  
*New Journal of Physics* **7**, Solid State Quantum Information (2005).
12. *Single-shot read-out of electron spin states in a quantum dot using spin-dependent tunnel rates*  
R. Hanson, L. H. Willems van Beveren, I. T. Vink, J. M. Elzerman, F. H. L. Koppens, L. P. Kouwenhoven, and L. M. K. Vandersypen,  
*Proceedings Electronic Properties of Two-Dimensional Systems (EP2DS)* (2005).
13. *Control and Detection of Singlet-Triplet Mixing in a Random Nuclear Field*  
F. H. L. Koppens, J. A. Folk, J. M. Elzerman, R. Hanson, L. H. Willems van Beveren, I. T. Vink, H. P. Tranitz, W. Wegscheider, L. P. Kouwenhoven and L. M. K. Vandersypen,  
*Science* **309**, 1346-1350 (2005).
14. *Single-shot read-out of electron spin states in a quantum dot using spin-dependent tunnel rates*  
R. Hanson, L. H. Willems van Beveren, I. T. Vink, J. M. Elzerman, W. J. M. Naber, F. H. L. Koppens, L. P. Kouwenhoven and L. M. K. Vandersypen,  
*Physical Review Letters* **94**, 196802 (2005).
15. *Semiconductor few-electron quantum dot operated as a bipolar spin filter*  
R. Hanson, L. M. K. Vandersypen, L. H. Willems van Beveren, J. M. Elzerman, I. T. Vink and L. P. Kouwenhoven,  
*Physical Review B* **70**, 241304(R) (2004).

16. *Determination of the tunnel rates through a few-electron quantum dot*  
R. Hanson, I. T. Vink, D. P. DiVincenzo, L. M. K. Vandersypen, J. M. Elzerman,  
L. H. Willems van Beveren and L. P. Kouwenhoven,  
Proceedings of XXXIXth Rencontres de Moriond (2004).





